

World Journal of *Radiology*

World J Radiol 2024 September 28; 16(9): 375-496



EDITORIAL

- 375 Innovative approaches beyond periprocedural hydration for preventing contrast-induced acute kidney injury
Cheng CH, Hao WR, Cheng TH

ORIGINAL ARTICLE**Retrospective Study**

- 380 Intentionally unilateral prostatic artery embolization: Patient selection, technique and potential benefits
Moschouris H, Stamatou K
- 389 Cryoablation of osteoid osteomas: Is it a valid treatment option?
Michailidis A, Panos A, Samoladas E, Dimou G, Mingou G, Kosmoliaptis P, Arvaniti M, Giankoulof C, Petsatodis E
- 398 Radiological findings of February 2023 twin earthquakes-related spine injuries
Bolukçu A, Erdemir AG, İdilman İS, Yıldız AE, Çoban Çiğci G, Onur MR, Akpınar E

Observational Study

- 407 Retinal microcirculation changes in prediabetic patients with short-term increased blood glucose using optical coherence tomography angiography
Ly BJ, Zuo HJ, Li QF, Huang FF, Zhang T, Huang RX, Zheng SJ, Wan WJ, Hu K
- 418 Nomogram for predicting short-term response to anti-vascular endothelial growth factor treatment in neovascular age-related macular degeneration: An observational study
Huang ZH, Tu XZ, Lin Q, Tu M, Lin GC, Zhang KP
- 429 Cerebral perfusion in patients with unilateral internal carotid artery occlusion by dual post-labeling delays arterial spin labeling imaging
Zhang GR, Zhang YY, Liang WB, Ding D

CASE REPORT

- 439 Acquired factor XIII deficiency presenting with multiple intracranial hemorrhages and right hip hematoma: A case report
Wang L, Zhang N, Liang DC, Zhang HL, Lin LQ
- 446 Myelin oligodendrocyte glycoprotein-associated transverse myelitis after SARS-CoV-2 infection: A case report
Zheng JR, Chang JL, Hu J, Lin ZJ, Lin KH, Lu BH, Chen XH, Liu ZG
- 453 Extralobar pulmonary sequestration in children with abdominal pain: Four case reports
Jiang MY, Wang YX, Lu ZW, Zheng YJ

- 460 Behcet's disease-related panuveitis following COVID-19 vaccination: A case report
Lin RT, Liu PK, Chang CW, Cheng KC, Chen KJ, Chang YC
- 466 Hyperparathyroidism presented as multiple pulmonary nodules in hemodialysis patient status post parathyroidectomy: A case report
Chiang PH, Ko KH, Peng YJ, Huang TW, Tang SE
- 473 Secondary rectal linitis plastica caused by prostatic adenocarcinoma - magnetic resonance imaging findings and dissemination pathways: A case report
Labra AA, Schiappacasse G, Cocio RA, Torres JT, González FO, Cristi JA, Schultz M
- 482 *Pneumocystis* pneumonia in stage IIIA lung adenocarcinoma with immune-related acute kidney injury and thoracic radiotherapy: A case report
Zheng YW, Pan JC, Wang JF, Zhang J
- 489 Prolonged course of Paxlovid administration in a centenarian with COVID-19: A case report
Zhang YX, Tang J, Zhu D, Wu CY, Liang ML, Huang YT

ABOUT COVER

Editorial Board Member of *World Journal of Radiology*, Roberto Grassi, MD, Professor, Chief, Department of Radiology, University of Campania Luigi Vanvitelli, Napoli, 80138, Italy. roberto.grassi@unicampania.it

AIMS AND SCOPE

The primary aim of *World Journal of Radiology (WJR, World J Radiol)* is to provide scholars and readers from various fields of radiology with a platform to publish high-quality basic and clinical research articles and communicate their research findings online.

WJR mainly publishes articles reporting research results and findings obtained in the field of radiology and covering a wide range of topics including state of the art information on cardiopulmonary imaging, gastrointestinal imaging, genitourinary imaging, musculoskeletal imaging, neuroradiology/head and neck imaging, nuclear medicine and molecular imaging, pediatric imaging, vascular and interventional radiology, and women's imaging.

INDEXING/ABSTRACTING

The *WJR* is now abstracted and indexed in PubMed, PubMed Central, Emerging Sources Citation Index (Web of Science), Reference Citation Analysis, China Science and Technology Journal Database, and Superstar Journals Database. The 2024 Edition of Journal Citation Reports® cites the 2023 journal impact factor (JIF) for *WJR* as 1.4; JIF without journal self cites: 1.4; 5-year JIF: 1.8; JIF Rank: 132/204 in radiology, nuclear medicine and medical imaging; JIF Quartile: Q3; and 5-year JIF Quartile: Q3.

RESPONSIBLE EDITORS FOR THIS ISSUE

Production Editor: *Wen-Bo Wang*; Production Department Director: *Xu Guo*; Cover Editor: *Jia-Ping Yan*.

NAME OF JOURNAL

World Journal of Radiology

ISSN

ISSN 1949-8470 (online)

LAUNCH DATE

January 31, 2009

FREQUENCY

Monthly

EDITORS-IN-CHIEF

Thomas J Vogl

EDITORIAL BOARD MEMBERS

<https://www.wjgnet.com/1949-8470/editorialboard.htm>

PUBLICATION DATE

September 28, 2024

COPYRIGHT

© 2024 Baishideng Publishing Group Inc

INSTRUCTIONS TO AUTHORS

<https://www.wjgnet.com/bpg/gerinfo/204>

GUIDELINES FOR ETHICS DOCUMENTS

<https://www.wjgnet.com/bpg/GerInfo/287>

GUIDELINES FOR NON-NATIVE SPEAKERS OF ENGLISH

<https://www.wjgnet.com/bpg/gerinfo/240>

PUBLICATION ETHICS

<https://www.wjgnet.com/bpg/GerInfo/288>

PUBLICATION MISCONDUCT

<https://www.wjgnet.com/bpg/gerinfo/208>

ARTICLE PROCESSING CHARGE

<https://www.wjgnet.com/bpg/gerinfo/242>

STEPS FOR SUBMITTING MANUSCRIPTS

<https://www.wjgnet.com/bpg/GerInfo/239>

ONLINE SUBMISSION

<https://www.f6publishing.com>

Innovative approaches beyond periprocedural hydration for preventing contrast-induced acute kidney injury

Chun-Han Cheng, Wen-Rui Hao, Tzu-Hung Cheng

Specialty type: Radiology, nuclear medicine and medical imaging

Provenance and peer review: Invited article; Externally peer reviewed.

Peer-review model: Single blind

Peer-review report's classification

Scientific Quality: Grade B

Novelty: Grade A

Creativity or Innovation: Grade A

Scientific Significance: Grade A

P-Reviewer: Shao JW

Received: June 27, 2024

Revised: September 22, 2024

Accepted: September 24, 2024

Published online: September 28, 2024

Processing time: 92 Days and 5.6 Hours



Chun-Han Cheng, Department of Medical Education, Linkou Chang Gung Memorial Hospital, Taoyuan 33305, Taiwan

Wen-Rui Hao, Division of Cardiology, Department of Internal Medicine, Shuang Ho Hospital, Ministry of Health and Welfare, Taipei Medical University, Taipei 23561, Taiwan

Wen-Rui Hao, Division of Cardiology, Department of Internal Medicine, School of Medicine, College of Medicine, Taipei Medical University, Taipei 11002, Taiwan

Tzu-Hung Cheng, Department of Biochemistry, School of Medicine, College of Medicine, China Medical University, Taichung 404328, Taiwan

Co-corresponding authors: Wen-Rui Hao and Tzu-Hung Cheng.

Corresponding author: Tzu-Hung Cheng, PhD, Professor, Department of Biochemistry, School of Medicine, College of Medicine, China Medical University, No. 91 Xueshi Road, North District, Taichung 404328, Taiwan. thcheng@mail.cmu.edu.tw

Abstract

Contrast-induced acute kidney injury (CI-AKI) is a major concern in clinical practice, particularly among high-risk patients with preexisting renal and cardiovascular conditions. Although periprocedural hydration has long been the primary approach for CI-AKI prevention, recent advancements have led to the development of novel approaches such as RenalGuard and contrast removal systems. This editorial explores these emerging approaches and highlights their potential for enhancing CI-AKI prevention. By incorporating the latest evidence into clinical practice, health-care professionals can more effectively maintain renal function and improve outcomes for patients undergoing contrast-enhanced procedures.

Key Words: Contrast-induced acute kidney injury; Contrast-induced acute kidney injury prevention; Periprocedural hydration; RenalGuard; Contrast removal systems

©The Author(s) 2024. Published by Baishideng Publishing Group Inc. All rights reserved.

Core Tip: Preventing contrast-induced acute kidney injury (CI-AKI) is crucial for patients undergoing contrast-enhanced procedures, particularly those with preexisting renal or cardiovascular conditions. Although periprocedural hydration remains a fundamental preventive measure, emerging approaches such as RenalGuard and contrast removal systems are promising alternatives. Recent research has demonstrated that these innovative approaches have the potential to substantially improve CI-AKI prevention and patient outcomes. Staying updated on these advancements and incorporating them into clinical practice are essential for optimizing renal protection.

Citation: Cheng CH, Hao WR, Cheng TH. Innovative approaches beyond periprocedural hydration for preventing contrast-induced acute kidney injury. *World J Radiol* 2024; 16(9): 375-379

URL: <https://www.wjgnet.com/1949-8470/full/v16/i9/375.htm>

DOI: <https://dx.doi.org/10.4329/wjr.v16.i9.375>

INTRODUCTION

This editorial provides a commentary on the review article “Navigating nephrotoxic waters: A comprehensive overview of contrast-induced acute kidney injury prevention”, authored by Theofilis and Kalaitzidis[1] and published in *World Journal of Radiology*. The review extensively examines strategies for preventing contrast-induced acute kidney injury (CI-AKI). CI-AKI is a major clinical concern and is the third leading cause of acute kidney injury after the administration of contrast media in diagnostic and therapeutic procedures. The pathophysiology of CI-AKI, although not completely elucidated, involves medullary hypoxia and direct nephrotoxicity from contrast agents. Patients with preexisting renal and cardiovascular conditions and patients with critical illnesses are especially vulnerable; they are at increased risk of prolonged hospital stays and elevated mortality rates. The aforementioned review describes the importance of periprocedural hydration as the primary measure for CI-AKI prevention. However, recent advancements have led to the development of approaches that may enhance CI-AKI prevention, particularly for high-risk patients. Among these approaches, RenalGuard and contrast removal systems are prominent innovative options. Studies, including those by Du *et al*[2] and Nardi *et al*[3], have highlighted the potential of these innovations. For example, the RenalGuard system facilitates high-volume urine output, thus aiding in the rapid elimination of contrast media from the kidneys. Moreover, contrast removal systems can effectively reduce the adverse effects of contrast agents on renal function.

EMERGING APPROACHES FOR CI-AKI PREVENTION

The traditional approach to preventing CI-AKI primarily involves periprocedural hydration, which dilutes and eliminates contrast agents, thereby minimizing their nephrotoxic effects. Although this approach is relatively effective, it has limited efficacy, especially in patients at high risk of CI-AKI. Considering these limitations, scholars have recently proposed several innovative approaches that offer enhanced protection against CI-AKI. Recent reviews, including that by Theofilis and Kalaitzidis[1], have highlighted the potential of new interventions, such as the RenalGuard system and contrast removal techniques, for enhanced CI-AKI prevention. The RenalGuard system promotes high-volume urine output, which can facilitate the rapid elimination of contrast media from the kidneys[1]. Additionally, contrast removal systems have been demonstrated to be effective in reducing the renal burden of contrast agents, offering an additional layer of protection for at-risk patients[2]. Other promising approaches involve the use of inorganic nitrates and novel pharmacological agents. For example, the NITRATE-CIN trial demonstrated that inorganic nitrates could mitigate contrast-induced nephropathy in patients undergoing coronary angiography[4]. Similarly, a study revealed that the use of tetramethylpyrazine can attenuate renal tubular epithelial cell ferroptosis, thereby reducing the risk of contrast-induced nephropathy [5]. By staying updated on these emerging approaches and incorporating them into clinical practice, health-care professionals can substantially enhance CI-AKI prevention for their patients.

RENALGUARD SYSTEM

The RenalGuard system is one of the most promising advancements for preventing CI-AKI. By combining hydration and diuretics, this system facilitates controlled diuresis, thereby increasing urine output and enhancing the clearance of contrast media[1]. The RenalGuard system maintains a high urine flow rate, which helps mitigate the nephrotoxic effects of contrast agents[6]. Initial studies have highlighted the efficacy of this system in reducing the incidence of CI-AKI, particularly in high-risk patients such as those with critical illness or preexisting renal and cardiovascular conditions[3,7]. By promoting adequate urine flow, the system can optimize renal function during procedures involving contrast media, thus potentially improving patient outcomes[2]. Incorporating the RenalGuard system into clinical practice represents an advancement in CI-AKI preventive approaches. By adopting such innovative approaches, health-care professionals can mitigate the renal injury risks associated with contrast-enhanced procedures, thus improving patient care[1,6]. Considering these advancements, health-care professionals should stay updated on evolving research on CI-AKI pre-

vention to optimize patient safety and outcomes in clinical settings[8,9].

CONTRAST REMOVAL SYSTEMS

Contrast removal systems are designed to actively eliminate contrast agents from the bloodstream before these agents can cause substantial renal damage[1]. These systems selectively filter contrast media during and immediately after procedures, thereby reducing the renal burden[6]. Clinical trials have demonstrated promising outcomes for contrast removal systems, indicating their effectiveness in decreasing the incidence of CI-AKI, particularly in patients with preexisting renal conditions[3,5]. By facilitating the timely removal of contrast agents, these systems contribute to preserving renal function during contrast-enhanced procedures[2]. Incorporating contrast removal systems into clinical practice represents a major advancement in CI-AKI preventive approaches. These systems provide a proactive approach to managing exposure to contrast agents and the related adverse effects, potentially improving patient outcomes by mitigating the risk of renal injury associated with the administration of contrast media[3]. Staying updated on the latest research and incorporating innovative technologies such as contrast removal systems are crucial for optimizing renal protection and CI-AKI prevention[8,9], mitigating the nephrotoxic effects of contrast agents, and enhancing the safety of contrast-enhanced procedures in high-risk patient populations[1,6].

TAILORED PREVENTIVE APPROACHES

Tailored preventive approaches can facilitate the integration of novel approaches into clinical practice for CI-AKI prevention; such tailored approaches emphasize individualized care that is based on patient-specific risk factors and comorbidities[1]. Advanced preventive measures have substantial benefits for high-risk patients, including those with chronic kidney disease (CKD), diabetes mellitus, or heart failure[3,6]. Personalized approaches are tailored to each patient's unique medical profile and procedural risks, thus optimizing CI-AKI prevention[2,7]. For instance, intense preventive measures such as RenalGuard or contrast removal systems must be implemented in patients with underlying cardiovascular conditions or CKD for mitigating the nephrotoxic effects of contrast media[5,10]. Recent research has demonstrated the importance of incorporating emerging technologies and evidence-based practices into clinical workflows for improving outcomes in high-risk populations[11,12]. By staying updated on these advancements and by customizing preventive approaches according to each patient, health-care providers can effectively reduce the incidence of CI-AKI and enhance patient safety during contrast-enhanced procedures[8,9]. In summary, the implementation of tailored preventive approaches is pivotal for the management of CI-AKI; moreover, tailored preventive approaches can optimize patient outcomes through individualized risk assessment and intervention planning[3,6].

EVIDENCE-BASED PRACTICE

Evidence-based practice stipulates that the incorporation of emerging approaches into CI-AKI prevention protocols should be guided by the latest clinical evidence and guidelines[1]. Continual research and clinical trials are crucial for validating the efficacy of these approaches and for refining their application across diverse patient populations[2,3]. By staying updated on recent developments, health-care professionals can effectively incorporate novel preventive approaches such as RenalGuard and contrast removal systems into routine clinical practice[4,5]. These innovations are promising for high-risk individuals with preexisting renal or cardiovascular conditions; they can effectively mitigate the nephrotoxic effects of contrast media[6,10]. By staying updated on advancements in CI-AKI prevention, health-care providers can deliver optimal care through the implementation of treatment strategies that align with the latest scientific evidence[7,12]. In addition, by continually updating their knowledge base and adapting practices accordingly, clinicians can maximize the improvement of patient safety and outcomes during contrast-enhanced procedures[8,9]. In conclusion, the integration of evidence-based practice into CI-AKI prevention protocols represents a dynamic approach that considers recent research results and clinical insights. This dynamic approach fosters the incorporation of innovative strategies and ensures that preventive approaches are tailored to individual patient needs, thereby optimizing health-care delivery and patient outcomes[8,9].

INTERDISCIPLINARY COLLABORATION

CI-AKI prevention requires a collaborative approach involving radiologists, nephrologists, and other health-care professionals who are directly engaged in the care of patients undergoing contrast-enhanced procedures[1]. Effective interdisciplinary communication and coordination among these health-care professionals are fundamental to implementing comprehensive CI-AKI preventive approaches and achieving optimal patient outcomes[2,3]. Radiologists play pivotal roles in optimizing imaging protocols to minimize exposure to contrast agents without compromising diagnostic quality, thereby contributing to a reduced risk of CI-AKI[4,5]. Nephrologists also contribute to the reduction of CI-AKI risk by assessing patient risk factors and implementing personalized hydration protocols or pharmacological interventions

tailored to individual patient profiles[6,10]. Through the collaborative efforts of these specialists, appropriate CI-AKI preventive approaches can be selected, and any complications that develop can be promptly managed[7,12]. Moreover, continual interdisciplinary communication ensures that health-care providers stay updated on emerging research and innovative approaches, such as RenalGuard and contrast removal systems[8,9]. By staying updated on these advancements and by incorporating evidence-based practices into clinical workflows, interdisciplinary teams can enhance CI-AKI prevention and improve overall patient outcomes[8,9]. In conclusion, fostering collaboration among radiologists, nephrologists, and other health-care professionals is crucial for mitigating CI-AKI-associated risks. This collaborative approach not only optimizes patient safety during contrast-enhanced procedures but also supports the delivery of individualized care based on the latest scientific evidence and clinical guidelines[8,9].

CONCLUSION

In conclusion, this editorial verifies the pivotal insights from Theofilis and Kalaitzidis's comprehensive review of CI-AKI preventive approaches[1]. This review meticulously examines the current and emerging approaches for CI-AKI prevention, particularly highlighting innovative approaches such as RenalGuard and contrast removal systems[2,3]. CI-AKI remains a major challenge in clinical settings, especially among patients with underlying renal or cardiovascular conditions. Although traditional periprocedural hydration is fundamental, it has limited efficacy in high-risk individuals. The review verifies that new preventive measures must be adopted for providing enhanced renal protection and ensuring more favorable patient outcomes[1]. The RenalGuard system, which facilitates controlled diuresis, and contrast removal systems, which actively filter contrast agents from the circulation, represent notable advancements[4,5]. These innovations not only overcome the limitations of conventional methods but also align with personalized medicine principles by tailoring preventive approaches to individual patient profiles[7,12]. In the future, health-care providers must stay updated on these emerging techniques and must integrate them into clinical practice. Continual interdisciplinary collaboration and rigorous research are essential for validating these approaches across diverse patient populations[8,9]. By incorporating these advances into clinical practice, health-care providers can mitigate CI-AKI-associated risks, which can substantially improve patient outcomes.

FOOTNOTES

Author contributions: Cheng CH and Hao WR wrote the paper; Hao WR and Cheng TH revised the paper; All authors have read and approved the final manuscript.

Conflict-of-interest statement: The authors declare that they have no conflict of interest.

Open-Access: This article is an open-access article that was selected by an in-house editor and fully peer-reviewed by external reviewers. It is distributed in accordance with the Creative Commons Attribution NonCommercial (CC BY-NC 4.0) license, which permits others to distribute, remix, adapt, build upon this work non-commercially, and license their derivative works on different terms, provided the original work is properly cited and the use is non-commercial. See: <https://creativecommons.org/licenses/by-nc/4.0/>

Country of origin: Taiwan

ORCID number: Tzu-Hung Cheng [0000-0002-9155-4169](https://orcid.org/0000-0002-9155-4169).

S-Editor: Fan M

L-Editor: A

P-Editor: Wang WB

REFERENCES

- 1 **Theofilis P**, Kalaitzidis R. Navigating nephrotoxic waters: A comprehensive overview of contrast-induced acute kidney injury prevention. *World J Radiol* 2024; **16**: 168-183 [PMID: [38983842](https://pubmed.ncbi.nlm.nih.gov/38983842/) DOI: [10.4329/wjr.v16.i6.168](https://doi.org/10.4329/wjr.v16.i6.168)]
- 2 **Du Q**, Jiang T, Yuan Q, Bai Y, Lin D, Liu D. NMR-based metabolomic analysis of plasma from elderly patients with CVD before and after using contrast media. *Heliyon* 2024; **10**: e30434 [PMID: [38737248](https://pubmed.ncbi.nlm.nih.gov/38737248/) DOI: [10.1016/j.heliyon.2024.e30434](https://doi.org/10.1016/j.heliyon.2024.e30434)]
- 3 **Nardi G**, Marchi E, Allinovi M, Lugli G, Biagiotti L, Di Muro FM, Valenti R, Muraca I, Tomberli B, Ciardetti N, Alterini B, Meucci F, Di Mario C, Mattesini A. Contrast-Induced Acute Kidney Injury in Patients with Heart Failure on Sodium-Glucose Cotransporter-2 Inhibitors Undergoing Radiocontrast Agent Invasive Procedures: A Propensity-Matched Analysis. *J Clin Med* 2024; **13** [PMID: [38610806](https://pubmed.ncbi.nlm.nih.gov/38610806/) DOI: [10.3390/jcm13072041](https://doi.org/10.3390/jcm13072041)]
- 4 **Jones DA**, Beirne AM, Kelham M, Wynne L, Andiapien M, Rathod KS, Parakaw T, Adams J, Learoyd A, Khan K, Godec T, Wright P, Antoniou S, Wragg A, Yaqoob M, Mathur A, Ahluwalia A. Inorganic nitrate benefits contrast-induced nephropathy after coronary angiography for acute coronary syndromes: the NITRATE-CIN trial. *Eur Heart J* 2024; **45**: 1647-1658 [PMID: [38513060](https://pubmed.ncbi.nlm.nih.gov/38513060/) DOI: [10.1093/eurheartj/ehae100](https://doi.org/10.1093/eurheartj/ehae100)]
- 5 **Zhu Z**, Li J, Song Z, Li T, Li Z, Gong X. Tetramethylpyrazine attenuates renal tubular epithelial cell ferroptosis in contrast-induced nephropathy by inhibiting transferrin receptor and intracellular reactive oxygen species. *Clin Sci (Lond)* 2024; **138**: 235-249 [PMID: [38357976](https://pubmed.ncbi.nlm.nih.gov/38357976/)]

DOI: [10.1042/CS20231184](https://doi.org/10.1042/CS20231184)]

- 6 **Mehta R**, Sorbo D, Ronco F, Ronco C. Key Considerations regarding the Renal Risks of Iodinated Contrast Media: The Nephrologist's Role. *Cardiorenal Med* 2023; **13**: 324-331 [PMID: [37757781](https://pubmed.ncbi.nlm.nih.gov/37757781/) DOI: [10.1159/000533282](https://doi.org/10.1159/000533282)]
- 7 **Liu Q**, Duan SB, Wang L, Luo XQ, Wang HS, Deng YH, Wu X, Wu T, Yan And P, Kang YX. Apelin-13 alleviates contrast-induced acute kidney injury by inhibiting endoplasmic reticulum stress. *Ren Fail* 2023; **45**: 2179852 [PMID: [37723076](https://pubmed.ncbi.nlm.nih.gov/37723076/) DOI: [10.1080/0886022X.2023.2179852](https://doi.org/10.1080/0886022X.2023.2179852)]
- 8 **Cheng AS**, Li X. The Potential Biotherapeutic Targets of Contrast-Induced Acute Kidney Injury. *Int J Mol Sci* 2023; **24** [PMID: [37175958](https://pubmed.ncbi.nlm.nih.gov/37175958/) DOI: [10.3390/ijms24098254](https://doi.org/10.3390/ijms24098254)]
- 9 **Lee CD**, Hinson J, Davenport MS. Avoiding Contrast-Enhanced Imaging to Prevent Contrast-Induced Acute Kidney Injury. *N Engl J Med* 2022; **387**: 1809-1812 [PMID: [36351273](https://pubmed.ncbi.nlm.nih.gov/36351273/) DOI: [10.1056/NEJMcide2204693](https://doi.org/10.1056/NEJMcide2204693)]
- 10 **Ge L**, Chen J, Ren X, Huang C, Dong D, Yin Z. JQ1 attenuates contrast-induced acute kidney injury through the upregulation of autophagy and inhibition of inflammation. *Int Urol Nephrol* 2024; **56**: 739-749 [PMID: [37548899](https://pubmed.ncbi.nlm.nih.gov/37548899/) DOI: [10.1007/s11255-023-03718-7](https://doi.org/10.1007/s11255-023-03718-7)]
- 11 **Ahmadimoghaddam D**, Talebi SS, Rahmani A, Zamanirafe M, Parvaneh E, Ranjbar A, Poorolajal J, Mehrpooya M. Prevention of contrast induced-acute kidney injury using coenzyme Q10 in patients with ST-segment elevation myocardial infarction undergoing primary percutaneous coronary intervention. *Eur J Clin Pharmacol* 2023; **79**: 1341-1356 [PMID: [37524929](https://pubmed.ncbi.nlm.nih.gov/37524929/) DOI: [10.1007/s00228-023-03546-9](https://doi.org/10.1007/s00228-023-03546-9)]
- 12 **Yu R**, Wu C, Xiao Y, Li Q, Chen J, Song J, Chen H, Wang Z, Wang W. The clinical predictive value and regulation mechanism of microRNA-188-5p in contrast-induced acute kidney injury. *Biochem Biophys Res Commun* 2023; **679**: 215-223 [PMID: [37713958](https://pubmed.ncbi.nlm.nih.gov/37713958/) DOI: [10.1016/j.bbrc.2023.09.019](https://doi.org/10.1016/j.bbrc.2023.09.019)]

Retrospective Study

Intentionally unilateral prostatic artery embolization: Patient selection, technique and potential benefits

Hippocrates Moschouris, Konstantinos Stamatiou

Specialty type: Radiology, nuclear medicine and medical imaging**Provenance and peer review:** Invited article; Externally peer reviewed.**Peer-review model:** Single blind**Peer-review report's classification****Scientific Quality:** Grade B**Novelty:** Grade B**Creativity or Innovation:** Grade B**Scientific Significance:** Grade B**P-Reviewer:** Nithiyaraj E**Received:** April 16, 2024**Revised:** August 8, 2024**Accepted:** August 22, 2024**Published online:** September 28, 2024**Processing time:** 163 Days and 14.3 Hours**Hippocrates Moschouris**, Department of Radiology, General Hospital "Tzanio", Piraeus 18536, Greece**Konstantinos Stamatiou**, Department of Urology, General Hospital "Tzanio", Piraeus 18536, Greece**Corresponding author:** Hippocrates Moschouris, MD, MSc, PhD, Chairman, Doctor, Department of Radiology, General Hospital "Tzanio", Zanni and Afentouli 1 Street, Piraeus 18536, Greece. hipmosch@gmail.com**Abstract****BACKGROUND**

Prostatic artery embolization (PAE) is a promising but also technically demanding interventional radiologic treatment for symptomatic benign prostatic hyperplasia. Many technical challenges in PAE are associated with the complex anatomy of prostatic arteries (PAs) and with the systematic attempts to catheterize the PAs of both pelvic sides. Long procedure times and high radiation doses are often the result of these attempts and are considered significant disadvantages of PAE. The authors hypothesized that, in selected patients, these disadvantages could be mitigated by intentionally embolizing PAs of only one pelvic side.

AIM

To describe the authors' approach for intentionally unilateral PAE (IU-PAE) and its potential benefits.

METHODS

This was a single-center retrospective study of patients treated with IU-PAE during a period of 2 years. IU-PAE was applied in patients with opacification of more than half of the contralateral prostatic lobe after angiography of the ipsilateral PA (subgroup A), or with markedly asymmetric prostatic enlargement, with the dominant prostatic lobe occupying at least two thirds of the entire gland (subgroup B). All patients treated with IU-PAE also fulfilled at least one of the following criteria: Severe tortuosity or severe atheromatosis of the pelvic arteries, non-visualization, or visualization of a tiny (< 1 mm) contralateral PA on preprocedural computed tomographic angiography. Intraprocedural contrast-enhanced ultrasonography (iCEUS) was applied to monitor prostatic infarction. IU-PAE patients were compared to a control group treated with bilateral PAE.

RESULTS

IU-PAE was performed in a total 13 patients (subgroup A, $n = 7$; subgroup B, $n = 6$). Dose-area product, fluoroscopy time and operation time in the IU-PAE group (9767.8 $\mu\text{Gy}\cdot\text{m}^2$, 30.3 minutes, 64.0 minutes, respectively) were significantly shorter (45.4%, 35.9%, 45.8% respectively, $P < 0.01$) compared to the control group. Clinical and imaging outcomes did not differ significantly between the IU-PAE group and the control group. In the 2 clinical failures of IU-PAE (both in subgroup A), the extent of prostatic infarction (demonstrated by iCEUS) was significantly smaller compared to the rest of the IU-PAE group.

CONCLUSION

In selected patients, IU-PAE is associated with comparable outcomes, but with lower radiation exposure and a shorter procedure compared to bilateral PAE. iCEUS could facilitate patient selection for IU-PAE.

Key Words: Prostatic artery embolization; Unilateral; Computed tomographic angiography; Dose area product; Fluoroscopy time; Prostatic infarction

©The Author(s) 2024. Published by Baishideng Publishing Group Inc. All rights reserved.

Core Tip: In this retrospective study, intentionally unilateral prostatic artery embolization (IU-PAE) was performed in 13 patients with opacification of more than half of the contralateral prostatic lobe after angiography of the ipsilateral prostatic artery or with markedly asymmetric prostatic enlargement. Compared to bilateral PAE, IU-PAE was associated with significantly lower radiation exposure and a shorter procedure, but with no significant difference in clinical efficacy. Contrast-enhanced ultrasonography was applied during IU-PAE and revealed only limited prostatic infarction in the 2 clinical failures of IU-PAE, in contrast to the rest of the patients.

Citation: Moschouris H, Stamatou K. Intentionally unilateral prostatic artery embolization: Patient selection, technique and potential benefits. *World J Radiol* 2024; 16(9): 380-388

URL: <https://www.wjgnet.com/1949-8470/full/v16/i9/380.htm>

DOI: <https://dx.doi.org/10.4329/wjr.v16.i9.380>

INTRODUCTION

Unilateral prostatic artery embolization (PAE) for symptomatic benign hyperplasia is usually the result of failed catheterization of the contralateral prostatic artery (PA) due to pelvic arterial atherosclerotic stenoses, tortuosities, or due to unfavorable anatomy of the contralateral PA itself[1]. Unilateral PAE is also associated with reduced clinical efficacy (with a clinical success rate of 50% or lower)[1] compared to bilateral PAE, most likely as a result of the limited ischemic effect[2] and of early reperfusion from the contralateral branches. Exceptionally, an earlier small case series[3] demonstrated satisfactory short-term clinical outcomes of unilateral PAE, thanks to peri- and intra-prostatic arterial anastomoses, that enabled the operators to embolize both prostatic lobes through a single PA. Obviating the need to angiographically investigate and catheterize the contralateral PA, was translated in radiation dose savings. A more recent, multicenter study[4], also showed that “intended” unilateral PAE was a significant predictor of reduced dose-area product (DAP) and was associated with a 32.4% decrease in DAP on multivariate analysis. However, further details regarding selection criteria and technique of unilateral PAE were not provided; it was also acknowledged that 41% of the patients (initially treated with unilateral PAE) had to undergo a second PAE procedure due to suboptimal results.

The application of unilateral PAE when the largest part of the prostate has a unilateral arterial supply appears to be a reasonable way to maximize the efficacy of the procedure. A modality for on-site evaluation of the ischemic effect could also be helpful in this context. This report describes the patient selection, and technical aspects of intentionally unilateral PAE (IU-PAE) in a single tertiary center. The potential benefits of this approach are evaluated. Utilization of contrast-enhanced ultrasonography (CEUS) for intraprocedural monitoring of IU-PAE is also described.

MATERIALS AND METHODS

Study design

This is a retrospective review of benign hyperplasia patients who were treated with IU-PAE at a single institution during a 2-year period (September 2021 to August 2023). The initial selection of patients for PAE was based on standard, widely accepted criteria[5]. Written informed consent was obtained from all patients prior to treatment. The study was approved by the institutional review board.

Preprocedural computed tomographic angiography (CTA) was conducted for vascular planning in all patients. IU-PAE was applied, if superselective angiography of the ipsilateral PA resulted in opacification of more than half of the contralateral prostatic lobe, as assessed visually by the operator during the intervention (subgroup A), or if markedly asymmetric prostatic enlargement was observed on CTA, with the dominant prostatic lobe occupying at least two thirds of the entire gland (subgroup B). Volumetry of the dominant lobe and of the entire prostate was performed with the ellipsoid formula using measurements (length, width and height) performed on the appropriate CTA images. Patients selected for IU-PAE should also fulfill at least one of the following criteria: Severe tortuosity or severe atheromatosis of the pelvic arteries, non-visualization, or visualization of a tiny (with a diameter of less than 1 mm) contralateral PA on preprocedural CTA. The tortuosity of the pelvic arteries was evaluated with a system used in a previous PAE study[6], as follows: Grade 1 (mild: Kinking < 30° in both pelvic sides); Grade 2 (moderate: Maximum kinking 30°-60° in at least 1 pelvic side); Grade 3 (severe: Multiple kinking 30°-60° in both sides and kinking of > 60° in at least 1 pelvic side). Angles were measured in coronal maximum intensity projection images of the preprocedural CTA. The severity of pelvic arterial atheromatosis was visually evaluated on CTA and was given a Grade (0, 1, 2 and 3, for no, mild, moderate and severe stenosis, respectively), also in line with a classification applied in a previous study[7].

The IU-PAE procedure differed from the standard PAE in that no attempt for identification and catheterization of contralateral PA(s) was performed during the intervention. Vascular access was obtained *via* the right or left common femoral artery with the Seldinger technique. The internal iliac artery was catheterized with a 5 French (Fr) angiographic catheter, usually with a reverse curve. The PA was catheterized with a 1.98 Fr microcatheter (Parkway Soft-Asahi Intecc Co.) and with a double-angled 0.016 microguidewire (Meister-Asahi). Distal advancement of the microcatheter in intraprostatic branches (“PERFecTED technique”)[8,9] was attempted in all cases. Embolization was performed with microspheres (Embosphere 100-300 or 300-500, Merit Medical) until complete flow stasis in the treated PA. At this point, contrast-enhanced ultrasonography [intraprocedural CEUS (iCEUS)] was performed transabdominally and infarction (represented by newly appearing, non-enhancing intraprostatic areas) was visually evaluated on 3 different prostate levels (base, middle part and apex) and compared to the whole prostate area. This visual estimate of prostatic infarction was semiquantitatively expressed in classes of ten percent, similar to a previous report[10]. All PAE procedures were performed with the same angiographic unit (Axiom Artis Zee, Siemens Healthineers, Erlangen, Germany) and by the same first operator with 5 years of previous experience in PAE. For iCEUS, a second-generation echo enhancer (SonoVue, Bracco, Milan, Italy) was administered in an antecubital vein and a low mechanical index, contrast-specific algorithm was utilized. iCEUS was performed with a portable ultrasonographic unit (M8 Mindray, Nanshan, Shenzhen, China).

Evaluation of clinical success was based on reduction of the International Prostate Symptom Score or on the relief from indwelling bladder catheter according to standard, widely accepted criteria[5]. Clinical assessment of all treated patients was scheduled within the first week post PAE, one and three months post PAE and then every three months. Complications were recorded and graded using the modified (for PAE) Clavien-Dindo system[11]. Prostate shrinkage and prostate infarction were evaluated postoperatively with transabdominal ultrasonography: Unenhanced ultrasonography (US) was performed at least twice: (1) During the patient’s first visit, within one week post PAE; and (2) Three months post PAE. Prostatic volume (PV) was calculated with the ellipsoid formula using the measurements of transabdominal US. Post-PAE CEUS was performed at least once (during the patient’s first visit, within one week post PAE). The extent (volume) of each prostatic infarction was calculated using the ellipsoid formula; the volumes of all prostatic infarcts were summed and divided by PV, thus calculating the percentage of prostatic infarction, in line with previous work[2].

Radiation parameters [DAP, fluoroscopy time (FT)] and operation time (OT) (calculated from the moment of arterial introducer placement until its removal) were also recorded. IU-PAE patients were compared to a control group of patients who had undergone bilateral PAE during the same period and with the same equipment, angiographic protocol and with the same catheterization and embolization materials.

Statistical analysis

Descriptive statistics were calculated for quantitative and qualitative data. Several variables of the IU-PAE group were compared with the corresponding variables of the control group. Depending on the type and distribution of each variable, the appropriate test was utilized (Welch’s *t* test, Mann-Whitney *U* test, *Z* test). Pearson correlation coefficient was used to assess the correlation between the visual estimate of prostatic infarction (measured by iCEUS during the procedure) and the percentage of prostatic infarction (measured by CEUS within the first week post PAE). The Kaplan-Meier method was used to calculate the clinical success rates of PAE over time; the log-rank test was used to evaluate differences in clinical success rates between the IU-PAE group and the control group, and between subgroups A and B. Statistical significance was defined as $P < 0.05$.

RESULTS

IU-PAE was performed in a total 13 patients during the study period (Table 1). Subgroup A was represented by 7/13 patients. After catheterization and superselective angiography of the ipsilateral PA, complete opacification of the contralateral lobe was observed in 2/7 patients; incomplete opacification exceeding half of the contralateral lobe was observed in 5/7 patients. In 2/7 patients (one with complete contralateral opacification and one with opacification of more than half of the contralateral lobe) the microcatheter could be advanced in contralateral prostatic branches. Regarding iCEUS, in 5/7 patients of subgroup A, infarcts were demonstrated in both prostatic lobes, occupying at least 20% of the entire prostate on visual evaluation (Figure 1). In 2/7 patients, iCEUS demonstrated small infarcts limited to the ipsilateral lobe and occupying less than 10% of the entire prostate. Of note, both of these patients had undergone

Table 1 Baseline demographic, anatomic and clinical data of the two patient groups in this study (intentionally unilateral prostatic artery embolization group vs control)

	IU-PAE (n = 13)	Control (n = 30)	P value
Age (mean ± SD, years)	76.5 ± 8.2	71.8 ± 10.6	0.166
BMI (mean ± SD, kg/m ²)	28.7 ± 4.6	27.0 ± 2.8	0.300
PV (mean ± SD, mL)	106.7 ± 43.8	92.8 ± 27.1	0.330
Grade of tortuosity (mean ± SD)	2.2 ± 0.9	2.1 ± 0.8	0.736
Grade of atheroma (mean ± SD)	1.5 ± 0.7	1.2 ± 0.6	0.360
LUTS, proportion of pts	9/13	22/30	0.779
IPSS (mean ± SD)	26.0 ± 4.0	26.5 ± 3.9	0.708
IBC proportion of pts	4/13	8/30	0.779

IU-PAE: Intentionally unilateral prostatic artery embolization; BMI: Body mass index; PV: Prostate volume; LUTS: Lower urinary tract symptoms; IPSS: International prostate symptom score; IBC: Indwelling bladder catheter.

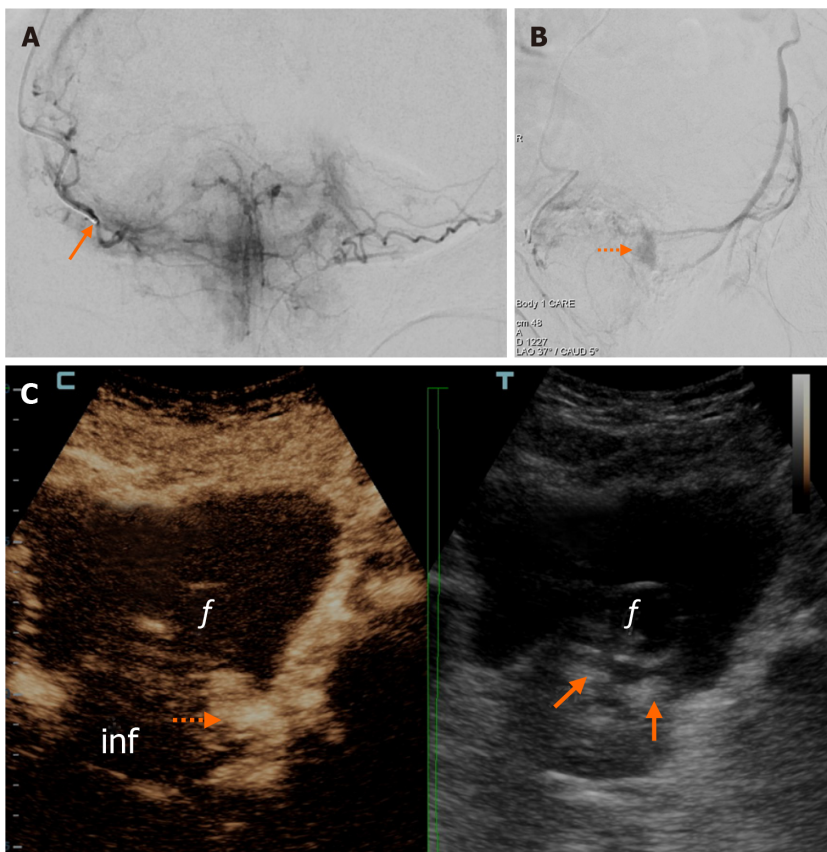


Figure 1 Representative images from a clinically successful case of intentionally unilateral prostatic artery embolization (subgroup A). A: Right prostatic artery (PA) angiogram (frontal projection) with the microcatheter tip at the extraprostatic part of the PA (arrow) shows opacification of the largest part of both prostatic lobes; B: Right PA angiogram (oblique projection) post embolization shows extensive devascularization of the prostate and a small area of residual enhancement at the left lobe (dotted arrow); C: Dual image from intraprocedural contrast-enhanced ultrasonography (contrast-enhanced image on the left, unenhanced reference B-mode image on the right) 2 minutes post embolization, confirms the absence of enhancement in the largest part of the prostate (inf), with residual enhancement only at the periphery of the left lobe (dotted arrow). Echogenic areas (arrows) in the unenhanced image of the prostate are caused by accumulation of the embolic mixture. The balloon of the Foley catheter is indicated by "f".

embolization with the relatively larger microspheres (300-500 microns).

Subgroup B was represented by 6/13 patients, with a volume of the dominant prostatic lobe representing 67%-90% (mean: 74.7%) of the entire PV. In all patients of subgroup B, catheterization and injection of the embolic agent were limited to the PA(s) of the dominant lobe. The latter was fed by a single PA in 5 cases and by a duplicate PA in one case. Immediately post-embolization, iCEUS showed ipsilateral infarction occupying at least 30% of the prostate in all 6

Table 2 Comparison of technical and radiation dose-related features for the two groups (intentionally unilateral prostatic artery embolization group vs control)

	IU-PAE (n = 13)	Control (n = 30)	P value
Operation time (mean ± SD, minutes)	64.0 ± 20.2	118.2 ± 22.6	< 0.001 ^a
Fluoroscopy time (mean ± SD, minutes)	30.3 ± 10.6	47.3 ± 14.8	0.002 ^a
DAP (mean ± SD, μGy·m ²)	9767.8 ± 5873.5	17891.5 ± 9087.1	0.004 ^a
“PErFecTED” technique (proportion of pts)	7/13	14/30	0.667
Embo with 100-300 vs 300-500 (proportion of pts)	10/3	23/7	0.984
MC advancement in contralateral side (proportion of pts)	2/13	1/30	0.155

^aP < 0.05.

IU-PAE: Intentionally unilateral prostatic artery embolization; DAP: Dose area product; MC: Microcatheter.

Table 3 Comparison of outcome parameters for the two groups (intentionally unilateral prostatic artery embolization group vs control)

	IU-PAE (n = 13)	Control (n = 30)	P value
Percentage of prostatic infarction ¹ (mean ± SD, %)	36.1 ± 16.0	33.1 ± 14.5	0.478
PV reduction ² (mean ± SD, %)	28.0 ± 12.5	32.9 ± 9.6	0.065
IPSS reduction ² (mean ± SD, %)	58.0 ± 16.3	56.6 ± 22.3	0.819
Clinical success rate ² (%)	84.6	90.0	0.995
Complications ³ - proportion of pts	2/13	7/30	0.555

¹Calculated within the first week post prostatic artery embolization.

²Calculated 3 months post prostatic artery embolization (prostate volume and international prostate symptom score reduction was defined in comparison to baseline measurement).

³Only minor complications were observed.

IU-PAE: Intentionally unilateral prostatic artery embolization; PV: Prostate volume; IPSS: International prostate symptom score.

patients (Figure 2). Additionally, in 2 of them, limited infarction of the contralateral lobe was also observed.

Radiation parameters (DAP, FT) and OT in the IU-PAE group (9767.8 μGy·m², 30.3 minutes, 64.0 minutes, respectively) were significantly lower (45.4%, 35.9%, 45.8% respectively, P < 0.01) compared to the control group of 30 patients who underwent bilateral PAE (Table 2). Regarding efficacy, the clinical success rates of IU-PAE were 92.3%, 84.6%, 84.6%, 84.6% and 84.6% at 2, 3, 6, 12 and 24 months post-PAE, respectively. These did not significantly differ from the clinical success rates of the control group (Figure 3). Follow-up time ranged from 2-37 (mean: 17) months.

Early clinical failures of IU-PAE were observed in the 2 aforementioned patients with limited unilateral prostatic infarction (Figure 4). Although both clinical failures occurred in subgroup A, clinical success rates did not significantly differ between subgroup A and subgroup B (P = 0.173). The percentage of prostatic infarction and the degree of prostate shrinkage were also lower in subgroup A; however, these differences were not statistically significant either (31.1% ± 17.6% vs 41.8% ± 13.1%, P = 0.389 and 26.6% ± 9.5% vs 29.7% ± 16.2%, P = 1.000).

Only 2 minor complications (acute urinary retention, n = 1; inguinal hematoma, n = 1) occurred in the IU-PAE group, vs 7 minor complications in the control group (acute urinary retention, n = 3; hemospermia, n = 1, mild rectal bleeding, n = 2; urinary infection, n = 1). Prostate shrinkage and the extent of prostatic infarction were also comparable between the IU-PAE group and the control group. A more detailed comparison between the IU-CEUS group and control group in terms of imaging and clinical outcomes is provided in Table 3. Finally, there was excellent correlation between iCEUS and post-PAE CEUS regarding the evaluation of prostatic infarction (r = 0.95, P < 0.001), although prostatic infarction tended to be overestimated with iCEUS (mean visual estimate of prostatic infarction with iCEUS: 49.2% ± 22.2%; mean percentage of prostatic infarction with post-PAE CEUS: 36.1% ± 16.0%).

DISCUSSION

In this report, IU-PAE was performed in 2 subgroups of patients. In subgroup A, opacification of more than half of the contralateral prostatic lobe was observed after catheterization of the ipsilateral PA, with or without additional advancement of the microcatheter in contralateral prostatic branches. Subgroup A is somewhat similar to the case series of Amouyal *et al*[3], although in the present work we also included patients with more than half, but less than total

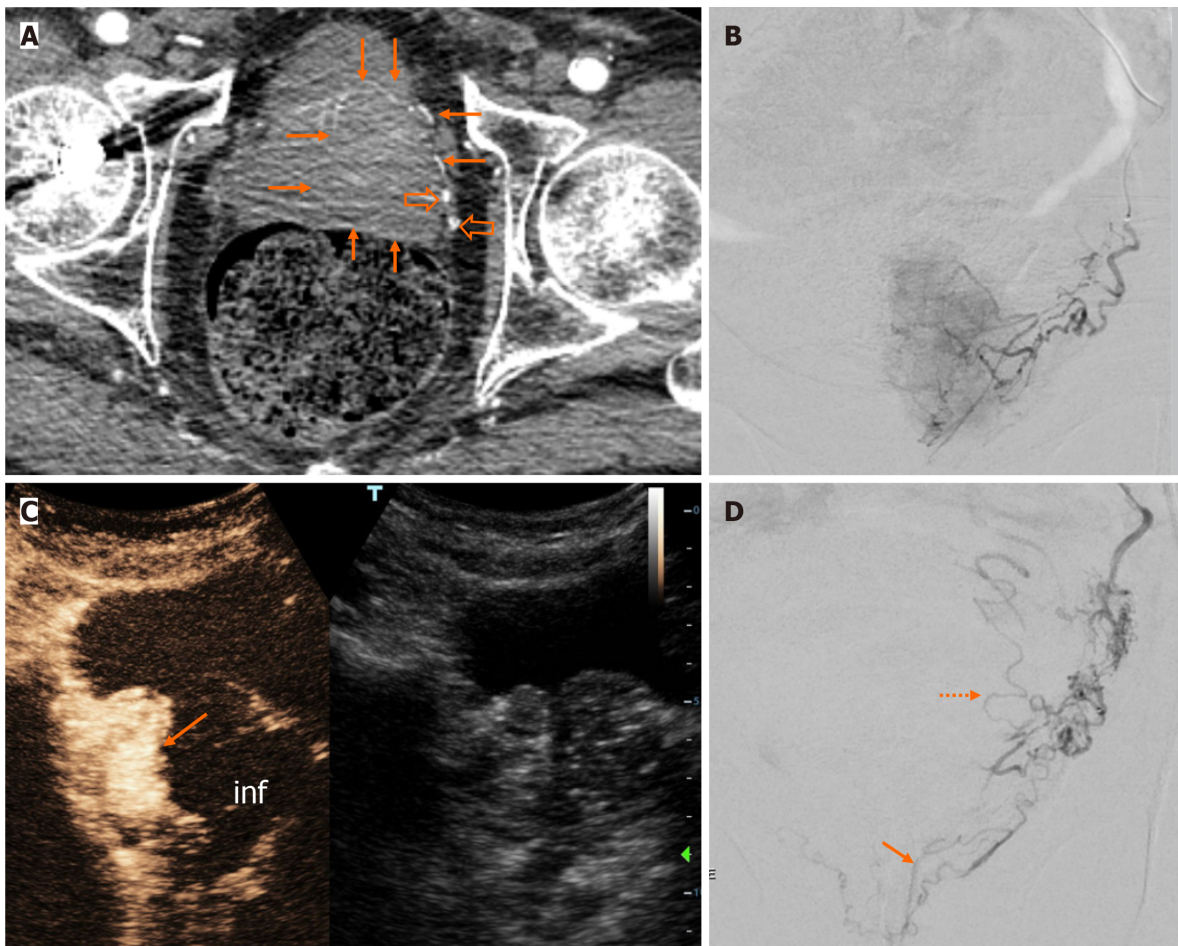


Figure 2 Representative images from a clinically successful case of intentionally unilateral prostatic artery embolization (subgroup B). A: Axial computed tomographic angiography image shows a dominant left prostatic lobe (arrows). Left prostatic artery (PA) branches (empty arrows) are also prominent compared to the right side; B: Left PA angiogram shows dense blush of the ipsilateral prostatic lobe; C: Dual image from intraprocedural contrast-enhanced ultrasonography (contrast-enhanced image on the left, unenhanced, reference B-mode image on the right) 2 minutes post-embolization, shows almost complete absence of enhancement of the left lobe (inf) and persistent enhancement of the right lobe (arrow); D: Post-embolization angiogram with microcatheter position near the origin of the left PA shows disappearance of the left prostatic blush and activation of anastomoses with rectal (arrow) and vesical (dotted arrow) branches.

opacification of the contralateral lobe. Two patients showed early clinical failures in subgroup A. As these patients underwent embolization with the relatively larger microspheres (300-500 microns), we speculate that these microspheres failed to cross the tiny intraprostatic anastomoses with contralateral prostatic branches and never reached the contralateral lobe. This is supported by the respective iCEUS findings (*i.e.*, limited, unilateral infarction in these 2 cases, as opposed to more extensive and bilateral infarction in the rest of the patients of subgroup A).

Subgroup B consisted of patients with markedly asymmetric prostatic enlargement. The “dominant” prostatic lobe (which was exclusively embolized) was arbitrarily defined as the lobe that occupied at least two thirds of the entire gland. In an earlier study[12], it was also arbitrarily defined that the prostate was dominantly vascularized by a unilateral PA, when the proportion of prostatic arterial supply *via* one side PA was over 70%. Of note, such a dominant unilateral arterial supply of the prostate was noted in 67.3% of the patients in this study; however, it was not reported whether this feature was exploited in order to perform IU-PAE. In the present series, unilateral embolization of the dominant lobe resulted in a significant extent of prostatic infarction and in satisfactory prostate shrinkage and clinical improvement. It is likely that the relatively larger size of the arteries in the dominant lobe facilitated the antegrade flow of the embolic agent and the accumulation of microspheres into the more distal prostatic branches and thus increased the efficacy of embolization.

Compared to bilateral PAE in the control group, IU-PAE was associated with a significant reduction in radiation exposure, with a 45.4% reduction in DAP and 35.9% reduction in FT. The herein reported mean DAP of IU-PAE (9767.8 $\mu\text{Gy}\cdot\text{m}^2$), is lower than the corresponding value reported in the aforementioned small series of bilateral PAE through a single PA[3]; it is also lower than the mean DAP reported in a previous work (13981.5 $\mu\text{G}\cdot\text{m}^2$), where the same equipment as in the present study was used and several techniques (but not IU-PAE) were combined to minimize radiation exposure during PAE[13]. The IU-PAE procedure was also significantly faster compared to bilateral PAE; this could be a crucial advantage when anxious and less cooperative patients are treated. Remarkably, these benefits of IU-PAE were not associated with any compromise in short- to mid-term clinical efficacy. The satisfactory clinical success rate of IU-PAE (84.6% up to 30 months post PAE) is clearly higher than that of “traditional” unilateral PAE[1] and comparable to that of bilateral PAE. However, it should be acknowledged that the long-term efficacy of IU-PAE has not been investigated and

there is (at least theoretically) a risk of early reperfusion from the untreated contralateral branches.

In this work, iCEUS was applied to monitor prostatic infarction in the angio-suite, immediately post embolization. iCEUS proved feasible and practical, with no significant delay in the procedure and no additional radiation. Although iCEUS did not alter treatment strategy in the present work, it could be used in this way in the future: If iCEUS demonstrates limited or no infarction immediately post IU-PAE, the operator should probably consider additional contralateral embolization, to improve imaging and clinical outcomes. The relationship between prostatic ischemia and clinical efficacy of PAE is still a matter of debate and of clinical and laboratory investigation[10,14-17]. Nevertheless, there are both CEUS- and MRI-based studies[2,18-20] supporting the role of extensive prostatic ischemia as a predictor of clinical success of PAE.

Several limitations of this study should be acknowledged: The small sample size (13 patients) limits the generalizability of the findings. No long-term follow-up data were available. Selection criteria for IU-PAE were arbitrarily set by the authors. Imaging evaluation was performed with US and computed tomography; magnetic resonance imaging (which is probably the most accurate and comprehensive modality for peri-interventional imaging of the prostate)[21] was not utilized.

CONCLUSION

This work provides additional evidence regarding IU-PAE. In selected patients, this approach appears to be comparable to bilateral PAE in terms of safety and short- to mid-term clinical efficacy, but with significantly lower radiation exposure and significantly shorter OT. Clearly, larger studies are required to validate the herein presented findings, and to explore the long-term outcomes of IU-PAE. iCEUS appears to be a practical modality for on-site monitoring of the ischemic effect of embolization, with a potential role in patient selection for IU-PAE. iCEUS also appears to be a feasible and versatile variant of the standard CEUS technique and its place in the context of other interventional radiology procedures warrants further research.

FOOTNOTES

Author contributions: Moschouris H wrote the paper, performed the prostatic artery embolization procedures and imaging studies and collected and analyzed the imaging data; Stamatiou K collected and analyzed the clinical data and was responsible for patient follow up.

Institutional review board statement: The study was reviewed and approved by the General Hospital “Tzanio” Institutional Review Board (Approval No. 15/9-3-2024).

Informed consent statement: All study participants, or their legal guardian, provided informed written consent prior to study enrollment.

Conflict-of-interest statement: All the authors report no relevant conflicts of interest for this article.

Data sharing statement: Dataset available from the corresponding author at hipmosch@gmail.com. Participants gave informed consent for data sharing.

Open-Access: This article is an open-access article that was selected by an in-house editor and fully peer-reviewed by external reviewers. It is distributed in accordance with the Creative Commons Attribution NonCommercial (CC BY-NC 4.0) license, which permits others to distribute, remix, adapt, build upon this work non-commercially, and license their derivative works on different terms, provided the original work is properly cited and the use is non-commercial. See: <https://creativecommons.org/licenses/by-nc/4.0/>

Country of origin: Greece

ORCID number: Hippocrates Moschouris 0000-0002-8940-8218; Konstantinos Stamatiou 0000-0001-7574-3069.

S-Editor: Wang JJ

L-Editor: Webster JR

P-Editor: Zhao S

REFERENCES

- 1 **Bilhim T**, Pisco J, Rio Tinto H, Fernandes L, Campos Pinheiro L, Duarte M, Pereira JA, Oliveira AG, O'Neill J. Unilateral versus bilateral prostatic arterial embolization for lower urinary tract symptoms in patients with prostate enlargement. *Cardiovasc Intervent Radiol* 2013; **36**: 403-411 [PMID: 23232858 DOI: 10.1007/s00270-012-0528-4]
- 2 **Moschouris H**, Stamatiou K, Malagari K, Marmaridou K, Kladis-Kalentzis K, Kiltenis M, Papadogeorgopoulos N, Tsavari A, Manoloudaki K. The value of contrast-enhanced ultrasonography in detection of prostatic infarction after prostatic artery embolization for the treatment of symptomatic benign prostatic hyperplasia. *Diagn Interv Radiol* 2019; **25**: 134-143 [PMID: 30860077 DOI: 10.5152/dir.2019.18410]

- 3 **Amouyal G**, Pellerin O, Del Giudice C, Déan C, Thiounn N, Sapoval M. Bilateral Arterial Embolization of the Prostate Through a Single Prostatic Artery: A Case Series. *Cardiovasc Intervent Radiol* 2017; **40**: 780-787 [PMID: 27999920 DOI: 10.1007/s00270-016-1540-x]
- 4 **Svarc P**, Hagen T, Waltenburg H, Andersson C, Bläckberg M, Baco E, Taudorf M, Röder MA, Lindgren H, Klöw NE, Lönn LB. Center experience and other determinants of patient radiation exposure during prostatic artery embolization: a retrospective study in three Scandinavian centers. *Eur Radiol* 2022; **32**: 2404-2413 [PMID: 34786614 DOI: 10.1007/s00330-021-08351-5]
- 5 **Cornelis FH**, Bilhim T, Hacking N, Sapoval M, Tapping CR, Carnevale FC. CIRSE Standards of Practice on Prostatic Artery Embolisation. *Cardiovasc Intervent Radiol* 2020; **43**: 176-185 [PMID: 31792588 DOI: 10.1007/s00270-019-02379-3]
- 6 **Enderlein GF**, Lehmann T, von Rundstedt FC, Aschenbach R, Grimm MO, Teichgräber U, Franiel T. Prostatic Artery Embolization-Anatomic Predictors of Technical Outcomes. *J Vasc Interv Radiol* 2020; **31**: 378-387 [PMID: 31735482 DOI: 10.1016/j.jvir.2019.09.005]
- 7 **Hacking N**, Vigneswaran G, Maclean D, Modi S, Dyer J, Harris M, Bryant T. Technical and Imaging Outcomes from the UK Registry of Prostate Artery Embolization (UK-ROPE) Study: Focusing on Predictors of Clinical Success. *Cardiovasc Intervent Radiol* 2019; **42**: 666-676 [PMID: 30603967 DOI: 10.1007/s00270-018-02156-8]
- 8 **Dias US Jr**, de Moura MRL, Viana PCC, de Assis AM, Marcelino ASZ, Moreira AM, Leite CC, Cerri GG, Carnevale FC, Horvat N. Prostatic Artery Embolization: Indications, Preparation, Techniques, Imaging Evaluation, Reporting, and Complications. *Radiographics* 2021; **41**: 1509-1530 [PMID: 34415807 DOI: 10.1148/rg.2021200144]
- 9 **Carnevale FC**, Moreira AM, Antunes AA. The "PERFecTED technique": proximal embolization first, then embolize distal for benign prostatic hyperplasia. *Cardiovasc Intervent Radiol* 2014; **37**: 1602-1605 [PMID: 24943914 DOI: 10.1007/s00270-014-0908-z]
- 10 **Barat M**, Boeken T, Moussa N, Di Gaeta A, Déan C, Thioun N, Del Giudice C, Pellerin O, Sapoval M. Contrast-Enhanced Ultrasonography for the Early Evaluation of Prostate Artery Embolization. *Cardiovasc Intervent Radiol* 2020; **43**: 1498-1504 [PMID: 32435835 DOI: 10.1007/s00270-020-02518-1]
- 11 **Moreira AM**, de Assis AM, Carnevale FC, Antunes AA, Srougi M, Cerri GG. A Review of Adverse Events Related to Prostatic Artery Embolization for Treatment of Bladder Outlet Obstruction Due to BPH. *Cardiovasc Intervent Radiol* 2017; **40**: 1490-1500 [PMID: 28795212 DOI: 10.1007/s00270-017-1765-3]
- 12 **Zhang G**, Wang M, Duan F, Yuan K, Li K, Yan J, Chang Z, Wang Y. Radiological Findings of Prostatic Arterial Anatomy for Prostatic Arterial Embolization: Preliminary Study in 55 Chinese Patients with Benign Prostatic Hyperplasia. *PLoS One* 2015; **10**: e0132678 [PMID: 26191796 DOI: 10.1371/journal.pone.0132678]
- 13 **Moschouris H**, Stamatiou K, Spanomanolis N, Vasilopoulos A, Tzamarias S, Malagari K. A Retrospective, Single-Center Study of Technical-Procedural Factors Affecting Radiation Dose During Prostatic Artery Embolization. *Cureus* 2022; **14**: e27728 [PMID: 36106246 DOI: 10.7759/cureus.27728]
- 14 **Maclean D**, Francis Bryant CT, Vigneswaran G, Bryant TJ, Harris M, Somani B, Modi S. Comprehensive Review on Current Controversies and Debate in Prostate Artery Embolization. *Turk J Urol* 2022; **48**: 166-173 [PMID: 35634934 DOI: 10.5152/tud.2022.21337]
- 15 **Lucas-Cava V**, Sánchez-Margallo FM, Moreno-Lobato B, Dávila-Gómez L, Lima-Rodríguez JR, García-Martínez V, López-Sánchez C, Sun F. Prostatic artery occlusion: initial findings on pathophysiological response in a canine prostate model. *Transl Androl Urol* 2022; **11**: 1655-1666 [PMID: 36632152 DOI: 10.21037/tau-22-423]
- 16 **Wang MQ**, Zhang JL, Xin HN, Yuan K, Yan J, Wang Y, Zhang GD, Fu JX. Comparison of Clinical Outcomes of Prostatic Artery Embolization with 50-µm Plus 100-µm Polyvinyl Alcohol (PVA) Particles versus 100-µm PVA Particles Alone: A Prospective Randomized Trial. *J Vasc Interv Radiol* 2018; **29**: 1694-1702 [PMID: 30297313 DOI: 10.1016/j.jvir.2018.06.019]
- 17 **Sun F**, Crisóstomo V, Báez-Díaz C, Sánchez FM. Prostatic Artery Embolization (PAE) for Symptomatic Benign Prostatic Hyperplasia (BPH): Part 2, Insights into the Technical Rationale. *Cardiovasc Intervent Radiol* 2016; **39**: 161-169 [PMID: 26563245 DOI: 10.1007/s00270-015-1238-5]
- 18 **Kisilevzky N**, Faintuch S. MRI assessment of prostatic ischaemia: best predictor of clinical success after prostatic artery embolisation for benign prostatic hyperplasia. *Clin Radiol* 2016; **71**: 876-882 [PMID: 27296474 DOI: 10.1016/j.crad.2016.05.003]
- 19 **Schmidt VF**, Schirren M, Heimer MM, Kazmierczak PM, Cyran CC, Wildgruber M, Seidensticker M, Ricke J, Solyanik O. Semi-Automatic MRI Feature Assessment in Small- and Medium-Volume Benign Prostatic Hyperplasia after Prostatic Artery Embolization. *Diagnostics (Basel)* 2022; **12** [PMID: 35328138 DOI: 10.3390/diagnostics12030585]
- 20 **Wang RL**, Lin FF, Ruan DD, Li SJ, Zhou YF, Luo JW, Fang ZT, Tang Y. A correlation study between prostate necrosis rate calculated by 3D Slicer software and clinical efficacy of prostatic artery embolization, along with an analysis of predictors of clinical success after prostatic artery embolization. *Abdom Radiol (NY)* 2024; **49**: 927-938 [PMID: 38158423 DOI: 10.1007/s00261-023-04131-5]
- 21 **Walker SM**, Turkbey B. Role of mpMRI in Benign Prostatic Hyperplasia Assessment and Treatment. *Curr Urol Rep* 2020; **21**: 55 [PMID: 33104969 DOI: 10.1007/s11934-020-01005-x]

Retrospective Study

Cryoablation of osteoid osteomas: Is it a valid treatment option?

Antonios Michailidis, Athanasios Panos, Efthimios Samoladas, Georgios Dimou, Georgia Mingou, Panagiotis Kosmoliaptsis, Maria Arvaniti, Christos Giankoulof, Evangelos Petsatodis

Specialty type: Radiology, nuclear medicine and medical imaging

Provenance and peer review:

Invited article; Externally peer reviewed.

Peer-review model: Single blind

Peer-review report's classification

Scientific Quality: Grade B

Novelty: Grade A

Creativity or Innovation: Grade B

Scientific Significance: Grade B

P-Reviewer: Adwan H

Received: April 17, 2024

Revised: August 20, 2024

Accepted: September 2, 2024

Published online: September 28, 2024

Processing time: 156 Days and 9.4 Hours



Antonios Michailidis, Georgios Dimou, Georgia Mingou, Panagiotis Kosmoliaptsis, Christos Giankoulof, Evangelos Petsatodis, Department of Interventional Radiology, Georgios Papanikolaou General Hospital of Thessaloniki, Thessaloniki 57010, Greece

Athanasios Panos, Efthimios Samoladas, Department of 1st Orthopaedic Clinic, Georgios Papanikolaou General Hospital of Thessaloniki, Aristotle University of Thessaloniki, Thessaloniki 57010, Greece

Maria Arvaniti, Dental School, EKPA, Athens 15773, Greece

Corresponding author: Evangelos Petsatodis, PhD, Consultant Physician-Scientist, Doctor, Department of Interventional Radiology, Georgios Papanikolaou General Hospital of Thessaloniki, Leoforos Papanikolaou, Exohi, Thessaloniki 57010, Greece.
irpapanikolaou@gmail.com

Abstract

BACKGROUND

Osteoid osteoma is a benign bone tumor with characteristic clinical symptomatology. The selected method for its treatment is percutaneous radiofrequency ablation. However, percutaneous cryoablation is an alternative method with certain advantages.

AIM

To evaluate percutaneous computed tomography (CT)-guided cryoablation for the treatment of osteoid osteoma in young patients and adults.

METHODS

A total of 25 patients were treated with percutaneous CT-guided cryoablation for osteoid osteomas between October 2020 and March 2023 at a single institution. All patients were above 14-years-old (mean age, 24-years-old), and all procedures were performed under local anesthesia. Of the 25 patients, 8 were female and 17 were male. Tumor sites included the femur ($n = 9$), medial malleolus ($n = 4$), sacral ala ($n = 4$), facets ($n = 4$), humerus ($n = 3$), and tibia ($n = 1$). One cryoprobe was used in each procedure and, when possible, the lesion was covered by the ice-ball using an extraosseous position without penetrating the nidus. All necessary thermal protective techniques were used depending on the anatomical structure at risk.

RESULTS

All patients treated had complete response (100% clinical success rate) starting on the day of the procedure. Technical success was achieved in all cases. Visual analog scale (VAS) scores at 1 year were 0, compared to a mean VAS score of 8.5 ± 1 (SD) before the procedure. No recurrences were reported at the 1-year follow-up and no complications were observed. In 11/25 cases, an extraosseous position of the cryoprobe was used with less procedural time achieving technical and clinical success and no complications with less patient discomfort. All patients were discharged from the hospital on the same day as the procedure.

CONCLUSION

Cryoablation of osteoid osteomas is an efficacious and safe procedure with durable clinical results. Its greatest advantage is that the procedure can be performed under local anesthesia using an extraosseous position of the cryoprobe when possible.

Key Words: Cryoablation; Osteoid osteoma; Computed tomography guidance; Interventional radiology; Orthopedics; Bone tumors

©The Author(s) 2024. Published by Baishideng Publishing Group Inc. All rights reserved.

Core Tip: This study aims to evaluate percutaneous cryoablation for the treatment of osteoid osteomas. Our results prove that cryoablation is safe and effective as a treatment option for these tumors and has certain advantages over other ablative methods. Cryoablation has the advantage of extraosseous positioning of the cryoprobe, avoiding bone drilling, less procedural and post-procedural pain, making it possible for the procedure to be performed strictly under local anesthesia and the ability to treat larger lesions with a single probe placement.

Citation: Michailidis A, Panos A, Samoladas E, Dimou G, Mingou G, Kosmoliaptis P, Arvaniti M, Giankoulof C, Petsatodis E. Cryoablation of osteoid osteomas: Is it a valid treatment option? *World J Radiol* 2024; 16(9): 389-397

URL: <https://www.wjgnet.com/1949-8470/full/v16/i9/389.htm>

DOI: <https://dx.doi.org/10.4329/wjr.v16.i9.389>

INTRODUCTION

Osteoid osteoma is a benign bone tumor, ranking third in frequency among bone tumors and accounting for about 14% of all cases. The first case was described in 1930, and it was recognized as a distinct entity in 1935[1]. This tumor predominantly occurs during the second decade of life, affecting males four times more often than females. Patients typically present with dull, night-time pain that subsides after taking aspirin or non-steroidal anti-inflammatory drugs (NSAIDs) [2]. The tumor consists of a nidus surrounded by thick sclerotic bone, and the nidus is formed by prostaglandin-producing cells. Although the exact pain mechanism remains unclear[3], the composition of the nidus is believed to contribute to the pain.

Osteoid osteomas are most commonly found in the cortex of the femur, tibia, and vertebral pedicles. Diagnosis is typically based on the characteristic clinical presentation of night pain and is confirmed by imaging techniques such as X-rays, computed tomography (CT), magnetic resonance imaging (MRI), or even SPECT scans[4]. CT scans are preferred for diagnosing osteoid osteomas because they clearly depict the nidus and assist in differentiating the tumor from conditions like Brodie's abscess and osteomyelitis. MRI is highly sensitive in detecting surrounding bone marrow and soft tissue edema, which can resemble tumors and osteomyelitis. Double-density scintigraphy is also effective in imaging osteoid osteomas and is often followed by a CT scan[5].

Treatment options include conservative management with analgesics or NSAIDs while awaiting spontaneous regression, and surgical excision, which comes with disadvantages like large incisions, prolonged hospitalization, and the potential need for reoperation in cases of incomplete excision. Minimally invasive techniques, such as trephine excision of the nidus and radiofrequency (RF) ablation, considered the gold standard, have been established as effective solutions that improve outcomes and offer better post-procedure recovery for patients. Percutaneous cryoablation is a well-established method for treating bone tumors and other malignancies, offering optimal oncologic outcomes[6]. Its major advantages in bone ablation include the ability to penetrate dense bone, reduced procedural pain, and the visualization of the ice ball. Additionally, cryoablation can create larger ablation volumes, which is particularly beneficial for treating osteoid osteomas with eccentric shapes, potentially improving treatment outcomes.

Our study aims to highlight the efficacy and safety of performing cryoablation under local anesthesia in a series of 25 cases of osteoid osteoma, reinforcing the validity of this method as a treatment option.

MATERIALS AND METHODS

Included patients

Cryoablation therapy was performed on 25 patients, all diagnosed with osteoid osteoma. These patients were initially examined at our orthopedic outpatient department before being referred to the interventional radiology department for treatment. This retrospective study was approved by the scientific committee of our hospital, which oversees research ethics, and written consent was obtained from all patients for reviewing their clinical and imaging data. The study included patients over 14-years-old with typical clinical presentation and imaging findings of osteoid osteoma. Exclusion criteria included coagulation disorders, pain of different origin, acute infection, and previous interventions for treating osteoid osteoma. One patient who had undergone two unsuccessful RF ablations for a femoral osteoid osteoma, resulting in massive periostitis, was excluded from the study.

The clinical presentation in all cases was characteristic night pain relieved by aspirin or NSAIDs. Diagnosis was confirmed through imaging, including MRI, unenhanced CT scans, and in some cases, Technetium-99 bone scans. Typical CT findings included a lucent nidus surrounded by reactive sclerotic bone. MRI showed bone edema, and intravenous gadolinium administration revealed osteoid osteoma nidus. Bone scintigraphy was used when additional diagnostic information was needed and typically showed focal uptake and the characteristic double-density sign. Of the 25 patients, 8 were female and 17 were male, with a mean age of 28-years-old (range: 15 years to 53 years). The procedures were performed between October 2020 and March 2023. Tumor sites included the femur ($n = 9$), medial malleolus ($n = 4$), sacral ala ($n = 4$), facets ($n = 4$), humerus ($n = 3$), and tibia ($n = 1$) (Table 1).

Procedure

All procedures were performed under CT guidance with local anesthesia using 1% lidocaine at the skin entry site and the periosteum. Paracetamol (1 g) and tramadol (100-200 mg) were administered intravenously before the procedure for pain control. Prophylactic IV antibiotics (1 g cefoxitin) were given to all patients. Even patients requiring direct nidus penetration were treated under local anesthesia. The entire procedure was conducted under strictly aseptic conditions. The cryoprobe was positioned either adjacent to the lesion without penetrating the cortex or directly into the nidus with bone penetration, depending on the location of the osteoid osteoma.

To ensure complete coverage of the lesion from an extraosseous position, the cryoprobe was placed parallel to the cortex, covering the entire lesion with the ice ball (11/25 cases). In other cases, the nidus was penetrated with a bone trocar, and the cryoprobe was then coaxially inserted. The access needle was withdrawn at least 3 cm to expose the cryoprobe and prevent contact between the ice ball and the needle.

For each procedure, an IceSeed Cryoprobe 17 g or IceSphere Cryoprobe 17 g (Boston Scientific, Marlborough, MA, United States) was used, capable of creating an ice ball measuring 15 mm × 20 mm and 23 mm × 29 mm, respectively, at -20°C. A freeze-thaw-freeze protocol was applied, consisting of two 10-minute freezing cycles with an intermediate thawing cycle, divided into a 9-minute passive thaw and a 1-minute active thaw. The ice ball formation was monitored by consecutive CT scans, appearing as a hypodense area in the soft tissues, but not visible in the bone, with the ability to penetrate sclerotic bone.

When the ice ball adequately covered the lesion and the cryosphere approached within 1 cm of a critical structure, the generator power was reduced to 60%. Depending on the case, passive and active thermoprotection techniques were applied to avoid thermal injury to adjacent sensitive structures, such as nerves, cartilage, and skin. Techniques like hydrodissection, neurostimulation, and thermocouple placement were used to monitor the temperature and function of adjacent nerve roots. A warm glove combined with hydrodissection was used for skin protection, while direct injection of warm saline was employed for joint protection (Figures 1, 2, and 3).

Performing the procedure under local anesthesia allowed communication with patients to assess any discomfort and enabled real-time nerve monitoring by asking patients to perform specific movements related to the nerve at risk. At the end of the procedure, the ice ball adequately enclosed the nidus of the osteoid osteoma. Peri- and post-procedural pain was significantly less compared to RF ablation, and all patients were able to ambulate and were discharged on the same day after the procedure.

Anti-inflammatory drugs were prescribed for 4 days, and patients were advised to refrain from heavy sports activities for 2 weeks.

Follow-up

All patients were clinically evaluated 1 week after the procedure to assess any complications and to evaluate their post-procedural visual analog scale (VAS) scores. Clinical data were also collected at 6 months and 1 year after the procedure. No imaging studies were conducted if patients experienced complete relief of their symptoms. Complete pain relief at 1 year was defined as clinical success.

RESULTS

For statistical analyses in this study, the Shapiro-Wilk test was employed to assess the normality of continuous variables. Depending on the results of this test, continuous variables were then described using either the mean (SD) or the median (IQR). Categorical variables, such as sex, were reported as frequencies and percentages.

Table 1 Clinical and demographic data of the patients

No.	Sex	Age	Location	VAS pre	VAS post (1-12 months)	Complication
1	Female	53	Sacrum	7	1	Nothing
2	Female	18	Medial malleolus	8	0	"
3	Male	41	Humerus	9	0	"
4	Male		Femur	9	0	"
5	Male	24	O5 facet	7	0	"
6	Male	16	Femur	8	0	"
7	Female	27	O3 facet	8	1	"
8	Female	16	Medial malleolus	10	0	"
9	Male	18	Femur	8	0	"
10	Male	45	Sacrum	7	0	"
11	Male	19	Femur	8	1	"
12	Male	20	Humerus	9	1	"
13	Male	18	Tibia	9	0	"
14	Male	23	Femur	8	0	"
15	Male	18	Humerus	8	0	"
16	Female	51	Sacrum	7	1	"
17	Female	19	Medial malleolus	8	0	"
18	Male	44	Humerus	9	0	"
19	Male		Femur	9	0	"
20	Male	26	O4 facet	7	0	"
21	Male	17	Femur	8	0	"
22	Female	29	O5 facet	8	1	"
23	Female	15	Medial malleolus	10	0	"
24	Male	19	Femur	8	0	"
25	Male	40	Sacrum	7	0	"

VAS: Visual analog scale.

To evaluate differences in outcomes over time, such as pain levels before and after treatment, the Wilcoxon signed-rank test was used for comparing related samples. Additionally, generalized estimating equation (referred to as GEE) models were applied to examine changes in pain and other variables at different time points. The GEE models are particularly advantageous for analyzing longitudinal non-normal data, as they utilize all available data for each individual.

Statistical significance was determined using a *P*-value threshold of less than 0.05. The analyses were performed using IBM SPSS 27.0 (IBM Corp., Armonk, NY, United States).

Technical success was achieved in all cases, with the ice ball adequately covering the lesion. All procedures were performed under local anesthesia. An extraosseous position of the cryoprobe was used in 11 out of 25 cases (Figure 4). Biopsies were performed in only 2 cases where the nidus of the osteoid osteoma was larger than 1 cm.

Patient data were collected at 1 month, 6 months, and 1 year after the procedure, with all cases having at least a 1-year follow-up. All patients experienced complete pain relief starting the day after the procedure and reported no discomfort during follow-up. VAS scores at 1 year were 0, compared to a mean VAS score of 8.5 ± 1 (SD) before the procedure (Figure 5). No recurrences were reported at the 1-year follow-up, and no complications were observed.

All patients reported that they tolerated the procedure very well, with no discomfort and no post-procedural issues.

We also compared the results of the 11 cases where an extraosseous position was used *vs* the 14 cases where an intraosseous position of the cryoprobe was positioned *via* bone penetration. Technical success was achieved in both groups. The procedural time was similar between the intraosseous group and the subset of extraosseous positioning cases where hydrodissection was used [60 ± 10 (SD) minutes]. However, in the 4/11 extraosseous positioning cases where hydrodissection was not required, the procedural time was significantly faster [30 ± 10 (SD) minutes]. Neither group reported complications with minimal periprocedural pain, but patients in the extraosseous group reported less procedural discomfort. Patients from both groups were discharged the same day of the procedure.

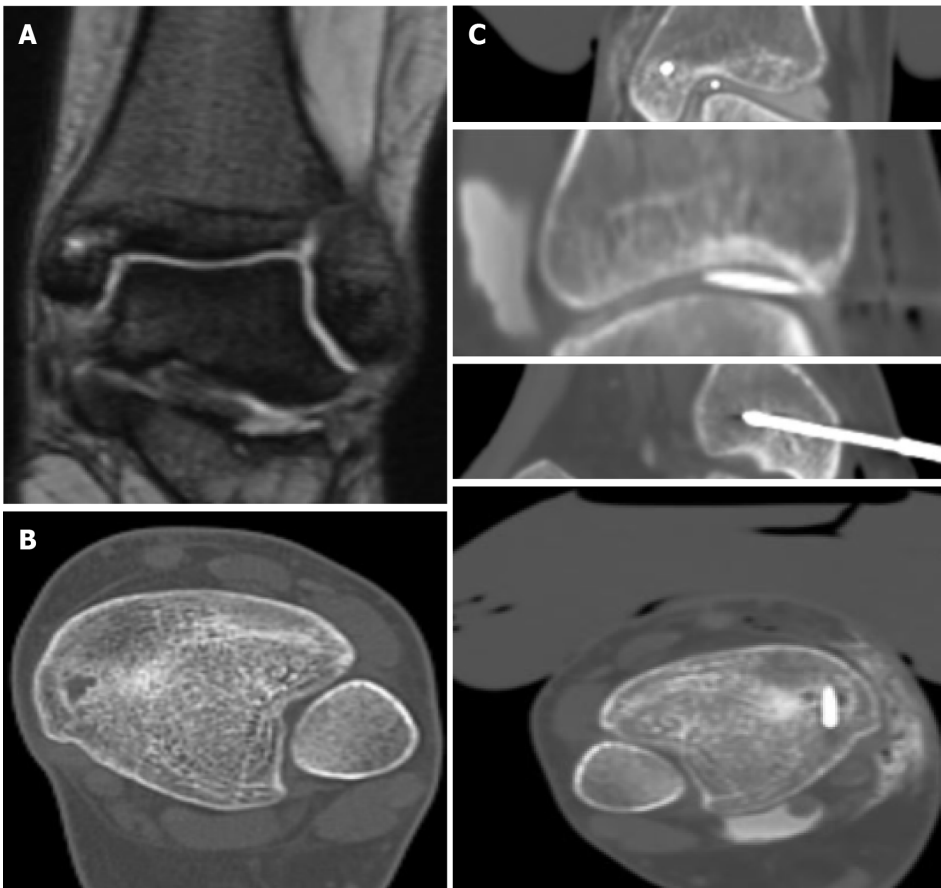


Figure 1 Eighteen-year-old female-osteoid osteoma of the medial malleolus (tibia). A: Coronal T2WI image reveals 1 cm lesion of the medial malleolus in close proximity to the skin and the ankle joint; B: Computed tomography image demonstrates a lytic lesion with reactive sclerosis. The lesion was biopsied and confirmed as an osteoid osteoma; C: Cryoablation procedure: Cryoprobe placement inside the nidus and a spinal needle in the joint for active warming during the procedure. Skin was hydrodissected with a mixture of saline and local anesthetic and a warm glove was applied for protection.

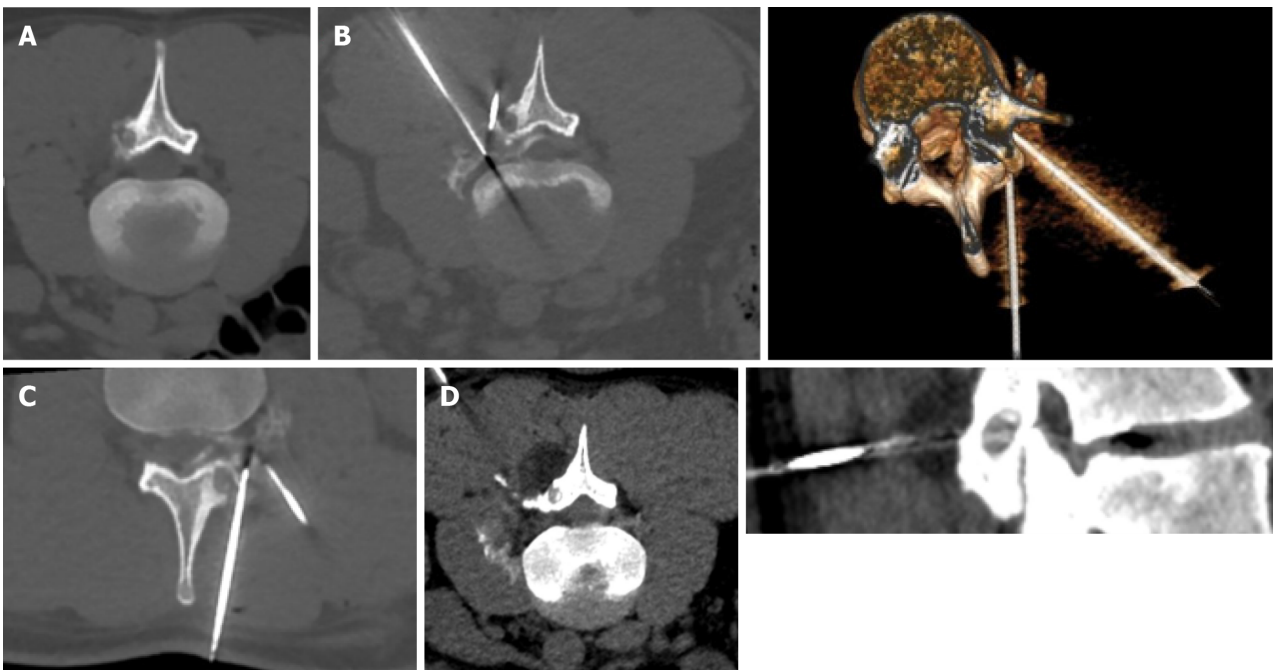


Figure 2 Twenty-four-year-old male-osteoid osteoma of the L4-L5 facet joint. A: Computed tomography axial image L4-L5 facet joint osteoid osteoma; B: Placement of the cryoprobe at an extraosseous position; C: Placement of a thermocouple near the nerve root for temperature monitoring. Spinal needle at the same level for epidural dissection and active warming; D: Iceball visualization as hypodense area covering the entire lesion.

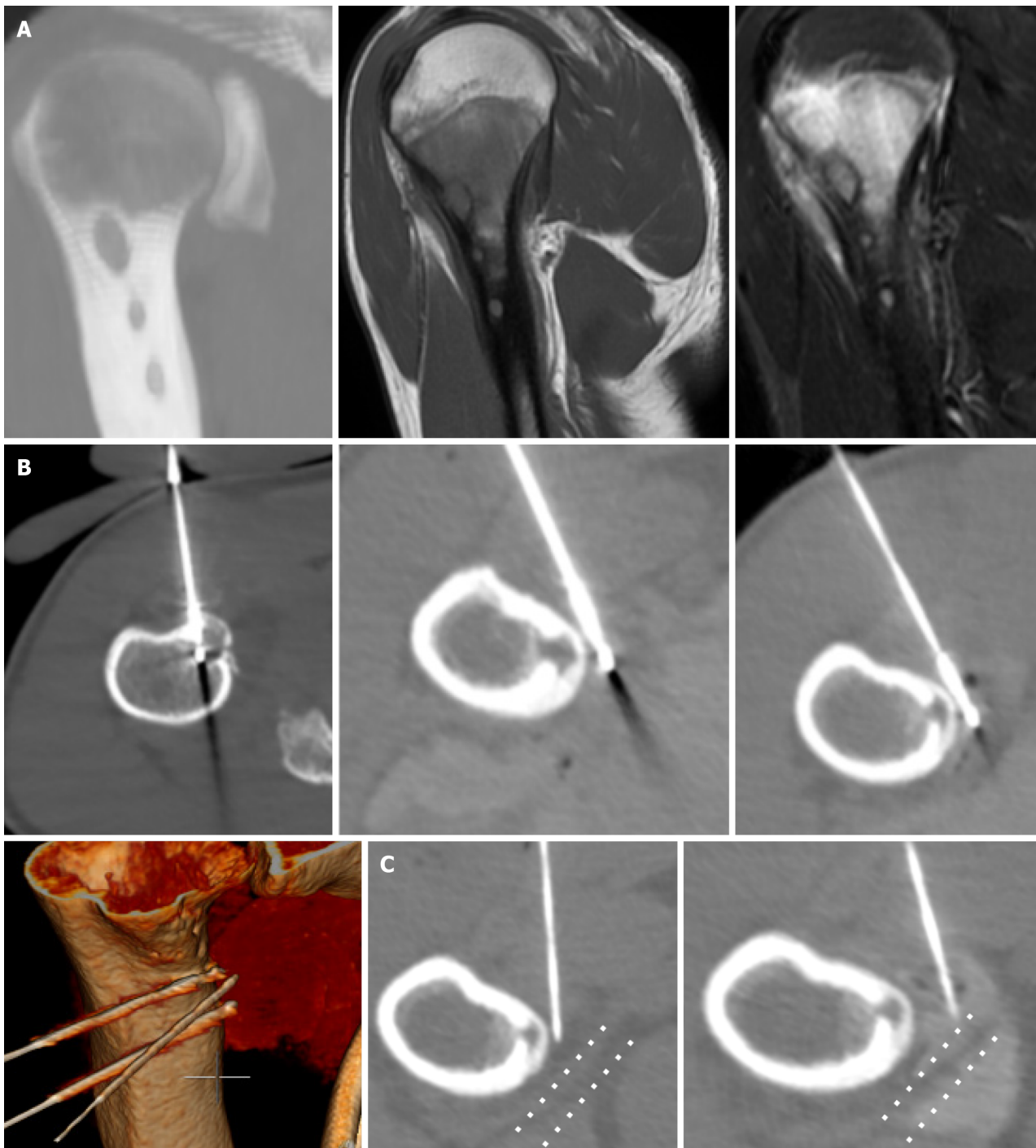


Figure 3 Seventeen-year-old male-humerus bone multiple osteoid osteomas. A: Computed tomography thick slice and magnetic resonance imaging showing three radiolucent lesions in head, epiphysis and diaphysis of right humerus bone with periosteal edema; B: Visualization of the three cryoprobes. Two of them were placed in extraosseous positions and one of them was placed in an intraosseous position; C: Hydrodissection of the axillary nerve with thermocouple for temperature monitoring, protection and active warming.

DISCUSSION

Osteoid osteoma, a benign bone tumor, presents a unique challenge in clinical management. The current study explores the efficacy and safety of percutaneous CT-guided cryoablation as a treatment option for osteoid osteomas in adults. The findings reveal compelling evidence supporting the validity of cryoablation in this context. The primary outcome of the study was a 100% clinical success rate, and it underscores the effectiveness of cryoablation in treating osteoid osteomas. This aligns with previous research that has demonstrated the ability of cryoablation to induce complete response and relief from the characteristic night pain associated with osteoid osteomas.

The excellent outcomes of cryoablation have been highlighted in other studies, as well. Le Corroller *et al*[7] presented a series of 50 cases that treated osteoid osteoma with cryoablation techniques. The patients had no post-procedural pain, VAS scores decreased from 8 before the procedure to 0 at 6-months follow-up, and had only 1 case that cryoablation

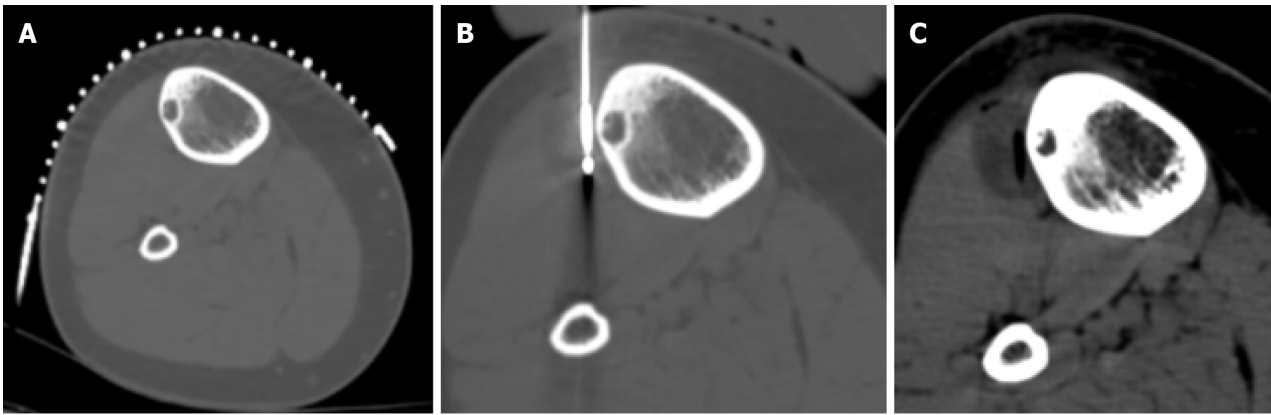


Figure 4 Twenty-three-year-old male-tibia osteoid osteoma. A: Axial computed tomography image of a tibia osteoid osteoma; B: Placement of the cryoprobe at an extraosseous position parallel to the cortex; C: Hypodense ice covering the whole lesion.

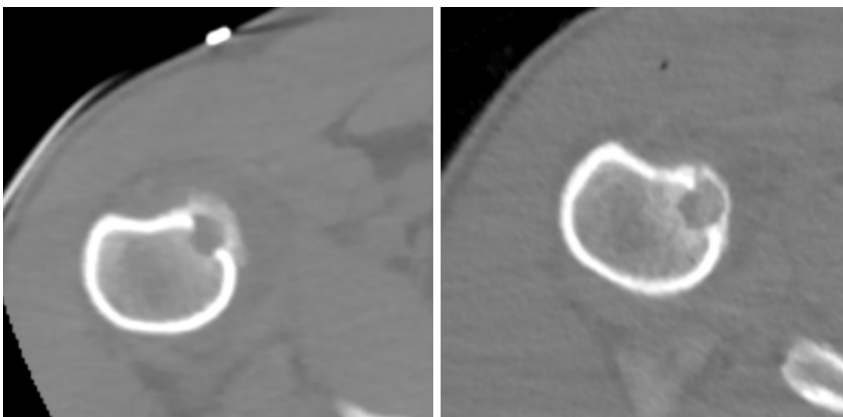


Figure 5 One month after cryoablation procedure of osteoid osteoma of humerus bone reduction of the periosteal reaction.

failed due to bad positioning of the probe. Coupal *et al*[8] reported similar outcomes in a 10-case series. All patients had reduced pain after the procedure and in the follow-up. All cases had technical and clinical success, and no complications were reported. Finally, Whitmore *et al*[9] reported 29 cases that included adults and children. They achieved 100% technical success rate and had long-term clinical outcomes of cryoablation around 90%. The high technical success rate further solidifies cryoablation as a reliable therapeutic option for this particular benign bone tumor.

An intriguing aspect of the study is the utilization of local anesthesia and the preference for an extraosseous position of the cryoprobe. These choices contribute to the overall patient experience and also underscore the adaptability of cryoablation in diverse clinical settings. Performing the procedure under local anesthesia is a notable advancement[10], potentially reducing the procedural burden on patients and minimizing the need for general anesthesia, which may be associated with additional risks.

The deliberate selection of an extraosseous position for the cryoprobe, without penetrating the nidus when possible, adds a layer of sophistication to the technique. This approach enhances the safety profile of the procedure and highlights the precision achievable with CT guidance. The ability to tailor the procedure to the individual characteristics of the lesion, considering its location and morphology, speaks to the versatility of cryoablation.

The cryoprobe was inserted at an extraosseous position when the lesion was accessible from outside the bone and not deeply embedded within it. This approach offers several advantages, such as avoiding bone penetration, which reduces procedural pain and shortens the procedural time. By not penetrating the bone, the risk of complications associated with bone damage is minimized. Additionally, this technique can effectively treat the lesion if the ice ball adequately covers the tumor and if any critical structures outside the bone are properly protected with techniques like hydrodissection and temperature monitoring, particularly for nearby nerves.

In the study, 11 patients underwent cryoablation with the cryoprobe positioned at an extraosseous location, while the remaining patients had the probe inserted intraosseously. Both groups achieved complete pain relief, with no reported recurrences or complications at the 1-year follow-up. The patients treated with extraosseous positioning benefited from reduced procedural pain and shorter procedural times due to the non-invasive nature of this approach. The main challenge with the extraosseous technique is ensuring that the ice ball adequately covers the lesion while also protecting surrounding anatomical structures. However, in this study, proper protection of critical structures, such as nerves, was achieved using hydrodissection and temperature monitoring, leading to successful outcomes without clinical implications.

Overall, both techniques were effective, but the extraosseous approach offers advantages in terms of reduced invasiveness and patient comfort, provided that adequate precautions are taken to protect nearby structures. This point highlights the versatility of cryoablation techniques and their ability to be tailored to the specific characteristics of each lesion.

An important consideration in any interventional procedure is its safety profile. In this study, the absence of reported complications and the same-day discharge of patients following cryoablation speak to the safety and minimal invasiveness of the procedure. The meticulous use of thermal protective techniques tailored to anatomical structures at risk further enhances the safety profile, addressing concerns that may arise in proximity to critical structures[11].

Drawing comparisons with established treatment modalities for osteoid osteomas enriches the discussion. While surgical excision[12], trephine excision, and RF ablation have been cornerstones in the management of osteoid osteomas, cryoablation and RF ablation are both effective techniques for treating osteoid osteomas with distinct advantages. Cryoablation is particularly noted for its lower periprocedural and postprocedural pain[13]. This is largely due to the anesthetic effect of the cold temperatures used during the procedure, which can significantly reduce discomfort. Another key advantage of cryoablation is the ability to visualize the ablation zone in real-time *via* imaging, as the "ice ball" formed around the cryoprobe is clearly visible. This visualization ensures precise targeting of the lesion and helps protect surrounding tissues. Moreover, cryoablation allows for the treatment of larger lesions by creating larger ablation zones. This is extremely useful in osteoid osteomas with excessive periosteal reaction and eccentric shape, which is an independent factor of treatment failure when using RF ablation[13]. Additionally, in some cases, the cryoprobe can be positioned in an extraosseous location, avoiding the need to penetrate the bone, which can reduce procedural complexity and risk[14].

In contrast, RF ablation offers the advantage of faster ablation times and a more established track record, with extensive long-term data supporting its use[15]. However, it lacks the ability to visualize the ablation zone as clearly as cryoablation and generally requires direct bone penetration, which may contribute to higher periprocedural pain[16]. RF ablation also lacks the ability of treating larger lesions. In such cases, the RF probe must be repositioned after the first treatment or multiple RF probes should be used. This comparative analysis suggests that cryoablation could offer unique advantages in specific clinical scenarios.

The clinical implications of these findings extend beyond statistical significance. Cryoablation is efficacious and appears to positively impact the patient experience. Considering its application in young patients and adults, the discussion should explore how cryoablation may influence recovery, hospital stay, and overall quality of life. The study prompts further investigation into age-related considerations and variations in treatment response.

As with any study, limitations exist. Acknowledging these limitations, such as the relatively small sample size and the absence of long-term follow-up, enhances the transparency of the research. Identifying areas for further research, such as larger-scale trials, extended follow-up periods, or comparative studies against alternative treatments[17,18], provides a roadmap for future investigations.

CONCLUSION

The study's findings robustly support cryoablation as an efficacious and safe treatment option for osteoid osteomas in adults. The emphasis on local anesthesia, extraosseous positioning, and the meticulous attention to safety considerations contribute to the evolving landscape of interventional radiology. While further research is warranted to establish the long-term efficacy and comparative advantages of cryoablation, this study marks a significant step forward in expanding the therapeutic options available for managing osteoid osteomas in adult patients.

FOOTNOTES

Author contributions: Petsatodis E and Samoladas E designed the research; Michailidis A, Kosmoliaptis P, Dimou G, and Mingou G performed the research; Petsatodis E and Arvaniti M contributed new reagents or analytic tools; Petsatodis E and Giankoulof C analyzed data; Michailidis A and Panos A wrote the paper.

Institutional review board statement: The study was conducted in accordance with the Declaration of Helsinki, and approved by the Institutional Review Board of General Hospital of Thessaloniki "G. Papanikolaou" (Protocol Code 77481-12 and 05-04-2024).

Informed consent statement: All procedures performed in studies involving human participants were in accordance with the ethical standards of the institutional and/or national research committee and with the 1964 Helsinki declaration and its later amendments or comparable ethical standards. Informed consent was obtained from all individual participants included in the study.

Conflict-of-interest statement: The authors declare that they have no conflicts of interest.

Data sharing statement: Consent for publication was obtained for every individual person's data included in the study.

Open-Access: This article is an open-access article that was selected by an in-house editor and fully peer-reviewed by external reviewers. It is distributed in accordance with the Creative Commons Attribution NonCommercial (CC BY-NC 4.0) license, which permits others to distribute, remix, adapt, build upon this work non-commercially, and license their derivative works on different terms, provided the

original work is properly cited and the use is non-commercial. See: <https://creativecommons.org/licenses/by-nc/4.0/>

Country of origin: Greece

ORCID number: Antonios Michailidis 0000-0003-2371-1879; Athanasios Panos 0009-0000-2960-8691; Efthimios Samoladas 0000-0002-1892-7707; Georgios Dimou 0009-0004-3003-7549; Georgia Mingou 0009-0002-9254-5501; Panagiotis Kosmoliaptis 0009-0005-7779-6005; Maria Arvaniti 0009-0001-6757-0804; Christos Giankoulof 0009-0005-6380-0878; Evangelos Petsatodis 0000-0002-6252-1130.

S-Editor: Qu XL

L-Editor: Filipodia

P-Editor: Wang WB

REFERENCES

- 1 **Jaffe HL.** "OSTEOID-OSTEOMA". *Arch Surg* 1935; **31**: 709 [DOI: [10.1001/archsurg.1935.01180170034003](https://doi.org/10.1001/archsurg.1935.01180170034003)]
- 2 **Tepelenis K,** Skandalakis GP, Papathanakos G, Kefala MA, Kitsouli A, Barbouti A, Tepelenis N, Varvarousis D, Vlachos K, Kanavaros P, Kitsoulis P. Osteoid Osteoma: An Updated Review of Epidemiology, Pathogenesis, Clinical Presentation, Radiological Features, and Treatment Option. *In Vivo* 2021; **35**: 1929-1938 [PMID: [34182465](https://pubmed.ncbi.nlm.nih.gov/34182465/) DOI: [10.21873/invivo.12459](https://doi.org/10.21873/invivo.12459)]
- 3 **Onashvili N,** Loria G, Gogichaishvili T, Mariamidze A, Sirbiladze M, Sainishvili N. Computed tomography guided radiofrequency ablation of multifocal osteoid osteoma. *Radiol Case Rep* 2020; **15**: 1275-1279 [PMID: [32577146](https://pubmed.ncbi.nlm.nih.gov/32577146/) DOI: [10.1016/j.radcr.2020.05.048](https://doi.org/10.1016/j.radcr.2020.05.048)]
- 4 **Çakar M,** Esenyele CZ, Seyran M, Tekin AÇ, Adaş M, Bayraktar MK, Coşkun Ü. Osteoid osteoma treated with radiofrequency ablation. *Adv Orthop* 2015; **2015**: 807274 [PMID: [25705522](https://pubmed.ncbi.nlm.nih.gov/25705522/) DOI: [10.1155/2015/807274](https://doi.org/10.1155/2015/807274)]
- 5 **Lee EH,** Shafi M, Hui JH. Osteoid osteoma: a current review. *J Pediatr Orthop* 2006; **26**: 695-700 [PMID: [16932114](https://pubmed.ncbi.nlm.nih.gov/16932114/) DOI: [10.1097/01.bpo.0000233807.80046.7c](https://doi.org/10.1097/01.bpo.0000233807.80046.7c)]
- 6 **Parmeggiani A,** Martella C, Ceccarelli L, Miceli M, Spinnato P, Facchini G. Osteoid osteoma: which is the best miniminvasive treatment option? *Eur J Orthop Surg Traumatol* 2021; **31**: 1611-1624 [PMID: [33839926](https://pubmed.ncbi.nlm.nih.gov/33839926/) DOI: [10.1007/s00590-021-02946-w](https://doi.org/10.1007/s00590-021-02946-w)]
- 7 **Le Corroller T,** Vives T, Mattei JC, Pauly V, Guenoun D, Rochwerger A, Champsaur P. Osteoid Osteoma: Percutaneous CT-guided Cryoablation Is a Safe, Effective, and Durable Treatment Option in Adults. *Radiology* 2022; **302**: 392-399 [PMID: [34812672](https://pubmed.ncbi.nlm.nih.gov/34812672/) DOI: [10.1148/radiol.2021211100](https://doi.org/10.1148/radiol.2021211100)]
- 8 **Coupal TM,** Mallinson PI, Munk PL, Liu D, Clarkson P, Ouellette H. CT-guided percutaneous cryoablation for osteoid osteoma: initial experience in adults. *AJR Am J Roentgenol* 2014; **202**: 1136-1139 [PMID: [24758671](https://pubmed.ncbi.nlm.nih.gov/24758671/) DOI: [10.2214/AJR.13.11336](https://doi.org/10.2214/AJR.13.11336)]
- 9 **Whitmore MJ,** Hawkins CM, Prologo JD, Marshall KW, Fabregas JA, Yim DB, Monson D, Oskouei SV, Fletcher ND, Williams RS. Cryoablation of Osteoid Osteoma in the Pediatric and Adolescent Population. *J Vasc Interv Radiol* 2016; **27**: 232-7; quiz 238 [PMID: [26683456](https://pubmed.ncbi.nlm.nih.gov/26683456/) DOI: [10.1016/j.jvir.2015.10.005](https://doi.org/10.1016/j.jvir.2015.10.005)]
- 10 **Pusceddu C,** Vergantino E, Santucci D, Marsico S, Cappucci M, Vaccarino F, Beomonte Zobel B, Grasso RF, Faiella E. Percutaneous Cryoablation under Conscious Sedation: A Safe, Effective and Painless Option for the Treatment of Pediatric Osteoid Osteoma. *J Clin Med* 2023; **12** [PMID: [37959354](https://pubmed.ncbi.nlm.nih.gov/37959354/) DOI: [10.3390/jcm12216889](https://doi.org/10.3390/jcm12216889)]
- 11 **Wu B,** Xiao YY, Zhang X, Zhao L, Carrino JA. CT-guided percutaneous cryoablation of osteoid osteoma in children: an initial study. *Skeletal Radiol* 2011; **40**: 1303-1310 [PMID: [21311882](https://pubmed.ncbi.nlm.nih.gov/21311882/) DOI: [10.1007/s00256-011-1119-1](https://doi.org/10.1007/s00256-011-1119-1)]
- 12 **Shu M,** Ke J. The surgical management of osteoid osteoma: A systematic review. *Front Oncol* 2022; **12**: 935640 [PMID: [35936708](https://pubmed.ncbi.nlm.nih.gov/35936708/) DOI: [10.3389/fonc.2022.935640](https://doi.org/10.3389/fonc.2022.935640)]
- 13 **Baal JD,** Pai JS, Chen WC, Joseph GB, O'Donnell RJ, Link TM. Factors Associated with Osteoid Osteoma Recurrence after CT-Guided Radiofrequency Ablation. *J Vasc Interv Radiol* 2019; **30**: 744-751 [PMID: [30879870](https://pubmed.ncbi.nlm.nih.gov/30879870/) DOI: [10.1016/j.jvir.2018.11.014](https://doi.org/10.1016/j.jvir.2018.11.014)]
- 14 **Santiago E,** Pauly V, Brun G, Guenoun D, Champsaur P, Le Corroller T. Percutaneous cryoablation for the treatment of osteoid osteoma in the adult population. *Eur Radiol* 2018; **28**: 2336-2344 [PMID: [29294152](https://pubmed.ncbi.nlm.nih.gov/29294152/) DOI: [10.1007/s00330-017-5164-6](https://doi.org/10.1007/s00330-017-5164-6)]
- 15 **Vogl TJ,** Bialek M, Eichler K, Hammerstingl R, Bielfeldt J, Zangos S, Scholtz JE, Adwan H. Short- and Long-Term Outcomes after Radiofrequency Ablation of Osteoid Osteomas. *J Pers Med* 2024; **14** [PMID: [38673028](https://pubmed.ncbi.nlm.nih.gov/38673028/) DOI: [10.3390/jpm14040401](https://doi.org/10.3390/jpm14040401)]
- 16 **Motamedi D,** Learch TJ, Ishimitsu DN, Motamedi K, Katz MD, Brien EW, Menendez L. Thermal ablation of osteoid osteoma: overview and step-by-step guide. *Radiographics* 2009; **29**: 2127-2141 [PMID: [19926767](https://pubmed.ncbi.nlm.nih.gov/19926767/) DOI: [10.1148/rg.297095081](https://doi.org/10.1148/rg.297095081)]
- 17 **Shanmugasundaram S,** Nadkarni S, Kumar A, Shukla PA. Percutaneous Ablative Therapies for the Management of Osteoid Osteomas: A Systematic Review and Meta-Analysis. *Cardiovasc Intervent Radiol* 2021; **44**: 739-749 [PMID: [33709278](https://pubmed.ncbi.nlm.nih.gov/33709278/) DOI: [10.1007/s00270-021-02804-6](https://doi.org/10.1007/s00270-021-02804-6)]
- 18 **Tsoumakidou G,** Thénint MA, Garnon J, Buy X, Steib JP, Gangi A. Percutaneous Image-guided Laser Photocoagulation of Spinal Osteoid Osteoma: A Single-Institution Series. *Radiology* 2016; **278**: 936-943 [PMID: [26383230](https://pubmed.ncbi.nlm.nih.gov/26383230/) DOI: [10.1148/radiol.2015150491](https://doi.org/10.1148/radiol.2015150491)]

Retrospective Study

Radiological findings of February 2023 twin earthquakes-related spine injuries

Ayşenur Bolukçu, Ahmet Gürkan Erdemir, İlkey Sedakat İdilman, Adalet Elçin Yıldız, Gökçen Çoban Çifçi, Mehmet Ruhi Onur, Erhan Akpınar

Specialty type: Radiology, nuclear medicine and medical imaging

Provenance and peer review:

Invited article; Externally peer reviewed.

Peer-review model: Single blind

Peer-review report's classification

Scientific Quality: Grade B

Novelty: Grade A

Creativity or Innovation: Grade A

Scientific Significance: Grade B

P-Reviewer: Elzeiny A

Received: May 27, 2024

Revised: August 20, 2024

Accepted: August 28, 2024

Published online: September 28, 2024

Processing time: 122 Days and 9 Hours



Ayşenur Bolukçu, Ahmet Gürkan Erdemir, İlkey Sedakat İdilman, Adalet Elçin Yıldız, Gökçen Çoban Çifçi, Mehmet Ruhi Onur, Erhan Akpınar, Department of Radiology, Hacettepe University, Faculty of Medicine, Ankara 06100, Türkiye

Erhan Akpınar, Department of Radiology, University of Chicago, Chicago, IL 60637, United States

Corresponding author: Ahmet Gürkan Erdemir, MD, Doctor, Instructor, Department of Radiology, Hacettepe University, Faculty of Medicine, No. 6/1 Adnan Saygun Street, Ankara 06100, Türkiye. a.gurkan.erdemir@gmail.com

Abstract**BACKGROUND**

The February 6, 2023, twin earthquakes in Türkiye caused significant structural damage and a high number of injuries, particularly affecting the spine, which underscores the importance of understanding the distribution and nature of vertebral injuries in disaster victims.

AIM

To investigate the distribution of radiological findings of vertebral injuries in patients referred to a major tertiary center during the February 6, 2023 twin earthquakes in Türkiye.

METHODS

With the approval of the institutional ethics committee, 1216 examinations of 238 patients transferred from the region to a tertiary major hospital after the twin earthquakes of February 6, 2023, were retrospectively analyzed for spine injuries.

RESULTS

Spine computed tomography (CT) scans were performed in 192 of 238 patients with a suspected spinal injury, 42 of whom also had an magnetic resonance imaging (MRI). In 86 of 192 patients (44.79%; M:F = 33:53) a spinal fracture was detected on CT and in 33 of 42 patients (78.57%; M:F = 20:13) a spinal injury was found on MRI. Of the 86 patients in whom vertebral injury was detected, fractures were detected in the Denis-B group in 33, Denis-C in 4, Denis-D in 20 and Denis-E in 11 patients. Among the vertebral bodies: 40 "compression fractures", 17 "burst fractures", 5 "translational dislocation fractures", 5 "flexion-distraction fractures" and

58 "prolonged forced fetal posture fractures" were detected. In addition, isolated transverse or spinous process fractures were found in eighteen vertebrae.

CONCLUSION

Our study highlights the prevalence and diverse spectrum of spinal injuries following the February 6, 2023 twin earthquakes in Turkey underscoring the urgent need for effective management strategies in similar disaster scenarios, and emphasizing the "prolonged forced fetal posture" damage we encountered in earthquake victims who remained under the collapse for a long time.

Key Words: Accidental injuries; Compression fractures; Crush injuries; Earthquakes; Spine

©The Author(s) 2024. Published by Baishideng Publishing Group Inc. All rights reserved.

Core Tip: In the classification of damages from the earthquakes in Turkey on February 6, 2023, it was found that the injuries were predominantly crush-related rather than escape-related. Observations revealed that patients frequently sustained damage to the thoracolumbar regions due to prolonged fetal positioning under debris. It was determined that a significant portion of patients with spinal canal injuries had damage consistent with the thoracolumbar junction.

Citation: Bolukçu A, Erdemir AG, İdilman İS, Yıldız AE, Çoban Çifçi G, Onur MR, Akpınar E. Radiological findings of February 2023 twin earthquakes-related spine injuries. *World J Radiol* 2024; 16(9): 398-406

URL: <https://www.wjgnet.com/1949-8470/full/v16/i9/398.htm>

DOI: <https://dx.doi.org/10.4329/wjr.v16.i9.398>

INTRODUCTION

The catastrophic twin earthquakes measuring 7.8 and 7.7 on the Richter scale struck Kahramanmaraş, Turkey, on February 6, 2023, marked a shattering chapter in the region's history, claiming the lives of over 50000 people and leaving thousands more injured[1,2]. The aftermath of these seismic events, saw a saturation of health services, as the scale of the devastation exceeded the capacity of local medical facilities. Unlike other natural disasters, earthquakes impose a disproportionately high toll on human lives, underscoring the urgent need for effective response mechanisms in the face of such crises[3]. Among the myriad of injuries, spinal trauma is of particular concern as it affects a significant proportion of earthquake survivors. In particular, the unique circumstances surrounding these injuries, including the prevalence of crush injuries and falls, pose a particular challenge in diagnosis and treatment[4].

Following the earthquakes, the increase in crush injuries and falls precipitated a wave of spinal trauma that strained already overstretched healthcare resources[5]. Notably, earthquake survivors were found to be at heightened risk of developing crush syndrome, a potentially life-threatening condition characterized by the myonecrosis, rapid hypovolemia and excessive third-space edema[6,7]. In addition, the prevalence of vertebral fractures, often due to the high-force impacts associated with earthquakes, underscored the complex nature of spinal injuries in this context[8].

Compression fractures typically occur due to axial loading, where the vertebral body is crushed under excessive pressure, leading to a wedge-shaped deformity. Of particular concern was the emergence of a specific injury pattern known as "forced prolonged fetal posture", observed predominantly among earthquake survivors and requires specialized diagnostic approaches for accurate assessment[9]. The likely mechanism for a consecutive spine flexion injury due to forced prolonged fetal posture involves excessive and sustained forward bending of the spine, which specifically exerts abnormal compressive forces on the vertebral bodies. This stress can lead to microfractures, compression fractures, or other traumatic injuries to the vertebrae, compromising their structural integrity and resulting in significant spinal damage. Burst fractures, caused by a more severe axial load, result in the vertebral body shattering and dispersing fragments, which can impinge on the spinal canal. Translational dislocation fractures, on the other hand, involve the vertebrae being displaced horizontally, often due to high-energy trauma, leading to severe instability. Flexion-distraction fractures arise from hyperflexion, where the anterior vertebral structures are compressed while the posterior elements are distracted, causing a failure in the vertebral integrity.

The main objective of this paper is to describe the distribution and characteristics of spinal injuries in the survivors of the February 6 twin earthquakes. By analyzing multidetector row computed tomography (CT) and magnetic resonance imaging (MRI) findings from a cohort of individuals who had spinal injuries after the earthquake, we attempt to clarify the incidence and patterns of spinal trauma in this population.

MATERIALS AND METHODS

Study design

The study was conducted following the guidelines of the Declaration of Helsinki and approval for this retrospective study was obtained from the Institutional Ethics Board. Our study included patients who were referred to our hospital from the disaster area during the period from February 6 to February 28, 2023. We included all patients from the disaster area in our study, without considering any age restrictions.

CT and MRI protocol

All CT examinations were performed in the emergency radiology station, *via* Somatom Perspective 64-Slice Siemens® CT device (Erlangen/Germany). CT scan parameters were as follows: Tube voltage: 120 kV, tube current set with optimized automatic exposure control (the ref mAs value of CT was 140 mAs), collimation thickness: 0.6-2 mm, tube rotation time: 0.6-1 seconds and collimated section thickness: 2-5 mm. The iterative reconstruction (ADMIRE, strength 2) with 30 seconds soft tissue and 60 seconds bone kernel was used as a reconstruction algorithm to reduce the radiation dose.

MRI imaging was performed with a Siemens® 1.5 Tesla Aera device (Erlangen/Germany). Imaging parameters for the cervical, thoracic, lumbar and sacral regions included a slice thickness of approximately 3-5 mm, a repetition time of approximately 2000-2500 ms, an Time to Echo of approximately 20-40 ms, a matrix size of approximately 256 × 256 and a field of view of 200-350 mm, depending on the region scanned. The MRI protocol for the spine examination included axial T1-weighted, axial T2-weighted, axial fat-suppressed T2-weighted, sagittal T1-weighted, sagittal T2-weighted, and sagittal fat-suppressed T2-weighted sequences.

Data collection and statistics

All CT and MRI examinations of the spine of these patients were included in the study. The distribution of spinal fractures across the anatomical regions, including the cervical, lumbar, thoracic and sacral regions, was delineated. Fractures were categorized using the Denis, Association for Osteosynthesis (AO), and TLICS classifications[10-13]. Patients were classified according to the AO classification and grouped according to their instabilities, considering the Denis spinal column distributions. To investigate the traumatic effects of prolonged fetal position due to confinement under the debris, we also investigated the incidence of typical consecutive spinal fractures of the thoracolumbar junction, which are more vulnerable and correspond to levels T10-L2.

Statistical analysis included descriptive statistics and incidence calculations to describe the distribution of CT and MRI findings of spinal fractures and to investigate consecutive spinal fractures due to prolonged fetal position.

RESULTS

1216 examinations were carried out on 238 patients who were transferred from the disaster area to our hospital. Of these, 192 patients underwent a CT scan and 42 an MRI scan. Of the 192 CT scans, 163 examinations of the cervical, thoracic and lumbar vertebra were performed, while the remaining scans examined specific anatomical regions based on clinical symptoms.

Of the patients who underwent CT scans, 86 patients had vertebral fractures, of which 63 (73.25%) had multiple fractures and 23 (27.75%) had single fractures. Total fracture number was 287. In addition, 47 patients out of 63 (74.60%) with multiple fractures had consecutive fractures, while 16 patients (25.40%) had scattered fractures. Grouping patients according to TLICS groups of involvement revealed various types of vertebral fractures, including 40 compression fractures, 17 burst fractures, 5 flexion-distraction fractures, 5 translational dislocation fractures, and 58 fractures due to prolonged fetal posture. For examples of vertebral fractures in these patients, please see Figures 1, 2, 3, 4, and 5.

Most injuries occurred in the lumbar region. Sixty-three patients out of 86 patients (73.25%) sustained lumbar vertebra fractures. Furthermore, 140 vertebral fractures were assessed within lumbar region. Of these 63 patients, 33 patients (52.38%) had type B fractures according to the Denis classification, and 26 patients (41.26%) had type A4 fractures according to the AO classification.

Injuries to the thoracolumbar junction (T10-L2) were most common in earthquake victims. Fifty-eight patients had fractures at this level with total 93 fractures. Looking at the distribution of thoracolumbar region injuries based on their vertebral levels, ten (10.75%) fractures were at the T10 Level, sixteen (17.20%) at the T11 level, nineteen (20.43%) at the T12 level, twenty-three (24.73%) at the L1 level and twenty-five (26.88%) at the L2 level. In addition, according to the Denis classification, 27 of them had unstable 3-column fractures in the lumbar region.

Fractures affecting the thoracic vertebrae were identified in 48 out of 86 earthquake victims. Among detected 287 vertebral fractures, 131 were localized to the thoracic vertebrae. Patients with thoracic fractures had different fracture types, with A0 fractures being the most common. Of the 48 patients with thoracic vertebral fractures, 13 patients (27.08%) had thoracic A0 fractures with 44 A0 fractures (33.58%) identified among the 131 thoracic vertebral fractures. According to the Denis classification, nine patients had unstable 3-column fractures in the thoracic region.

No unstable 3-column fractures were observed in patients with cervical vertebral fractures. Ten patients with fractures in the sacral region were grouped according to the Denis zonal distribution classification, and an equal number of zone 2 and zone 3 fractures were observed.

Concomitant fractures in patients with vertebral fractures included ribs (43), upper extremities (10), lower extremities (19), scapulas (11), sternum (4), viscerocranium (6), clavicles (6), and neurocranium (2).

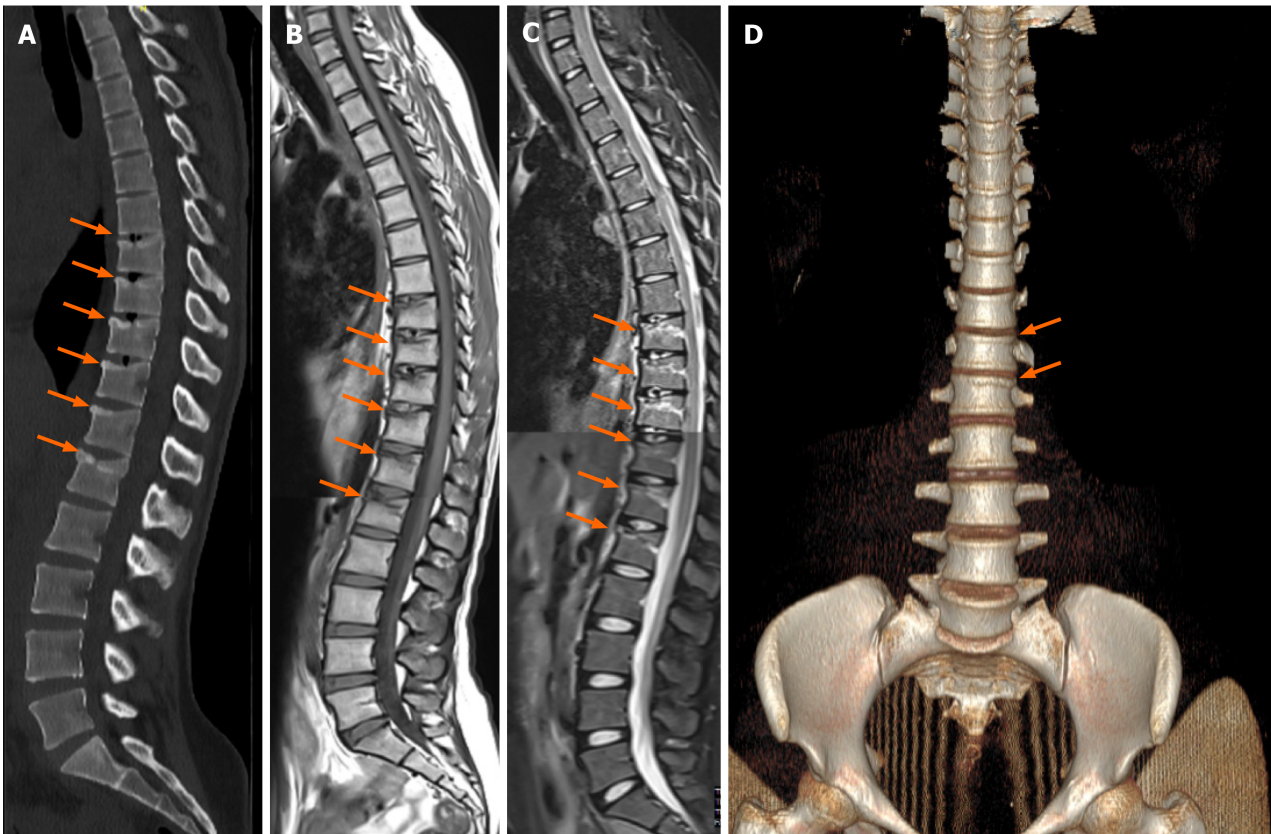


Figure 1 Prolonged fetal posture injury. A 23-year old male who jammed under debris about 15 minutes. A: Computed tomography image reveals T8 to L1 consecutive mild compression fractures (arrows), which corresponds to thoracolumbar area injury; B and C: T1W image and T2-STIR sequence show T8 to L1 vertebrae fracture and edema around them; D: The image of the volume rendering technique shows especially the fractures of the T12 and L1 vertebrae.

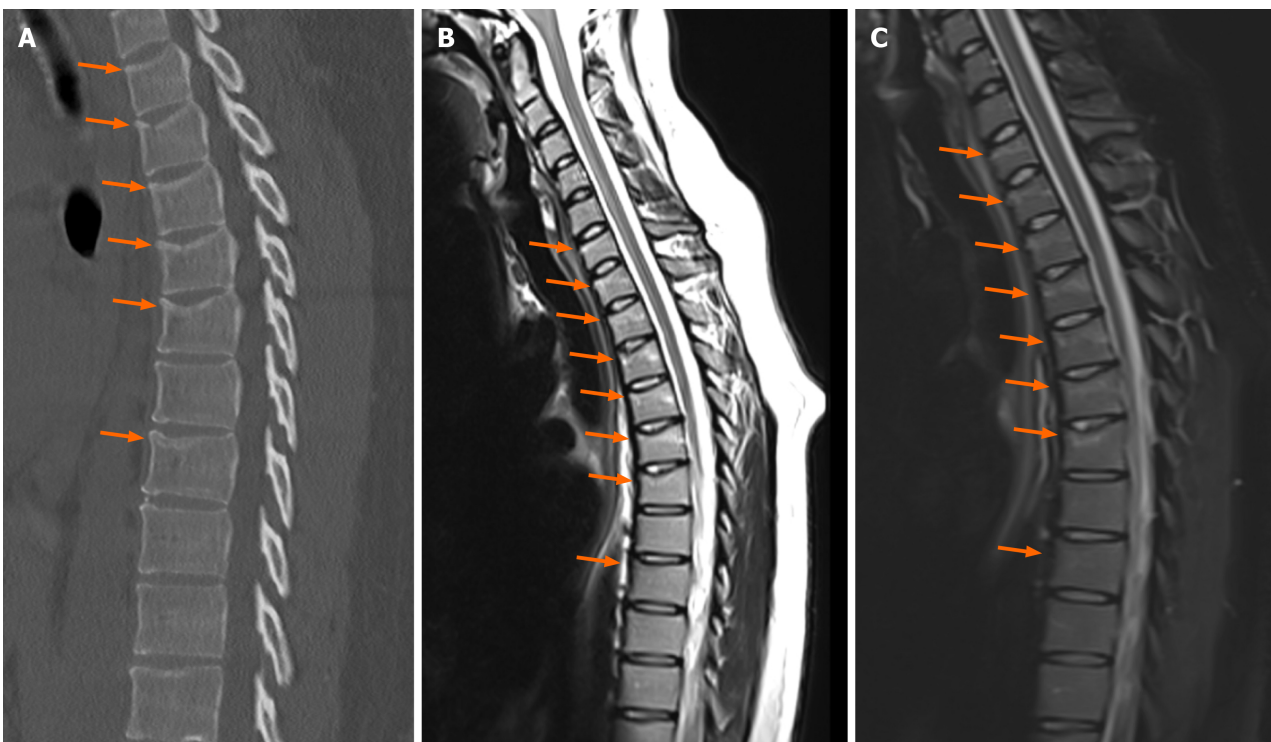


Figure 2 Compression fracture. A 27-year old male who was injured while escaping from the earthquake. A: Computed tomography image reveals T1-T5 vertebrae and T7 vertebra compression fractures (arrows); B and C: T2-STIR and T2W images show C6-T5 vertebrae and T7 vertebra compression fractures (arrows) and edema around them.

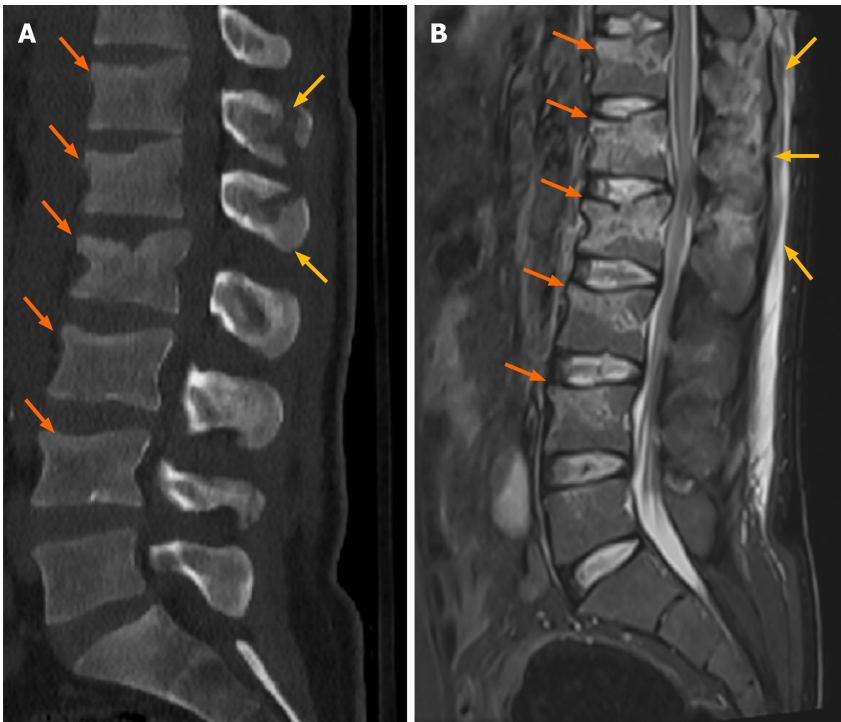


Figure 3 Flexion-distraction fracture. A 35-year old male who jammed under debris about 3 hours. A: Computed tomography image reveals the flexion-distraction type of fracture involving T12 to L4 vertebrae, especially with anteriorly losing height (orange arrows) and distraction of posterior processes (yellow arrows); B: STIR sequence shows fractures of T12 to L4 vertebrae and edema around fractures.

MRI showed retropulsion and narrowing of the spinal canal in 12 patients, and CT showed this in 19 patients. When examining the distribution of fractures causing spinal canal narrowing with retro-pulsed fragments, the most common fractures occurred at the L1 vertebra in 7 patients, followed by the T12 and L2 vertebrae in every three patients, the L4 vertebra in 2 patients, and one patient each in the L3, L5, T11, and T9 vertebrae.

Detailed information on the distribution of fracture types and the positive CT and MRI findings can be found in Tables 1, 2 and 3.

DISCUSSION

The twin earthquakes that struck southeastern Turkey on February 6, 2023, represent a major disaster. Considering the persistent presence of humanity, various types of disasters, especially earthquakes, remain inevitable. A critical aspect requiring attention among earthquake victims is the incidence of vertebral fractures, as documented in the existing literature from various earthquakes worldwide and corroborated by our observations following the twin earthquakes[5, 14]. Analysis of earthquake victims reveals that a substantial portion sustain injuries from being trapped under debris, while others experience vertebral fractures during attempts to escape the earthquake's effects. Li *et al*[15] demonstrated in their research (focused on an earthquake with a magnitude of 8.0) that crush-related injuries constitute the majority of cases; similarly, our study found that most patients were trapped under debris. Consequently, contrast material examination was limited in these patients due to the potential risk of renal damage from crush injuries. Additionally, literature indicates that spinal injuries related to non-earthquake crush injuries are less common[5]. Our demographic analysis of earthquake victims shows a predominance of female patients, mirroring findings from another study and suggesting a possible link to how individuals cope with earthquake hazards. Since crush injuries are the primary cause of trauma rather than escape-related injuries, it is likely that young male victims are better able to avoid injury[5]. This observation aids in understanding the characteristics of the earthquake victim patient group.

In our earthquake-related cohort, the risk of lumbar spinal injury due to retro-pulsed bony fragments was most prevalent, with the highest incidence of fractures occurring in the lumbar region. This finding is consistent with both our observations and results from a study on spinal cord injuries sustained during an earthquake in China (Sichuan, 2008) [16]. Furthermore, another study on earthquakes in China suggests that the extensive coverage area of the lumbar region may contribute to its increased susceptibility to crush injuries, further validating our findings. Our study makes a unique contribution to the existing literature by observing that a substantial proportion of patients exhibited fractures in multiple vertebrae, a finding that aligns with previous studies. However, unlike the study by Dong *et al*[5], which identified minor fractures across multiple widely dispersed areas, our patient cohort predominantly involved consecutive fractures.

A study examining spinal fractures during the Wenchuan earthquake (with a magnitude of 8.0) identified burst and compression fractures as the most prevalent types[15]. Similarly, in our patient group, compression fractures emerged as the most frequently observed fracture type. Additionally, as indicated in the study by Dong *et al*[5], compression fractures

Table 1 Positivity rates and age-gender distribution

Total number of patients	Positive findings (%)	Gender distribution (%)	Mean age	Standard deviation	Median
CT (192)	86 (44.79)	Female: 53 (61.62); Male: 33 (38.37)	45.25	19.56	46.00
MRI (42)	33 (78.57)	Female: 20 (60.60); Male: 13 (39.39)	52.00	19.91	55.00

MRI: Magnetic resonance imaging; CT: Computed tomography.

Table 2 The distribution of injury types

Injury type	Number of patients (86 pts w 287 vertebra fractures) (%)	Mean age	Standard deviation	Median
Compression	40 (46.51)	40.82	20.97	38.50
Burst	17 (19.76)	53.47	18.53	61.00
Translation dislocation	5 (5.81)	49.40	14.97	52.00
Flexion distraction	5 (5.81)	30.20	17.66	26.00
Isolated transverse or spinous process fracture	18 (20.93)	49.88	15.72	52.00
Prolonged fetal posture injury	58 (67.44)	45.22	19.52	48.00

Table 3 The distribution of injury types according Denis-grading system

Denis	Number of patients (86 pts w 287 vertebra fractures) (%)	Mean age	Standard deviation	Median
B	33 (38.37)	40.06	22.04	36.00
C	4 (4.65)	54.00	11.31	54.00
D	20 (23.25)	50.75	18.38	60.00
E	11 (12.79)	43.09	20.95	52.00

may result from direct vertical force or axial loading due to falling objects, indicative of crush injury mechanisms. The high number of compression fractures in our study is correlated with the predominance of patients presenting with crush injuries. Although literature on patients with triple column fractures is limited, our study observed a significant occurrence of these unstable fractures among patients. The prevalence of such fractures in earthquake-related trauma exhibits high-energy trauma characteristics. Upon assessing the likelihood of spinal cord injury in our patient group through clinical evaluation and MRI findings, positive indications were observed in a minority of cases, consistent with findings reported in the literature[16,17]. Furthermore, the absence of myelopathy despite evident spinal canal compression on MRI was correlated with the lack of clinical symptoms in these patients.

The thoracolumbar junction, corresponding to the T10-L2 vertebral levels, is one of the most frequently traumatized areas due to its mechanical vulnerability. This region serves as a transition zone between the thoracic levels, which are stabilized by the ribs and sternum, and the more mobile lumbar levels[18]. Various studies have demonstrated how different body positions affect spinal injuries, and the thoracolumbar region is particularly susceptible to injury in earthquake scenarios[5,9,19-22]. Our research supports this, revealing that the majority of earthquake victims with vertebral fractures had injuries at the thoracolumbar junction (T10-L2). Specifically, when examining patients likely to experience neurological damage due to bony fragment retropulsion into the spinal canal, we found that the majority of these cases, totaling fourteen patients, involved the thoracolumbar junction.

The literature suggests that fractures in the thoracolumbar region occur more frequently due to the kyphotic posture patients often adopt, particularly within the "life triangle," as a protective mechanism against crush injuries[9,23]. This kyphosis-related damage is more likely because earthquake victims tend to minimize their surface area and adopt a hyper-flexed fetal position instinctively to shield themselves from harm. Additionally, the human spine's center of gravity is located anterior to the thoracolumbar junction, further contributing to the tendency of patients to assume this protective fetal position.

The study has several limitations. It is retrospective in nature and confined to a single-center setting. Additionally, while all patients underwent CT imaging, the availability of MRI imaging was limited. A significant limitation of our study is the lack of comprehensive data, as we only have information on the duration patients were trapped under rubble and the time elapsed between their rescue and hospital admission, which limits our ability to investigate the impact of time on vertebral injury patterns and distribution, highlighting the need for further research in this area. Despite these

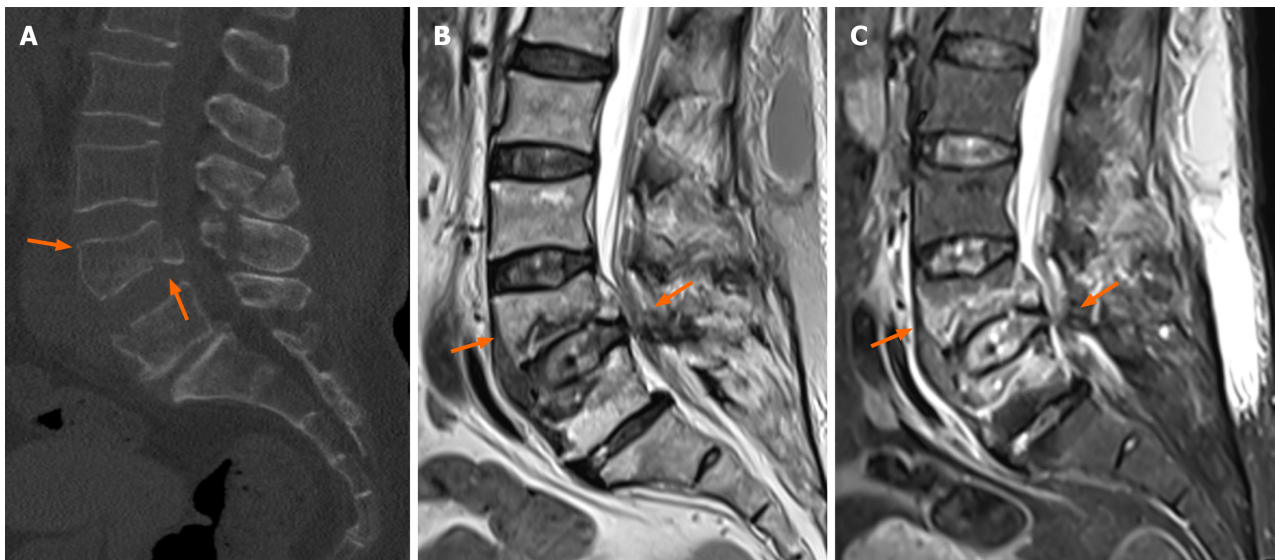


Figure 4 Burst fracture. A 63-year old female who jammed under debris about 48 hours. A: Computed tomography image reveals the burst fracture of the L4 vertebra (arrows) with the loss of height; B and C: T2W and STIR sequence show the retropulsed bone fragment and narrowing of the spinal canal (arrows).

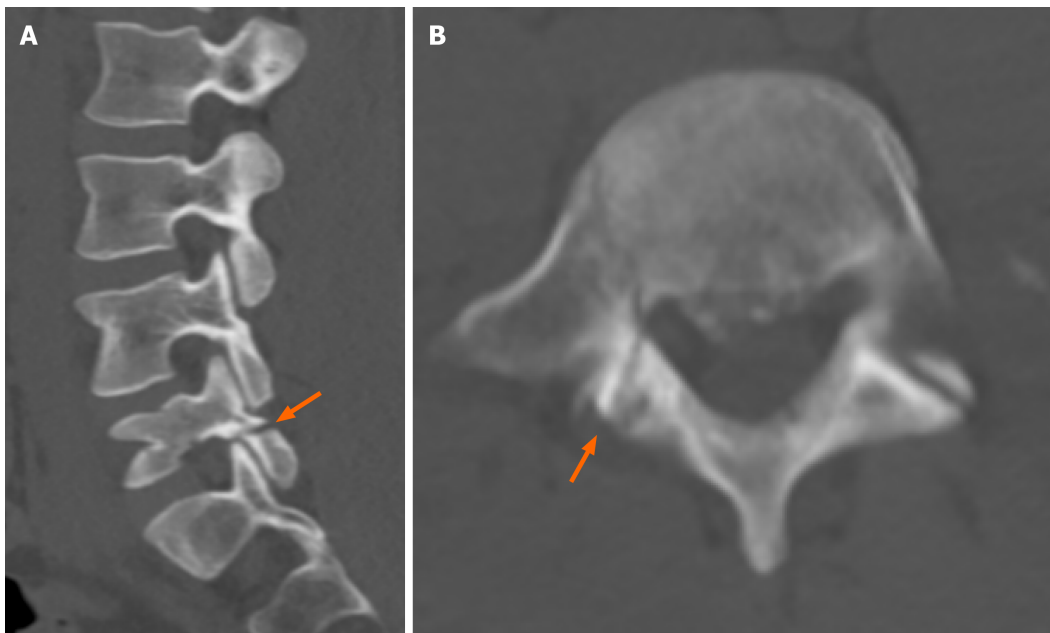


Figure 5 Translation-dislocation fracture. A 52-year old male who jammed under debris about 12 hours. A: Sagittal reformat computed tomography (CT) image reveals the translation type of L4 vertebra fracture (arrow), extending into the right facet joint. B: Axial CT image of the same patient reveals the right transverse process fracture of L4 extending into the right facet joint.

limitations, the study's strengths lie in its comprehensive analysis of vertebral fractures among earthquake victims, particularly its focus on the thoracolumbar junction and the correlation between injury patterns and trauma mechanisms.

CONCLUSION

In the classification of damages from the earthquakes in Turkey on February 6, 2023, it was found that the injuries were predominantly crush-related rather than escape-related. Observations revealed that patients frequently sustained damage to the thoracolumbar regions due to prolonged fetal positioning under debris. It was determined that a significant portion of patients with spinal canal injuries had damage consistent with the thoracolumbar junction.

FOOTNOTES

Author contributions: Bolukçu A designed research and wrote the paper; Erdemir AG performed research and wrote the paper; İdilman İS, Yildiz AE, Çifçi GC contributed figures, analytic tools and analyzed data; Onur MR conceptualized the research; Akpınar E supervised the research.

Institutional review board statement: The study was conducted following the guidelines of the Declaration of Helsinki and approval for this retrospective study was obtained from the Institutional Ethics Board (SBA 24/077).

Informed consent statement: Informed consent was not obtained due to the retrospective nature of the study.

Conflict-of-interest statement: There is no conflict of interest.

Data sharing statement: There is no data to be shared.

Open-Access: This article is an open-access article that was selected by an in-house editor and fully peer-reviewed by external reviewers. It is distributed in accordance with the Creative Commons Attribution NonCommercial (CC BY-NC 4.0) license, which permits others to distribute, remix, adapt, build upon this work non-commercially, and license their derivative works on different terms, provided the original work is properly cited and the use is non-commercial. See: <https://creativecommons.org/licenses/by-nc/4.0/>

Country of origin: Türkiye

ORCID number: Ahmet Gürkan Erdemir 0000-0001-7427-1039; İlky Sedakat İdilman 0000-0002-1913-2404; Adalet Elçin Yildiz 0000-0001-7208-8097; Gökçen Çoban Çifçi 0000-0002-0277-2042; Mehmet Ruhi Onur 0000-0003-1732-7862; Erhan Akpınar 0000-0001-8245-4804.

S-Editor: Qu XL

L-Editor: A

P-Editor: Zhao YQ

REFERENCES

- 1 Provost F, Van der Woerd J, Malet J, Maggi A, Klinger Y, Michéa D, Pointal E, Pacini F. Mapping the ruptures of the Mw7.8 and Mw7.7 Turkey-Syria Earthquakes using optical offset tracking with Sentinel-2 images. *EGU General Assembly 2023*; 2023 Apr 23–28; Vienna, Austria. EGU23-17612 [DOI: [10.5194/egusphere-egu23-17612](https://doi.org/10.5194/egusphere-egu23-17612)]
- 2 Naddaf M. One MRI for 4.7 million people: the battle to treat Syria's earthquake survivors. *Nature* 2023; **615**: 193-194 [PMID: [36849818](https://pubmed.ncbi.nlm.nih.gov/36849818/) DOI: [10.1038/d41586-023-00547-7](https://doi.org/10.1038/d41586-023-00547-7)]
- 3 Erdemir AG, Yurtutan N, Onur MR, İdilman İS, Öztürk MH, Ertürk ŞM, Çevikol C, Akpınar E. Radiological management and challenges of the twin earthquakes of February 6th. *Emerg Radiol* 2023; **30**: 659-666 [PMID: [37535144](https://pubmed.ncbi.nlm.nih.gov/37535144/) DOI: [10.1007/s10140-023-02162-5](https://doi.org/10.1007/s10140-023-02162-5)]
- 4 Wolfson N, Lerner A, Roshal L. Orthopedics in Disasters. Orthopedic Injuries in Natural Disasters and Mass Casualty Events. Heidelberg: Springer Berlin, 2016 [DOI: [10.1007/978-3-662-48950-5](https://doi.org/10.1007/978-3-662-48950-5)]
- 5 Dong ZH, Yang ZG, Chen TW, Chu ZG, Wang QL, Deng W, Denor JC. Earthquake-related versus non-earthquake-related injuries in spinal injury patients: differentiation with multidetector computed tomography. *Crit Care* 2010; **14**: R236 [PMID: [21190568](https://pubmed.ncbi.nlm.nih.gov/21190568/) DOI: [10.1186/cc9391](https://doi.org/10.1186/cc9391)]
- 6 Bywaters EG, Beall D. Crush Injuries with Impairment of Renal Function. *Br Med J* 1941; **1**: 427-432 [PMID: [20783577](https://pubmed.ncbi.nlm.nih.gov/20783577/) DOI: [10.1136/bmj.1.4185.427](https://doi.org/10.1136/bmj.1.4185.427)]
- 7 Bywaters EG. 50 years on: the crush syndrome. *BMJ* 1990; **301**: 1412-1415 [PMID: [2279155](https://pubmed.ncbi.nlm.nih.gov/2279155/) DOI: [10.1136/bmj.301.6766.1412](https://doi.org/10.1136/bmj.301.6766.1412)]
- 8 Dong ZH, Yang ZG, Chu ZG, Chen TW, Bai HL, Shao H, Tang SS, Denor JC. Earthquake-related injuries: evaluation with multidetector computed tomography and digital radiography of 1491 patients. *J Crit Care* 2012; **27**: 103.e1-103.e6 [PMID: [21514091](https://pubmed.ncbi.nlm.nih.gov/21514091/) DOI: [10.1016/j.jcrc.2011.03.007](https://doi.org/10.1016/j.jcrc.2011.03.007)]
- 9 Alpergin BC, Mete EB, Zaimoglu M, Caglar YS, Orhan O, Hasimoglu S, Eroglu U. Common Vertebral Fracture Level After the 2023 Turkey Earthquake: Thoracolumbar Junction - Due to Hyper-Flexed and Fixed Posture - at Triangle of Life Areas. *Turk Neurosurg* 2024; **34**: 485-489 [PMID: [37528724](https://pubmed.ncbi.nlm.nih.gov/37528724/) DOI: [10.5137/1019-5149.JTN.44241-23.1](https://doi.org/10.5137/1019-5149.JTN.44241-23.1)]
- 10 Reinhold M, Audigé L, Schnake KJ, Bellabarba C, Dai LY, Oner FC. AO spine injury classification system: a revision proposal for the thoracic and lumbar spine. *Eur Spine J* 2013; **22**: 2184-2201 [PMID: [23508335](https://pubmed.ncbi.nlm.nih.gov/23508335/) DOI: [10.1007/s00586-013-2738-0](https://doi.org/10.1007/s00586-013-2738-0)]
- 11 Vaccaro AR, Koerner JD, Radcliff KE, Oner FC, Reinhold M, Schnake KJ, Kandziora F, Fehlings MG, Dvorak MF, Aarabi B, Rajasekaran S, Schroeder GD, Kepler CK, Vialle LR. AOSpine subaxial cervical spine injury classification system. *Eur Spine J* 2016; **25**: 2173-2184 [PMID: [25716661](https://pubmed.ncbi.nlm.nih.gov/25716661/) DOI: [10.1007/s00586-015-3831-3](https://doi.org/10.1007/s00586-015-3831-3)]
- 12 Pneumatics SG, Karampinas PK, Triantafilopoulos G, Koufos S, Polyzois V, Vlamis J. Evaluation of TLICS for thoracolumbar fractures. *Eur Spine J* 2016; **25**: 1123-1127 [PMID: [25808483](https://pubmed.ncbi.nlm.nih.gov/25808483/) DOI: [10.1007/s00586-015-3889-y](https://doi.org/10.1007/s00586-015-3889-y)]
- 13 Weng Dennis HH, Tak HH. A Review of Thoracolumbar Spine Fracture Classifications. *JOT* 2011; **1** [DOI: [10.4303/jot/235406](https://doi.org/10.4303/jot/235406)]
- 14 Chen R, Song Y, Kong Q, Zhou C, Liu L. Analysis of 78 patients with spinal injuries in the 2008 Sichuan, China, earthquake. *Orthopedics* 2009; **32**: 322 [PMID: [19472966](https://pubmed.ncbi.nlm.nih.gov/19472966/) DOI: [10.3928/01477447-20090501-01](https://doi.org/10.3928/01477447-20090501-01)]
- 15 Li T, Zhou C, Liu L, Gong Q, Zeng J, Liu H, Kong Q, Song Y. [Analysis of spinal injuries in Wenchuan earthquake]. *Zhongguo Xiu Fu Chong Jian Wai Ke Za Zhi* 2009; **23**: 415-418 [PMID: [19431977](https://pubmed.ncbi.nlm.nih.gov/19431977/)]
- 16 Dong ZH, Yang ZG, Chen TW, Feng YC, Wang QL, Chu ZG. Spinal injuries in the Sichuan earthquake. *N Engl J Med* 2009; **361**: 636-637 [PMID: [19657135](https://pubmed.ncbi.nlm.nih.gov/19657135/) DOI: [10.1056/NEJMc0903047](https://doi.org/10.1056/NEJMc0903047)]
- 17 Ghabili K, Golzari SE, Salehpour F, Imani T, Bazzazi AM, Ghaffari A, Khanli HM, Tizro P, Taghizade S, Shakouri SK. Spinal injuries in the

- 2012 twin earthquakes, northwest iran. *PLoS Curr* 2013; **5** [PMID: 23568085 DOI: 10.1371/currents.dis.39b14d88c93fe04ef1a2ce180b24f8d1]
- 18 **Giotta Lucifero A**, Bruno N, Luzzi S. Surgical management of thoracolumbar junction fractures: An evidence-based algorithm. *World Neurosurg X* 2023; **17**: 100151 [PMID: 36793355 DOI: 10.1016/j.wnsx.2022.100151]
- 19 **Zheng Z**, Hu W, Tian T, Liu W, Wang X, Gao M, You Y, Zhang X. Dynamic Spine Hyperflexion Is Related to Vertebral Compression Fractures in Postmenopausal Women. *Orthop Surg* 2023; **15**: 111-117 [PMID: 36394084 DOI: 10.1111/os.13473]
- 20 **Li WJ**, Guo LX. Influence of different postures under vertical impact load on thoracolumbar burst fracture. *Med Biol Eng Comput* 2020; **58**: 2725-2736 [PMID: 32880092 DOI: 10.1007/s11517-020-02254-1]
- 21 **Aydin S**, Kazci O, Ece B, Kantarci M. Earthquakes from a radiological perspective: what is demanded from the radiologists, and what can we do? A pictorial review. *Diagn Interv Radiol* 2024; **30**: 30-41 [PMID: 37095695 DOI: 10.4274/dir.2023.232157]
- 22 **Erdemir AG**, İdilman İS, Çifçi GÇ, Yıldız AE, Demirkazık F, Onur MR, Akpınar E, Aydingöz Ü. Imaging in crush injury: a spectrum of findings in survivors of the twin earthquakes on February 6, 2023. *Emerg Radiol* 2023; **30**: 513-523 [PMID: 37270438 DOI: 10.1007/s10140-023-02147-4]
- 23 **Wei Y**, Tian W, Zhang GL, Lv YW, Cui GY. Thoracolumbar kyphosis is associated with compressive vertebral fracture in postmenopausal women. *Osteoporos Int* 2017; **28**: 1925-1929 [PMID: 28251286 DOI: 10.1007/s00198-017-3971-x]

Observational Study

Retinal microcirculation changes in prediabetic patients with short-term increased blood glucose using optical coherence tomography angiography

Bing-Jing Lv, Hang-Jia Zuo, Qi-Fu Li, Fan-Fan Huang, Tong Zhang, Rong-Xi Huang, Shi-Jie Zheng, Wen-Juan Wan, Ke Hu

Specialty type: Radiology, nuclear medicine and medical imaging

Provenance and peer review:

Unsolicited article; Externally peer reviewed.

Peer-review model: Single blind

Peer-review report's classification

Scientific Quality: Grade C, Grade D

Novelty: Grade B, Grade C

Creativity or Innovation: Grade B, Grade C

Scientific Significance: Grade B, Grade C

P-Reviewer: Saloň A

Received: January 30, 2024

Revised: August 3, 2024

Accepted: September 9, 2024

Published online: September 28, 2024

Processing time: 240 Days and 16.3 Hours



Bing-Jing Lv, Chongqing Medical University, Chongqing 400000, China

Bing-Jing Lv, Department of Ophthalmology, Dianjiang People's Hospital of Chongqing, Chongqing 4008300, Chongqing, China

Hang-Jia Zuo, Tong Zhang, Wen-Juan Wan, Ke Hu, The First Affiliated Hospital of Chongqing Medical University, Chongqing Medical University, Chongqing 400016, China

Qi-Fu Li, Department of Endocrinology, The First Affiliated Hospital of Chongqing Medical University, Chongqing 400016, China

Fan-Fan Huang, Shi-Jie Zheng, Department of Ophthalmology, The First Affiliated Hospital of Chongqing Medical University, Chongqing 400016, China

Rong-Xi Huang, Chongqing People's Hospital, Chongqing 400000, China

Co-first authors: Bing-Jing Lv and Hang-Jia Zuo.

Co-corresponding authors: Wen-Juan Wan and Ke Hu.

Corresponding author: Ke Hu, MD, PhD, Doctor, Professor, Researcher, The First Affiliated Hospital of Chongqing Medical University, Chongqing Medical University, No. 1 Yuanjiagang Youyi Road, Yuzhong District, Chongqing 400016, China. cqhuke@hospital.cqmu.edu.cn

Abstract**BACKGROUND**

Retinal microcirculation alterations are early indicators of diabetic microvascular complications. Optical coherence tomography angiography (OCTA) is a noninvasive method to assess these changes. This study analyzes changes in retinal microcirculation in prediabetic patients during short-term increases in blood glucose using OCTA.

AIM

To investigate the changes in retinal microcirculation in prediabetic patients experiencing short-term increases in blood glucose levels using OCTA.

METHODS

Fifty volunteers were divided into three groups: Group 1 [impaired fasting glucose (IFG) or impaired glucose tolerance (IGT)], Group 2 (both IFG and IGT), and a control group. Retinal microcirculation parameters, including vessel density (VD), perfusion density (PD), and foveal avascular zone (FAZ) metrics, were measured using OCTA. Correlations between these parameters and blood glucose levels were analyzed in both the fasting and postprandial states.

RESULTS

One hour after glucose intake, the central VD ($P = 0.023$), central PD ($P = 0.026$), and parafoveal PD ($P < 0.001$) were significantly greater in the control group than in the fasting group. In Group 1, parafoveal PD ($P < 0.001$) and FAZ circularity ($P = 0.023$) also increased one hour after glucose intake. However, no significant changes were observed in the retinal microcirculation parameters of Group 2 before or after glucose intake ($P > 0.05$). Compared with the control group, Group 1 had a larger FAZ area ($P = 0.032$) and perimeter ($P = 0.018$), whereas Group 2 had no significant differences in retinal microcirculation parameters compared with the control group ($P > 0.05$). Compared with Group 1, Group 2 had greater central VD ($P = 0.013$) and PD ($P = 0.008$) and a smaller FAZ area ($P = 0.012$) and perimeter ($P = 0.010$). One hour after glucose intake, Group 1 had a larger FAZ area ($P = 0.044$) and perimeter ($P = 0.038$) than did the control group, whereas Group 2 showed no significant differences in retinal microcirculation parameters compared with the control group ($P > 0.05$). Group 2 had greater central VD ($P = 0.042$) and PD ($P = 0.022$) and a smaller FAZ area ($P = 0.015$) and perimeter ($P = 0.016$) than Group 1. At fasting, central PD was significantly positively correlated with blood glucose levels ($P = 0.044$), whereas no significant correlations were found between blood glucose levels and OCTA parameters one hour after glucose intake.

CONCLUSION

A short-term increase in blood glucose has a more pronounced effect on retinal microcirculation in prediabetic patients with either IFG or IGT.

Key Words: Prediabetes; Blood glucose; Optical coherence tomography angiography; Retinal microcirculation; Central vessel density; Impaired fasting glucose; Impaired glucose tolerance

©The Author(s) 2024. Published by Baishideng Publishing Group Inc. All rights reserved.

Core Tip: Explore prediabetes-related retinal microcirculation changes with Optical coherence tomography angiography. Categorizing volunteers into Impaired fasting glucose (IFG), impaired glucose tolerance (IGT), and controls, our study reveals postprandial shifts in vessel density, perfusion density (PD), and foveal avascular zone (FAZ) metrics. Noteworthy findings include increased FAZ circularity in IFG/IGT, larger FAZ area/perimeter in IFG, and positive correlation of fasting PD with blood glucose. This novel analysis provides insights into the nuanced impact of short-term blood glucose elevation on retinal microcirculation in prediabetes. Clinicians and researchers, stay tuned for potential clinical implications!

Citation: Lv BJ, Zuo HJ, Li QF, Huang FF, Zhang T, Huang RX, Zheng SJ, Wan WJ, Hu K. Retinal microcirculation changes in prediabetic patients with short-term increased blood glucose using optical coherence tomography angiography. *World J Radiol* 2024; 16(9): 407-417

URL: <https://www.wjgnet.com/1949-8470/full/v16/i9/407.htm>

DOI: <https://dx.doi.org/10.4329/wjr.v16.i9.407>

INTRODUCTION

Diabetes is a common chronic metabolic disease, and its incidence continues to rise with improvements in living standards and changes in eating habits[1,2]. The disease mainly manifests clinically as typical symptoms such as polydipsia, polyuria, polydipsia, and weight loss, which have a serious impact on health[3,4]. The main complications of diabetes include diabetic retinopathy (DR), nephropathy, and neuropathy[5]. Among these, DR involves pathological changes in the retinal microcirculation and is the leading cause of blindness in most developing countries[6]. During the transition from the high-risk stage to the diagnosis of diabetes, patients experience the prediabetes stage, which is characterized by impaired fasting glucose (IFG) and impaired glucose tolerance (IGT), as determined through oral glucose tolerance tests (OGTTs). IFG is defined as a fasting blood glucose level greater than 5.6 mmol/L, with a blood glucose level of less than 7.8 mmol/L two hours after the administration of an oral glucose solution; the other is IGT, which is defined as a level of blood glucose greater than 7.8 mmol/L but less than 11.1 mmol/L two hours after the administration of an oral glucose solution[7,8]. A short-term increase in blood sugar may cause insulin resistance[9]. In patients with prediabetes, it is necessary to observe changes in the retinal microcirculation for early diagnosis, intervention and prevention of DR and other complications of diabetes.

Optical coherence tomography angiography (OCTA) has emerged as a novel, noninvasive imaging technology that visualizes the microvascular structures of the retina and choroid[10-12]. This method provides detailed images of the retinal and choroidal vasculature without the need for dye injections, making it a safer and more convenient alternative to traditional angiographic techniques[13]. In recent years, as an auxiliary examination, OCTA has been widely used in systemic diseases that cause pathological manifestations in the eyes[14,15]. It can be employed to quantify relevant indicators of the fundus, including vessel density (VD), perfusion density (PD), and the area, perimeter and circularity of the foveal avascular zone (FAZ). Studies have suggested that OCTA can diagnose a significant proportion of diabetic patients with fundus microvascular abnormalities overlooked by other ocular tests, indicating its importance in the early diagnosis of diabetes[16]. However, most research has focused on patients with type 2 diabetes, whose retinal microcirculation are affected by factors such as age, hypertension, and coronary heart disease[17,18]. Additionally, older diabetic patients may face issues such as unclear refractive media, poor examination coordination, and susceptibility to OCTA motion artifacts, which can affect measurement accuracy[19,20].

Prediabetic patients, primarily those who are young or middle-aged, generally exhibit greater examination tolerance and fewer ocular and systemic diseases, leading to more reliable OCTA results. However, the literature on retinal microcirculation changes in prediabetic patients remains limited[21-23]. This study aimed to explore the effects of short-term blood glucose increases on retinal microcirculation in the macular area of prediabetic patients, emphasizing the importance of early detection and intervention.

MATERIALS AND METHODS

Basic information

In this prospective study, 50 patients underwent OGTTs at the Laboratory of the Endocrinology Department of the First Affiliated Hospital of Chongqing Medical University. All participants were informed, and their consent was obtained. The experimental data were collected from September 1 to November 30, 2020, and patients were divided into a control group (22 patients, 22 eyes), a group with either IFG or IGT (14 patients, 14 eyes, Group 1), and a group with both IFG and IGT (13 patients, 13 eyes, Group 2). After the subjects signed the informed consent form, their basic information, including sex, age, history of systemic diseases, and best corrected visual acuity, was collected. Then, OGTTs were performed after fasting blood glucose levels were recorded. To conduct the OGTTs, we dissolved 75 g of glucose powder in 200 mL of warm water, mixed it well, and instructed the patients to take it within 5 minutes, after which their blood sugar levels were recorded 1 and 2 hours after oral intake of the glucose solution. This study was approved by the Ethics Committee of The First Affiliated Hospital of Chongqing Medical University, with approval No. 2021-648 and an approval date of December 30, 2024.

Inclusion and exclusion criteria

The inclusion criteria were as follows: (1) Aged 20-60 years; (2) Best-corrected visual acuity of 0.8 or above; (3) The refractive media of both eyes is transparent under slit lamp examination; (4) Normal intraocular pressure; and (5) No history of ocular trauma or surgery.

The exclusion criteria were as follows: (1) The subject was diagnosed with other ophthalmological diseases, such as glaucoma, high myopia (≥ -6.0 DS), uveitis, hypertensive retinopathy, *etc.*; (2) The signal strength of OCTA image scanning was less than 6 (total signal strength was 10); (3) The patient poorly cooperated, and the OCTA image had obvious artifacts; or (4) The patient had been diagnosed with diabetes, had recently used glucose-controlling drugs, or had been diagnosed with malignant tumors, autoimmune system diseases, or blood system diseases.

Image acquisition

All images were collected independently by two experienced ophthalmologists from the entire study group, and the average of their results was used as statistical data. All images were collected using the Zeiss OCTA (Cirrus HD-OCT, 5000, Germany) in angiography 3 mm × 3 mm mode. Each region was scanned three times to ensure data validity, and images with a signal strength greater than 6 were selected. The built-in Forum software automatically identified and displayed indicators of the superficial retina in the macular area. The OCTA images revealed four layers: The choroidal, choriocapillaris and retinal nerve epithelium layers and the vitreoretinal interface. We analyzed data from the avascular layer, deep retinal layer, superficial retinal layer, and color depth encoding map. This study focused on the superficial retinal layer, with the scanning area divided on the basis of ETDRS standards into concentric circles centered on the fovea (1 mm and 3 mm in diameter). The retina was segmented into a 1 mm circular area, a 1 mm to 3 mm annular area, and a 3 mm circular area. The VD and PD were calculated for each area. The quantitative parameters included the VD, PD, and the area, perimeter, and circularity index of the FAZ. VD was the ratio of vessel length to area[24], PD was the ratio of vascular coverage to area, and the FAZ circularity index ranged from 0 (no circularity) to 1 (perfect circle), indicating the impact of disease on FAZ morphology. We collected data from the same eye (left eye) for each subject, as a literature review indicated that most OCTA measurements analyze data from the same eye for consistency[25,26]. Each subject underwent measurements at two time points: Fasting and one hour after oral glucose solution intake. Each time, three measurements were taken, and the average of these measurements was used for statistical analysis.

Statistical analysis

SPSS 23.0 software was used for statistical analysis and processing. Fisher's exact test was used for the statistical analysis of categorical data. Normality and homogeneity of variance tests were used on continuous data. According to the results, a one-way analysis of variance or the Kruskal-Wallis *H* test was performed for group comparisons, and Bonferroni correction was used for pairwise comparisons. The data are expressed as the means and standard deviations. The comparison between patients before and after the OGTT was performed *via* paired *t* tests; otherwise, the paired Wilcoxon signed-rank test was used. According to the normality of the data, Pearson's or Spearman's correlation analysis between blood glucose and OCTA indicators was used. A *P* value < 0.05 indicated that the difference was statistically significant.

RESULTS

General information

The average ages of the normal control group (CN), Group 1 and Group 2 were 29.57 ± 3.92 , 30.79 ± 6.92 and 34.15 ± 8.53 years, respectively. The male-to-female ratios of these three groups were 2:21, 1:13 and 2:11, respectively (Table 1). There were no statistically significant differences in age ($P = 0.248$) or sex ($P = 0.707$) between the control group, Group 1 and Group 2.

Comparison of OCTA indices in the superficial retina between fasting conditions and after one hour of OGTT

In the control group, the central VD and PD increased one hour after the subjects consumed the glucose solution ($P = 0.023$, $P = 0.026$). One hour after the oral intake of the glucose solution in Group 1, the FAZ circularity was greater than that in the fasting condition ($P = 0.023$). In Group 2, there were no significant changes in the retinal microcirculation one hour before or after the OGTT ($P > 0.05$; Table 2). Detailed data on the vascular density, perfusion density, and FAZ under fasting conditions and after one hour of glucose intake can be found in Supplementary Table 1.

Comparison of OCTA indices in the superficial retinal layer among the three groups during fasting

The FAZ area and perimeter were greater in Group 1 than in the control group ($P = 0.032$, $P = 0.018$). There was no significant difference in the retinal microcirculation indices between the control group and Group 2 ($P > 0.05$). The central VD and PD of Group 2 were greater ($P = 0.013$, $P = 0.008$) than those of Group 1, while the FAZ area and perimeter were smaller ($P = 0.012$, $P = 0.010$; Table 3).

Comparison of OCTA indices in the superficial retinal layer among the three groups after one hour of OGTT

One hour after oral intake of the glucose solution, the FAZ area and perimeter of Group 1 were greater than those of the control group ($P = 0.044$, $P = 0.038$), whereas there was no significant difference between the retinal microcirculation indices of the control group and those of Group 2 ($P > 0.05$). The center VD and PD of Group 2 were greater ($P = 0.042$, $P = 0.022$) than those of Group 1, while the FAZ area and perimeter were lower ($P = 0.015$, $P = 0.016$; Table 4). Typical examples of VD and PD changes in a 30-year-old female from the control group, a 23-year-old female from Group 1 and a 33-year-old female from Group 2 under fasting conditions and one hour after the OGTT are shown in Figure 1.

Correlations between blood glucose levels and OCTA indices in the superficial retina

Under fasting conditions, the central PD and blood glucose of the three groups were significantly positively correlated ($r = 0.286$, $P = 0.044$), while the other OCTA indices were not significantly correlated with blood glucose (all $P > 0.05$). There was no significant correlation between the blood glucose level one hour after the OGTT and the OCTA metrics (all $P > 0.05$; Table 5).

DISCUSSION

This study aimed to investigate the changes in retinal microcirculation in prediabetic patients during short-term blood glucose elevation. Our study subjects were divided into three groups: The CN, the group with IFG or IGT (Group 1), and the group with both IFG and IGT (Group 2).

In the control group, the blood glucose level peaked one hour after the OGTT. Therefore, we examined blood glucose levels and performed OCTA examinations at this time point for all participants. One hour after the administration of the glucose solution, the central VD and PD in the macular area of the retina in the control group were significantly greater than those in the fasting group. This increase may be attributed to the relatively stable and normal function of the vascular endothelial cells in the control group. These cells can respond to short-term changes in blood glucose levels by increasing microvascular blood flow and oxygen-carrying capacity, demonstrating a stress response to glycemic variation [26,27]. When blood glucose levels rise, as observed one hour after glucose intake, these endothelial cells can respond promptly and efficiently. The increased central VD and PD in the CN are likely due to the ability of these endothelial cells to produce nitric oxide (NO) and other vasodilatory substances in response to elevated glucose levels, thereby increasing blood flow and perfusion in the retinal microcirculation. This response helps ensure adequate oxygen and nutrient delivery to retinal tissues during short-term glucose fluctuations. In Group 1, which was characterized by prediabetes with either IFG or IGT, FAZ circularity was greater one hour after the OGTT than during fasting. This could be due to the

Table 1 The average ages and male-to-female ratios of the control group, group 1, and group 2 were not significantly different ($P > 0.05$)

Group	Control (CN)	Group 1 (IFG or IGT)	Group 2 (IFG and IGT)	P value
Average age (years)	29.57 ± 3.92	30.79 ± 6.92	34.15 ± 8.53	0.248
Male to female ratio	2:21	1:13	2:11	0.707

CN: Control group; IFG: Impaired fasting glucose; IGT: Impaired glucose tolerance.

Table 2 Correlations between blood glucose levels and optical coherence tomography angiography indicators in the superficial retinal layer of the three groups

Index	Fasting		After OGTT	
	Coefficient	P value	Coefficient	P value
Central VD	0.264	0.064	-0.145	0.314
Lateral VD	0.093	0.520	0.020	0.891
Full VD	0.148	0.306	-0.038	0.793
Central PD	0.286	0.044	-0.137	0.344
Lateral PD	0.127	0.379	0.038	0.792
Full PD	0.231	0.106	-0.016	0.915
FAZ area	-0.190	0.187	0.147	0.308
FAZ perimeter	-0.216	0.131	0.162	0.261
FAZ circularity	0.049	0.734	-0.079	0.586 ¹

¹Correlations between blood glucose level and optical coherence tomography angiography metrics *via* Spearman's correlation analysis; the others were evaluated *via* Pearson's correlation analysis.

OGTT: Oral glucose tolerance test; VD: Vessel density; PD: Perfusion density; FAZ: Foveal avascular zone.

Table 3 Comparison of optical coherence tomography angiography indices in the superficial retina between fasting conditions and one hour after the oral glucose tolerance test

Index	CN (n = 23)			Group 1 (n = 14)			Group 2 (n = 13)		
	Fasting	Postprandial	P value	Fasting	Postprandial	P value	Fasting	Postprandial	P value
Central VD	9.21 ± 2.35	9.74 ± 2.61	0.023	7.58 ± 2.82	7.81 ± 2.96	0.464	10.49 ± 2.50	10.37 ± 2.15	0.733
Lateral VD	21.44 ± 1.07	21.71 ± 1.29	0.268	21.35 ± 1.16	21.75 ± 1.03	0.321	21.44 ± 1.70	21.90 ± 1.21	0.722 ¹
Full VD	20.06 ± 1.02	20.38 ± 1.28	0.186	19.79 ± 1.17	20.15 ± 1.12	0.347	20.21 ± 1.65	20.59 ± 1.14	0.807 ¹
Central PD	0.15 ± 0.04	0.16 ± 0.04	0.026	0.13 ± 0.05	0.13 ± 0.05	0.662	0.18 ± 0.04	0.18 ± 0.04	0.616
Lateral PD	0.38 ± 0.02	0.38 ± 0.02	0.270	0.38 ± 0.02	0.39 ± 0.02	0.306	0.38 ± 0.03	0.39 ± 0.02	0.649 ¹
Full PD	0.35 ± 0.02	0.36 ± 0.02	0.231	0.35 ± 0.02	0.36 ± 0.02	0.741	0.36 ± 0.03	0.36 ± 0.02	0.834 ¹
FAZ area	0.31 ± 0.11	0.32 ± 0.11	0.207	0.41 ± 0.13	0.41 ± 0.13	0.716	0.28 ± 0.09	0.29 ± 0.09	0.357
FAZ perimeter	2.35 ± 0.38	2.34 ± 0.38	0.581 ¹	2.73 ± 0.44	2.69 ± 0.45	0.232	2.26 ± 0.38	2.25 ± 0.36	0.509
FAZ circularity	0.70 ± 0.08	0.71 ± 0.07	0.602	0.69 ± 0.06	0.72 ± 0.05	0.023	0.69 ± 0.06	0.71 ± 0.08	0.162

¹Comparison between fasting conditions and one hour after the oral glucose tolerance test *via* the paired Wilcoxon signed-rank test; the other tests were paired *t* tests.

Group 1 comprised patients with either impaired fasting glucose (IFG) or impaired glucose tolerance (IGT); Group 2 comprised patients with both IFG and IGT. CN: Control group; VD: Vessel density; PD: Perfusion density; FAZ: Foveal avascular zone.

Table 4 Comparison of optical coherence tomography angiography indicators in the superficial retinal layer among the three groups during fasting

Index	CN (n = 23)	Group 1 (n = 14)	Group 2 (n = 13)	Statistics value	P value	P1	P2	P3
Central VD	9.21 ± 2.35	7.58 ± 2.82	10.49 ± 2.50	4.525	0.016 ¹	0.188	0.455	0.013
Lateral VD	21.44 ± 1.07	21.35 ± 1.16	21.44 ± 1.70	0.026	0.974 ¹			
Full VD	20.06 ± 1.02	19.79 ± 1.17	20.21 ± 1.65	2.652	0.266 ²			
Central PD	0.15 ± 0.04	0.13 ± 0.05	0.18 ± 0.04	4.999	0.011 ¹	0.280	0.218	0.008
Lateral PD	0.38 ± 0.02	0.38 ± 0.02	0.38 ± 0.03	0.775	0.679 ²			
Full PD	0.35 ± 0.02	0.35 ± 0.02	0.36 ± 0.03	2.078	0.354 ²			
FAZ area	0.31 ± 0.11	0.41 ± 0.13	0.28 ± 0.09	5.312	0.008 ¹	0.032	1.000	0.012
FAZ perimeter	2.35 ± 0.38	2.73 ± 0.44	2.26 ± 0.38	5.804	0.006 ¹	0.018	1.000	0.010
FAZ circularity	0.70 ± 0.08	0.69 ± 0.06	0.69 ± 0.06	0.257	0.775 ¹			

¹Comparisons among groups were performed *via* one-way analysis of variance.

²Comparisons among groups were performed *via* the Kruskal-Wallis H test.

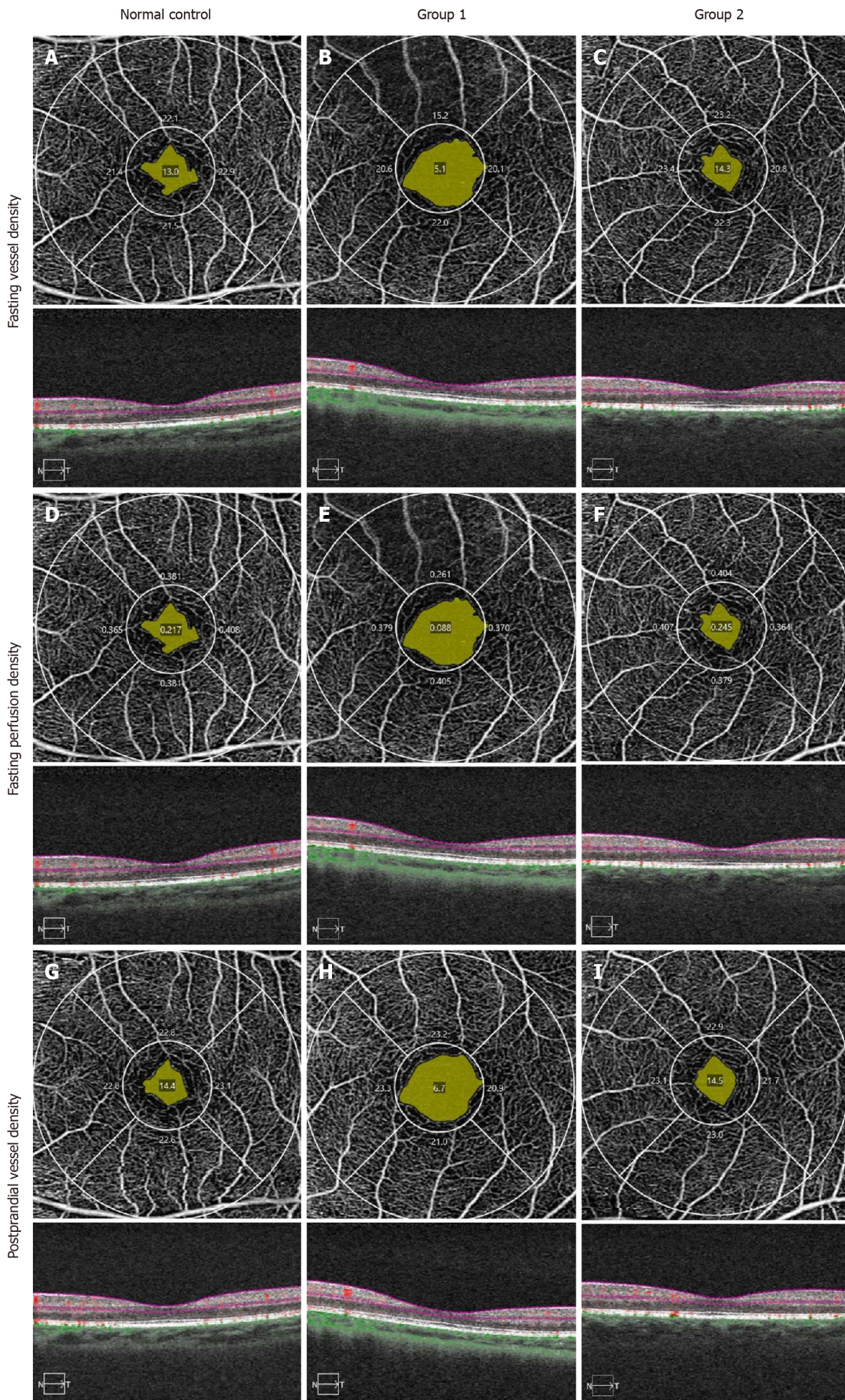
P1: Comparisons between the control group (CN) and group 1; P2: Comparisons between the CN and group 2; P3: Comparisons between group 1 and group 2. All P values were adjusted with the Bonferroni correction. Group 1 comprised patients with either impaired fasting glucose (IFG) or impaired glucose tolerance (IGT); Group 2 comprised patients with both IFG and IGT. CN: Control group; VD: Vessel density; PD: Perfusion density; FAZ: Foveal avascular zone.

Table 5 Comparison of oral glucose tolerance test indicators in the superficial retinal layer among the three groups after one hour of oral glucose tolerance test

Index	CN (n = 23)	Group 1 (n = 14)	Group 2 (n = 13)	Statistics value	P value	P1	P2	P3
Central VD	9.74 ± 2.61	7.81 ± 2.96	10.37 ± 2.15	3.706	0.032	0.101	1.000	0.042
Lateral VD	21.71 ± 1.29	21.75 ± 1.03	21.90 ± 1.21	0.106	0.899			
Full VD	20.38 ± 1.28	20.15 ± 1.12	20.59 ± 1.14	0.449	0.641			
Central PD	0.16 ± 0.04	0.13 ± 0.05	0.18 ± 0.04	4.271	0.020	0.092	1.000	0.022
Lateral PD	0.38 ± 0.02	0.39 ± 0.02	0.39 ± 0.02	0.093	0.911			
Full PD	0.36 ± 0.02	0.36 ± 0.02	0.36 ± 0.02	0.241	0.787			
FAZ area	0.32 ± 0.11	0.41 ± 0.13	0.29 ± 0.09	4.963	0.011	0.044	1.000	0.015
FAZ perimeter	2.34 ± 0.38	2.69 ± 0.45	2.25 ± 0.36	4.967	0.011	0.038	1.000	0.016
FAZ circularity	0.71 ± 0.07	0.72 ± 0.05	0.71 ± 0.08	0.115	0.891			

P1: Comparisons between the control group (CN) and Group 1; P2: Comparisons between the CN and Group 2; P3: Comparison between Group 1 and Group 2. All P values were adjusted with the Bonferroni correction. Group 1 comprised patients with either impaired fasting glucose (IFG) or impaired glucose tolerance (IGT); Group 2 comprised patients with both IFG and IGT. P: Comparisons among groups were performed *via* one-way analysis of variance. CN: Control group; VD: Vessel density; PD: Perfusion density; FAZ: Foveal avascular zone.

partial insulin resistance present in these individuals. Although insulin efficiency in promoting glucose uptake and utilization is reduced, the body compensates by secreting more insulin[28,29]. This compensatory mechanism may still allow some level of glucose regulation, enabling a stress response to short-term glucose changes, thereby maintaining a more regular FAZ shape. Conversely, in Group 2, which included individuals with both IFG and IGT, no significant changes were observed in retinal microcirculation indicators one hour after glucose intake. This lack of response may be attributed to severe and persistent insulin resistance in these patients. Specifically, insulin resistance impairs the ability of endothelial cells to produce NO and other vasodilatory substances in response to elevated glucose levels[30]. Additionally, chronic hyperglycemia can cause endothelial dysfunction through increased oxidative stress and inflammation, further compromising the ability of retinal blood vessels to adapt to short-term changes in blood glucose[31]. Consequently, the microvasculature in the retina becomes less responsive to acute fluctuations in blood glucose. This diminished capacity for vascular adaptation may lead to a consistent state of poor blood flow regulation and reduced



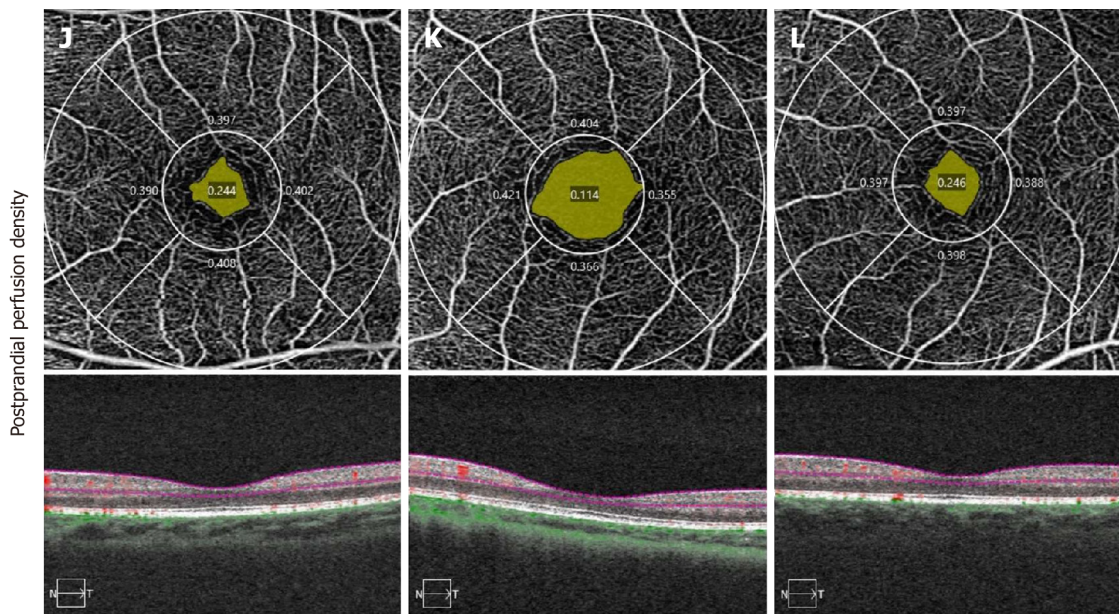


Figure 1 Comparison of central vessel density in fasting state and one hour after oral glucose solution intake across different glycemic groups. A: The central vessel density (VD) in the fasting state of the normal control group; B: The central VD in the fasting state of the impaired fasting glucose or impaired glucose tolerance group; C: The central VD in the fasting state of the group with both impaired fasting glucose and impaired glucose tolerance; D: The central perfusion density (PD) in the fasting state of the normal control group; E: The central PD in the fasting state of the impaired fasting glucose or impaired glucose tolerance group; F: The central PD in the fasting state of the group with both impaired fasting glucose and impaired glucose tolerance; G: The central VD one hour after oral glucose solution intake in the normal control group; H: The central VD one hour after oral glucose solution intake in the impaired fasting glucose or impaired glucose tolerance group; I: The central VD one hour after oral glucose solution intake in the group with both impaired fasting glucose and impaired glucose tolerance; J: The central PD one hour after oral glucose administration in the normal control group; K: The central PD one hour after oral glucose administration in the impaired fasting glucose or impaired glucose tolerance group; L: The central PD one hour after oral glucose administration in the group with both impaired fasting glucose and impaired glucose tolerance.

nutrient and oxygen delivery to retinal tissues.

Both under fasting conditions and one hour after the oral intake of the glucose solution, the FAZ area and perimeter of Group 1 were larger than those of the control group. Al-Sheikh *et al*[32] reported that during the nonproliferative DR period, the VD of the superficial blood vessels of the affected eye was lower than that of the control eye, and the FAZ area of the superficial capillary plexus in the early stage of DR was larger than that of the deep capillary plexus[32]. Moreover, macular ischemia is a typical feature of DR. In patients who have not been diagnosed with diabetes but tend to develop the disease, the FAZ area can be used as a sensitive indicator of microcirculation changes. Relevant studies have confirmed that the area of the FAZ expands as the condition of diabetic patients worsens[33,34], which is consistent with our experimental results. However, compared with those of Group 1, the central VD and PD of Group 2 were greater, and the FAZ area and perimeter were smaller. This may be due to severe insulin resistance in patients with both IFG and abnormal glucose tolerance, which entails an insignificant response to blood sugar fluctuations. Given the effect of diabetes on fundus microcirculation, increased expression of adhesion molecules such as intercellular adhesion molecule-1 and vascular cell adhesion molecule-1 in the retina occurs when blood sugar levels are elevated. These molecules play crucial roles in mediating leukocyte adhesion and infiltration, contributing to local inflammation. This inflammatory response can lead to blood-retinal barrier damage and microvascular endothelial cell injury, causing stenosis, occlusion, and atrophy or degeneration of the capillary lumen. The chronic increase in glucose levels can activate several signaling pathways, including the NF- κ B pathway, further amplifying the expression of these adhesion molecules and exacerbating retinal vascular pathology[32]. The inflammatory response under elevated blood sugar conditions causes monocytes and granulocytes to block retinal capillaries[35], which also affects the formation of capillaries. In addition, increases in blood sugar may also destroy the neurovascular self-regulatory mechanism, resulting in a decrease in retinal VD[36]. In fasting patients, the blood glucose level was significantly positively correlated with central PD, indicating that PD may be more sensitive to changes in blood glucose than the VD- and FAZ-associated metrics.

In OCTA imaging, the scan size of the image is inversely proportional to its resolution, implying that the image resolution in the scope of 3 mm \times 3 mm is the highest; thus, it was chosen as the scanning scope of this study[37]. Kim *et al*[23] reported that the superficial capillary plexus of the retina was less prone to delamination errors than the deep capillary plexus, the blood VD of the superficial capillary plexus was a sensitive vascular indicator for early DR, and the superficial retinal blood vessels were thicker than the deep ones were[24]. Considering that microvascular changes in early diabetic patients may first appear in the superficial retina[24,38], this study measured the data through OCTA of the superficial capillary plexus of the retina.

This study has the following limitations: (1) The sample size is small, which may affect the representativeness and reliability of the results. Future studies should consider increasing the sample size for more robust data and conclusions; (2) The study was only conducted in the 3 mm \times 3 mm area of the superficial retina in the macular region. While this area

is significant for visual function, this limitation may restrict the applicability of the results to larger areas and deeper retinal microcirculation; and (3) Blood glucose levels and microcirculation indices (through OCTA) were measured before and one hour after the OGTT. However, there was no long-term follow-up of the fundus condition of the patients, which may reveal chronic or cumulative changes in microcirculation rather than just immediate responses.

This study demonstrated that a short-term increase in blood glucose had a more significant effect on central retinal microcirculation in patients with either IFG or IGT. Specifically, we found that in the control group, central VD and PD increased significantly one hour after glucose intake. In Group 1, the circularity of the FAZ increased, whereas no significant changes were observed in Group 2. Additionally, under fasting conditions, the FAZ area and perimeter of Group 1 were greater than those of the control group, and Group 2 presented greater central VD and PD and a smaller FAZ area and perimeter than Group 1. These findings suggest that OCTA can be a valuable tool for monitoring retinal microcirculation changes in the macular area of prediabetic patients. This study provides insights into the early alterations in the retinal microvasculature associated with prediabetes, which could help in the early detection, intervention, and prevention of diabetes and DR. Future research should focus on larger sample sizes and long-term follow-up to validate these findings and further explore the utility of OCTA in predicting and managing the progression of diabetes and its complications.

CONCLUSION

This study demonstrated that a short-term increase in blood glucose had a more significant effect on central retinal microcirculation in patients with either IFG or IGT. Specifically, we found that in the control group, central VD and PD increased significantly one hour after glucose intake. In Group 1, the circularity of the FAZ increased, whereas no significant changes were observed in Group 2. Additionally, under fasting conditions, the FAZ area and perimeter of Group 1 were greater than those of the control group, and Group 2 presented greater central VD and PD and a smaller FAZ area and perimeter than Group 1. These findings suggest that OCTA can be a valuable tool for monitoring retinal microcirculation changes in the macular area of prediabetic patients. This study provides insights into the early alterations in the retinal microvasculature associated with prediabetes, which could help in the early detection, intervention, and prevention of diabetes and DR. Future research should focus on larger sample sizes and long-term follow-up to validate these findings and further explore the utility of OCTA in predicting and managing the progression of diabetes and its complications.

ACKNOWLEDGEMENTS

We are indebted to the help and cooperation of the First Affiliated Hospital of Chongqing Medical University, Chongqing Key Laboratory of Ophthalmology, Chongqing Eye Institute, and Endocrinology Laboratory, Chongqing Medical University, Chongqing, China.

FOOTNOTES

Author contributions: Lv BJ and Zuo HJ participated in the data curation, investigation, methodology, writing, and original draft of this article; Li QF, Huang FF, and Zhang T participated in the formal analysis and data curation; Wan WJ was involved in the formal analysis and validation; Ke H participated in the conceptualization, funding acquisition, writing, review and editing, and supervision; Lv BJ and Zuo HJ contributed equally to this work, and Hu K and Wan WJ contributed equally to this work.

Supported by The Project Foundation of Chongqing Science and Technology Commission of China, No. cstc2018jcyjAX0798.

Institutional review board statement: This study was approved by the Ethics Committee of the First Affiliated Hospital of Chongqing Medical University, with approval No. 2021-648 and an approval date of December 30, 2021.

Informed consent statement: Informed consent was obtained from all subjects involved in the study.

Conflict-of-interest statement: The authors declare that they have no known competing financial interests or personal relationships that could have appeared to influence the work reported in this paper.

Data sharing statement: No additional data are available.

STROBE statement: The authors have read the STROBE Statement – checklist of items, and the manuscript was prepared and revised according to the STROBE Statement – checklist of items.

Open-Access: This article is an open-access article that was selected by an in-house editor and fully peer-reviewed by external reviewers. It is distributed in accordance with the Creative Commons Attribution NonCommercial (CC BY-NC 4.0) license, which permits others to distribute, remix, adapt, build upon this work non-commercially, and license their derivative works on different terms, provided the original work is properly cited and the use is non-commercial. See: <https://creativecommons.org/licenses/by-nc/4.0/>

Country of origin: China

ORCID number: Hang-Jia Zuo 0009-0005-0881-6252; Ke Hu 0000-0002-8055-389X.

S-Editor: Li L

L-Editor: A

P-Editor: Yuan YY

REFERENCES

- 1 **American Diabetes Association.** 2. Classification and Diagnosis of Diabetes: Standards of Medical Care in Diabetes-2020. *Diabetes Care* 2020; **43**: S14-S31 [PMID: 31862745 DOI: 10.2337/dc20-S002]
- 2 **Saedi P,** Petersohn I, Salpea P, Malanda B, Karuranga S, Unwin N, Colagiuri S, Guariguata L, Motala AA, Ogurtsova K, Shaw JE, Bright D, Williams R; IDF Diabetes Atlas Committee. Global and regional diabetes prevalence estimates for 2019 and projections for 2030 and 2045: Results from the International Diabetes Federation Diabetes Atlas, 9(th) edition. *Diabetes Res Clin Pract* 2019; **157**: 107843 [PMID: 31518657 DOI: 10.1016/j.diabres.2019.107843]
- 3 **Xie Z,** Xiao X. Novel biomarkers and therapeutic approaches for diabetic retinopathy and nephropathy: Recent progress and future perspectives. *Front Endocrinol (Lausanne)* 2022; **13**: 1065856 [PMID: 36506068 DOI: 10.3389/fendo.2022.1065856]
- 4 **Wu Y,** Ding Y, Tanaka Y, Zhang W. Risk factors contributing to type 2 diabetes and recent advances in the treatment and prevention. *Int J Med Sci* 2014; **11**: 1185-1200 [PMID: 25249787 DOI: 10.7150/ijms.10001]
- 5 **Wolter JR.** Diabetic retinopathy. *Am J Ophthalmol* 1961; **51**: 1123-1141 [PMID: 13786453 DOI: 10.1016/0002-9394(61)91802-5]
- 6 **Resnikoff S,** Pascolini D, Etya'ale D, Kocur I, Pararajasegaram R, Pokharel GP, Mariotti SP. Global data on visual impairment in the year 2002. *Bull World Health Organ* 2004; **82**: 844-851 [PMID: 15640920]
- 7 **Nassif A,** Katoue MG, Wake DJ, George J. Management of Low Density Lipoprotein Cholesterol at a primary care diabetes clinic in Kuwait. *Prim Care Diabetes* 2019; **13**: 259-265 [PMID: 30578166 DOI: 10.1016/j.pcd.2018.11.003]
- 8 **Alberti KG,** Zimmet PZ. Definition, diagnosis and classification of diabetes mellitus and its complications. Part 1: diagnosis and classification of diabetes mellitus provisional report of a WHO consultation. *Diabet Med* 1998; **15**: 539-553 [PMID: 9686693 DOI: 10.1002/(SICI)1096-9136(199807)15:7<539::AID-DIA668>3.0.CO;2-S]
- 9 **Plummer MP,** Deane AM. Dysglycemia and Glucose Control During Sepsis. *Clin Chest Med* 2016; **37**: 309-319 [PMID: 27229647 DOI: 10.1016/j.ccm.2016.01.010]
- 10 **Spaide RF,** Klancnik JM Jr, Cooney MJ. Retinal vascular layers imaged by fluorescein angiography and optical coherence tomography angiography. *JAMA Ophthalmol* 2015; **133**: 45-50 [PMID: 25317632 DOI: 10.1001/jamaophthalmol.2014.3616]
- 11 **de Carlo TE,** Romano A, Waheed NK, Duker JS. A review of optical coherence tomography angiography (OCTA). *Int J Retina Vitreous* 2015; **1**: 5 [PMID: 27847598 DOI: 10.1186/s40942-015-0005-8]
- 12 **Coscas G,** Lupidi M, Coscas F, Chhablani J, Cagini C. Optical Coherence Tomography Angiography in Healthy Subjects and Diabetic Patients. *Ophthalmologica* 2018; **239**: 61-73 [PMID: 29268269 DOI: 10.1159/000485323]
- 13 **Tan ACS,** Tan GS, Denniston AK, Keane PA, Ang M, Milea D, Chakravarthy U, Cheung CMG. An overview of the clinical applications of optical coherence tomography angiography. *Eye (Lond)* 2018; **32**: 262-286 [PMID: 28885606 DOI: 10.1038/eye.2017.181]
- 14 **Karaca I,** Yilmaz SG, Afrashi F, Nalçacı S. Assessment of macular capillary perfusion in patients with inactive Vogt-Koyanagi-Harada disease: an optical coherence tomography angiography study. *Graefes Arch Clin Exp Ophthalmol* 2020; **258**: 1181-1190 [PMID: 32363500 DOI: 10.1007/s00417-020-04676-x]
- 15 **Yang JY,** Wang Q, Yan YN, Zhou WJ, Wang YX, Wu SL, Yuan MX, Wei WB, Jonas JB. Microvascular retinal changes in pre-clinical diabetic retinopathy as detected by optical coherence tomographic angiography. *Graefes Arch Clin Exp Ophthalmol* 2020; **258**: 513-520 [PMID: 31897704 DOI: 10.1007/s00417-019-04590-x]
- 16 **Ayhan Z,** Kaya M, Ozturk T, Karti O, Hakan Oner F. Evaluation of Macular Perfusion in Healthy Smokers by Using Optical Coherence Tomography Angiography. *Ophthalmic Surg Lasers Imaging Retina* 2017; **48**: 617-622 [PMID: 28810036 DOI: 10.3928/23258160-20170802-03]
- 17 **Lee WH,** Park JH, Won Y, Lee MW, Shin YI, Jo YJ, Kim JY. Retinal Microvascular Change in Hypertension as measured by Optical Coherence Tomography Angiography. *Sci Rep* 2019; **9**: 156 [PMID: 30655557 DOI: 10.1038/s41598-018-36474-1]
- 18 **von Jagow B,** Ohrloff C, Kohnen T. Macular thickness after uneventful cataract surgery determined by optical coherence tomography. *Graefes Arch Clin Exp Ophthalmol* 2007; **245**: 1765-1771 [PMID: 17619896 DOI: 10.1007/s00417-007-0605-6]
- 19 **Anvari P,** Ashrafkhorasani M, Habibi A, Falavarjani KG. Artifacts in Optical Coherence Tomography Angiography. *J Ophthalmic Vis Res* 2021; **16**: 271-286 [PMID: 34055264 DOI: 10.18502/jovr.v16i2.9091]
- 20 **Li Rudvan AL,** Can ME, Efe FK, Keskin M, Beyan E. Evaluation of retinal microvascular changes in patients with prediabetes. *Niger J Clin Pract* 2021; **24**: 911-918 [PMID: 34121741 DOI: 10.4103/njcp.njcp_193_20]
- 21 **Arias JD,** Arango FJ, Parra MM, Sánchez-Ávila RM, Parra-Serrano GA, Hoyos AT, Granados SJ, Viteri EJ, Gaibor-Santos I, Perez Y. Early microvascular changes in patients with prediabetes evaluated by optical coherence tomography angiography. *Ther Adv Ophthalmol* 2021; **13**: 25158414211047020 [PMID: 34708184 DOI: 10.1177/25158414211047020]
- 22 **Ratra D,** Dalan D, Prakash N, Kaviarasan K, Thanikachalam S, Das UN, Angayarkanni N. Quantitative analysis of retinal microvascular changes in prediabetic and diabetic patients. *Indian J Ophthalmol* 2021; **69**: 3226-3234 [PMID: 34708778 DOI: 10.4103/ijo.IJO_1254_21]
- 23 **Kim AY,** Chu Z, Shahidzadeh A, Wang RK, Puliafito CA, Kashani AH. Quantifying Microvascular Density and Morphology in Diabetic Retinopathy Using Spectral-Domain Optical Coherence Tomography Angiography. *Invest Ophthalmol Vis Sci* 2016; **57**: OCT362-OCT370 [PMID: 27409494 DOI: 10.1167/iovs.15-18904]
- 24 **Javed A,** Khanna A, Palmer E, Wilde C, Zaman A, Orr G, Kumudhan D, Lakshmanan A, Panos GD. Optical coherence tomography angiography: a review of the current literature. *J Int Med Res* 2023; **51**: 3000605231187933 [PMID: 37498178 DOI: 10.1177/03000605231187933]

- 25 **Félétou M**, Vanhoutte PM. Endothelial dysfunction: a multifaceted disorder (The Wiggers Award Lecture). *Am J Physiol Heart Circ Physiol* 2006; **291**: H985-1002 [PMID: 16632549 DOI: 10.1152/ajpheart.00292.2006]
- 26 **Joussen AM**, Poulaki V, Le ML, Koizumi K, Esser C, Janicki H, Schraermeyer U, Kociok N, Fauser S, Kirchhof B, Kern TS, Adamis AP. A central role for inflammation in the pathogenesis of diabetic retinopathy. *FASEB J* 2004; **18**: 1450-1452 [PMID: 15231732 DOI: 10.1096/fj.03-1476fje]
- 27 **Catrina SB**, Zheng X. Disturbed hypoxic responses as a pathogenic mechanism of diabetic foot ulcers. *Diabetes Metab Res Rev* 2016; **32** Suppl 1: 179-185 [PMID: 26453314 DOI: 10.1002/dmrr.2742]
- 28 **Fujii H**, Kawada N; Japan Study Group Of Nafld Jsg-Nafld. The Role of Insulin Resistance and Diabetes in Nonalcoholic Fatty Liver Disease. *Int J Mol Sci* 2020; **21** [PMID: 32485838 DOI: 10.3390/ijms21113863]
- 29 **Kahn SE**, Prigeon RL, McCulloch DK, Boyko EJ, Bergman RN, Schwartz MW, Neifing JL, Ward WK, Beard JC, Palmer JP. Quantification of the relationship between insulin sensitivity and beta-cell function in human subjects. Evidence for a hyperbolic function. *Diabetes* 1993; **42**: 1663-1672 [PMID: 8405710 DOI: 10.2337/diab.42.11.1663]
- 30 **Sena CM**, Pereira AM, Seica R. Endothelial dysfunction - a major mediator of diabetic vascular disease. *Biochim Biophys Acta* 2013; **1832**: 2216-2231 [PMID: 23994612 DOI: 10.1016/j.bbdis.2013.08.006]
- 31 **Ting DS**, Cheung GC, Wong TY. Diabetic retinopathy: global prevalence, major risk factors, screening practices and public health challenges: a review. *Clin Exp Ophthalmol* 2016; **44**: 260-277 [PMID: 26716602 DOI: 10.1111/ceo.12696]
- 32 **Al-Sheikh M**, Akil H, Pfaum M, Sadda SR. Swept-Source OCT Angiography Imaging of the Foveal Avascular Zone and Macular Capillary Network Density in Diabetic Retinopathy. *Invest Ophthalmol Vis Sci* 2016; **57**: 3907-3913 [PMID: 27472076 DOI: 10.1167/iovs.16-19570]
- 33 **Simonett JM**, Scarinci F, Picconi F, Giorno P, De Geronimo D, Di Renzo A, Varano M, Frontoni S, Parravano M. Early microvascular retinal changes in optical coherence tomography angiography in patients with type 1 diabetes mellitus. *Acta Ophthalmol* 2017; **95**: e751-e755 [PMID: 28211261 DOI: 10.1111/aos.13404]
- 34 **de Carlo TE**, Chin AT, Bonini Filho MA, Adhi M, Branchini L, Salz DA, Bauman CR, Crawford C, Reichel E, Witkin AJ, Duker JS, Waheed NK. Detection of microvascular changes in eyes of patients with diabetes but not clinical diabetic retinopathy using optical coherence tomography angiography. *Retina* 2015; **35**: 2364-2370 [PMID: 26469537 DOI: 10.1097/IAE.0000000000000882]
- 35 **Schröder S**, Palinski W, Schmid-Schönbein GW. Activated monocytes and granulocytes, capillary nonperfusion, and neovascularization in diabetic retinopathy. *Am J Pathol* 1991; **139**: 81-100 [PMID: 1713023]
- 36 **Abcouwer SF**, Gardner TW. Diabetic retinopathy: loss of neuroretinal adaptation to the diabetic metabolic environment. *Ann N Y Acad Sci* 2014; **1311**: 174-190 [PMID: 24673341 DOI: 10.1111/nyas.12412]
- 37 **Borrelli E**, Sacconi R, Brambati M, Bandello F, Querques G. In vivo rotational three-dimensional OCTA analysis of microaneurysms in the human diabetic retina. *Sci Rep* 2019; **9**: 16789 [PMID: 31728070 DOI: 10.1038/s41598-019-53357-1]
- 38 **Toprak I**, Fenkci SM, Fidan Yaylali G, Martin C, Yaylali V. Early retinal neurodegeneration in preclinical diabetic retinopathy: a multifactorial investigation. *Eye (Lond)* 2020; **34**: 1100-1107 [PMID: 31654034 DOI: 10.1038/s41433-019-0646-1]

Observational Study

Nomogram for predicting short-term response to anti-vascular endothelial growth factor treatment in neovascular age-related macular degeneration: An observational study

Zhen-Huan Huang, Xue-Zhao Tu, Qi Lin, Mei Tu, Guo-Cai Lin, Kai-Ping Zhang

Specialty type: Radiology, nuclear medicine and medical imaging**Provenance and peer review:** Unsolicited article; Externally peer reviewed.**Peer-review model:** Single blind**Peer-review report's classification****Scientific Quality:** Grade A**Novelty:** Grade A**Creativity or Innovation:** Grade A**Scientific Significance:** Grade A**P-Reviewer:** Glumac S**Received:** May 7, 2024**Revised:** August 12, 2024**Accepted:** August 14, 2024**Published online:** September 28, 2024**Processing time:** 142 Days and 12.5 Hours**Zhen-Huan Huang, Qi Lin,** Department of Radiology, Longyan First Affiliated Hospital of Fujian Medical University, Longyan 364000, Fujian Province, China**Xue-Zhao Tu,** Department of Orthopedics, Longyan First Affiliated Hospital of Fujian Medical University, Longyan 364000, Fujian Province, China**Mei Tu,** Department of Endocrinology, Longyan First Affiliated Hospital of Fujian Medical University, Longyan 364000, Fujian Province, China**Guo-Cai Lin, Kai-Ping Zhang,** Department of Ophthalmology, Longyan First Affiliated Hospital of Fujian Medical University, Longyan 364000, Fujian Province, China**Corresponding author:** Zhen-Huan Huang, MD, Associate Chief Physician, Department of Radiology, Longyan First Affiliated Hospital of Fujian Medical University, No. 105 North 91 Road, Xinluo District, Longyan 364000, Fujian Province, China. tuxuezhao@163.com

Abstract

BACKGROUND

Anti-vascular endothelial growth factor (anti-VEGF) therapy is critical for managing neovascular age-related macular degeneration (nAMD), but understanding factors influencing treatment efficacy is essential for optimizing patient outcomes.

AIM

To identify the risk factors affecting anti-VEGF treatment efficacy in nAMD and develop a predictive model for short-term response.

METHODS

In this study, 65 eyes of exudative AMD patients after anti-VEGF treatment for ≥ 1 mo were observed using optical coherence tomography angiography. Patients were classified into non-responders ($n = 22$) and responders ($n = 43$). Logistic regression was used to determine independent risk factors for treatment response. A predictive model was created using the Akaike Information Criterion, and its performance was assessed with the area under the receiver operating characteristic curve, calibration curves, and decision curve analysis (DCA) with 500 bootstrap re-samples.

RESULTS

Multivariable logistic regression analysis identified the number of junction voxels [odds ratio = 0.997, 95% confidence interval (CI): 0.993-0.999, $P = 0.010$] as an independent predictor of positive anti-VEGF treatment outcomes. The predictive model incorporating the fractal dimension, number of junction voxels, and longest shortest path, achieved an area under the curve of 0.753 (95%CI: 0.622-0.873). Calibration curves confirmed a high agreement between predicted and actual outcomes, and DCA validated the model's clinical utility.

CONCLUSION

The predictive model effectively forecasts 1-mo therapeutic outcomes for nAMD patients undergoing anti-VEGF therapy, enhancing personalized treatment planning.

Key Words: Vascular endothelial growth factor; Macular degeneration; Neovascularization; Age-related macular degeneration; Choroidal neovascularization; Optical coherence tomography angiography; Nomogram

©The Author(s) 2024. Published by Baishideng Publishing Group Inc. All rights reserved.

Core Tip: This study developed a predictive model using optical coherence tomography angiography to identify factors affecting the effectiveness of anti-vascular endothelial growth factor treatment in neovascular age-related macular degeneration (nAMD). The number of junction voxels emerged as an independent predictor of positive treatment outcomes. Integrating several parameters, the predictive model demonstrated strong performance in forecasting 1-mo therapeutic outcomes, providing a valuable tool for personalized treatment planning in nAMD patients.

Citation: Huang ZH, Tu XZ, Lin Q, Tu M, Lin GC, Zhang KP. Nomogram for predicting short-term response to anti-vascular endothelial growth factor treatment in neovascular age-related macular degeneration: An observational study. *World J Radiol* 2024; 16(9): 418-428

URL: <https://www.wjgnet.com/1949-8470/full/v16/i9/418.htm>

DOI: <https://dx.doi.org/10.4329/wjr.v16.i9.418>

INTRODUCTION

The global rise in the incidence of age-related macular degeneration (AMD)[1,2] is emerging as the primary cause of irreversible vision loss in individuals aged 50 and above. Neovascular AMD (nAMD) is a particularly severe form that can result in blindness if not adequately treated[3,4]. The intravitreal administration of anti-vascular endothelial growth factor (anti-VEGF) agents is emerging as the primary therapeutic approach[5], substantially improving the condition of eyes with nAMD. The response to this therapy is suboptimal in many patients, as they often experience persistent intraretinal, subretinal, or subretinal pigment epithelial fluid and ongoing or new hemorrhages, along with progressive lesion fibrosis[6].

To customize treatment plans, clinicians often prioritize reducing exudative symptoms such as intraretinal cystoid fluid, subretinal fluid, and fluid or hemorrhage beneath the retinal pigment epithelium (RPE) layer[7]. These approaches often vary significantly among patients due to differences in baseline clinical characteristics and choroidal neovascularization (CNV) lesions[8]. Optical coherence tomography angiography (OCTA) provides a non-invasive, high-resolution imaging technique that offers both qualitative and quantitative assessment of CNV[9]. While OCTA-measured CNV parameters, such as the growth of macular neovascularization (MNV)[10], vessel junction density[11], the change in most excellent vascular caliber[12], and vessel density[1], have demonstrated effectiveness in monitoring changes in CNV due to anti-VEGF therapy, the ability of these parameters to predict treatment outcomes remains a topic of ongoing debate.

Considering the complexities and diverse responses to anti-VEGF therapy among individuals, the primary objective of this study was to identify potential biomarkers that can predict treatment response in nAMD patients following anti-VEGF therapy based on baseline clinical characteristics and OCTA-measured parameters. Subsequently, we constructed a predictive model through logistic regression analysis and filtered variables based on the Akaike Information Criterion (AIC) to develop individualized, precision-based treatment plans, thereby maximizing the efficacy of nAMD interventions and potentially improving the quality of life for affected individuals.

MATERIALS AND METHODS

Participants

The study received approval from the Medical Ethics Committee of our hospital and followed the principles outlined in the Declaration of Helsinki. Written consent was not required due to the retrospective nature of the study. Eighty-three patients with unilateral nAMD who had not undergone any prior treatment were included in this study. They were

followed up for at least 1 mo using OCTA from January 2020 to September 2023. However, 18 patients were excluded based on the following exclusion criteria: (1) nAMD with prior anti-VEGF injection treatment or intraocular surgery other than cataract surgery ($n = 9$); (2) Lack of clinical history ($n = 1$); (3) Absence of follow-up using OCTA for at least 1 mo ($n = 1$); (4) Poor-quality images obtained by OCTA ($n = 2$); and (5) Macular neovascularization caused by high myopia (≥ -6.00 diopters), glaucoma, diabetic retinopathy, uveitis, or endophthalmitis ($n = 5$). Consequently, the study comprised 65 eyes from 65 eligible patients (20 females and 45 males; median age: 68 years; age range: 51-87 years) experiencing unilateral nAMD. A flow chart of the enrollment process is shown in [Figure 1](#).

Grouping of response to antiVEGF therapies

Three initial loading doses of intravitreal anti-VEGF injections were administered for treatment-naïve eyes with exudative AMD, followed by achieving the first remission, defined as a dry macula on optical coherence tomography. Once remission was achieved, a *pro re nata* or treat-and-extend regimen was implemented for recurrent exudation.

Patients were classified into response and non-response groups according to their OCTA follow-up outcomes after a month-long loading phase of anti-VEGF therapy. Specifically, the response group comprised 43 individuals, while the non-response group included 22. According to the criteria established by Amoaku *et al*[8], patients in the response group demonstrated an improvement in visual acuity of ≥ 5 ETDRS letters, a reduction in central retinal thickness of $> 25\%$, or a decrease in subretinal or intraretinal fluid and cysts. In the non-response group, patients failed to meet these criteria. In case of classification disagreements between two evaluators, a third evaluator was consulted to reach a consensus.

Collection of clinical data and analysis of OCTA imaging features

The hospital's electronic medical record management system was utilized to systematically collect comprehensive clinical data of patients, including information on age, gender, hypertension, diabetes mellitus, alcohol consumption, and smoking habits. CNV lesions were captured using a high-quality 3 mm \times 3 mm OCTA scanning device (Heidelberg Engineering, Heidelberg Germany) at baseline and during each subsequent visit. The OCTA device's built-in software automatically segmented the en-face images of the CNV complex based on two horizontal lines extending from the inner plexiform layer/inner nuclear layer to enhance visualization.

The morphology of the CNV complex was classified as ([Figure 2](#)): (1) "Medusa" or "sea fan," which is characterized by central feeder vessels with main vascular trunks and numerous tiny capillaries radiating from the center; (2) "Long linear vessels," which lack prominent capillary ramifications; and (3) "Indistinct network," which is defined by the visualization of only main vascular trunks and thin branches without detectable feeder vessels. Quantitative features of the CNV, including area, fractal dimension, branch number, junction number, the number of end-point voxels, the number of junction voxels, the number of slab voxels, average branch length, maximum branch length, and longest shortest path, were assessed using ImageJ software on the segmented OCTA images. Two masked retina specialists independently evaluated both qualitative and quantitative parameters. In cases of interpretive disagreement, a consensus was reached through open adjudication involving others.

Predictive model construction

Using univariate and multivariate logistic regression analyses, clinical data and OCTA imaging characteristics were collected to identify independent risk factors associated with the response of patients diagnosed with nAMD following anti-VEGF therapy. Odds ratios (OR) and 95% confidence intervals (CI) were employed as effect measures. Variables demonstrating a P value < 0.2 in the univariate logistic regression analysis were included in subsequent multivariate logistic regression analysis, which was further refined based on AIC for selection. AIC measures goodness-of-fit for statistical models, selecting the model that best interprets data while containing minimal free parameters among n models. For predictive model construction, the multivariate logistic regression analysis included variables selected through AIC refinement, with all identified variables entered into the regression equation.

The discrimination efficacy of the predictive model was assessed by calculating the area under the receiver operating characteristic (ROC) curve (AUC) using 500 bootstrap re-samples. The DeLong test was used to compare AUC values among different models. In addition, integrated discrimination improvement (IDI) was used to measure how much better average sensitivity was compared to other models while maintaining average specificity. The agreement between predicted outcomes from predictive models and actual responses was evaluated using calibration plots with 500 bootstrap re-samples and the Hosmer-Lemeshow test's application. Decision curve analysis (DCA) with 500 bootstrap re-samples was conducted to examine this predictive model's clinical utility and effectiveness.

Statistical analysis

The statistical analyses were conducted utilizing IBM SPSS Statistics 22 software and R software (version 4.2.0). A two-tailed P value < 0.05 was considered statistically significant. Continuous variables are described as the mean \pm SD or median with interquartile range, and group comparisons were made using the Student's t -test or Wilcoxon test. Categorical variables are presented as counts and percentages, with group comparisons performed using the χ^2 test or Fisher's exact test. The sample size estimation was based on the multivariate regression analysis requirements, where the recommended sample size is 15 to 20 times the number of variables. The sample size was increased by 10% to account for potential data loss.

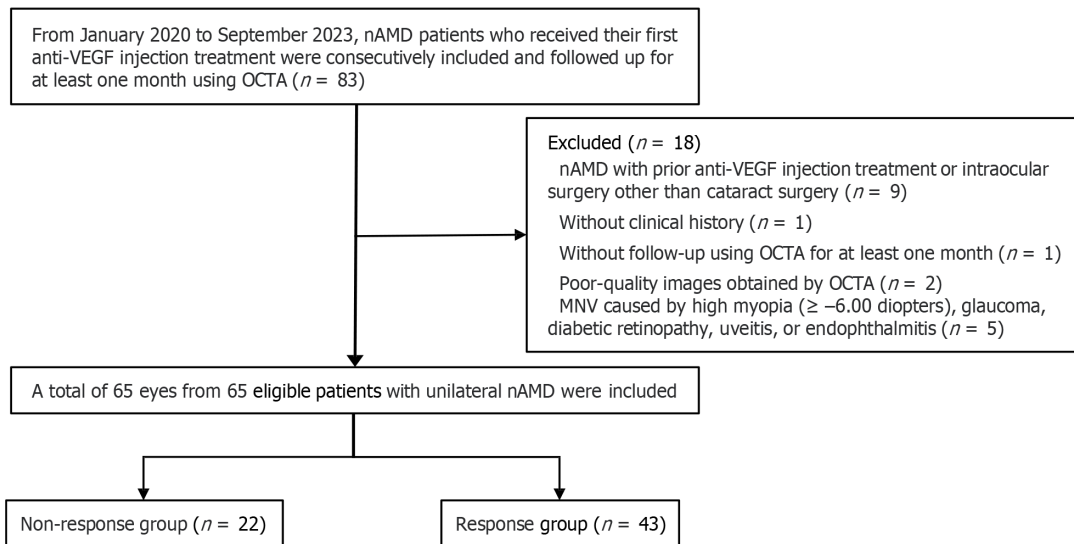


Figure 1 Flowchart of study cohort selection. nAMD: Neovascular age-related macular degeneration; anti-VEGF: Anti-vascular endothelial growth factor; OCTA: Optical coherence tomography angiography.

RESULTS

Clinical and OCTA characteristics of the study cohort

The age and gender distributions did not differ significantly between the non-response and response groups ($P = 0.792$ and 0.878 , respectively). Personal and medical histories, including smoking habits, alcohol consumption, hypertension, and diabetes mellitus, also showed no statistically significant disparities ($P = 0.378$ - 1.000). No significant variations were observed in the morphology of the CNV complex between the non-response and response groups ($P = 1.000$). The baseline quantitative features of the CNV demonstrated no substantial discrepancies between the non-response and response groups ($P = 0.050$ - 0.368).

Risk factors related to response to antiVEGF therapies

Univariate and multivariate logistic analyses were conducted to identify independent risk factors associated with the response to anti-VEGF agents, as presented in [Table 1](#). Variables with a P value < 0.2 in the univariate logistic regression analysis, including fractal dimension, branch number, junction number, and the number of junction voxels, were further screened using multivariate logistic regression analysis, which demonstrated a significant correlation between the response to anti-VEGF therapies and the number of junction voxels (OR = 0.997, 95% CI: 0.993-0.999, $P = 0.010$).

Performance of the predictive model

The predictive model, depicted by a nomogram in [Figure 3](#), used AIC to screen variables and ultimately included fractal dimension, the number of junction voxels, and the longest shortest path ([Figure 4](#)). Mathematically represented as $Y = 31.901 - 16.294 \times \text{fractal dimension} - 0.002 \times \text{the number of junction voxels} + 0.003 \times \text{the longest shortest path}$, this model enables precise evaluation of treatment on the risks and probabilities of adverse response. The discriminatory capacity of the predictive model was evaluated using a ROC curve. The pooled AUC (95% CI) of 0.753 (0.622-0.873) demonstrates a moderately good performance for the predictive model ([Figure 5A and B](#)). The predictive model showed an accuracy of 0.723 (95% CI: 0.717-0.729), a sensitivity of 0.744 (95% CI = 0.614-0.875), and a specificity of 0.682 (95% CI = 0.487-0.876) at a threshold value of 0.709. [Figure 5C](#) shows that the AUC values of the variables screened using AIC were not statistically different from the AUC of the nomogram ($P = 0.078$ for fractal dimension *vs* nomogram, $P = 0.181$ for the number of junction voxels *vs* nomogram, and $P = 0.083$ for the longest shortest path *vs* nomogram).

The inclusion of fractal dimension [IDI (95% CI) = 0.613 (0.059-0.267), $P = 0.002$], the number of junction voxels [IDI (95% CI) = 0.136 (0.049-0.223), $P = 0.002$], and the longest shortest path [IDI (95% CI) = 0.204 (0.089-0.319), $P = 0.001$] significantly enhanced the predictive value of the model compared to variables selected using AIC. The calibration curves of the nomogram ([Figure 5D](#)), based on 500 bootstrap re-samples, demonstrated a significant correlation between the predicted probability by the model and the reference line (Hosmer-Lemeshow test: $\chi^2 = 7.320$ $P = 0.604$), indicating robust alignment. [Figure 5E](#) shows the calibration curves of different models for predicting anti-VEGF therapy response. The application of DCA has demonstrated the potential to enhance net benefits and exhibit a diverse range of threshold probabilities ([Figure 5F and G](#)).

Table 1 Univariate and multivariate analyses of clinical and optical coherence tomography angiography characteristics associated with response to anti-vascular endothelial growth factor therapy

Characteristic	Univariate		Multivariate	
	OR (95%CI)	P value	OR (95%CI)	P value
Age (years)	0.997 (0.947-1.049)	0.901		
Gender (male)	0.777 (0.237-2.356)	0.663		
Hypertension	1.920 (0.649-6.229)	0.252		
Diabetes mellitus	0.650 (0.13-3.571)	0.596		
Smoking habits (active and former smoker)	0.602 (0.198-1.852)	0.368		
Alcohol consumption (active and former drinker)	0.917 (0.292-3.072)	0.883		
Morphological feature (long linear vessels)	1.029 (0.190-5.409)	0.973		
Morphological feature (indistinct network)	1.187 (0.271-4.694)	0.810		
Area (mm ²)	0.448 (0.053-3.733)	0.444		
Fractal dimension	0.000 (0.000-6.103)	0.093	0.000 (0.000-486.4)	0.195
Branch number	0.999 (0.998-1.000)	0.171	1.004 (0.995-1.014)	0.362
Junction number	0.997 (0.991-1.001)	0.179	1.013 (0.977-1.056)	0.489
Number of end-point voxels	1.000 (0.999-1.001)	0.517		
Number of junction voxels	0.999 (0.999-1.000)	0.047	0.997 (0.993-0.999)	0.010
Number of slab voxels	1.000 (0.999-1.000)	0.214		
Average branch length (mm)	1.000 (0.998-1.001)	0.601		
Maximum branch length (mm)	1.000 (0.999-1.001)	0.575		
Longest shortest path (mm)	1.000 (0.999-1.000)	0.555		

OR: Odds ratio; CI: Confidence interval.

DISCUSSION

This study identified the number of junction voxels as a critical predictor of positive treatment outcomes in patients with nAMD undergoing anti-VEGF therapy. The developed predictive model, incorporating the fractal dimension, number of junction voxels, and longest shortest path, demonstrated high accuracy in forecasting 1-mo therapeutic responses. This model offers a valuable tool for personalized treatment planning in nAMD patients.

There is significant inter-individual variability in terms of disease progression and response to anti-VEGF therapy among patients with nAMD. Consequently, the challenge lies in tailoring precise, individualized treatment for each patient. Even though qualitative analysis of morphological CNV findings using OCTA can offer direct insights into the disease stage and activity status of CNV and hold clinical significance for treatment and prognosis[13-16], its application in clinical practice is subject to significant limitations. Indeed, our study revealed no significant correlation between the morphology of CNV on OCTA and the response to anti-VEGF treatment. Therefore, this study aimed to assess the vascular architecture of CNV using quantitative OCTA parameters at baseline to identify potential predictors of treatment response. Subsequently, this study aimed to construct a predictive model that provides insights into the risks and probabilities of adverse responses 1 mo after treatment.

The present study aimed to develop and evaluate a nomogram that integrates fractal dimension, the number of junction voxels, and the longest shortest path for predicting response to anti-VEGF therapy. Our comprehensive evaluation, encompassing ROC analysis, calibration curve assessment, and DCA, demonstrated satisfactory predictive accuracy and discriminative ability.

The fractal dimension represents a geometric index that delineates the complexity of vascular anatomy (normal range: 0-2; a higher fractal dimension value indicates a more complex vascular network structure). Al-Sheikh *et al*[13] postulated that active CNV had a higher fractal dimension. Similar results were reported by Faatz *et al*[17], suggesting that the fractal dimension serves as a valuable parameter for assessing the activity of CNV, with a higher fractal dimension being positively associated with increased CNV activity. Furthermore, they concluded that the baseline fractal dimension of CNV can serve as a predictive factor for the response to anti-VEGF therapy. However, Coscas *et al*[16] showed conflicting results, suggesting that active CNV had a lower fractal dimension. A study conducted by Serra *et al*[18] also showcased that the fractal dimension could be helpful in objectively assessing the activity status of CNV and highlighted that a significantly lower fractal dimension characterized active CNV. As previously hypothesized by Carnevali *et al*[19], the fractal dimension was associated with the absence of core vessels, which likely indicates a more complex vascular

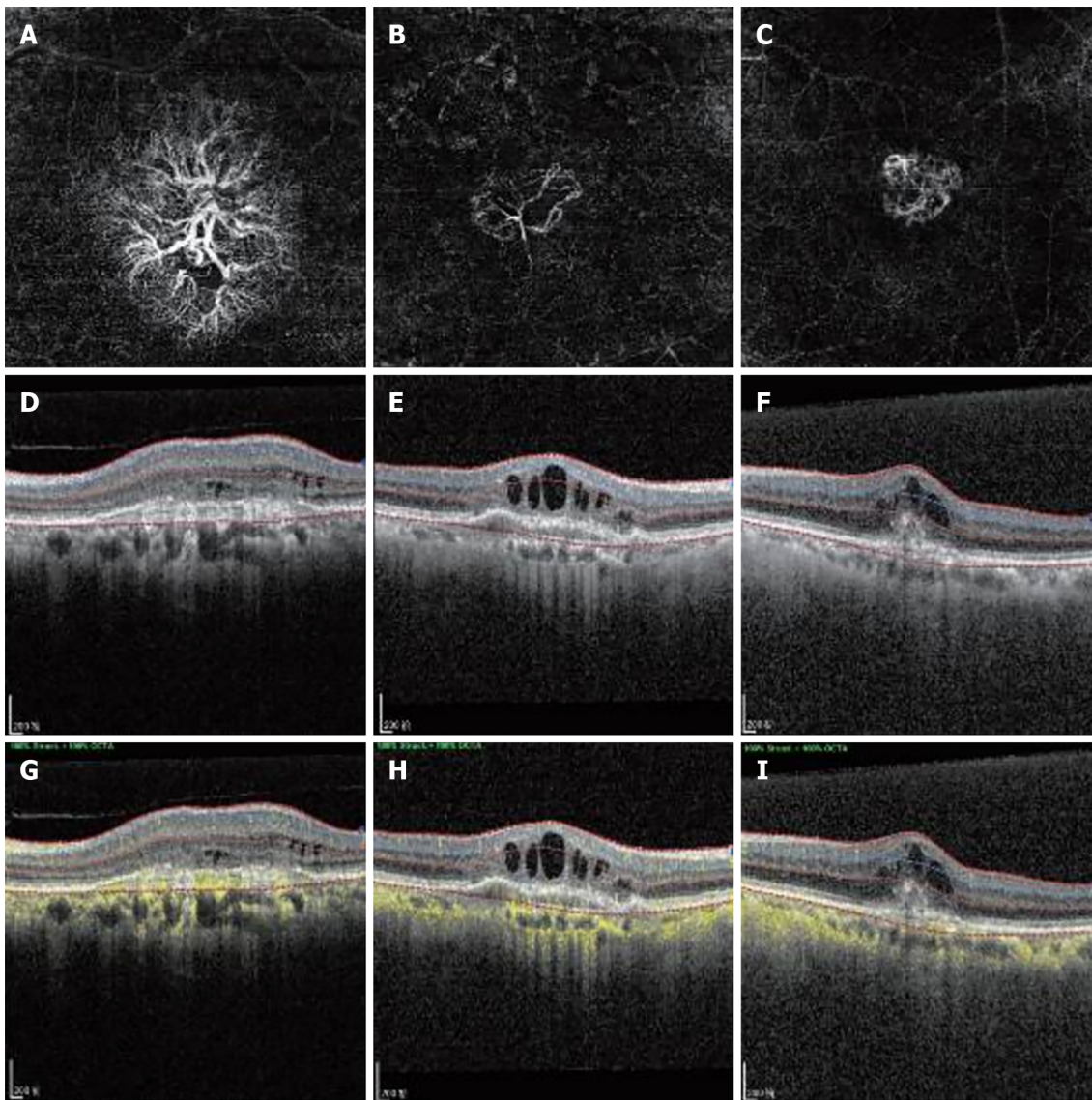


Figure 2 Morphological findings of choroidal neovascularization evaluated through qualitative analysis of optical coherence tomography angiography. A: A 51-year-old female patient with a "medusa" or "sea fan" pattern of choroidal neovascularization (CNV) in the oculus sinister; B: An 85-year-old male patient with a "long linear vessels" pattern of CNV in the oculus dexter; C: A 65-year-old female patient with an "indistinct network" pattern of CNV in the oculus sinister; D-F: Corresponding B-scan images showing the segmentation lines; G-I: Corresponding B-scan images with flow signals.

structure and may be considered a protective factor against exudative activity, thereby enhancing the effectiveness of anti-VEGF therapy. The fractal dimension was identified as a significant predictor in our study's univariate logistic regression analysis; however, it did not demonstrate independent significance as a risk factor for predicting response to anti-VEGF therapy in the multivariate logistic regression analysis, contrary to findings from previous studies. Different studies have yielded partially inconsistent results, which may be attributed to variations in sample size or discrepancies between observers across various studies. Although fractal dimension was not a significant predictor in multivariate logistic regression analysis, the final predictive model had the best diagnostic performance when it was included in the model.

The OCTA images of type 1 CNV have been previously described as exhibiting "sea fan," "medusa," or "tangled" patterns[20,21], while type 2 CNV has been characterized by a branching network of densely packed smaller caliber vessels radiating from the main trunk with a distinct demarcation[22,23]. The study by Suzuki *et al*[24] revealed that patients with type 1 CNV tend to develop resistance to anti-VEGF therapy, which can be attributed, at least partially, to the preserved barrier function of the RPE, impeding the rapid penetration of anti-VEGF drugs. The study conducted by Nakano *et al*[11], demonstrated that the mean vessel junction density of type 2 CNVs ($8.69 \pm 2.05/\text{mm}$) was significantly higher than that of type 1 CNVs ($7.30 \pm 2.40/\text{mm}$, $P = 0.008$). This finding suggested that type 1 CNVs exhibited a more significant presence of mature vessels and indicated their potential resistance against anti-VEGF therapy. Therefore, it could be inferred that vessel maturation contributed to the anti-VEGF resistance observed in type 1 CNVs. In line with this assumption, the study conducted by Kuehlewein *et al*[25] observed a higher incidence of large mature neovascular complexes in eyes with type 1 CNV compared to those with type 2 CNV, indicating an increased likelihood of poor responses to anti-VEGF treatment. Similarly, Jia *et al*[12] and Mettu *et al*[6] have identified that the specific subtype of

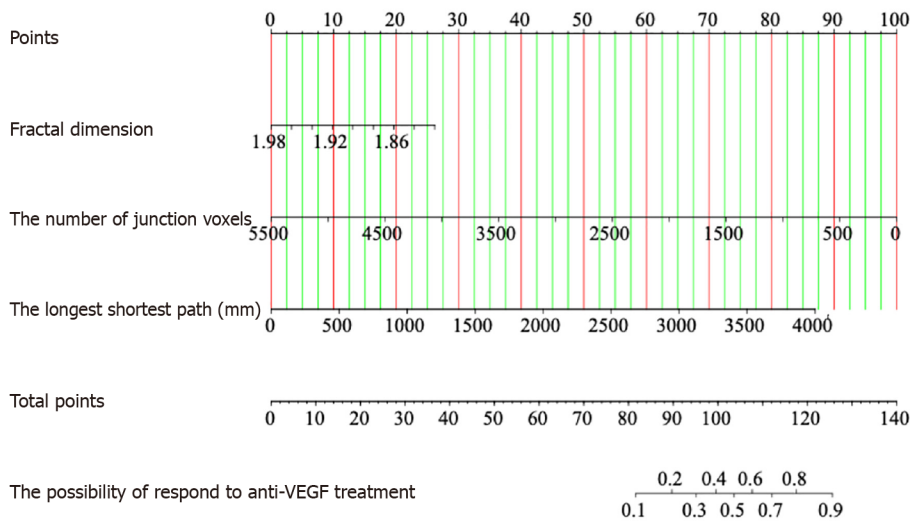


Figure 3 The constructed nomogram for predicting response to anti-vascular endothelial growth factor therapy. VEGF: Vascular endothelial growth factor.

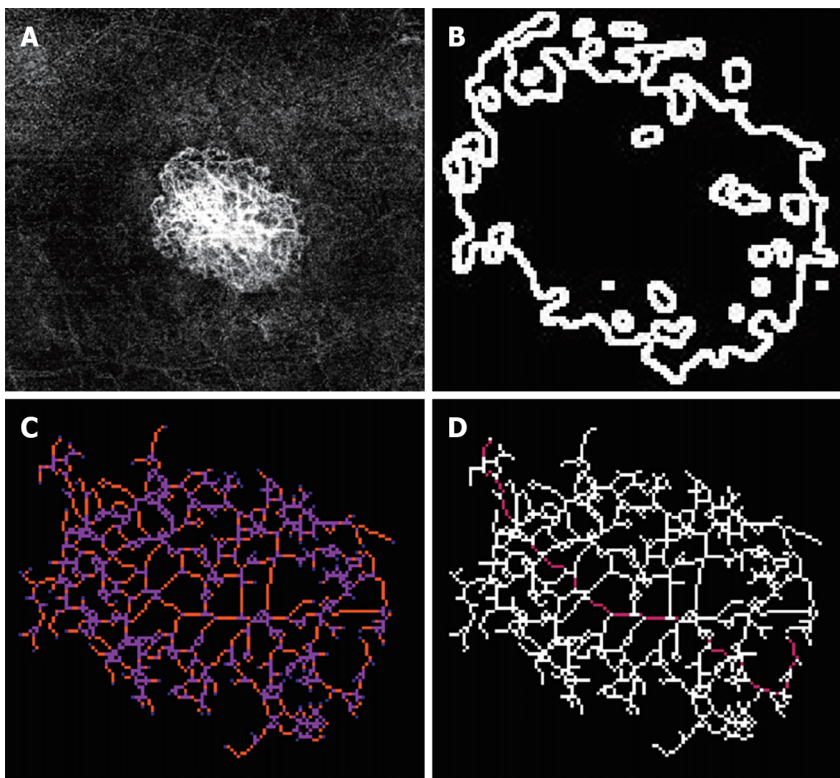


Figure 4 A 74-year-old female patient with an "indistinct network" pattern of choroidal neovascularization in the oculus dexter. A: 3 mm × 3 mm en-face optical coherence tomography angiography image showing the dense small vessels after removal of projection artifacts; B: Corresponding en-face choriocapillaris images were imported into ImageJ software for quantitative measurement of choroidal neovascularization parameters, including fractal dimension; C: End-point voxels in blue, slab voxels in orange, and junction voxels in purple; D: Longest shortest path in red.

CNV was significantly associated with the response to anti-VEGF therapy, suggesting that type 2 CNV exhibited a more favorable response to anti-VEGF treatment. Nevertheless, the response to long-term treatment may vary, particularly in cases of type 2 CNV. Daniel *et al*[26] and Daniel *et al*[27] revealed that patients with type 2 CNV exhibited an elevated risk of experiencing a suboptimal response to anti-VEGF therapy after five years of treatment compared to patients with other CNV subtypes, regardless of the specific drug or treatment regimen employed.

Three-dimensional skeletonization has been developed as an ImageJ plugin[28]; the plugin performs voxel segmentation in a skeleton image, accurately identifying junctions, triple and quadruple points, and branches while measuring their average and maximum length. Each voxel is classified into one of three types based on its neighboring voxels: (1) End-point voxels with less than two neighbors; (2) Junction voxels with more than two neighbors; and (3) Slab

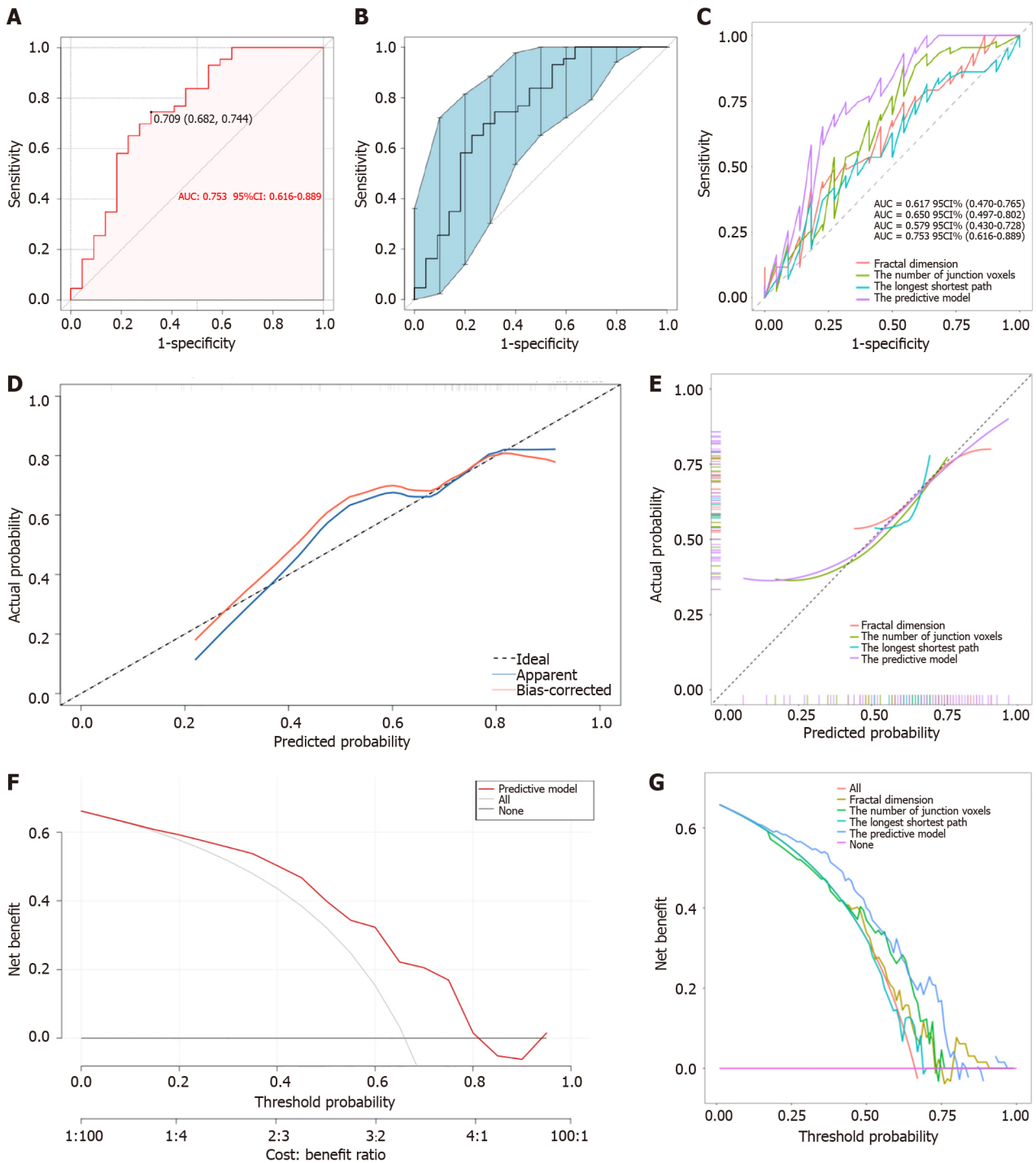


Figure 5 Area under the receiver operating characteristic curve, calibration curve, and decision curve analysis for the model predicting anti-vascular endothelial growth factor therapy response. A: Receiver operating characteristic (ROC) curve for the predictive model; B: ROC curves based on 500 bootstrap re-samples; C: ROC curves comparing different models; D: Calibration curves based on 500 bootstrap re-samples; E: Calibration curves comparing different models; F: Decision curve analysis based on 500 bootstrap re-samples; G: Decision curve analysis comparing different models.

voxels with precisely two neighbors. The resulting classifications are displayed in a new window, where a unique color represents each classification. Note that, according to this notation, the number of junction voxels may differ from the number of junctions due to potential voxel adjacency. Despite previous studies explaining the seemingly superior anti-VEGF responses in type 2 CNV cases, controversy remains. Our research not only observed an independent association between the number of junction voxels and predicting anti-VEGF response but also discovered that eyes with fewer junction voxels were more likely to exhibit a favorable response to anti-VEGF therapy, aligning with Daniel *et al*'s and Daniel *et al*'s findings suggesting poor anti-VEGF response in type 2 CNV cases characterized by dense vessel branching networks[26,27]. The variation in follow-up duration may account for the difference from most previous studies.

Although this study's univariate and multivariate analyses showed that the longest shortest path was not a significant and independent risk factor for anti-VEGF response, this study included the longest shortest path in the final prediction

model according to AIC screening variables. To our knowledge, the longest shortest path refers to the maximum distance that the shortest paths within the skeleton can cover in skeletal structure analysis. By comparing the longest and shortest paths of skeletal structures in different images, researchers can identify which structures are larger, more complex, or more interconnected. The longest shortest path offers information about the size and extent of the skeletal structure, with longer shortest paths typically indicating larger structures or longer branches. Complex structures often exhibit longer shortest paths due to multiple branches and junctions. If the shortest path is exceptionally long, it may indicate that certain parts of the structure are not interconnected through short paths, potentially indicating isolated or separate regions within the structure.

Our study has some limitations. On the one hand, the single-center study with a limited sample size had inherent selection biases. In order to mitigate this concern, we conducted 500 bootstrap re-samples to generate additional virtual samples from the original dataset, thereby increasing the sample size and mitigating the impact of sampling bias on the statistical power of the analysis. On the other hand, external data have not validated the risk prediction model, and its generalization performance remains unclear. Therefore, future studies should include external validation using larger datasets from other centers that can reliably predict outcomes.

CONCLUSION

In summary, the findings of our study suggest that the number of junction voxels is an independent predictor of the response to anti-VEGF therapy. The predictive model was established in combination with OCTA-measured parameters of CNV vascular architecture (including fractal dimension, the number of junction voxels, and the longest shortest path), demonstrating moderately good predictive efficacy and can assist clinicians in selecting individualized treatment for nAMD by predicting outcomes.

FOOTNOTES

Author contributions: Huang ZH and Lin GC conceived and designed the study; Huang ZH, Zhang KP, and Tu XZ collected and assembled the data; Huang ZH, Tu XZ, Lin Q, and Tu M analyzed and interpreted the data. All authors have read and approved the final manuscript.

Supported by Fujian Province Natural Science Foundation of China, No. 2020J011321.

Institutional review board statement: The study was reviewed and approved by the Longyan First Affiliated Hospital of Fujian Medical University (approval No. 202014).

Informed consent statement: As this retrospective observational study used anonymous clinical data from patients who have already consented to treatment, no additional consent was needed. Patients were informed of potential research use at the time of treatment consent.

Conflict-of-interest statement: There are no conflicts of interest to report.

Data sharing statement: The datasets generated and analyzed during the current study are available from the corresponding author on reasonable request.

STROBE statement: The authors have read the STROBE Statement-checklist of items, and the manuscript was prepared and revised according to the STROBE Statement-checklist of items.

Open-Access: This article is an open-access article that was selected by an in-house editor and fully peer-reviewed by external reviewers. It is distributed in accordance with the Creative Commons Attribution NonCommercial (CC BY-NC 4.0) license, which permits others to distribute, remix, adapt, build upon this work non-commercially, and license their derivative works on different terms, provided the original work is properly cited and the use is non-commercial. See: <https://creativecommons.org/licenses/by-nc/4.0/>

Country of origin: China

ORCID number: Zhen-Huan Huang [0000-0002-2472-3102](https://orcid.org/0000-0002-2472-3102).

S-Editor: Qu XL

L-Editor: Wang TQ

P-Editor: Yu HG

REFERENCES

- 1 Hsu CR, Lai TT, Hsieh YT, Ho TC, Yang CM, Yang CH. Combined quantitative and qualitative optical coherence tomography angiography

- biomarkers for predicting active neovascular age-related macular degeneration. *Sci Rep* 2021; **11**: 18068 [PMID: 34508170 DOI: 10.1038/s41598-021-97652-2]
- 2 **Song P**, Du Y, Chan KY, Theodoratou E, Rudan I. The national and subnational prevalence and burden of age-related macular degeneration in China. *J Glob Health* 2017; **7**: 020703 [PMID: 29302323 DOI: 10.7189/jogh.07.020703]
 - 3 **Spaide RF**, Jaffe GJ, Sarraf D, Freund KB, Sadda SR, Staurengi G, Waheed NK, Chakravarthy U, Rosenfeld PJ, Holz FG, Souied EH, Cohen SY, Querques G, Ohno-Matsui K, Boyer D, Gaudric A, Blodi B, Baurnal CR, Li X, Coscas GJ, Brucker A, Singerman L, Luthert P, Schmitz-Valckenberg S, Schmidt-Erfurth U, Grossniklaus HE, Wilson DJ, Guymer R, Yannuzzi LA, Chew EY, Csaky K, Monés JM, Pauleikhoff D, Tadayoni R, Fujimoto J. Consensus Nomenclature for Reporting Neovascular Age-Related Macular Degeneration Data: Consensus on Neovascular Age-Related Macular Degeneration Nomenclature Study Group. *Ophthalmology* 2020; **127**: 616-636 [PMID: 31864668 DOI: 10.1016/j.ophtha.2019.11.004]
 - 4 **Thomas CJ**, Mirza RG, Gill MK. Age-Related Macular Degeneration. *Med Clin North Am* 2021; **105**: 473-491 [PMID: 33926642 DOI: 10.1016/j.mcna.2021.01.003]
 - 5 **Bakri SJ**, Thorne JE, Ho AC, Ehlers JP, Schoenberger SD, Yeh S, Kim SJ. Safety and Efficacy of Anti-Vascular Endothelial Growth Factor Therapies for Neovascular Age-Related Macular Degeneration: A Report by the American Academy of Ophthalmology. *Ophthalmology* 2019; **126**: 55-63 [PMID: 30077616 DOI: 10.1016/j.ophtha.2018.07.028]
 - 6 **Mettu PS**, Allingham MJ, Cousins SW. Incomplete response to Anti-VEGF therapy in neovascular AMD: Exploring disease mechanisms and therapeutic opportunities. *Prog Retin Eye Res* 2021; **82**: 100906 [PMID: 33022379 DOI: 10.1016/j.preteyeres.2020.100906]
 - 7 **Waldstein SM**, Simader C, Staurengi G, Chong NV, Mitchell P, Jaffe GJ, Lu C, Katz TA, Schmidt-Erfurth U. Morphology and Visual Acuity in Aflibercept and Ranibizumab Therapy for Neovascular Age-Related Macular Degeneration in the VIEW Trials. *Ophthalmology* 2016; **123**: 1521-1529 [PMID: 27157149 DOI: 10.1016/j.ophtha.2016.03.037]
 - 8 **Amoaku WM**, Chakravarthy U, Gale R, Gavin M, Ghanchi F, Gibson J, Harding S, Johnston RL, Kelly SP, Lotery A, Mahmood S, Menon G, Sivaprasad S, Talks J, Tufail A, Yang Y. Defining response to anti-VEGF therapies in neovascular AMD. *Eye (Lond)* 2015; **29**: 721-731 [PMID: 25882328 DOI: 10.1038/eye.2015.48]
 - 9 **Giorno P**, Iacono P, Scarinci F, Di Renzo A, Varano M, Parravano M. Microvasculature Changes of Myopic Choroidal Neovascularization and the Predictive Value of Feeder Vessel Disappearance after Ranibizumab Treatment Revealed Using Optical Coherence Tomography Angiography. *Ophthalmologica* 2020; **243**: 263-270 [PMID: 31838464 DOI: 10.1159/000504755]
 - 10 **Wang Y**, Sun J, Wu J, Jia H, Feng J, Chen J, Yan Q, Huang P, Wang F, Bo Q, Sun X. Growth of nonexudative macular neovascularization in age-related macular degeneration: an indicator of biological lesion activity. *Eye (Lond)* 2023; **37**: 2048-2054 [PMID: 36434285 DOI: 10.1038/s41433-022-02282-1]
 - 11 **Nakano Y**, Kataoka K, Takeuchi J, Fujita A, Kaneko H, Shimizu H, Ito Y, Terasaki H. Vascular maturity of type 1 and type 2 choroidal neovascularization evaluated by optical coherence tomography angiography. *PLoS One* 2019; **14**: e0216304 [PMID: 31034505 DOI: 10.1371/journal.pone.0216304]
 - 12 **Jia H**, Lu B, Zhao Z, Yu Y, Wang F, Zhou M, Sun X. Prediction of the short-term efficacy of anti-VEGF therapy for neovascular age-related macular degeneration using optical coherence tomography angiography. *Eye Vis (Lond)* 2022; **9**: 16 [PMID: 35505390 DOI: 10.1186/s40662-022-00287-1]
 - 13 **Al-Sheikh M**, Iafe NA, Phasukkijwatana N, Sadda SR, Sarraf D. BIOMARKERS OF NEOVASCULAR ACTIVITY IN AGE-RELATED MACULAR DEGENERATION USING OPTICAL COHERENCE TOMOGRAPHY ANGIOGRAPHY. *Retina* 2018; **38**: 220-230 [PMID: 28582276 DOI: 10.1097/IAE.0000000000001628]
 - 14 **Coscas F**, Lupidi M, Boulet JF, Sellam A, Cabral D, Serra R, François C, Souied EH, Coscas G. Optical coherence tomography angiography in exudative age-related macular degeneration: a predictive model for treatment decisions. *Br J Ophthalmol* 2019; **103**: 1342-1346 [PMID: 30467129 DOI: 10.1136/bjophthalmol-2018-313065]
 - 15 **Miere A**, Butori P, Cohen SY, Semoun O, Capuano V, Jung C, Souied EH. Vascular Remodeling of Choroidal Neovascularization After Anti-Vascular Endothelial Growth Factor Therapy Visualized on Optical Coherence Tomography Angiography. *Retina* 2019; **39**: 548-557 [PMID: 29210939 DOI: 10.1097/IAE.0000000000001964]
 - 16 **Coscas F**, Cabral D, Pereira T, Galdes C, Narotamo H, Miere A, Lupidi M, Sellam A, Papoila A, Coscas G, Souied E. Quantitative optical coherence tomography angiography biomarkers for neovascular age-related macular degeneration in remission. *PLoS One* 2018; **13**: e0205513 [PMID: 30300393 DOI: 10.1371/journal.pone.0205513]
 - 17 **Faatz H**, Rothaus K, Ziegler M, Book M, Spital G, Lange C, Lommatzsch A. The Architecture of Macular Neovascularizations Predicts Treatment Responses to Anti-VEGF Therapy in Neovascular AMD. *Diagnostics (Basel)* 2022; **12** [PMID: 36428867 DOI: 10.3390/diagnostics12112807]
 - 18 **Serra R**, Coscas F, Pinna A, Cabral D, Coscas G, Souied EH. Quantitative Optical Coherence Tomography Angiography Features of Inactive Macular Neovascularization in Age-Related Macular Degeneration. *Retina* 2021; **41**: 93-102 [PMID: 32281767 DOI: 10.1097/IAE.0000000000002807]
 - 19 **Carnevali A**, Cicinelli MV, Capuano V, Corvi F, Mazzaferro A, Querques L, Scordia V, Souied EH, Bandello F, Querques G. Optical Coherence Tomography Angiography: A Useful Tool for Diagnosis of Treatment-Naïve Quiescent Choroidal Neovascularization. *Am J Ophthalmol* 2016; **169**: 189-198 [PMID: 27394033 DOI: 10.1016/j.ajo.2016.06.042]
 - 20 **Dansingani KK**, Freund KB. Optical Coherence Tomography Angiography Reveals Mature, Tangled Vascular Networks in Eyes With Neovascular Age-Related Macular Degeneration Showing Resistance to Geographic Atrophy. *Ophthalmic Surg Lasers Imaging Retina* 2015; **46**: 907-912 [PMID: 26469229 DOI: 10.3928/23258160-20151008-02]
 - 21 **Iafe NA**, Phasukkijwatana N, Sarraf D. Optical Coherence Tomography Angiography of Type 1 Neovascularization in Age-Related Macular Degeneration. *Dev Ophthalmol* 2016; **56**: 45-51 [PMID: 27023719 DOI: 10.1159/000442776]
 - 22 **Kuehlewein L**, Sadda SR, Sarraf D. OCT angiography and sequential quantitative analysis of type 2 neovascularization after ranibizumab therapy. *Eye (Lond)* 2015; **29**: 932-935 [PMID: 25976641 DOI: 10.1038/eye.2015.80]
 - 23 **Farecki ML**, Gutfleisch M, Faatz H, Rothaus K, Heimes B, Spital G, Lommatzsch A, Pauleikhoff D. Characteristics of type 1 and 2 CNV in exudative AMD in OCT-Angiography. *Graefes Arch Clin Exp Ophthalmol* 2017; **255**: 913-921 [PMID: 28233061 DOI: 10.1007/s00417-017-3588-y]
 - 24 **Suzuki M**, Nagai N, Izumi-Nagai K, Shinoda H, Koto T, Uchida A, Mochimaru H, Yuki K, Sasaki M, Tsubota K, Ozawa Y. Predictive factors for non-response to intravitreal ranibizumab treatment in age-related macular degeneration. *Br J Ophthalmol* 2014; **98**: 1186-1191 [PMID: 24711658 DOI: 10.1136/bjophthalmol-2013-304670]

- 25 **Kuchlewein L**, Bansal M, Lenis TL, Iafe NA, Satta SR, Bonini Filho MA, De Carlo TE, Waheed NK, Duker JS, Sarraf D. Optical Coherence Tomography Angiography of Type 1 Neovascularization in Age-Related Macular Degeneration. *Am J Ophthalmol* 2015; **160**: 739-48.e2 [PMID: 26164826 DOI: 10.1016/j.ajo.2015.06.030]
- 26 **Daniel E**, Pan W, Ying GS, Kim BJ, Grunwald JE, Ferris FL 3rd, Jaffe GJ, Toth CA, Martin DF, Fine SL, Maguire MG; Comparison of Age-related Macular Degeneration Treatments Trials. Development and Course of Scars in the Comparison of Age-Related Macular Degeneration Treatments Trials. *Ophthalmology* 2018; **125**: 1037-1046 [PMID: 29454660 DOI: 10.1016/j.ophtha.2018.01.004]
- 27 **Daniel E**, Toth CA, Grunwald JE, Jaffe GJ, Martin DF, Fine SL, Huang J, Ying GS, Hagstrom SA, Winter K, Maguire MG; Comparison of Age-related Macular Degeneration Treatments Trials Research Group. Risk of scar in the comparison of age-related macular degeneration treatments trials. *Ophthalmology* 2014; **121**: 656-666 [PMID: 24314839 DOI: 10.1016/j.ophtha.2013.10.019]
- 28 **Arganda-Carreras I**, Fernández-González R, Muñoz-Barrutia A, Ortiz-De-Solorzano C. 3D reconstruction of histological sections: Application to mammary gland tissue. *Microsc Res Tech* 2010; **73**: 1019-1029 [PMID: 20232465 DOI: 10.1002/jemt.20829]

Observational Study

Cerebral perfusion in patients with unilateral internal carotid artery occlusion by dual post-labeling delays arterial spin labeling imaging

Gui-Rong Zhang, Yan-Yan Zhang, Wen-Bin Liang, Dun Ding

Specialty type: Radiology, nuclear medicine and medical imaging**Provenance and peer review:**

Unsolicited article; Externally peer reviewed.

Peer-review model: Single blind**Peer-review report's classification****Scientific Quality:** Grade B**Novelty:** Grade B**Creativity or Innovation:** Grade B**Scientific Significance:** Grade B**P-Reviewer:** Jiang T**Received:** July 12, 2024**Revised:** August 29, 2024**Accepted:** September 6, 2024**Published online:** September 28, 2024**Processing time:** 76 Days and 19.2 Hours**Gui-Rong Zhang, Yan-Yan Zhang, Wen-Bin Liang, Dun Ding**, Department of Medical Imaging, The Second Affiliated Hospital of Xi'an Jiaotong University, Xi'an 710043, Shaanxi Province, China**Corresponding author:** Dun Ding, MD, PhD, Assistant Professor, Department of Medical Imaging, The Second Affiliated Hospital of Xi'an Jiaotong University, No. 157 West Fifth Road, Xi'an 710043, Shaanxi Province, China. hequren521@163.com**Abstract****BACKGROUND**

Global and regional cerebral blood flow (CBF) changes in patients with unilateral internal carotid artery occlusion (ICAO) are unclear when the dual post-labeling delays (PLD) arterial spin labeling (ASL) magnetic resonance imaging (MRI) technique is used. Manual delineation of regions of interest for CBF measurement is time-consuming and laborious.

AIM

To assess global and regional CBF changes in patients with unilateral ICAO with the ASL-MRI perfusion technique.

METHODS

Twenty hospitalized patients with ICAO and sex- and age-matched controls were included in the study. Regional CBF was measured by Dr. Brain's ASL software. The present study evaluated differences in global, middle cerebral artery (MCA) territory, anterior cerebral artery territory, and Alberta Stroke Program Early Computed Tomography Score (ASPECTS) regions (including the caudate nucleus, lentiform nucleus, insula ribbon, internal capsule, and M1-M6) and brain lobes (including frontal, parietal, temporal, and insular lobes) between ICAO patients and controls at PLD 1.5 s and PLD 2.5 s.

RESULTS

When comparing CBF between ICAO patients and controls, the global CBF in ICAO patients was lower at both PLD 1.5 s and PLD 2.5 s; the CBF on the occluded side was lower in 15 brain regions at PLD 1.5 s, and it was lower in 9 brain regions at PLD 2.5 s; the CBF in the contralateral hemisphere was lower in the caudate nucleus and internal capsule at PLD 1.5 s and in M6 at PLD 2.5 s. The global CBF in ICAO patients was lower at PLD 1.5 s than at PLD 2.5 s. The ipsilateral CBF at PLD 1.5 s was lower than that at PLD 2.5 s in 15 regions, whereas

the contralateral CBF was lower at PLD 1.5 s than at PLD 2.5 s in 12 regions. The ipsilateral CBF was lower than the contralateral CBF in 15 regions at PLD 1.5 s, and in M6 at PLD 2.5 s.

CONCLUSION

Unilateral ICAO results in hypoperfusion in the global and MCA territories, especially in the ASPECTS area. Dual PLD settings prove more suitable for accurate CBF quantification in ICAO.

Key Words: Arterial spin labeling; Internal carotid artery occlusion; Ischemic stroke; Cerebral blood flow; Hemodynamic

©The Author(s) 2024. Published by Baishideng Publishing Group Inc. All rights reserved.

Core Tip: In this study, the dual post-labeling delays (PLD) arterial spin labeling (ASL) technique was used for cerebral blood flow (CBF) imaging in unilateral internal carotid artery occlusion (ICAO) patients. Intelligent ASL analysis software was used for rapid quantification of regional CBF, including the Alberta Stroke Program Early Computed Tomography Score (ASPECTS) regions. A comparison with the controls suggests that unilateral ICAO resulted in hypoperfusion in the global and middle cerebral artery territory, affecting most of the ASPECTS area on the occluded side and a small part of the ASPECTS area on the nonoccluded side. The dual PLD settings are more suitable for accurate CBF quantification in ICAO.

Citation: Zhang GR, Zhang YY, Liang WB, Ding D. Cerebral perfusion in patients with unilateral internal carotid artery occlusion by dual post-labeling delays arterial spin labeling imaging. *World J Radiol* 2024; 16(9): 429-438

URL: <https://www.wjgnet.com/1949-8470/full/v16/i9/429.htm>

DOI: <https://dx.doi.org/10.4329/wjr.v16.i9.429>

INTRODUCTION

Internal carotid artery occlusion (ICAO) is less common but still significant for the etiology of transient ischemic attack (TIA) and cerebral infarction[1]. Atherosclerosis is the major contributing etiology[2]. ICAO diminishes the perfusion pressure on the occluded side, potentially leading to blood redistribution from the contralateral ICA or posterior circulation, along with collateral blood flow towards the affected hemisphere[3]. ICAO patients exhibit ischemic symptoms involving the middle cerebral artery (MCA) and/or anterior cerebral artery (ACA) territories in the anterior circulation[4]. Therefore, assessing changes in global and regional cerebral blood flow (CBF) within the ACA and MCA territories is crucial.

Previous studies have predominantly used single post-labeling delay (PLD) or manual region-of-interest selection for CBF measurement, but these approaches are time-consuming and labor-intensive. Leveraging advances in artificial intelligence, Dr. Brain's software enables the automatic calculation of global and anatomical regional CBF. This facilitates easier adoption of advanced magnetic resonance imaging (MRI) technology for patient diagnosis and monitoring.

The Alberta Stroke Program Early Computed Tomography Score (ASPECTS) serves as a straightforward and reliable qualitative scoring system widely used to assess early ischemic cerebral infarction severity. It plays a critical role in decision-making in endovascular treatment (EVT)[5-8], assisting in treatment prediction and prognosis. However, a notable gap in perfusion research focused on ASPECTS regions remains.

This retrospective study aims to analyze global and regional CBF changes in unilateral atherosclerotic ICAO patients with the aforementioned tools.

MATERIALS AND METHODS

Subjects

The hospital ethics committee approved the current retrospective study, and informed consent was obtained from all the participants. Between September 2021 and March 2024, patients who were diagnosed with unilateral ICAO confirmed by digital subtraction angiography and who underwent dual PLDs ASL imaging were included. The exclusion criteria were as follows: (1) Moderate or severe stenosis ($\geq 50\%$) in contralateral vessels; (2) Poor image quality or ASL with single or other PLD; and (3) Brain injury, a history of brain surgery, psychiatric disorders, or other conditions affecting brain function. The patient enrolment process is illustrated in [Figure 1](#).

Finally, twenty functionally independent ICAO patients (three women and seventeen men; mean age: 57.50 ± 10.841 years) and sex- and age-matched control subjects were examined.

All stroke patients had an ASPECTS score of 8-10 on diffusion weighted imaging (DWI), and the infarctions were located in the MCA territory. All stroke patients had subcortical watershed infarctions, 2 of them had cortical infarctions, and one of which with a basal area infarction. None of the patients presented infarct lesions exceeding 30 mm in diameter in the territory ipsilateral to the ICA occlusion.

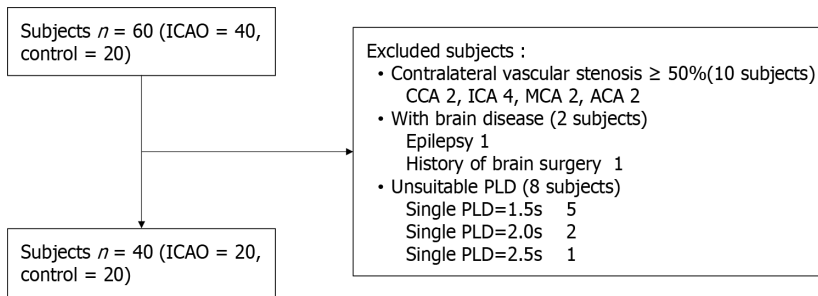


Figure 1 Study enrollment showing exclusion criteria. CCA: Common carotid artery; ICA: Internal carotid artery; MCA: Middle cerebral artery; ACA: Anterior cerebral artery; ICAO: Internal carotid artery occlusion; PLD: Post-labeling delay.

MRI

The ASL and DWI sequences were scanned with a 3.0T scanner (HDxt Signa; GE Healthcare) outfitted with an 8-channel head coil for signal acquisition. A three-dimensional pseudo-continuous ASL (PCASL) sequence was used for the whole brain. The parameters of ASL were as follows: Repetition time (TR) 4599 ms (PLD 1525 ms), TR5294 ms (PLD 2525 ms), echo time (TE) 10.86 ms, labelling duration 1500 ms, field of view (FOV) 24 cm × 24 cm, layer thickness 4.0 mm, 36 slices, with background suppression. The parameters of DWI were as follows: TR, 5500 ms; TE, 75 ms; FOV, 22 cm × 22 cm; and layer thickness, 5.0 mm.

Statistical analysis

The original ASL sequence data (PLD 1.5 s and PLD 2.5 s were anonymized and uploaded to the Dr. Brain software ASL module (YIWEI Medical Technology, China). The Buxton hemodynamic model was processed with blood T1 and brain tissue T1 constants set at 1650 and 11665 ms, respectively. **Figure 2** depicts the processing flow diagram and schematic for brain region segmentation.

This study evaluated differences in regional CBF across several areas: Global, MCA territory; ACA territory; ASPECTS regions (including the caudate nucleus, lentiform nucleus, insula ribbon, internal capsule, and M1-M6); and brain lobes (including the frontal, parietal, temporal, and insular lobes). This analysis compared CBF differences between the ipsilateral and contralateral hemispheres to the occlusion and control subjects at PLD 1.5 s and PLD 2.5 s.

Owing to the absence of differences in CBF between the left and right hemispheres in control subjects, the CBF values for these hemispheres were averaged for analysis.

The Statistical Package for the Social Sciences for Windows, Version 21.0 (SPSS, Chicago), was used for statistical analysis in this study. All measurement data were tested for normality *via* the Shapiro-Wilk test. Data that conformed to a normal distribution and exhibited homogeneous variance are presented as the means ± SD; otherwise, the data are presented as medians (quartile ranges). As the data conformed to a normal distribution and the variance was homogeneous, paired sample or two independent sample *t* tests were used for intergroup comparisons; otherwise, nonparametric Wilcoxon (W) or Mann-Whitney *U* tests were used. Differences were considered significant when $P < 0.05$.

RESULTS

The fundamental features of the ICAO patients are shown in **Table 1**. Regional CBF data are shown in **Table 2**.

Differences in regional CBF between ICAO and control group

The global CBF of ICAO patients was significantly lower than that of the control group at PLD 1.5 s (24.152 ± 4.517 vs 30.194 ± 7.164 mL/min/100 g, $P = 0.011$) and PLD 2.5 s (28.904 ± 4.564 vs 34.028 ± 6.730 mL/min/100 g, $P = 0.024$).

Compared with that of the control subjects, the CBF in the occluded hemisphere was significantly lower in 15 brain regions at PLD 1.5 s ($P < 0.05$), but no differences were found in the ACA territory ($P > 0.05$) (as shown in **Table 3**). The CBF in the occluded hemisphere was lower in the MCA territory, insula ribbon, M2, M3, M4, M5, M6, parietal lobe ($P < 0.05$), and temporal lobe at PLD 2.5 s ($P < 0.05$), but no differences were found in the ACA territory, caudate nucleus, lentiform nucleus, internal capsule, M1, frontal lobe, or insular lobe ($P > 0.05$) (as shown in **Table 3**).

Compared with that of the control subjects, the CBF in the contralateral hemisphere was significantly lower in the caudate nucleus and internal capsule at PLD 1.5 s ($P < 0.05$), but no differences were found in the other 14 brain regions ($P > 0.05$) (as shown in **Table 3**). The CBF in the contralateral hemisphere was lower in M6 at PLD 2.5 s ($P < 0.05$), but no differences were found in the other 15 brain regions ($P > 0.05$) (as shown in **Table 3**).

Differences in regional CBF between PLD 1.5 s and PLD 2.5 s

The global CBF at PLD 1.5 s was significantly lower than that at PLD 2.5 s (24.152 ± 4.517 vs 28.904 ± 4.564 mL/min/100 g, $P = 0.000$).

Table 1 Patient characteristics of internal carotid artery occlusion

Patient Number	Age (year)	Sex	Symptoms/Onset time	Imaging	Occlusion side	Occlusion site	Contralateral side	Collateral flow pathway
1	47	Female	Headache/1 month		R	Initial		ACoA
2	51	Male	Neuro-deficiency/5 days	Stroke	R	Ophthalmic		ACoA
3	50	Male	Neuro-deficiency/1 week	Stroke	R	Ophthalmic		ACoA + PCoA + L
4	57	Male	Neuro-deficiency/1 week	Stroke	L	Initial		ACoA + PCoA + OA
5	58	Male	TIA/4 days		R	Initial	CCA 20%	ACoA + L + OA
6	55	Male	Neuro-deficiency/2 weeks	Stroke	R	Clinoid		OA
7	82	Male	TIA/1 month		L	Initial	ICA 20%	ACoA + PCoA
8	67	Male	Neuro-deficiency/4 days	Stroke	L	Initial	ICA 20%	ACoA
9	66	Male	Neuro-deficiency/2 weeks	Stroke	R	Initial	ICA 20%	PCoA
10	61	Female	Headache/2 months		L	Ophthalmic		ACoA + PCoA + L
11	56	Male	Dizziness/1 month	Stroke	R	Initial	MCA 20%	ACoA + PCoA + OA
12	57	Male	Dizziness/3 years		L	Communicating	ICA 20%	PCoA
13	42	Male	Dizziness/3 days		L	Ophthalmic		ACoA + PCoA
14	59	Male	TIA/1 week		R	Initial	ICA 20%	ACoA + PCoA + OA + L
15	35	Male	Neuro-deficiency/2 months	Stroke	R	Terminal		New vessels + L
16	70	Male	Neuro-deficiency/2 months	Stroke	R	Ophthalmic	ICA 20%-30%	ACoA + PCoA
17	46	Female	Neuro-deficiency/5 days	Stroke	R	Ophthalmic		ACoA
18	62	Male	TIA/3 days		L	Initial	ICA 40%	OA
19	71	Male	Neuro-deficiency/10 days	Stroke	L	Initial	ICA 40%	
20	58	Male	Neuro-deficiency/3 days	Stroke	L	Ophthalmic	ICA 20%	ACoA

CCA: Common carotid artery; TIA: Transient ischemic attack; ICA: Internal carotid artery; MCA: Middle cerebral artery; ICA: Internal carotid artery; MCA: Middle cerebral artery; ACA: Anterior cerebral artery; ACoA: Anterior communicating artery; PCoA: Posterior communicating artery; OA: Ophthalmic artery; L: Leptomeningeal.

When comparing PLD 1.5 s with PLD 2.5 s, the CBF on the occluded side was significantly lower in 15 brain regions ($P < 0.05$), but no differences were found in the internal capsule ($P > 0.05$) (as shown in Table 3). The CBF of the nonoccluded side was significantly lower in 12 brain regions ($P < 0.05$), but no differences were found in the caudate nucleus, lentiform nucleus, insula ribbon, or M2 region ($P > 0.05$) (as shown in Table 3).

Differences in regional CBF between ipsilateral and contralateral to the ICAO

At PLD 1.5 s, the CBF in 15 brain regions ipsilateral to the ICAO was significantly lower than that in the contralateral hemisphere ($P < 0.05$), but no differences were found in the ACA territory ($P > 0.05$) (as shown in Table 3).

At PLD 2.5 s, the CBF in the M6 region ipsilateral to the ICAO was significantly lower than that in the contralateral hemisphere ($P < 0.05$), but no differences were found in the other 15 brain regions at PLD 2.5 s ($P > 0.05$) (as shown in Table 3).

Table 2 The regional cerebral blood flow value, mean \pm SD/ Median (quartile)

Variables brain region	Ips-CBF at PLD 1.5	Ips-CBF at PLD 2.5	Con-CBF at PLD 1.5	Con-CBF at PLD 2.5	HC CBF at PLD 1.5	HC CBF at PLD 2.5
Anterior	27.968 \pm 7.941	32.687 \pm 7.409	29.728 \pm 4.828	32.24 (11.3)	33.353 \pm 7.966	38.226 \pm 6.900
Middle	18.818 \pm 6.485	29.09 (6.93)	27.504 \pm 4.243	30.71 (4.05)	31.687 \pm 7.907	35.710 \pm 7.602
Caudate nucleus	17.57 \pm 4.573	21.67 \pm 5.603	22.175 \pm 3.355	23.714 \pm 5.898	26.442 \pm 4.510	31.393 \pm 5.603
Lentiform nucleus	19.812 \pm 7.299	25.054 \pm 5.531	28.816 \pm 4.572	27.412 \pm 4.750	33.222 \pm 6.785	29.205 \pm 6.178
Insula ribbon	24.313 \pm 8.122	31.186 \pm 5.886	33.001 \pm 3.984	32.176 \pm 3.502	38.537 \pm 8.69	36.881 \pm 8.136
Internal capsule	24.464 \pm 3.627	24.449 \pm 4.307	20.248 \pm 5.343	23.861 \pm 5.089	29.292 \pm 4.519	24.958 \pm 4.429
M1	19.764 \pm 6.796	28.01 (5.47)	27.172 \pm 4.373	29.05 (4.35)	31.417 \pm 7.361	33.463 \pm 7.962
M2	19.735 \pm 9.102	28.088 \pm 7.164	31.633 \pm 4.568	32.035 (5.61)	37.329 \pm 9.097	36.49 \pm 8.590
M3	20.208 \pm 7.954	29.376 \pm 7.442	29.249 \pm 6.268	33.245 \pm 5.028	32.575 (7.83)	38.132 \pm 9.422
M4	19.293 \pm 6.837	29.59 (9.53)	25.399 \pm 4.554	29.64 (5.81)	28.413 \pm 7.149	35.048 \pm 6.726
M5	16.271 \pm 7.443	25.099 \pm 7.604	25.688 \pm 5.449	29.03 (4.48)	26.45 (4.22)	33.933 \pm 6.944
M6	15.902 \pm 6.986	24.869 \pm 7.918	25.057 \pm 5.284	30.209 \pm 3.750	29.28 (5.58)	36.683 \pm 7.377
Frontal lobe	19.933 \pm 6.746	29.98 (7.99)	27.238 \pm 4.513	30.21 (4.62)	30.712 \pm 7.051	34.558 \pm 7.166
Parietal lobe	19.471 \pm 6.988	26.906 \pm 7.273	26.378 \pm 5.135	30.42 (2.81)	28.698 (4.82)	36.092 \pm 6.995
Temporal lobe	19.931 \pm 7.940	28.557 \pm 7.084	29.646 \pm 5.311	32.257 \pm 4.582	33.393 \pm 8.285	36.518 \pm 8.837
Insular lobe	25.732 \pm 6.496	32.083 \pm 7.257	30.485 \pm 4.243	32.29 (6.4)	34.371 \pm 7.031	35.689 \pm 6.415

Ips: Ipsilateral to internal carotid artery occlusion; Con: Contralateral to internal carotid artery occlusion; HC: Health control; PLD: Post-labeling delay.

DISCUSSION

ASL and dynamic susceptibility contrast (DSC) MRI perfusion imaging are commonly used to measure CBF; DSC requires intravenous bolus administration of gadolinium, while ASL is performed without exogenous contrast and uses arterial blood water as an endogenous diffusible tracer. Owing to current concerns about the use of contrast agents in patients with poor kidney function, an alternative approach with no harmful effects would be highly beneficial. ASL has become the most widely used perfusion imaging sequence in the clinic. ASL labelling approaches include continuous and pulsed labelling, and PCASL provides superior labelling efficiency and is compatible with modern body coil radiofrequency transmission hardware that is recommended for clinical imaging[9].

The labeling duration and PLDs are the most important information that can be used to interpret (quantify) CBF images[10]. ASL permits noninvasive estimation of CBF but relies upon the arterial transit time (ATT)[11]. While ATT is well defined for healthy vasculature, it can clearly differ in disease states, potentially making conventional single PLD ASL techniques unsuitable[12]. Owing to the formation of collateral blood flow, the transit time is prolonged in cerebral artery steno-occlusive diseases, which restricts the accurate measurement of CBF by ASL[12-14]. However, the use of a solitary traditional PLD results in an underestimation of CBF[9,12], which can be partially mitigated by using long PLD [2]. In addition to the PLD of 1.5 seconds, we employed a relatively longer PLD of 2.5 seconds, as seen in previous studies. Akiyama *et al*[11] reported the efficacy of using dual PLDs with 1.5- and 2.5-second techniques to evaluate the slow collateral blood flow that sustains the cerebrovascular reserve (CVR) in stenotic or occlusive ICA conditions[11,15].

Compared with those in the control group and contralateral hemisphere, the current findings indicate that nonacute unilateral atherosclerotic ICAO results in decreased CBF in the global, MCA territory and across most ASPECTS areas of the ipsilateral hemisphere at both PLD 1.5 s and PLD 2.5 s. ICAO leads to the interruption of blood flow on the occluding side. Owing to its anatomical characteristics, the MCA territory is most affected, and the ASPECTS area is located in the MCA territory, so it is also affected. This finding is consistent with previous research; for example, Jeroen Hendrikse's study demonstrated reduced CBF in the grey matter of the ipsilateral MCA territory[16]. Bokkers *et al*[17] reported significantly decreased CBF in the frontal and frontal parietal regions on the occluded side of the ICA[17]. Furthermore, studies using contrast-enhanced perfusion imaging have consistently shown reduced CBF in both grey and white matter of the occluded hemisphere of the ICA[18-20].

The CBF in the ACA territory was not affected in this study, which is inconsistent with previous research. Hartkamp *et al*[3] reported that in patients with ICAO, the CBF was significantly lower in the ACA and MCA territories on the occluded side of the ICA than in control subjects[3]. This may be related to the fact that 70% of the ICAO patients included in this study had anterior communicating artery compensation, and primary collateral circulation can quickly compensate for CBF.

Table 3 Statistical result

Variables brain region	P value	P value	P value	P value	P value	P value	P value	P value
Anterior	0.088	0.054	0.147	0.095	0.001 ^e	0.000 ^f	0.454	1.000
Middle	0.000 ^a	0.009 ^b	0.083	0.078	0.000 ^e	0.002 ^f	0.000 ^g	0.175
Caudate nucleus	0.000 ^a	0.176	0.008 ^c	0.715	0.001 ^e	0.191	0.003 ^g	0.323
Lentiform nucleus	0.000 ^a	0.073	0.050	0.393	0.000 ^e	0.117	0.001 ^g	0.206
Insula ribbon	0.000 ^a	0.041 ^b	0.068	0.073	0.001 ^e	0.267	0.003 ^g	0.567
Internal capsule	0.004 ^a	0.762	0.000 ^c	0.557	0.988	0.003 ^f	0.014 ^g	0.727
M1	0.000 ^a	0.063	0.068	0.137	0.000 ^e	0.006 ^f	0.001 ^g	0.546
M2	0.000 ^a	0.009 ^b	0.246	0.098	0.000 ^e	0.577	0.001 ^g	0.061
M3	0.001 ^a	0.011 ^b	0.286	0.088	0.000 ^e	0.006 ^f	0.001 ^g	0.095
M4	0.002 ^a	0.014 ^b	0.185	0.070	0.000 ^e	0.000 ^f	0.006 ^g	0.291
M5	0.002 ^a	0.004 ^b	0.577	0.099	0.000 ^e	0.000 ^f	0.000 ^g	0.090
M6	0.000 ^a	0.000 ^b	0.086	0.005 ^d	0.000 ^e	0.001 ^f	0.000 ^g	0.035 ^h
Frontal lobe	0.000 ^a	0.070	0.124	0.286	0.000 ^e	0.000 ^f	0.001 ^g	0.291
Parietal lobe	0.002 ^a	0.002 ^b	0.178	0.051	0.000 ^e	0.000 ^f	0.003 ^g	0.152
Temporal lobe	0.000 ^a	0.014 ^b	0.157	0.109	0.000 ^e	0.036 ^f	0.000 ^g	0.090
Insular lobe	0.002 ^a	0.184	0.080	0.286	0.000 ^e	0.042 ^f	0.002 ^g	0.985

^a $P < 0.01$, ipsilateral *vs* control at post-labeling delay 1.5 s.

^b $P < 0.05$, ipsilateral *vs* control at post-labeling delay 2.5 s.

^c $P < 0.01$, contralateral *vs* control at post-labeling delay 1.5 s.

^d $P < 0.01$, contralateral *vs* control at post-labeling delay 2.5 s.

^e $P < 0.001$, ipsilateral post-labeling delay 1.5 s *vs* post-labeling delay 2.5 s.

^f $P < 0.05$, contralateral post-labeling delay 1.5 s *vs* post-labeling delay 2.5 s.

^g $P < 0.05$, ipsilateral *vs* contralateral at post-labeling delay 1.5 s.

^h $P < 0.05$, ipsilateral *vs* contralateral at post-labeling delay 2.5 s.

The ASPECTS was originally developed to assess the volume of acute MCA infarction on non-contrast CT scans, but its applicability extends to multimodal MRI techniques as well. In the present study, all cerebral infarction patients had ASPECTS values ranging from 8 to 10. A previous meta-analysis revealed that higher ASPECTS values (8-10) are associated with significantly better outcomes following EVT than lower ASPECTS values[21]. In China, research on acute large-vessel occlusion in the anterior circulation has demonstrated that patients with larger infarctions (ASPECTS scores 3-5 and infarct volume 70-100 mL) benefit more from endovascular therapy than from medical management alone[22].

ASPECTS can be divided into subcortical (including the caudate nucleus, lentiform nucleus, insula ribbon, and internal capsule) and cortical regions (including M1-M6)[23]. The findings of the current study indicate that the hypoperfusion areas in ASPECTS regions are located mainly in the cortex, a detail not previously emphasized. Another study indicated that a higher baseline cortical ASPECTS was predictive of favorable clinical outcomes in patients with ASPECTS < 6 and large vessel occlusion treated with EVT[24]. Therefore, the ASPECTS has significant clinical importance, and perfusion evaluation is necessary.

The CBF at PLD 1.5 s was significantly lower than that at PLD 2.5 s globally, in MCA territories, and in most ASPECTS areas, and the hypoperfusion areas from PLD 1.5 s to PLD 2.5 s were reduced in the occluded hemisphere. These findings indicate the existence of slow flow and redistribution to compensate for ischemia in unilateral ICAO. The current results indicate that the selection of the parameter PLD for ASL can affect the evaluation of CBF correctly because of the presence of slow flow in ICAO patients, and a shorter PLD of 1.5 seconds may result in an underestimation of regional CBF in ICAO patients. An increase in collateral flow in ICAO patients results in longer blood flow pathways and a prolonged blood arrival time[25,26]. A shorter delay does not allow the labelled blood water to be fully delivered to the tissue, and a longer PLD must be included. Our results indicate that dual PLD settings can improve the quantification of CBF in ICAO patients. Presently, many clinical studies have been performed utilizing several PLDs with ATT correction to improve accurate quantification of CBF[12,14,25,26], and the latest work has shown a multi-PLD technique that gauges CBF and ATT, building regional ATT parametric maps to better display pathological tissue[27]. Single-PLD ASL is often sufficient for rapid evaluation of steno-occlusive disease hemodynamics, whereas multi-PLD potentially increases CBF accuracy and provides regional ATT information, and the ATT artefacts can be corrected[10].

Previous studies have shown various findings regarding CBF patterns in the contralateral hemisphere of ICAO patients. For example, one study reported no significant difference in grey matter CBF within the MCA territory between the hemisphere contralateral to the ICAO and a matched control group[16]. Conversely, Bokkers *et al*[17] reported

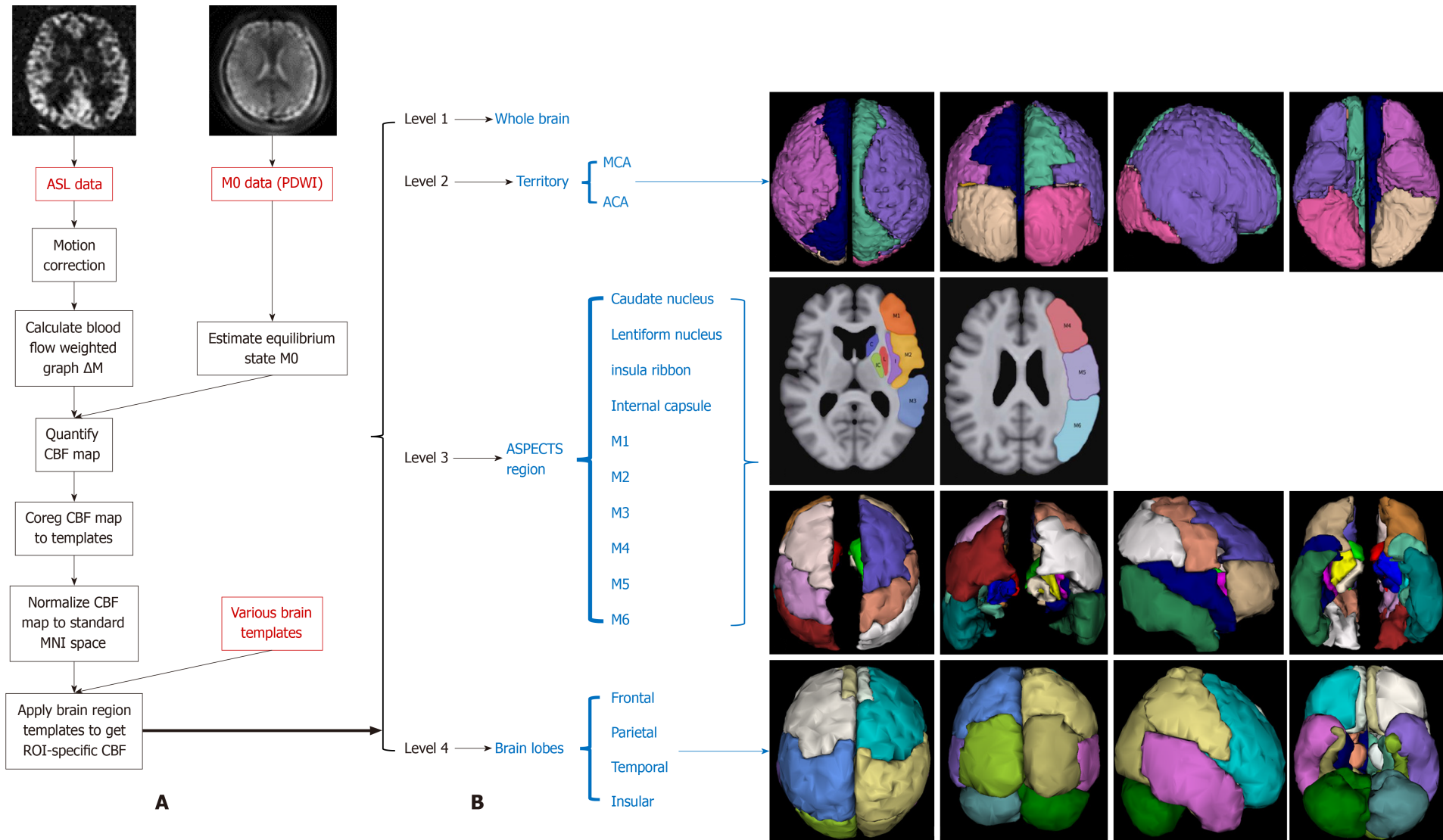


Figure 2 Data processing flow chart and brain segmentation diagram. A: Dr Brain's software arterial spin labeling module processing flow diagram; B: Segmentation brain structure of regions of interest. ASL: Arterial spin labeling; PDWI: Proton density weighted image; CBF: Cerebral blood flow; ROI: Region of interest; ASPECTS: Alberta Stroke Programme Early Computed Tomography Score; MCA: Middle cerebral artery; ACA: Anterior cerebral artery.

significantly lower CBF in the anterior frontal region of the nonoccluded hemisphere in ICAO patients than in controls [17]. Additionally, Hartkamp *et al*[3] demonstrated that the CVR was significantly lower in the ACA and MCA territories of the nonoccluded hemisphere in ICAO patients than in control subjects[13]. Given these discrepancies in previous findings, the results of our current study hold particular significance. We found that the CBF was significantly lower in some ASPECTS areas, such as the lower CBF in the caudate nucleus and internal capsule at PLD 1.5 s and in M6 at PLD 2.5 s, than in the control subjects. Furthermore, we observed that the CBF at PLD 1.5 s was significantly lower than that at PLD 2.5 s. The difference in CBF between PLD 1.5 s and PLD 2.5 s in the contralateral hemisphere represents the existence of slow flow and redistribution to compensate for ischemia. Occlusion of an artery results in a decrease in pressure in that territory, and this pressure gradient will cause blood to flow from healthy arteries to the territory of the occluded artery. Because the collateral blood flow path is long, when the blood flow arrives late, it cannot be detected with a short PLD, and the CBF measured with a long PLD can truly reflect cerebral perfusion. These findings suggest that unilateral ICAO not only affects the occluded side but also triggers regional redistribution of CBF in the contralateral hemisphere to compensate for cerebral ischemia. This finding was not recognized in the past because of the lack of detailed segmentation of brain regions.

In our current study, patients with internal ICAO presented with a spectrum of clinical manifestations ranging from asymptomatic to TIA to small infarcts within the MCA territory. Despite similar vascular occlusions, outcomes vary significantly on the basis of the ability to recruit collateral pathways that restore blood flow to the ischemic region during the minutes and hours after an acute event[9,11]. Collateral blood flow plays a crucial role in steno-occlusive ICA disease by preventing irreversible ischemic damage[3]. All patients in this study received collateral compensation, either through the primary pathway of the circle of Willis or secondary pathways involving the leptomeningeal and ophthalmic arteries or through neovascularization. Different clinical manifestations indicate that the quality of collateral status varies widely in patients with ICAO. A previous study suggested that the collection of secondary collateral is related to more severe damage, and its existence might be viewed as a marker of insufficiency of the primary collateral routes[28,29]. Owing to the limited sample size in this study, we were unable to explore collateral circulation extensively or assess differences in CBF according to symptoms, which will be a critical direction for future research.

Due to the limited sample size in our study, caution is warranted when interpreting and generalizing the current results to other populations. Future studies will continue to accumulate larger samples to increase the robustness and applicability of the findings. The CBF measured in our study primarily reflects a combination of regional brain grey and white matter. It is known that CBF values differ between grey and white matter, with generally lower CBF values observed in white matter than in grey matter[11]. Therefore, the CBF values reported in our study may be lower than those reported in previous studies that focused predominantly on grey matter[16]. However, this difference does not compromise the reliability of our findings. Nevertheless, our results hold clinical significance by providing a foundational understanding for further research and informing clinical therapeutic strategies.

CONCLUSION

In conclusion, unilateral ICAO results in hypoperfusion in the global and MCA territories, affecting most ASPECTS areas on the occluded side. The ACA territory was not significantly affected. Perfusion deficits were also observed in some ASPECTS areas on the nonoccluded side. Using a single PLD of 1.5 seconds underestimates regional CBF; dual PLD settings prove more suitable for accurate CBF quantification in ICAO cases.

FOOTNOTES

Author contributions: Ding D designed the research study; Zhang YY and Liang WB analyzed the data; Zhang GR analyzed the data and wrote the manuscript. All authors have read and approve the final manuscript.

Supported by The Key Research and Development Program Projects of Shaanxi Province of China, No. S2023-YF-YBSF-0273; and Natural Science Foundation of Shaanxi Province of China, No. 2022JQ-900.

Institutional review board statement: The study was reviewed and approved by the Second Affiliated Hospital of Xi'an Jiaotong University Institutional Review Board, (Approval No. 2022156).

Informed consent statement: All study participants, or their legal guardian, provided informed written consent prior to study enrollment.

Conflict-of-interest statement: No potential conflict of interest was reported by the authors.

Data sharing statement: Technical appendix, statistical code, and dataset available from the corresponding author at hequren521@163.com. Data sharing consent was not obtained but the presented data are anonymized and risk of identification is low.

STROBE statement: The authors have read the STROBE Statement – checklist of items, and the manuscript was prepared and revised according to the STROBE Statement – checklist of items.

Open-Access: This article is an open-access article that was selected by an in-house editor and fully peer-reviewed by external reviewers.

It is distributed in accordance with the Creative Commons Attribution NonCommercial (CC BY-NC 4.0) license, which permits others to distribute, remix, adapt, build upon this work non-commercially, and license their derivative works on different terms, provided the original work is properly cited and the use is non-commercial. See: <https://creativecommons.org/licenses/by-nc/4.0/>

Country of origin: China

ORCID number: Dun Ding [0009-0004-8736-1331](https://orcid.org/0009-0004-8736-1331).

S-Editor: Liu H

L-Editor: A

P-Editor: Zhao YQ

REFERENCES

- 1 **Flaherty ML**, Flemming KD, McClelland R, Jorgensen NW, Brown RD Jr. Population-based study of symptomatic internal carotid artery occlusion: incidence and long-term follow-up. *Stroke* 2004; **35**: e349-e352 [PMID: [15232124](https://pubmed.ncbi.nlm.nih.gov/15232124/) DOI: [10.1161/01.STR.0000135024.54608.3f](https://doi.org/10.1161/01.STR.0000135024.54608.3f)]
- 2 **Paciaroni M**, Caso V, Venti M, Milia P, Kappelle LJ, Silvestrelli G, Palmerini F, Acciarresi M, Sebastianelli M, Agnelli G. Outcome in patients with stroke associated with internal carotid artery occlusion. *Cerebrovasc Dis* 2005; **20**: 108-113 [PMID: [16006758](https://pubmed.ncbi.nlm.nih.gov/16006758/) DOI: [10.1159/000086800](https://doi.org/10.1159/000086800)]
- 3 **Hartkamp NS**, Petersen ET, Chappell MA, Okell TW, Uyttenboogaart M, Zeebregts CJ, Bokkers RP. Relationship between haemodynamic impairment and collateral blood flow in carotid artery disease. *J Cereb Blood Flow Metab* 2018; **38**: 2021-2032 [PMID: [28776469](https://pubmed.ncbi.nlm.nih.gov/28776469/) DOI: [10.1177/0271678X17724027](https://doi.org/10.1177/0271678X17724027)]
- 4 **Malhotra K**, Goyal N, Tsivgoulis G. Internal Carotid Artery Occlusion: Pathophysiology, Diagnosis, and Management. *Curr Atheroscler Rep* 2017; **19**: 41 [PMID: [28861849](https://pubmed.ncbi.nlm.nih.gov/28861849/) DOI: [10.1007/s11883-017-0677-7](https://doi.org/10.1007/s11883-017-0677-7)]
- 5 **Barber PA**, Demchuk AM, Zhang J, Buchan AM. Validity and reliability of a quantitative computed tomography score in predicting outcome of hyperacute stroke before thrombolytic therapy. ASPECTS Study Group. Alberta Stroke Programme Early CT Score. *Lancet* 2000; **355**: 1670-1674 [PMID: [10905241](https://pubmed.ncbi.nlm.nih.gov/10905241/) DOI: [10.1016/s0140-6736\(00\)02237-6](https://doi.org/10.1016/s0140-6736(00)02237-6)]
- 6 **Sorensen C**. Randomized Assessment of Rapid Endovascular Treatment of Ischemic Stroke. *J Emerg Med* 2015; **49**: 258-259 [DOI: [10.1016/j.jemermed.2015.06.046](https://doi.org/10.1016/j.jemermed.2015.06.046)]
- 7 **Lloyd M**. A Randomized Trial of Intraarterial Treatment for Acute Ischemic Stroke. *J Emerg Med* 2015; **48**: 521 [DOI: [10.1016/j.jemermed.2015.02.026](https://doi.org/10.1016/j.jemermed.2015.02.026)]
- 8 **Saver JL**, Goyal M, Bonafe A, Diener HC, Levy EI, Pereira VM, Albers GW, Cognard C, Cohen DJ, Hacke W, Jansen O, Jovin TG, Mattle HP, Nogueira RG, Siddiqui AH, Yavagal DR, Baxter BW, Devlin TG, Lopes DK, Reddy VK, du Mesnil de Rochemont R, Singer OC, Jahan R; SWIFT PRIME Investigators. Stent-retriever thrombectomy after intravenous t-PA vs. t-PA alone in stroke. *N Engl J Med* 2015; **372**: 2285-2295 [PMID: [25882376](https://pubmed.ncbi.nlm.nih.gov/25882376/) DOI: [10.1056/NEJMoa1415061](https://doi.org/10.1056/NEJMoa1415061)]
- 9 **Alsop DC**, Detre JA, Golay X, Günther M, Hendrikse J, Hernandez-garcia L, Lu H, Macintosh BJ, Parkes LM, Smits M, van Osch MJP, Wang DJJ, Wong EC, Zaharchuk G. Recommended implementation of arterial spin-labeled perfusion MRI for clinical applications: A consensus of the ISMRM perfusion study group and the European consortium for ASL in dementia. *Magn Reson Med* 2015; **73** [DOI: [10.1002/mrm.25607](https://doi.org/10.1002/mrm.25607)]
- 10 **Lindner T**, Bolar DS, Achten E, Barkhof F, Bastos-Leite AJ, Detre JA, Golay X, Günther M, Wang DJJ, Haller S, Ingala S, Jäger HR, Jahng GH, Juttukonda MR, Keil VC, Kimura H, Ho ML, Lequin M, Lou X, Petr J, Pinter N, Pizzini FB, Smits M, Sokolska M, Zaharchuk G, Mutsaerts HJMM; on behalf of the ISMRM Perfusion Study Group. Current state and guidance on arterial spin labeling perfusion MRI in clinical neuroimaging. *Magn Reson Med* 2023; **89**: 2024-2047 [PMID: [36695294](https://pubmed.ncbi.nlm.nih.gov/36695294/) DOI: [10.1002/mrm.29572](https://doi.org/10.1002/mrm.29572)]
- 11 **Akiyama T**, Morioka T, Shimogawa T, Haga S, Sayama T, Kanazawa Y, Muraio K, Arakawa S. Arterial Spin-Labeling Magnetic Resonance Perfusion Imaging with Dual Postlabeling Delay in Internal Carotid Artery Steno-occlusion: Validation with Digital Subtraction Angiography. *J Stroke Cerebrovasc Dis* 2016; **25**: 2099-2108 [PMID: [27339943](https://pubmed.ncbi.nlm.nih.gov/27339943/) DOI: [10.1016/j.jstrokecerebrovasdis.2016.06.005](https://doi.org/10.1016/j.jstrokecerebrovasdis.2016.06.005)]
- 12 **MacIntosh BJ**, Lindsay AC, Kyliantiras I, Kuker W, Günther M, Robson MD, Kennedy J, Choudhury RP, Jezzard P. Multiple inflow pulsed arterial spin-labeling reveals delays in the arterial arrival time in minor stroke and transient ischemic attack. *AJNR Am J Neuroradiol* 2010; **31**: 1892-1894 [PMID: [20110375](https://pubmed.ncbi.nlm.nih.gov/20110375/) DOI: [10.3174/ajnr.A2008](https://doi.org/10.3174/ajnr.A2008)]
- 13 **Yun TJ**, Sohn CH, Han MH, Kang HS, Kim JE, Yoon BW, Paeng JC, Choi SH, Kim JH, Song IC, Chang KH. Effect of delayed transit time on arterial spin labeling: correlation with dynamic susceptibility contrast perfusion magnetic resonance in moyamoya disease. *Invest Radiol* 2013; **48**: 795-802 [PMID: [23764569](https://pubmed.ncbi.nlm.nih.gov/23764569/) DOI: [10.1097/RLI.0b013e3182981137](https://doi.org/10.1097/RLI.0b013e3182981137)]
- 14 **Wang R**, Yu S, Alger JR, Zuo Z, Chen J, Wang R, An J, Wang B, Zhao J, Xue R, Wang DJ. Multi-delay arterial spin labeling perfusion MRI in moyamoya disease--comparison with CT perfusion imaging. *Eur Radiol* 2014; **24**: 1135-1144 [PMID: [24557051](https://pubmed.ncbi.nlm.nih.gov/24557051/) DOI: [10.1007/s00330-014-3098-9](https://doi.org/10.1007/s00330-014-3098-9)]
- 15 **Haga S**, Morioka T, Shimogawa T, Akiyama T, Muraio K, Kanazawa Y, Sayama T, Arakawa S. Arterial Spin Labeling Perfusion Magnetic Resonance Image with Dual Postlabeling Delay: A Correlative Study with Acetazolamide Loading (123)I-Iodoamphetamine Single-Photon Emission Computed Tomography. *J Stroke Cerebrovasc Dis* 2016; **25**: 1-6 [PMID: [26387043](https://pubmed.ncbi.nlm.nih.gov/26387043/) DOI: [10.1016/j.jstrokecerebrovasdis.2015.08.025](https://doi.org/10.1016/j.jstrokecerebrovasdis.2015.08.025)]
- 16 **Hendrikse J**, van Osch MJ, Rutgers DR, Bakker CJ, Kappelle LJ, Golay X, van der Grond J. Internal carotid artery occlusion assessed at pulsed arterial spin-labeling perfusion MR imaging at multiple delay times. *Radiology* 2004; **233**: 899-904 [PMID: [15486211](https://pubmed.ncbi.nlm.nih.gov/15486211/) DOI: [10.1148/radiol.2333031276](https://doi.org/10.1148/radiol.2333031276)]
- 17 **Bokkers RP**, van Laar PJ, van de Ven KC, Kapelle LJ, Klijn CJ, Hendrikse J. Arterial spin-labeling MR imaging measurements of timing parameters in patients with a carotid artery occlusion. *AJNR Am J Neuroradiol* 2008; **29**: 1698-1703 [PMID: [18701581](https://pubmed.ncbi.nlm.nih.gov/18701581/) DOI: [10.3174/ajnr.A1232](https://doi.org/10.3174/ajnr.A1232)]
- 18 **Kluytmans M**, van der Grond J, Viergever MA. Gray matter and white matter perfusion imaging in patients with severe carotid artery lesions. *Radiology* 1998; **209**: 675-682 [PMID: [9844658](https://pubmed.ncbi.nlm.nih.gov/9844658/) DOI: [10.1148/radiology.209.3.9844658](https://doi.org/10.1148/radiology.209.3.9844658)]

- 19 **Apruzzese A**, Silvestrini M, Floris R, Vernieri F, Bozzao A, Hagberg G, Caltagirone C, Masala S, Simonetti G. Cerebral hemodynamics in asymptomatic patients with internal carotid artery occlusion: a dynamic susceptibility contrast MR and transcranial Doppler study. *AJNR Am J Neuroradiol* 2001; **22**: 1062-1067 [PMID: [11415898](#)]
- 20 **van Osch MJ**, Rutgers DR, Vonken EP, van Huffelen AC, Klijn CJ, Bakker CJ, van der Grond J. Quantitative cerebral perfusion MRI and CO2 reactivity measurements in patients with symptomatic internal carotid artery occlusion. *Neuroimage* 2002; **17**: 469-478 [PMID: [12482099](#) DOI: [10.1006/nimg.2002.1214](#)]
- 21 **Phan K**, Saleh S, Dmytriw AA, Maingard J, Barras C, Hirsch JA, Kok HK, Brooks M, Chandra RV, Asadi H. Influence of ASPECTS and endovascular thrombectomy in acute ischemic stroke: a meta-analysis. *J Neurointerv Surg* 2019; **11**: 664-669 [PMID: [30415223](#) DOI: [10.1136/neurintsurg-2018-014250](#)]
- 22 **Huo X**, Ma G, Tong X, Zhang X, Pan Y, Nguyen TN, Yuan G, Han H, Chen W, Wei M, Zhang J, Zhou Z, Yao X, Wang G, Song W, Cai X, Nan G, Li D, Wang AY, Ling W, Cai C, Wen C, Wang E, Zhang L, Jiang C, Liu Y, Liao G, Chen X, Li T, Liu S, Li J, Gao F, Ma N, Mo D, Song L, Sun X, Li X, Deng Y, Luo G, Lv M, He H, Liu A, Zhang J, Mu S, Liu L, Jing J, Nie X, Ding Z, Du W, Zhao X, Yang P, Liu L, Wang Y, Liebeskind DS, Pereira VM, Ren Z, Wang Y, Miao Z; ANGEL-ASPECT Investigators. Trial of Endovascular Therapy for Acute Ischemic Stroke with Large Infarct. *N Engl J Med* 2023; **388**: 1272-1283 [PMID: [36762852](#) DOI: [10.1056/NEJMoa2213379](#)]
- 23 **Shin DH**, Shin DJ, Kim JR. Do All ASPECT Score Regions have the Same Predictive Power for Functional Outcomes? *J Stroke Cerebrovasc Dis* 2020; **29**: 104516 [PMID: [31791651](#) DOI: [10.1016/j.jstrokecerebrovasdis.2019.104516](#)]
- 24 **Xing PF**, Zhang YW, Zhang L, Li ZF, Shen HJ, Zhang YX, Li H, Hua WL, Liu P, Liu P, Yang PF, Hong B, Deng BQ, Liu JM. Higher Baseline Cortical Score Predicts Good Outcome in Patients With Low Alberta Stroke Program Early Computed Tomography Score Treated with Endovascular Treatment. *Neurosurgery* 2021; **88**: 612-618 [PMID: [33270112](#) DOI: [10.1093/neuros/nyaa472](#)]
- 25 **Dai W**, Garcia D, de Bazelaire C, Alsop DC. Continuous flow-driven inversion for arterial spin labeling using pulsed radio frequency and gradient fields. *Magn Reson Med* 2008; **60**: 1488-1497 [PMID: [19025913](#) DOI: [10.1002/mrm.21790](#)]
- 26 **Wang DJ**, Alger JR, Qiao JX, Gunther M, Pope WB, Saver JL, Salamon N, Liebeskind DS; UCLA Stroke Investigators. Multi-delay multi-parametric arterial spin-labeled perfusion MRI in acute ischemic stroke - Comparison with dynamic susceptibility contrast enhanced perfusion imaging. *Neuroimage Clin* 2013; **3**: 1-7 [PMID: [24159561](#) DOI: [10.1016/j.nicl.2013.06.017](#)]
- 27 **Bokkers RP**, Bremmer JP, van Berckel BN, Lammertsma AA, Hendrikse J, Pluim JP, Kappelle LJ, Boellaard R, Klijn CJ. Arterial spin labeling perfusion MRI at multiple delay times: a correlative study with H(2)(15)O positron emission tomography in patients with symptomatic carotid artery occlusion. *J Cereb Blood Flow Metab* 2010; **30**: 222-229 [PMID: [19809464](#) DOI: [10.1038/jcbfm.2009.204](#)]
- 28 **Hofmeijer J**, Klijn CJ, Kappelle LJ, Van Huffelen AC, Van Gijn J. Collateral circulation *via* the ophthalmic artery or leptomeningeal vessels is associated with impaired cerebral vasoreactivity in patients with symptomatic carotid artery occlusion. *Cerebrovasc Dis* 2002; **14**: 22-26 [PMID: [12097847](#) DOI: [10.1159/000063719](#)]
- 29 **Liebeskind DS**. Collateral circulation. *Stroke* 2003; **34**: 2279-2284 [PMID: [12881609](#) DOI: [10.1161/01.STR.0000086465.41263.06](#)]

Acquired factor XIII deficiency presenting with multiple intracranial hemorrhages and right hip hematoma: A case report

Lei Wang, Ning Zhang, Dong-Cheng Liang, Hao-Ling Zhang, Le-Qing Lin

Specialty type: Radiology, nuclear medicine and medical imaging

Provenance and peer review: Unsolicited article; Externally peer reviewed.

Peer-review model: Single blind

Peer-review report's classification

Scientific Quality: Grade B

Novelty: Grade B

Creativity or Innovation: Grade B

Scientific Significance: Grade B

P-Reviewer: Zhang XF

Received: March 15, 2024

Revised: August 14, 2024

Accepted: August 27, 2024

Published online: September 28, 2024

Processing time: 195 Days and 14.5 Hours



Lei Wang, Ning Zhang, Dong-Cheng Liang, Le-Qing Lin, Department of Intensive Care Medicine, Hangzhou Normal University Affiliated Hospital, Hangzhou 310015, Zhejiang Province, China

Hao-Ling Zhang, Department of Biomedical Science, Advanced Medical and Dental Institute, University Sains Malaysia, Penang 13200, Malaysia

Co-corresponding authors: Le-Qing Lin and Hao-Ling Zhang.

Corresponding author: Le-Qing Lin, PhD, Doctor, Department of Intensive Care Medicine, Hangzhou Normal University Affiliated Hospital, No. 126 Wenzhou Road, Gongshu District, Hangzhou 310015, Zhejiang Province, China. lqxdy83641@21cn.com

Abstract

BACKGROUND

Factor XIII (FXIII) deficiency is a rare yet profound coagulopathy. FXIII plays a pivotal role in hemostasis, and deficiencies in this factor can precipitate unchecked or spontaneous hemorrhaging. Immunological assays for detecting FXIII inhibitors are indispensable for diagnosing acquired FXIII deficiency; however, the availability of suitable testing facilities is limited, resulting in prolonged turnaround times for these assays.

CASE SUMMARY

In this case study, a 53-year-old male devoid of significant medical history presented with recurrent intracranial hemorrhages and a hematoma in the right hip. Subsequent genetic analysis revealed a homozygous mutation in the *ACE* gene, confirming the diagnosis of acquired FXIII deficiency.

CONCLUSION

This case underscores the significance of considering acquired deficiencies in clotting factors when evaluating patients with unexplained bleeding episodes.

Key Words: Factor XIII deficiency; Hematoma; Spontaneous; Bleeding disorder; Intracranial hemorrhages; Case report

©The Author(s) 2024. Published by Baishideng Publishing Group Inc. All rights reserved.

Core Tip: Factor XIII (FXIII) deficiency is a rare yet profound coagulopathy. FXIII plays a pivotal role in hemostasis, and deficiencies in this factor can precipitate unchecked or spontaneous hemorrhaging. Immunological assays for detecting FXIII inhibitors are indispensable for diagnosing acquired FXIII deficiency; however, the availability of suitable testing facilities is limited, resulting in prolonged turnaround times for these assays. In this case study, a 53-year-old male devoid of significant medical history presented with recurrent intracranial hemorrhages and a hematoma in the right hip. Subsequent genetic analysis revealed a homozygous mutation in the *ACE* gene, confirming the diagnosis of acquired FXIII deficiency. This case underscores the imperative of contemplating acquired coagulopathies in individuals experiencing unexplained and recurrent hemorrhagic episodes. Furthermore, it underscores the value of thorough genetic analysis in uncovering uncommon coagulation anomalies, which can substantially influence patient care and prognosis. Subsequent investigations could delve into elucidating the pathophysiological mechanisms underpinning mutations in the *ACE* gene and their interplay with coagulation pathways. Acquired FXIII deficiency, albeit uncommon, warrants consideration in individuals presenting with inexplicable hemorrhagic episodes. Genetic testing emerges as pivotal in the diagnosis and therapeutic approach to such instances.

Citation: Wang L, Zhang N, Liang DC, Zhang HL, Lin LQ. Acquired factor XIII deficiency presenting with multiple intracranial hemorrhages and right hip hematoma: A case report. *World J Radiol* 2024; 16(9): 439-445

URL: <https://www.wjgnet.com/1949-8470/full/v16/i9/439.htm>

DOI: <https://dx.doi.org/10.4329/wjr.v16.i9.439>

INTRODUCTION

Factor XIII (FXIII) deficiency represents an uncommon and frequently overlooked congenital hemorrhagic disorder typified by compromised fibrin stabilization, leading to an elevated predisposition to spontaneous and recurrent hemorrhagic episodes[1]. Although FXIII deficiency is acknowledged for its correlation with intracranial hemorrhages, the simultaneous occurrence of bleeding in diverse anatomical locales, such as the cranium and hip, remains a clinical rarity[2].

Presented is a case involving a 53-year-old male exhibiting recurrent intracranial hemorrhages and a right hip hematoma, devoid of notable medical antecedents, ultimately diagnosed with acquired FXIII deficiency. The deficit of FXIII, a pivotal clotting factor in the terminal phases of the coagulation cascade, presents distinctive hurdles in both diagnosis and management owing to its rarity and the array of clinical manifestations it may entail.

In FXIII deficiency, intracranial hemorrhages are extensively documented, frequently resulting in profound neurological ramifications[3]. Nevertheless, the manifestation of bleeding in extracranial locales, such as the hip, adds another layer of intricacy to this case[4]. A comprehensive comprehension of the interrelationships among clotting factors and the ramifications of FXIII deficiency is imperative for elucidating the underlying mechanisms contributing to the multifocal hemorrhagic incidents observed in this instance.

Delving into this case, our aim is to illuminate the clinical intricacies of FXIII deficiency, underscoring the imperative for heightened awareness among healthcare providers to promptly diagnose and appropriately manage this rare bleeding disorder. Furthermore, this report adds to the evolving understanding of the diverse and potentially life-threatening manifestations of FXIII deficiency, ultimately fostering improved patient outcomes through enhanced diagnostic accuracy and personalized therapeutic strategies[5].

CASE PRESENTATION

Chief complaints

In February 2023, a 53-year-old male without a medical history of hypertension, diabetes, heart disease, stroke, or renal disease underwent surgery for a right hip hematoma at a local hospital. The operation, which lasted three hours, resulted in a blood loss of 100 mL, fluid administration of 2000 mL, and a urine output of 200 mL. The procedure was conducted under general anesthesia, utilizing fentanyl and propofol for sedation and analgesia. Notably, anticoagulant and antiplatelet medications were not administered.

History of present illness

In June 2023, he was hospitalized with a fever persisting for 20 days following cerebral hemorrhage surgery. The admission diagnosis encompassed intracranial infection, postoperative left temporal lobe cerebral hemorrhage, pulmonary infection, stage 2 high blood pressure (very high risk), postoperative right hip hemorrhage, and right hip skin infection.

History of past illness

The patient denied having a history of high blood pressure, diabetes, heart disease, stroke or kidney disease. Immunization history: Vaccinations have been administered in full compliance with national guidelines. The patient

denies any history of hypersensitivity to food or medications. Anticoagulant and antiplatelet agents were not utilized. Underwent inguinal hernia repair over a decade ago. The patient denies any history of trauma, blood transfusion, poisoning, or chronic medication use. There is no history of addictive substance use. The patient also reports no other medical conditions, including anemia, epistaxis, gingival or dental bleeding, or ecchymosis.

Personal and family history

Despite the absence of a family history of genetic disorders and no reported similar cases among other family members, the patient's routine blood tests, morphology, coagulation profile, liver and kidney functions, platelet aggregation, antiphospholipid antibodies, and thromboelastography revealed no significant abnormalities (Table 1).

Physical examination

The patient is alert and fully responsive. Nutritional status is robust, with normal developmental progress. There are no indications of anemia, jaundice, cyanosis, or edema. Vital signs are as follows: Body temperature 36.8 °C, pulse rate 72 beats *per* minute, respiratory rate 18 breaths per minute, and blood pressure 120/75 mmHg. No evidence of dyspnea or palpitations is observed.

Laboratory examinations

Notably, FXIII antigen testing indicated levels below the normal range (49.2%, reference range 75.2%-154.8%). Following informed consent from the spouse, peripheral venous blood samples from the patient, his brother, and son were submitted to Di'an Medical Laboratory for whole-exome sequencing. This analysis revealed a homozygous mutation in the *ACE* gene c.140A>G (p.Gln47Arg), confirmed through sanger sequencing. While the patient exhibited heterozygosity for this mutation, his brother and son tested negative, indicating an acquired condition (Table 2).

Imaging examinations

On May 24, 2023, a neuro endoscopic evacuation of a left temporal lobe hematoma was performed on the patient. However, on June 5, 2023, bilateral mydriasis developed, and a head computed tomography (CT) scan revealed significant brain swelling and midline shift, necessitating an emergency craniotomy for hematoma evacuation and left-sided decompressive craniectomy. Subsequently, the patient experienced postoperative fever, and lumbar puncture indicated intracranial infection, which was managed with meropenem and vancomycin. On June 6, a subcutaneous hematoma emerged, leading to a left temporal extradural hematoma evacuation. Despite the procedure's repetition on June 10 due to recurrence, the patient's consciousness deteriorated on June 16 (Glasgow coma scale score E1V1M3), exhibiting unequal pupils and sluggish light reflex. A CT scan revealed increased subcutaneous effusion and pronounced rightward midline shift, indicative of local brain herniation. Another hematoma evacuation was conducted, followed by ongoing intensive care unit management (Figure 1A).

During hospitalization, a decline in the patient's hemoglobin levels was observed, and on June 30, swelling at the right hip incision site was noted. Subsequent CT imaging of the hip revealed a hematoma, while a head magnetic resonance imaging unveiled new brainstem hemorrhage, subdural/epidural hematoma at the left temporoparietal region, bleeding in the anterior horn of the left lateral ventricle, and ventricular hemorrhage. Hemostatic and plasma transfusion therapies were administered to address these conditions (Figure 2 and Figure 3). Following up on July 16, a repeat head CT scan revealed increased subcutaneous bleeding in the right surgical area and a slight rise in midline shift to the right. Intermittent transfusions of cryoprecipitate were provided to enhance coagulation (Figure 1B).

FINAL DIAGNOSIS

Given the clinical presentation and genetic analysis results, the diagnosis of acquired FXIII deficiency was established for the patient.

TREATMENT

As part of the treatment regimen, weekly infusions of 10 units of cryoprecipitate were administered as prophylaxis against future bleeding episodes. From July 19, 2023, through December 29, 2023.

OUTCOME AND FOLLOW-UP

Subsequently, the patient exhibited improved consciousness, characterized by clear mentation and restored mobility.

Table 1 Changes in hemostatic parameters throughout time

FXIII antigen (%)	INR	APTT ratio	Fibrinogen (mg/dL)	
Reference ranges	75.2-154.8	0.80-1.20	24.5-31.7	1.80-4.00
At diagnosis	49.2	1.06	29.6	5.3
Last blood sample	37.7	0.98	27.3	5.14

FXIII: Factor XIII; INR: International normalized ratio; APTT: Activated partial thromboplastin time.

Table 2 Blood test

	Patient	Reference ranges
Coagulation-active factor VII (%)	90.8	50-150
Coagulation-active factor VIII (%)	170.7	50-150
Antithrombin III activity (%)	100.5	70-125
Fibrinolytic-antifibrinolytic complex (ng/mL)	1.14	< 0.85
Thrombin regulatory protein antigen (IU/mL)	12.08	3.82-13.35
Platelet count ($\times 10^9/L$)	352	125-350
Protein C activity (%)	104.7	70-140
Protein S Activity (%)	113.5	55-130
IgG (mg/dL)	9.63	8.60-17.40
IgA (mg/dL)	1.94	1.00-4.20
IgM (mg/dL)	0.63	0.30-2.20
C3 (mg/dL)	0.70-1.40	1.1
C4 (mg/dL)	0.10-0.40	0.32

DISCUSSION

Acquired FXIII deficiency originates from the production of FXIII inhibitors by autoantibodies targeting FXIII[6]. This autoimmune phenomenon typically emerges in individuals of middle to advanced age, with a tendency towards onset in older individuals and no apparent gender predilection. Patients afflicted with acquired FXIII deficiency, characterized by the presence of FXIII inhibitors, are predisposed to severe episodes of bleeding. These inhibitors can hinder the activity, function, or alter the reactivity of fibrin substrates by obstructing the activation of FXI[7]. Consequently, this interference results in abnormal cross-linking between fibrin monomers, leading to the formation of unstable plasma fibrin clots. Clinically, this manifests as severe and recurrent spontaneous bleeding, spanning various anatomical sites[8]. Common presentations encompass bruising of the skin and mucosa, hematoma formation in soft tissues and muscles, visceral bleeding, postoperative bleeding delays, and, in severe instances, intracranial hemorrhage[9]. The wide array of bleeding manifestations underscores the intricate nature of acquired FXIII deficiency, underscoring the necessity for clinicians to exercise vigilance in identifying and managing this condition[10,11]. The profound impact on hemostasis, demonstrated by the instability of fibrin clots, mandates a multidisciplinary approach for accurate diagnosis, treatment, and ongoing patient care[12].

This case highlights a distinct occurrence of acquired FXIII deficiency, an uncommon hematological anomaly often eclipsed by more prevalent coagulation disorders. FXIII serves as a pivotal enzyme in the clotting cascade, crucial for fibrin cross-linkage and clot stabilization. Deficiency in FXIII can precipitate severe and recurring episodes of bleeding, mirroring the observations in our patient[13]. The patient's recurrent intracranial hemorrhages, notably following surgical procedures, alongside the emergence of a right hip hematoma in the absence of significant medical or familial bleeding history, presented a diagnostic conundrum. The lack of conventional risk factors such as hypertension, diabetes, or prior cerebrovascular ailments further added complexity to the clinical scenario. The persistent recurrence of hemorrhagic events despite surgical interventions and routine postoperative management suggested an underlying coagulopathic condition[14].

In the context of FXIII deficiency, intracranial hemorrhage poses a particularly grave risk due to its high mortality and morbidity rates[15]. The patient's deteriorating neurological status, marked by declining Glasgow coma scale scores and pupil asymmetry, warranted multiple neurosurgical interventions. The persistence of hemorrhagic events despite these interventions underscored the necessity for reevaluation of diagnosis and treatment strategies. The definitive diagnosis of acquired FXIII deficiency was established through genetic analysis, revealing a homozygous mutation in the *ACE* gene.

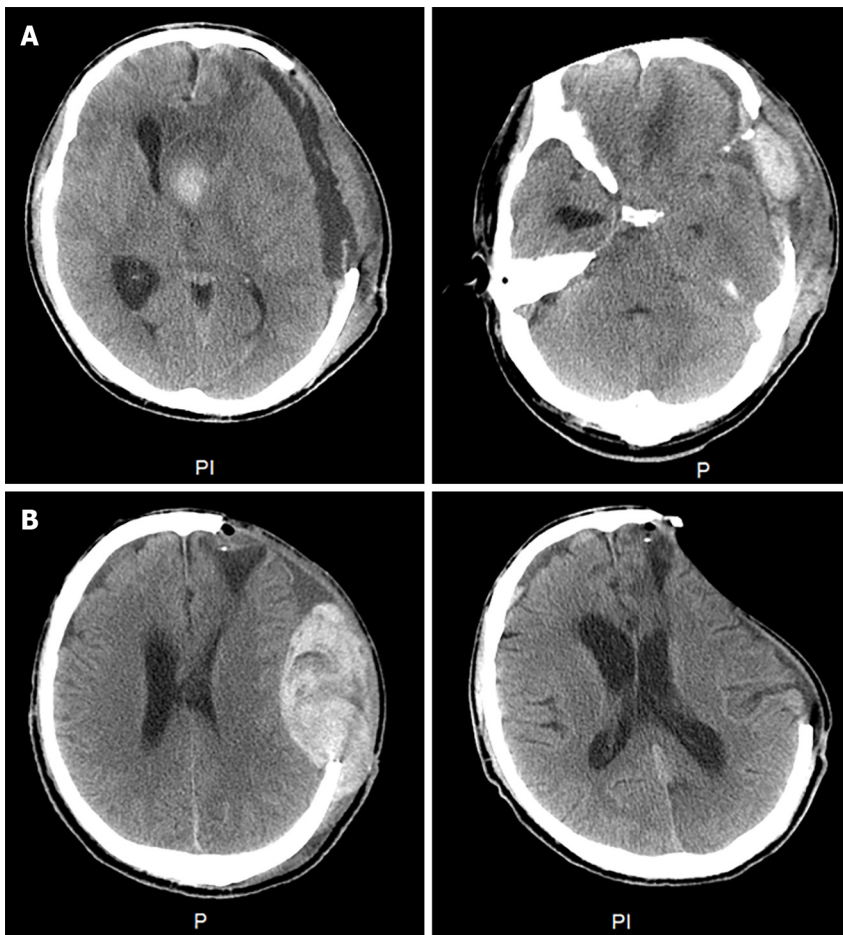


Figure 1 Head computed tomography scan. A: Head computed tomography scan at the time of initial treatment. The left side is a preoperative image. The right side is head computed tomography scan at rebleeding on day 4; B: Head computed tomography scan during treatment. The left side is a preoperative image. The right side is a postoperative image.

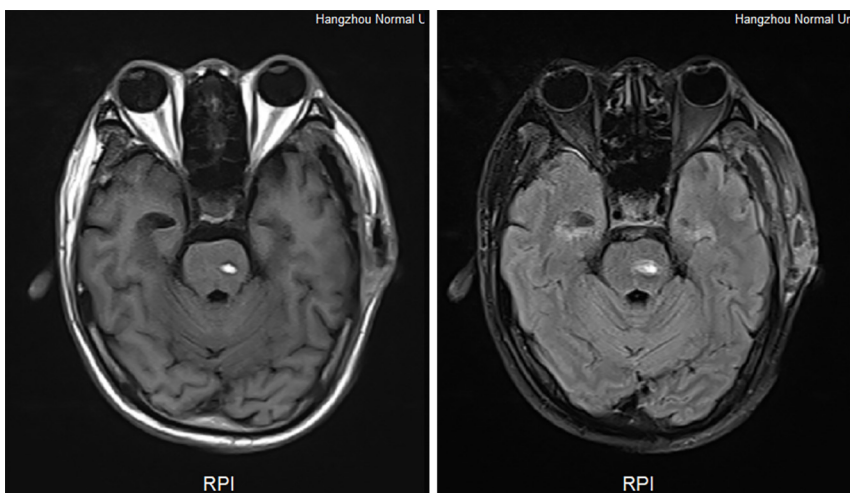


Figure 2 Head magnetic resonance imaging scan at rebleeding on day 18. The left side is T1-weighted imaging. The right side is T2-weighted imaging.

Notably, this mutation is not conventionally associated with coagulation disorders, suggesting a unique phenotype or a secondary mutation influencing FXIII levels. The patient's heterozygous genotype and the absence of the mutation in his immediate family members imply an acquired rather than an inherited etiology [16].

The management of acquired FXIII deficiency predominantly revolves around FXIII replacement therapy. Our patient exhibited a favorable response to prophylactic cryoprecipitate transfusions, which provide a concentrated source of FXIII [17]. The cessation of hemorrhagic episodes following the initiation of this treatment underscores the critical role of timely diagnosis and appropriate therapeutic interventions in such clinical scenarios. Additionally, this case prompts critical

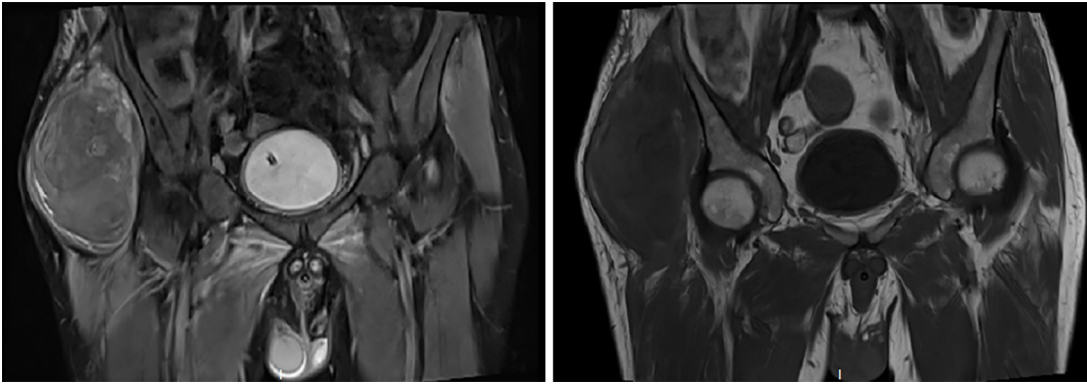


Figure 3 Right hip magnetic resonance imaging scan at rebleeding on day 18. The left side is T1-weighted imaging. The right side is T2-weighted imaging.

inquiry into the necessity of screening for coagulation disorders in individuals presenting with unexplained intracranial hemorrhage[18]. Existing guidelines typically do not advocate for routine coagulation factor assessments in the absence of suggestive clinical history[19]. Nonetheless, this case serves as a poignant reminder that rare coagulopathies may manifest even in patients lacking significant bleeding antecedents or identifiable risk factors.

Moreover, the treatment of individuals afflicted with acquired FXIII deficiency necessitates a multidisciplinary strategy, engaging hematologists, neurosurgeons, and critical care experts. Balancing the risk of recurrent hemorrhage, the prospect of immune-mediated inhibitor formation, and the requirement for sustained prophylactic measures demands meticulous consideration of the patient's holistic well-being and quality of life[20].

In conclusion, this case underscores the imperative of contemplating acquired coagulopathies in individuals experiencing unexplained and recurrent hemorrhagic episodes. Furthermore, it underscores the value of thorough genetic analysis in uncovering uncommon coagulation anomalies, which can substantially influence patient care and prognosis. Subsequent investigations could delve into elucidating the pathophysiological mechanisms underpinning mutations in the *ACE* gene and their interplay with coagulation pathways[21].

CONCLUSION

Acquired FXIII deficiency, albeit uncommon, warrants consideration in individuals presenting with inexplicable hemorrhagic episodes. Genetic testing emerges as pivotal in the diagnosis and therapeutic approach to such instances.

FOOTNOTES

Author contributions: Wang L conducted case data collection and initial analysis; Zhang N provided expert medical consultation and recommendations, particularly concerning the diagnosis and management of coagulation factor XIII deficiency; Liang DC executed imaging analysis and interpretation, with a focus on the radiological findings of intracranial hemorrhage and hip hematoma; Zhang HL and Lin LQ undertook a comprehensive review and revision of the manuscript to ensure academic rigor and integrity.

Supported by the Medical and Health Science Foundation of Zhejiang, No. 2023KY186; Hangzhou Science and Technology Development Plan Guide Project, No. 20220919Y023; and the Hangzhou Medical Key Discipline Construction Program, No. 2021.

Informed consent statement: Consent for publication of the case details was obtained from the patient's spouse.

Conflict-of-interest statement: The authors declare that they have no conflict of interest.

CARE Checklist (2016) statement: The authors have read the CARE Checklist (2016), and the manuscript was prepared and revised according to the CARE Checklist (2016).

Open-Access: This article is an open-access article that was selected by an in-house editor and fully peer-reviewed by external reviewers. It is distributed in accordance with the Creative Commons Attribution NonCommercial (CC BY-NC 4.0) license, which permits others to distribute, remix, adapt, build upon this work non-commercially, and license their derivative works on different terms, provided the original work is properly cited and the use is non-commercial. See: <https://creativecommons.org/licenses/by-nc/4.0/>

Country of origin: China

ORCID number: Le-Qing Lin [0009-0008-1220-7187](https://orcid.org/0009-0008-1220-7187).

S-Editor: Fan M

L-Editor: A

P-Editor: Yu HG

REFERENCES

- 1 **Inbal A**, Lubetsky A, Krapp T, Castel D, Shaish A, Dickneite G, Modis L, Muszbek L, Inbal A. Impaired wound healing in factor XIII deficient mice. *Thromb Haemost* 2005; **94**: 432-437 [PMID: [16113836](#) DOI: [10.1160/TH05-04-0291](#)]
- 2 **Dorgalaleh A**. The History of Factor XIII Deficiency. *Semin Thromb Hemost* 2024; **50**: 34-42 [PMID: [36706781](#) DOI: [10.1055/s-0043-1761217](#)]
- 3 **Yan MTS**, Rydz N, Goodyear D, Sholzberg M. Acquired factor XIII deficiency: A review. *Transfus Apher Sci* 2018; **57**: 724-730 [PMID: [30446212](#) DOI: [10.1016/j.transci.2018.10.013](#)]
- 4 **Sandouno TM**, Bachir H, Alaoui HB, Hamaz S, Eloumri AA, Berrimi M, Serraj K. Acute spontaneous subdural hematoma as an inaugural presentation of systemic lupus erythematosus with acquired factor XIII deficiency: a case report. *Pan Afr Med J* 2021; **39**: 207 [PMID: [34603588](#) DOI: [10.11604/pamj.2021.39.207.26336](#)]
- 5 **Ichinose A**; Japanese Collaborative Research Group on AH13. Autoimmune acquired factor XIII deficiency due to anti-factor XIII/13 antibodies: A summary of 93 patients. *Blood Rev* 2017; **31**: 37-45 [PMID: [27542511](#) DOI: [10.1016/j.blre.2016.08.002](#)]
- 6 **Aljabry M**. Factor XIII deficiency in the Saudi population, an underestimated bleeding risk. Review article and an illustrative case report with dental complications. *Saudi Dent J* 2023; **35**: 305-309 [PMID: [37251713](#) DOI: [10.1016/j.sdentj.2023.03.015](#)]
- 7 **Di Micco P**, Gussoni G, Pieralli F, Campanini M, Dentali F, Fontanella A. Acquired Factor XIII Deficiency Inducing Recurrent and Fatal Bleeding, Description of a Case. *J Blood Med* 2020; **11**: 43-45 [PMID: [32099500](#) DOI: [10.2147/JBM.S232115](#)]
- 8 **Benedetto C**, Marozio L, Tavella AM, Salton L, Grivon S, Di Giampaolo F. Coagulation disorders in pregnancy: acquired and inherited thrombophilias. *Ann N Y Acad Sci* 2010; **1205**: 106-117 [PMID: [20840261](#) DOI: [10.1111/j.1749-6632.2010.05674.x](#)]
- 9 **Schroeder V**, Kohler HP. Factor XIII deficiency: an update. *Semin Thromb Hemost* 2013; **39**: 632-641 [PMID: [23929307](#) DOI: [10.1055/s-0033-1353392](#)]
- 10 **Muszbek L**, Bereczky Z, Bagoly Z, Komáromi I, Katona É. Factor XIII: a coagulation factor with multiple plasmatic and cellular functions. *Physiol Rev* 2011; **91**: 931-972 [PMID: [21742792](#) DOI: [10.1152/physrev.00016.2010](#)]
- 11 **Fadoo Z**, Merchant Q, Rehman KA. New developments in the management of congenital Factor XIII deficiency. *J Blood Med* 2013; **4**: 65-73 [PMID: [23761984](#) DOI: [10.2147/JBM.S32693](#)]
- 12 **Hethershaw EL**, Cilia La Corte AL, Duval C, Ali M, Grant PJ, Ariëns RA, Philippou H. The effect of blood coagulation factor XIII on fibrin clot structure and fibrinolysis. *J Thromb Haemost* 2014; **12**: 197-205 [PMID: [24261582](#) DOI: [10.1111/jth.12455](#)]
- 13 **Schroeder V**, Kohler HP. New developments in the area of factor XIII. *J Thromb Haemost* 2013; **11**: 234-244 [PMID: [23279671](#) DOI: [10.1111/jth.12074](#)]
- 14 **Ivaskevicius V**, Windyga J, Baran B, Schroeder V, Junen J, Bykowska K, Seifried E, Kohler HP, Oldenburg J. Phenotype-genotype correlation in eight Polish patients with inherited Factor XIII deficiency: identification of three novel mutations. *Haemophilia* 2007; **13**: 649-657 [PMID: [17880458](#) DOI: [10.1111/j.1365-2516.2007.01517.x](#)]
- 15 **Marco A**, Marco P. Autoimmune Acquired Factor XIII Deficiency: A Case Report. *J Blood Med* 2021; **12**: 63-68 [PMID: [33603527](#) DOI: [10.2147/JBM.S288634](#)]
- 16 **Muszbek L**, Péntes K, Katona É. Auto- and alloantibodies against factor XIII: laboratory diagnosis and clinical consequences. *J Thromb Haemost* 2018; **16**: 822-832 [PMID: [29460500](#) DOI: [10.1111/jth.13982](#)]
- 17 **Ogawa Y**. [Acquired autoimmune coagulation factor XIII/13 deficiency]. *Rinsho Ketsueki* 2020; **61**: 799-808 [PMID: [32759568](#) DOI: [10.11406/rinketsu.61.799](#)]
- 18 **Ariëns RA**, Lai TS, Weisel JW, Greenberg CS, Grant PJ. Role of factor XIII in fibrin clot formation and effects of genetic polymorphisms. *Blood* 2002; **100**: 743-754 [PMID: [12130481](#) DOI: [10.1182/blood.v100.3.743](#)]
- 19 **Ejaz M**, Saleem A, Ali N, Tariq F. Factor XIII deficiency with intracranial haemorrhage. *BMJ Case Rep* 2019; **12** [PMID: [31451452](#) DOI: [10.1136/bcr-2018-228682](#)]
- 20 **Pelcovits A**, Schiffman F, Niroula R. Factor XIII Deficiency: A Review of Clinical Presentation and Management. *Hematol Oncol Clin North Am* 2021; **35**: 1171-1180 [PMID: [34607717](#) DOI: [10.1016/j.hoc.2021.07.009](#)]
- 21 **Shahraki H**, Dorgalaleh A, Fathi M, Tabibian S, Teimourian S, Mollanoori H, Khiabani A, Zaker F. How to Assess Founder Effect in Patients with Congenital Factor XIII Deficiency. *Int J Hematol Oncol Stem Cell Res* 2020; **14**: 265-273 [PMID: [33603988](#) DOI: [10.18502/ijhoscr.v14i4.4480](#)]

Myelin oligodendrocyte glycoprotein-associated transverse myelitis after SARS-CoV-2 infection: A case report

Jian-Rong Zheng, Jun-Lei Chang, Jun Hu, Zhi-Jian Lin, Kai-Hua Lin, Bi-Hua Lu, Xu-Hui Chen, Zhi-Gang Liu

Specialty type: Radiology, nuclear medicine and medical imaging

Provenance and peer review: Unsolicited article; Externally peer reviewed.

Peer-review model: Single blind

Peer-review report's classification

Scientific Quality: Grade C

Novelty: Grade C

Creativity or Innovation: Grade C

Scientific Significance: Grade B

P-Reviewer: Guo ZX

Received: April 2, 2024

Revised: August 23, 2024

Accepted: September 10, 2024

Published online: September 28, 2024

Processing time: 177 Days and 15.2 Hours



Jian-Rong Zheng, Jun Hu, Zhi-Jian Lin, Kai-Hua Lin, Xu-Hui Chen, Department of Neurology, Peking University Shenzhen Hospital, Shenzhen 518000, Guangdong Province, China

Jian-Rong Zheng, Department of Neurology, Shenzhen Xinhua Hospital, Shenzhen 518000, Guangdong Province, China

Jun-Lei Chang, Institute of Biomedicine and Biotechnology, Shenzhen Institute of Advanced Technology, Chinese Academy of Sciences, Shenzhen 518000, Guangdong Province, China

Bi-Hua Lu, Department of Neurology, The Sixth People's Hospital of Foshan Nanhai District, Foshan 528000, Guangdong Province, China

Zhi-Gang Liu, Laboratory of Functional Chemistry and Nutrition of Food, Northwest A&F University, Yangling 712100, Shaanxi Province, China

Co-corresponding authors: Xu-Hui Chen and Zhi-Gang Liu.

Corresponding author: Xu-Hui Chen, MD, Associate Chief Physician, Department of Neurology, Peking University Shenzhen Hospital, No. 1120 Lianhua Road, Futian District, Shenzhen 518000, Guangdong Province, China. xuhuichen@pkusz.com

Abstract

BACKGROUND

Cases of myelin oligodendrocyte glycoprotein (MOG) antibody-related disease have a history of coronavirus disease 2019 infection or its vaccination before disease onset. Severe acute respiratory syndrome virus 2 (SARS-CoV-2) infection has been considered to be a trigger of central nervous system autoimmune diseases.

CASE SUMMARY

Here we report a 20-year male with MOG-associated transverse myelitis after a SARS-CoV-2 infection. The patient received a near-complete recovery after standard immunological treatments.

CONCLUSION

Attention should be paid to the evaluation of typical or atypical neurological symptoms that may be triggered by SARS-CoV-2 infection.

Key Words: Myelin oligodendrocyte glycoprotein antibody-associated encephalomyelitis;

Myelin oligodendrocyte glycoprotein antibody-associated disease; SARS-CoV-2; COVID-19; Case report

©The Author(s) 2024. Published by Baishideng Publishing Group Inc. All rights reserved.

Core Tip: Here we present a case of myelin oligodendrocyte glycoprotein-associated disease after severe acute respiratory syndrome coronavirus type 2 (SARS-CoV-2) infection. The patient received a near-complete recovery after standard immunological treatments. We suggest that attention should be paid to the evaluation of typical or atypical neurological symptoms that may be triggered by SARS-CoV-2 infection, and focus on the exclusion of coexisting autoimmune reactions or diseases.

Citation: Zheng JR, Chang JL, Hu J, Lin ZJ, Lin KH, Lu BH, Chen XH, Liu ZG. Myelin oligodendrocyte glycoprotein-associated transverse myelitis after SARS-CoV-2 infection: A case report. *World J Radiol* 2024; 16(9): 446-452

URL: <https://www.wjgnet.com/1949-8470/full/v16/i9/446.htm>

DOI: <https://dx.doi.org/10.4329/wjr.v16.i9.446>

INTRODUCTION

Many cases of coronavirus disease 2019 (COVID-19) have been reported with co-existing neurological symptoms. Several co-existing autoimmune neurological diseases, including central (limbic and brainstem encephalitis, acute disseminated encephalomyelitis, and myelitis) and peripheral neurological diseases (Guillain-Barré and Miller fisher syndromes), have been reported[1]. The correlation between COVID-19 and neurological symptoms is yet not clear, with the possible mechanisms of autoimmunity and inflammation. Currently, the diagnosis standards and treatment options for COVID-related neurological diseases are ambiguous, leading to a possibly underestimated number of total cases and posing new challenges for clinical work in the neurological discipline.

Myelin oligodendrocyte glycoprotein (MOG) is a member of the immunoglobulin superfamily[2]. It is specifically expressed on the membrane surface of oligodendrocytes and the outermost layer of the myelin sheath, and its expression level usually reflects the degree of myelination. MOG has been proven to be one of the most common antigens in demyelinating diseases. MOG antibody-related disease (MOG-AD) accounts for 1.2% to 6.5% of all adult demyelinating syndromes, with acute disseminated encephalomyelitis, optic neuritis and myelitis as the common clinical symptoms[3].

In this case report, we report a case of rapidly progressing acute myelitis presented with motor sensory disorders of both lower extremities and urinary retention after severe acute respiratory syndrome coronavirus type 2 (SARS-CoV-2) infection. The patient was further diagnosed with MOG-associated transverse myelitis (TM) after being tested positive for anti-MOG-IgG in the cerebrospinal fluid (CSF). We also reviewed published cases of MOG-AD associated with SARS-CoV-2 infection, intending to improve clinicians' understanding of MOG-AD after SARS-CoV-2.

CASE PRESENTATION

Chief complaints

A 20-year-old young male of Asian ethnicity was admitted to our hospital for lower limb weakness and sensory disturbance and urinary retention for 3 days.

History of present illness

Eight days prior to admission, the patient developed weakness and a fever with chills, and was diagnosed with COVID-19 after confirmation of SARS-CoV-2 infection by a pharyngeal swab reverse transcription-polymerase chain reaction test. No other symptoms such as cough, sputum, chest tightness, or shortness of breath were present at that time. After 5 days of consistent fever, the patient began to develop symmetrical weakness in lower extremities, accompanied by symmetrical sensory impairment below the waist, inability to walk by himself, and difficulty in urination.

History of past illness

The patient was previously healthy.

Personal and family history

He had previously received the SARS-CoV-2 adenovirus vaccine before infection and had no symptoms or discomfort at the time of vaccination.

Physical examination

At administration, the patient had a fever of 38.5 °C. Neurological examination revealed pyramidal tract impairment and

sensory abnormalities, including decreased muscle strength in both legs (3/5 in medical research council scale of muscle strength rating system) and diminished tendon reflex, accompanied with hypesthesia below the T9 dermatome level [modified Rankin scale (mRS) 4 and expanded disability status scale (EDSS) 7.0]. His abdominal wall reflexes were elicited only at the left T7-T8 plane. And urinary retention resulted in his need for urinary catheterization.

Laboratory examinations

The initial laboratory tests showed an elevated level of white blood cell count ($15.69 \times 10^9/L$), C-reactive protein (84.590 mg/L), D-dimer (1.17 mg/L, fibrinogen equivalent units), and erythrocyte sedimentation rate (52 mm/hour), with no other general examination remarkable. A lumbar puncture was therefore performed. The pressure of the cerebral spinal fluid was remarkably over 330 mmH₂O, with a raised white blood cell count ($66 \times 10^6/L$), mononuclear cell percentage (91%), and elevated protein level (0.26 g/L). Oligoclonal bands were seen in both serum and CSF with the same pattern. A CSF test was positive for anti-MOG antibody (titration 1:32), while was negative for other antibodies, especially anti-aquaporin 4 antibodies.

Imaging examinations

A magnetic resonance imaging (MRI) scan of the spinal cord revealed an abnormal signal in the C3-C6, T7-T8 segment resembling demyelinating lesion (Figure 1), presuming a diagnosis of TM. Neither typical glassy nor solid shadows were observed in his lung from an immediate chest computerized tomography scan (Figure 2).

FINAL DIAGNOSIS

Based on this patient's recent history of SARS-CoV-2 infection, clinical presentation, laboratory findings, MRI, and CSF analysis, the diagnosis of MOG-TM was supported.

TREATMENT

Pulsed methylprednisolone therapy [1000 mg × 3 days; 500 mg × 3 days; 250 mg × 3 days; 120 mg × 3 days followed by 65 mg (1 mg/kg/day) orally] was administered by our medical team.

OUTCOME AND FOLLOW-UP

The patient responded well to steroid treatment with gradual improvements in symptoms. After a one-week of treatment, the patient's muscle strength of the lower limbs was restored (4 +/5 in medical research council scale of muscle strength rating system score). He could walk independently and was mostly self-care, despite slight sensory abnormalities and mild urinary retention, for which a catheter was still needed. At re-exam in the second week, an MRI scan showed reduced volume of the abnormal signals compared with the previous scan (Figure 3). At discharge, the mRS score was at 2, and the EDSS score was at 3.5. A prescription of a long-term oral prednisolone until further reevaluation was given, with a slow tapering plan.

DISCUSSION

With the accumulation of cases affected by the COVID-19 pandemic, studies have found that a range of neurological complications such as cerebrovascular disease, encephalitis, and myelitis could occur in addition to the respiratory and cardiovascular symptoms[4-7], which is gaining more attention in clinical practice. COVID-19 related myelitis was first reported by Zhao *et al*[8], despite a lack in CSF and spinal MRI findings.

The number of reported MOG-AD cases seems slightly higher than that in the pre-pandemic period of COVID-19, and its coincidental occurrence should not be neglected[9,10]. COVID-19-associated MOG-AD can occur in patients of all ages, but is more commonly seen in younger patients. In these patients, myelitis or TM is usually accompanied by encephalitis (acute disseminated encephalomyelitis) and optic neuritis[10,11]. Our patient presented with typical neurological symptoms including lower extremity weakness, sensory impairment and urination retention, which is consistent with the reported cases. Similar to other previously reported cases, in the cross-sectional MRI scans of this reported patient, the spinal cord lesion showed a typical "cloudy" and "H-shaped" pattern[11-14]. A recent multimodal meta-analysis exhibited that both structural and functional alterations of right superior temporal gyrus, left insula and right orbito-frontal cortex have been found in COVID-19 patients compared with healthy persons. This study prompted that the cortex is more susceptible than the white matter in brain after SARS-CoV-2 infection, which may accordingly make an explanation why patients with SARS-CoV-2 associated MOG-TM mainly manifest the dysfunction of the grey matter in spinal cord[15]. However, direct evidence especially the multimodal imaging and autopsy examination of the spinal cord demonstrating the pathophysiological link, is still lacking to date, and further clinical and preclinical studies are still needed to reveal the underlying mechanisms of MOG-TM associated with COVID-19.



Figure 2 A chest computerized tomography scan of the patient. Chest computerized tomography showed mild interstitial lesions in both lower lungs without the typical ground glass-like or solid shadows of severe acute respiratory syndrome virus 2 infection.



Figure 3 Magnetic resonance imaging scan of spinal cord one week after methylprednisolone treatment. A: Sagittal T2WI sequence of the cervical spine shows a reduced range of long T2 signals in C3-C6 and T7-T8 segments compared with the previous one (arrows); B: Sagittal T2WI sequence of the lumbar spine: A reduced range of long T2 signals in T7-T8 segments compared with the previous one (arrows); C: Sagittal enhancement sequence of the cervical spine: No abnormal enhancement was seen; D: Sagittal enhancement sequence of the lumbar spine: No abnormal enhancement was seen.

inflammatory markers [such as C-reactive protein, interleukin (IL)-2R, IL-6, IL-10, tumor necrosis factor- α] are significantly elevated in patients with severe COVID-19 infection, which underlie the cytokine inflammatory storm which leads to hyperpyrexia and respiratory failure[21,22]. However, in this reported case, neurological damage is much more evident than respiratory symptoms, suggesting that anti-MOG antibody activation, rather than inflammation itself, was playing a pivotal role. In addition, MOG-AD was found to be closely associated with SARS-CoV-2 vaccination. Indeed, MOG-AD after vaccination may induce more severe symptoms compared to non-vaccine related MOG-AD, represented by longer focal involvement of segments and even require multiple immunotherapy in some cases[23], while routine lab tests of CSF could be normal[23,24]. Therefore, according to the currently proposed criteria for a “probable” causal relationship between SARS-CoV-2 vaccination and neurological complications, SARS-CoV-2 infection or vaccination may lead to the process of molecular mimicry and epitope spread, which may contribute to the inflammation-associated MOG-Ig as a non-specific trigger releasing and finally result in MOG-AD[25].

As for disease regression, in this group of patients, immunotherapy with adequate steroid hormones is most commonly adopted in clinical practice, and most patients have good response to steroid treatments and are able to achieve clinical remission[1]. Immunoglobulin and plasma replacement are alternative clinical strategies. As with typical MOG-AD, patient with MOG-AD after SARS-CoV-2 infection could receive complete or near-complete recovery after treatments, and relapse cases are rare[1,11]. However, given the specificity of MOG antibodies, the current epidemiological setting of SARS-CoV-2, and the limited follow-up time, and it is recommended that such patients should be followed up for a longer period of time for assessment or to prevent relapse.

CONCLUSION

Here we present a case of MOG-AD after SARS-CoV-2 infection and a literature review of available reports. We suggest that attention should be paid to the evaluation of typical or atypical neurological symptoms that may be triggered by SARS-CoV-2 infection, and focus on the exclusion of coexisting autoimmune reactions or diseases. We suggest that SARS-CoV-2 infection may play a potential role in triggering and driving inflammation in the pathogenesis of MOG-AD, but direct pathophysiological evidence is still lacking. More prospective studies are needed to elucidate this possible association.

FOOTNOTES

Author contributions: Zheng JR and Chen XH conceptualized and designed the case report, drafted the initial manuscript and revised it; Liu ZG contributed to the conception and design of the manuscript; Chang JL supervised and coordinated the manuscript; Hu J, Lin Z, Lin KH and Lu BH were involved in patient care and data collection; All authors reviewed and approved of the manuscript.

Supported by the Shenzhen University Teaching Reform Fund, No. JG2023166; the Shenzhen Science and Technology Innovation Commission Fund, No. JCYJ2022081802810022; and the Shenzhen Science and Technology Innovation Commission Basic Research Key Projects Fund, No. JCYJ20210324115800003.

Informed consent statement: Written consent has been acquired from the patient.

Conflict-of-interest statement: The authors declare that they have no conflict of interest.

CARE Checklist (2016) statement: The authors have read the CARE Checklist (2016), and the manuscript was prepared and revised according to the CARE Checklist (2016).

Open-Access: This article is an open-access article that was selected by an in-house editor and fully peer-reviewed by external reviewers. It is distributed in accordance with the Creative Commons Attribution NonCommercial (CC BY-NC 4.0) license, which permits others to distribute, remix, adapt, build upon this work non-commercially, and license their derivative works on different terms, provided the original work is properly cited and the use is non-commercial. See: <https://creativecommons.org/licenses/by-nc/4.0/>

Country of origin: China

ORCID number: Xu-Hui Chen 0009-0004-3876-2462; Zhi-Gang Liu 0000-0002-6863-6561.

S-Editor: Fan M

L-Editor: A

P-Editor: Yuan YY

REFERENCES

- 1 Ariño H, Heartshorne R, Michael BD, Nicholson TR, Vincent A, Pollak TA, Vogrig A. Neuroimmune disorders in COVID-19. *J Neurol* 2022; **269**: 2827-2839 [PMID: 35353232 DOI: 10.1007/s00415-022-11050-w]
- 2 Pham-Dinh D, Mattei MG, Nussbaum JL, Roussel G, Pontarotti P, Roeckel N, Mather IH, Artzt K, Lindahl KF, Dautigny A. Myelin/oligodendrocyte glycoprotein is a member of a subset of the immunoglobulin superfamily encoded within the major histocompatibility complex. *Proc Natl Acad Sci U S A* 1993; **90**: 7990-7994 [PMID: 8367453 DOI: 10.1073/pnas.90.17.7990]
- 3 Marignier R, Hacohen Y, Cobo-Calvo A, Pröbstel AK, Aktas O, Alexopoulos H, Amato MP, Asgari N, Banwell B, Bennett J, Brilot F, Capobianco M, Chitnis T, Ciccarelli O, Deiva K, De Sèze J, Fujihara K, Jacob A, Kim HJ, Kleiter I, Lassmann H, Leite MI, Linington C, Meinel E, Palace J, Paul F, Petzold A, Pittock S, Reindl M, Sato DK, Selmaj K, Siva A, Stankoff B, Tintore M, Traboulsee A, Waters P, Waubant E, Weinshenker B, Derfuss T, Vukusic S, Hemmer B. Myelin-oligodendrocyte glycoprotein antibody-associated disease. *Lancet Neurol* 2021; **20**: 762-772 [PMID: 34418402 DOI: 10.1016/S1474-4422(21)00218-0]
- 4 Huang C, Wang Y, Li X, Ren L, Zhao J, Hu Y, Zhang L, Fan G, Xu J, Gu X, Cheng Z, Yu T, Xia J, Wei Y, Wu W, Xie X, Yin W, Li H, Liu M, Xiao Y, Gao H, Guo L, Xie J, Wang G, Jiang R, Gao Z, Jin Q, Wang J, Cao B. Clinical features of patients infected with 2019 novel coronavirus in Wuhan, China. *Lancet* 2020; **395**: 497-506 [PMID: 31986264 DOI: 10.1016/S0140-6736(20)30183-5]
- 5 Li Q, Guan X, Wu P, Wang X, Zhou L, Tong Y, Ren R, Leung KSM, Lau EHY, Wong JY, Xing X, Xiang N, Wu Y, Li C, Chen Q, Li D, Liu T, Zhao J, Liu M, Tu W, Chen C, Jin L, Yang R, Wang Q, Zhou S, Wang R, Liu H, Luo Y, Liu Y, Shao G, Li H, Tao Z, Yang Y, Deng Z, Liu B, Ma Z, Zhang Y, Shi G, Lam TTY, Wu JT, Gao GF, Cowling BJ, Yang B, Leung GM, Feng Z. Early Transmission Dynamics in Wuhan, China, of Novel Coronavirus-Infected Pneumonia. *N Engl J Med* 2020; **382**: 1199-1207 [PMID: 31995857 DOI: 10.1056/NEJMoa2001316]
- 6 Helms J, Kremer S, Merdji H, Clere-Jehl R, Schenck M, Kummerlen C, Collange O, Boulay C, Fafi-Kremer S, Ohana M, Anheim M, Meziani F. Neurologic Features in Severe SARS-CoV-2 Infection. *N Engl J Med* 2020; **382**: 2268-2270 [PMID: 32294339 DOI: 10.1056/NEJMc2008597]
- 7 Pascarella G, Strumia A, Piliago C, Bruno F, Del Buono R, Costa F, Scarlata S, Agrò FE. COVID-19 diagnosis and management: a comprehensive review. *J Intern Med* 2020; **288**: 192-206 [PMID: 32348588 DOI: 10.1111/joim.13091]
- 8 Zhao K, Huang J, Dai D, Feng Y, Liu L, Nie S. Acute myelitis after SARS-CoV-2 infection: a case report. Preprint from: medRxiv 2020

[DOI: [10.1101/2020.03.16.20035105](https://doi.org/10.1101/2020.03.16.20035105)]

- 9 **Mariotto S**, Carta S, Dinoto A, Lippi G, Salvagno GL, Masin L, Alberti D, Marignier R, Ferrari S. Is there a correlation between MOG-associated disorder and SARS-CoV-2 infection? *Eur J Neurol* 2022; **29**: 1855-1858 [PMID: [35224824](https://pubmed.ncbi.nlm.nih.gov/35224824/) DOI: [10.1111/ene.15304](https://doi.org/10.1111/ene.15304)]
- 10 **Johnsson M**, Asztely F, Hejnebo S, Axelsson M, Malmeström C, Olausson T, Lycke J. SARS-COV-2 a trigger of myelin oligodendrocyte glycoprotein-associated disorder. *Ann Clin Transl Neurol* 2022; **9**: 1296-1301 [PMID: [35713508](https://pubmed.ncbi.nlm.nih.gov/35713508/) DOI: [10.1002/acn3.51609](https://doi.org/10.1002/acn3.51609)]
- 11 **Lambe J**, McGinley MP, Moss BP, Mao-Draayer Y, Kassa R, Ciotti JR, Mariotto S, Kunchok A. Myelin oligodendrocyte glycoprotein-IgG associated disorders (MOGAD) following SARS-CoV-2 infection: A case series. *J Neuroimmunol* 2022; **370**: 577933 [PMID: [35878436](https://pubmed.ncbi.nlm.nih.gov/35878436/) DOI: [10.1016/j.jneuroim.2022.577933](https://doi.org/10.1016/j.jneuroim.2022.577933)]
- 12 **Sarma D**, Bilello LA. A Case Report of Acute Transverse Myelitis Following Novel Coronavirus Infection. *Clin Pract Cases Emerg Med* 2020; **4**: 321-323 [PMID: [32926676](https://pubmed.ncbi.nlm.nih.gov/32926676/) DOI: [10.5811/cpcem.2020.5.47937](https://doi.org/10.5811/cpcem.2020.5.47937)]
- 13 **Sotoca J**, Rodríguez-Álvarez Y. COVID-19-associated acute necrotizing myelitis. *Neurol Neuroimmunol Neuroinflamm* 2020; **7** [PMID: [32522767](https://pubmed.ncbi.nlm.nih.gov/32522767/) DOI: [10.1212/NXI.0000000000000803](https://doi.org/10.1212/NXI.0000000000000803)]
- 14 **Varga Z**, Flammer AJ, Steiger P, Haberecker M, Andermatt R, Zinkernagel AS, Mehra MR, Schuepbach RA, Ruschitzka F, Moch H. Endothelial cell infection and endotheliitis in COVID-19. *Lancet* 2020; **395**: 1417-1418 [PMID: [32325026](https://pubmed.ncbi.nlm.nih.gov/32325026/) DOI: [10.1016/S0140-6736\(20\)30937-5](https://doi.org/10.1016/S0140-6736(20)30937-5)]
- 15 **Guo Z**, Sun S, Xiao S, Chen G, Chen P, Yang Z, Tang X, Huang L, Wang Y. COVID-19 is associated with changes in brain function and structure: A multimodal meta-analysis of neuroimaging studies. *Neurosci Biobehav Rev* 2024; **164**: 105792 [PMID: [38969310](https://pubmed.ncbi.nlm.nih.gov/38969310/) DOI: [10.1016/j.neubiorev.2024.105792](https://doi.org/10.1016/j.neubiorev.2024.105792)]
- 16 **Lan J**, Ge J, Yu J, Shan S, Zhou H, Fan S, Zhang Q, Shi X, Wang Q, Zhang L, Wang X. Structure of the SARS-CoV-2 spike receptor-binding domain bound to the ACE2 receptor. *Nature* 2020; **581**: 215-220 [PMID: [32225176](https://pubmed.ncbi.nlm.nih.gov/32225176/) DOI: [10.1038/s41586-020-2180-5](https://doi.org/10.1038/s41586-020-2180-5)]
- 17 **Yan R**, Zhang Y, Li Y, Xia L, Guo Y, Zhou Q. Structural basis for the recognition of SARS-CoV-2 by full-length human ACE2. *Science* 2020; **367**: 1444-1448 [PMID: [32132184](https://pubmed.ncbi.nlm.nih.gov/32132184/) DOI: [10.1126/science.abb2762](https://doi.org/10.1126/science.abb2762)]
- 18 **Mao L**, Jin H, Wang M, Hu Y, Chen S, He Q, Chang J, Hong C, Zhou Y, Wang D, Miao X, Li Y, Hu B. Neurologic Manifestations of Hospitalized Patients With Coronavirus Disease 2019 in Wuhan, China. *JAMA Neurol* 2020; **77**: 683-690 [PMID: [32275288](https://pubmed.ncbi.nlm.nih.gov/32275288/) DOI: [10.1001/jamaneurol.2020.1127](https://doi.org/10.1001/jamaneurol.2020.1127)]
- 19 **Netland J**, Meyerholz DK, Moore S, Cassell M, Perlman S. Severe acute respiratory syndrome coronavirus infection causes neuronal death in the absence of encephalitis in mice transgenic for human ACE2. *J Virol* 2008; **82**: 7264-7275 [PMID: [18495771](https://pubmed.ncbi.nlm.nih.gov/18495771/) DOI: [10.1128/JVI.00737-08](https://doi.org/10.1128/JVI.00737-08)]
- 20 **Zhou L**, Zhang M, Wang J, Gao J. Sars-Cov-2: Underestimated damage to nervous system. *Travel Med Infect Dis* 2020; **36**: 101642 [PMID: [32220634](https://pubmed.ncbi.nlm.nih.gov/32220634/) DOI: [10.1016/j.tmaid.2020.101642](https://doi.org/10.1016/j.tmaid.2020.101642)]
- 21 **Mehta P**, McAuley DF, Brown M, Sanchez E, Tattersall RS, Manson JJ; HLH Across Speciality Collaboration, UK. COVID-19: consider cytokine storm syndromes and immunosuppression. *Lancet* 2020; **395**: 1033-1034 [PMID: [32192578](https://pubmed.ncbi.nlm.nih.gov/32192578/) DOI: [10.1016/S0140-6736\(20\)30628-0](https://doi.org/10.1016/S0140-6736(20)30628-0)]
- 22 **McCray PB Jr**, Pewe L, Wohlford-Lenane C, Hickey M, Manzel L, Shi L, Netland J, Jia HP, Halabi C, Sigmund CD, Meyerholz DK, Kirby P, Look DC, Perlman S. Lethal infection of K18-hACE2 mice infected with severe acute respiratory syndrome coronavirus. *J Virol* 2007; **81**: 813-821 [PMID: [17079315](https://pubmed.ncbi.nlm.nih.gov/17079315/) DOI: [10.1128/JVI.02012-06](https://doi.org/10.1128/JVI.02012-06)]
- 23 **Jarius S**, Bieber N, Haas J, Wildemann B. MOG encephalomyelitis after vaccination against severe acute respiratory syndrome coronavirus type 2 (SARS-CoV-2): case report and comprehensive review of the literature. *J Neurol* 2022; **269**: 5198-5212 [PMID: [35737110](https://pubmed.ncbi.nlm.nih.gov/35737110/) DOI: [10.1007/s00415-022-11194-9](https://doi.org/10.1007/s00415-022-11194-9)]
- 24 **Sechi E**, Buciu M, Flanagan EP, Pittock SJ, Banks SA, Lopez-Chiriboga AS, Bhatti MT, Chen JJ. Variability of cerebrospinal fluid findings by attack phenotype in myelin oligodendrocyte glycoprotein-IgG-associated disorder. *Mult Scler Relat Disord* 2021; **47**: 102638 [PMID: [33276239](https://pubmed.ncbi.nlm.nih.gov/33276239/) DOI: [10.1016/j.msard.2020.102638](https://doi.org/10.1016/j.msard.2020.102638)]
- 25 **Butler M**, Tamborska A, Wood GK, Ellul M, Thomas RH, Galea I, Pett S, Singh B, Solomon T, Pollak TA, Michael BD, Nicholson TR. Considerations for causality assessment of neurological and neuropsychiatric complications of SARS-CoV-2 vaccines: from cerebral venous sinus thrombosis to functional neurological disorder. *J Neurol Neurosurg Psychiatry* 2021; **92**: 1144-1151 [PMID: [34362855](https://pubmed.ncbi.nlm.nih.gov/34362855/) DOI: [10.1136/jnnp-2021-326924](https://doi.org/10.1136/jnnp-2021-326924)]

Extralobar pulmonary sequestration in children with abdominal pain: Four case reports

Meng-Yuan Jiang, Yuan-Xiang Wang, Zhi-Wei Lu, Yue-Jie Zheng

Specialty type: Radiology, nuclear medicine and medical imaging

Provenance and peer review: Unsolicited article; Externally peer reviewed.

Peer-review model: Single blind

Peer-review report's classification

Scientific Quality: Grade D

Novelty: Grade B

Creativity or Innovation: Grade C

Scientific Significance: Grade B

P-Reviewer: Chun H

Received: April 17, 2024

Revised: August 22, 2024

Accepted: August 26, 2024

Published online: September 28, 2024

Processing time: 163 Days and 5 Hours



Meng-Yuan Jiang, Zhi-Wei Lu, Yue-Jie Zheng, Department of Respiratory Diseases, Shenzhen Children's Hospital, Shenzhen 518038, Guangdong Province, China

Yuan-Xiang Wang, Department of Cardiothoracic Surgery, Shenzhen Children's Hospital, Shenzhen 518038, Guangdong Province, China

Corresponding author: Zhi-Wei Lu, MD, Chief Doctor, Department of Respiratory Diseases, Shenzhen Children's Hospital, No. 7019 Yitian Road, Futian District, Shenzhen 518038, Guangdong Province, China. luzhiwei1950@163.com

Abstract

BACKGROUND

Extralobar pulmonary sequestration (ELS) with torsion is extremely rare, consequently, the diagnosis of ELS with torsion in children presents a challenge for clinicians. Herein, we report four cases of ELS with torsion that presented with abdominal pain, and further review the relevant literature to summarize the clinical features.

CASE SUMMARY

Four children presented to our department with abdominal pain. All underwent chest computed tomography, which revealed an intrathoracic soft tissue mass with pleural effusion. All four children underwent thoracoscopic resection of the identified pulmonary sequestration, and the vascular pedicle was clipped and excised. None of the patients experienced any postoperative complications.

CONCLUSION

Clinicians should consider the possibility of ELS with torsion in children presenting with abdominal pain as the chief complaint.

Key Words: Extralobar pulmonary sequestration; Abdominal pain; Torsion; Children; Case report

©The Author(s) 2024. Published by Baishideng Publishing Group Inc. All rights reserved.

Core Tip: Extralobar pulmonary sequestration (ELS) with torsion is relatively rare, and typically occurs in the left hemithorax. It generally presents in children; however, there is a high probability of misdiagnosis or missed diagnosis because of its atypical symptoms. As such, clinicians need to be more aware of the possibility of torsion of an ELS.

Citation: Jiang MY, Wang YX, Lu ZW, Zheng YJ. Extralobar pulmonary sequestration in children with abdominal pain: Four case reports. *World J Radiol* 2024; 16(9): 453-459

URL: <https://www.wjgnet.com/1949-8470/full/v16/i9/453.htm>

DOI: <https://dx.doi.org/10.4329/wjr.v16.i9.453>

INTRODUCTION

Pulmonary sequestration (PS) is a rare congenital lung malformation, which can be classified as either intralobar PS, or extralobar PS (ELS), based on the presence or absence of visceral pleura covering the lung parenchyma. Currently, the pathogenesis and etiology of PS remain unclear, while the clinical manifestations of ELS lack specificity. Asymptomatic children can be identified incidentally; however, some are not identified until they suddenly develop non-specific symptoms such as cough, sputum production, fever, hemoptysis, chest pain, chest tightness, shortness of breath, fatigue, and abdominal pain. Thus, missed and misdiagnosis of ELS with torsion are common because of its atypical symptoms.

Herein, we report four pediatric cases of abdominal pain caused by ELS torsion. All patients underwent thoracoscopic resection of the PS, following which postoperative pathological examination confirmed ELS with hemorrhagic infarction.

CASE PRESENTATION

Chief complaints

Case 1: A 3-year-old boy admitted to our hospital with abdominal pain for 7 days and fever for 5 days.

Case 2: A 7-year-old boy admitted to our hospital with abdominal pain and vomiting for 2 days.

Case 3: A 6-year-old girl admitted to our hospital with abdominal and chest pain for 10 days.

Case 4: A 10-year-old girl admitted to our hospital with abdominal pain for 4 days, and chest pain and fever for 3 days.

History of present illness

Case 1: The patient had a history of presentation to another hospital with abdominal pain and fever. Computed tomography (CT) of the abdomen revealed no intra-abdominal abnormalities; however, left-sided pleural effusion was observed. Subsequently, chest CT revealed a left-sided hyperdense opacity with pleural effusion, after which the patient was transferred to our hospital.

Case 2: The patient presented to our hospital with abdominal pain and vomiting.

Case 3: The patient had a history of presentation to another hospital with abdominal and chest pain. CT of the abdomen and chest revealed a mass with pleural effusion in the right chest, after which the patient transferred to our hospital.

Case 4: The patient presented to our hospital with abdominal and chest pain and fever.

History of past illness

All of the patients were previously healthy, and had no history of recurrent respiratory tract infection. All had been vaccinated with the tuberculosis (TB) vaccine, and denied any history of exposure to TB. Further, none had any history of eating contaminated or raw food.

Personal and family history

Case 1: The patient's grandfather had nasopharyngeal cancer.

Cases 2-4: These patients had no remarkable personal or family history.

Physical examination

Case 1: The patient had decreased breathing sounds and voice tremors at the left lung base.

Cases 2-4: Physical examination was unremarkable.

Laboratory examinations

Case 1: Laboratory examinations at admission revealed no abnormalities in blood cell count, blood biochemistry, or coagulation function. Tumor marker levels [carcinoembryonic antigen (CEA) and alpha-fetoprotein (AFP)] were unremarkable, while cytological analysis of the pleural fluid yielded negative results for malignancy, and pleural fluid culture showed no growth of infectious organisms.

Case 2: Routine blood analysis revealed an elevated leukocyte count of $18.62 \times 10^9/L$, with 87.5% neutrophils and 5.0% lymphocytes; eosinophils were within the normal range. Tumor marker levels [CEA, AFP, neuron-specific-enolase (NSE), human chorionic gonadotropin (HCG), and urinary vanillylmandelic acid (VMA)] were unremarkable. No abnormalities were identified in other parameters related to blood biochemistry or coagulation.

Case 3: Tumor marker levels (CEA, AFP, NSE, HCG, and urinary VMA) were unremarkable. No abnormalities were identified in other laboratory tests results upon admission.

Case 4: Routine blood analysis revealed 82.4% neutrophils and 9.3% lymphocytes; the leukocyte count was $14.23 \times 10^9/L$; eosinophils were within the normal range. Tumor marker levels (CEA, AFP, NSE and HCG) were unremarkable. No abnormalities were identified in other laboratory tests upon admission.

Imaging examinations

Chest CT revealed an intrathoracic soft tissue mass shadow with pleural effusion in all cases (Figure 1). Abdominal imaging showed no signs indicative of masses in the abdominal cavity.

FINAL DIAGNOSIS

Based on the postoperative pathological examination findings, the final diagnosis of ELS with torsion was confirmed in all four cases.

TREATMENT

All patients underwent planned thoracoscopic resection of PS. Grayish-brown or purplish-dark masses with congestion and necrosis were observed during surgery, accompanied by bloody pleural effusion. The feeding arteries were identified and clipped.

OUTCOME AND FOLLOW-UP

None of the children experienced any intra- or postoperative complications; their symptoms were relieved after surgery, and they have reported no discomfort since discharge.

DISCUSSION

ELS is characterized by the presence of non-functional lung tissue encased in its own visceral pleura, with little or no communication with the tracheobronchial tree. The supply artery normally originates from the thoracic or abdominal aorta, while the venous drainage primarily reaches the inferior vena cava, azygos vein, or hemiazygos vein. ELS is commonly associated with other congenital abnormalities, of which congenital diaphragmatic hernia is the most common [1,2]. This is inconsistent with the 13 cases reported in the English literature (Table 1). None of the 17 reported patients, including our four, had other congenital malformations; indeed, all were previously healthy and did not undergo routine examination. As a result, ELS was not detected until symptom onset. Most congenital anomalies in children are diagnosed and surgically treated in the neonatal period. One study characterized the epidemiology of PS in a Chinese population, extracted from a nationwide database from 2010 to 2019. The authors found that 90.25% of children with PS were identified by prenatal ultrasound. Although the majority of the PS cases could be diagnosed prenatally, a few mild, asymptomatic cases of PS or complex syndrome may be missed, particularly in rural areas, which may be related to the diagnostic capacity of the examiners, location of the mass, socioeconomic status, and prenatal health care services [3].

In the present study, we searched the PubMed, CNKI, Wanfang, and VIP databases from their inception to October 2021 for literature on ELS in children with abdominal pain as the primary manifestation. This search identified 13 cases of ELS with torsion previously reported in the literature (Table 1). The patients' ages ranged from 4 to 15 years, and all were previously healthy. All patients presented with abdominal pain, while other symptoms include chest pain, vomiting, and fever. Except for the identification of a mass that was found in the left lower abdomen of one child [4] and massive consolidation accompanied by pleural effusion on chest radiography in another child [5], chest CTs of the other 11 children revealed a low-density soft tissue mass shadow in a triangular, oval, or round shape, and the ratio of the left and right parts of the lesion was 11:2. Only 2 of the 13 patients did not show pleural effusion [4,6]. Only 1 patient was diagnosed

Table 1 Summary of all previously-reported cases of extralobar pulmonary sequestration in children with abdominal pain

No.	Ref.	Published year	Age (year)	Sex	Main symptoms	Location	Pleural effusion	Imaging findings
1	Shih <i>et al</i> [4]	1990	8	F	Abdominal pain	Left abdomen	-	Contrast-enhanced abdominal CT revealed a thin-walled mass in the left retroperitoneum
2	Mammen <i>et al</i> [5]	1994	8	F	Abdominal and chest pain	Right	+	Chest radiographs revealed a right-side pleural effusion with collapse and consolidation of the right middle and lower lobes
3	Yokota <i>et al</i> [6]	2019	15	M	Abdominal pain and coughing	Right	-	Contrast-enhanced chest CT revealed a soft tissue density mass adjacent to the vertebral body at the posterior mediastinum
4	Lima <i>et al</i> [7]	2010	11	F	Abdominal pain	Left	+	Chest CT revealed a paraspinal mass in the inferior portion of the left chest
5	Walcutt <i>et al</i> [8]	2021	13	M	Abdominal and vomiting	Left	+	Contrast-enhanced chest CT revealed a hyperdense polygonal mass in the inferior medial left pleural space
6	Kirkendall <i>et al</i> [10]	2013	13	M	Abdominal and chest pain	Left	+	Chest CT revealed a paraspinal soft tissue mass in the inferior portion of the left chest
7	Chen <i>et al</i> [11]	2011	13	M	Abdominal pain and vomiting	Left	+	Chest CT revealed a well-defined posterior mediastinal soft tissue mass
8	Shah <i>et al</i> [13]	2010	11	F	Abdominal and chest pain	Left	+	Contrast-enhanced Chest CT revealed an ovoid soft-tissue density shadow
9	Uchida <i>et al</i> [14]	2010	4	M	Abdominal pain	Left	+	Contrast-enhanced Chest CT revealed an oval-shaped mass in the posteromedial left lower chest
10	Son <i>et al</i> [15]	2020	13	F	Abdominal and chest pain	Left	+	Chest CT revealed amass-like lesion in left hemithorax
11	Choe and Goo[17]	2015	10	M	Abdominal pain and fever	Left	+	Chest CT revealed well-defined hypodense soft tissue lesion in the left pleural space
12	Zucker <i>et al</i> [18]	2013	6	M	Abdominal pain and chest pain	Left	+	Contrast-enhanced chest CT revealed an oval-shaped mass in the left lower chest
13	Gawlitza <i>et al</i> [19]	2014	11	M	Abdominal and vomiting	Left	+	Contrast-enhanced chest CT revealed a mass with intermediate density in the left chest

M: Male; F: Female; CT: Computed tomography.

with two left ELS, of which one had torsion[7]. All children underwent surgical treatment. Based on postoperative pathological examination findings, a final diagnosis of ELS with torsion was confirmed in all cases. All patients were cured after surgery, with favorable outcomes and no deaths.

The ELS usually attaches to the mediastinal side of the pleural cavity only through the vascular pedicle and lower pulmonary ligament, while torsion of the ELS can easily occur during vigorous exercise, resulting in infarction, hemorrhage, and necrosis[6,8]. In addition, pleural effusion, which is usually bloody, can be attributed to the blockage of the draining venous and lymphatic vessels by torsion of the vascular pedicle. ELS is a rare congenital malformation characterized by acute onset and rapid progression. In adulthood, ELS most commonly presents as chest pain or discomfort[9]. In contrast, the most common clinical symptom in children is abdominal pain, which may be accompanied by vomiting and fever; thus, the initial evaluation generally focuses on abdominal diseases, such as acute abdomen[5,6, 10] and neurogenic tumors[4,11]. Among the previously reported cases, one patient was preoperatively diagnosed with neuroblastoma with negative chest radiography findings and elevated urinary VMA, which is suggestive of tumors of neural crest origin[4].

The four children with ELS with torsion hospitalized in our institution all had abdominal pain as the first or primary symptom, while accompanying symptoms included fever, chest pain, and vomiting. Further, in all patients, chest CT revealed an intrathoracic soft tissue mass shadow between the lower lobe of the lung and the diaphragm, combined with pleural effusion. The preoperative differential diagnoses of ELS include tumor, diaphragmatic herniation, and unusual infections such as TB infection, parasitic infection, and unclear disease. We progressively excluded these differential diagnoses based on the following findings: (1) All patients had received the TB vaccine, and denied a history of exposure to TB; (2) None of the patients had any history of eating contaminated or raw food; and (3) Tumor marker levels (CEA, AFP, NSE, HCG, and urinary VMA) were unremarkable, while routine blood analysis revealed normal levels of eosinophils.

As mentioned, abdominal pain is one of the common symptoms of ELS in children. Abdominal pain in children has many potential causes, which can be broadly categorized into intra-abdominal disease, extra-abdominal, and systemic disease; further, thoracic diseases such as pneumonia, pleurisy, pulmonary infarction, and pericarditis can cause

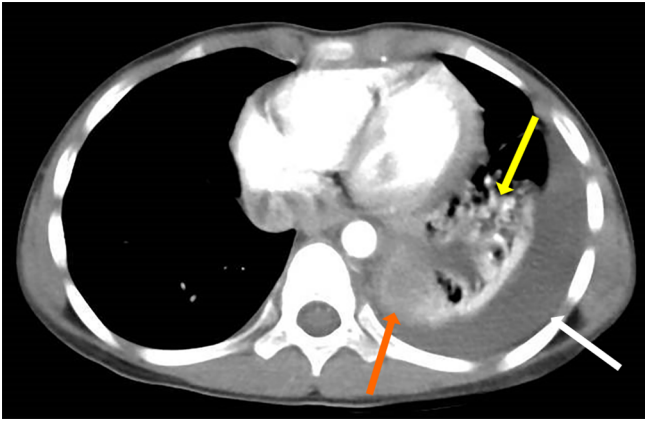


Figure 1 Exemplar chest contrast-enhanced computed tomography results in case 2 (a 7-year-old boy), showing an approximately 52.9 mm × 40.5 mm × 40.8 mm-sized oval lesion at the level of the 9th-10th thoracic vertebra (orange arrow), with a pleural effusion (white arrow) and pneumonia (yellow arrow). No obvious enhancement was observed.

abdominal referred pain. The pathogenesis of abdominal pain is divided into visceral abdominal pain[12], somatic abdominal pain, and referred pain. The ELS is usually located between the lower lobe of the lung and the diaphragm. In all 17 reported cases, including our own, imaging evaluation revealed a soft tissue lesion located between the diaphragm and lower lobe. In our 4 cases, the mass was densely adherent to the chest wall and diaphragm at operation. However, at present, literature reports on ELS in children with abdominal pain as the main manifestation are rare, and most of those that have been published are retrospective case reports. The mechanism of abdominal pain is not clear and requires further exploration. The causes of abdominal pain caused by ELS with torsion could be: (1) Pneumonia or pleurisy caused by the torsion of ELS causes referred pain; (2) ELS is generally located between the diaphragm and the lower lobe, and abdominal pain could be attributed to irritation to the diaphragm caused by torsion of the ELS; (3) ELS can be found infra-diaphragmatically, representing an extremely rare type of PS. In such cases, peritonitis or peritoneal effusion caused by the torsion of this kind of ELS causes abdominal pain.

Currently, chest imaging examination is the key method for establishing a correct diagnosis of ELS when a feeding artery arising from the systemic circulation into the isolated lung tissue is identified. Chest imaging tests should be performed as early as possible to exclude ELS with torsion when school-age children present with abdominal pain, while chest imaging should range from the lower thorax to the level of the pulmonary veins[13], with the entire chest ideally being examined. Routine chest radiography or chest CT without contrast-enhanced imaging may reveal a mass shadow in the lung; however, it has a high rate of misdiagnosis. Particularly in the early stage of the disease, it may be missed or misdiagnosed as atelectasis[10,14]. Son *et al*[15] indicated that an image might be misdiagnosed as a tumorous or infectious condition, if an inflammatory reaction occurs. Contrast-enhanced CT with 3D reconstruction is more effective at diagnosing ELS, as it provides more information about the mass, such as the degree of enhancement of the mass and the vascular shadow of the lesion, which makes it easier to distinguish pulmonary cystic lesions, consolidation, atelectasis, and mass shadow. However, torsion of the vessels can hinder the visibility of the blood supply, while contrast-enhanced CT may not identify an abnormal blood supply. Ou *et al*[16] Previously reported the clinical characteristics of 48 cases (including 30 confirmed and 18 suspected cases) of PS in children. Among them, only 16 were confirmed by imaging preoperatively, including four cases by chest CT-enhanced scanning, nine cases by enhanced CT combined with three-dimensional reconstruction, and three cases by digital subtraction angiography; the misdiagnosis rate was 36.7%, and the missed diagnosis rate was 10%. Torsion of the ELS prevents the blood supply from being filled with contrast medium, resulting in unrecognizable blood supply vessels and atypical imaging findings. This leads to difficulty in diagnosing ELS with torsion. As such, it is also difficult to identify the abnormal supply artery of the ELS with torsion using contrast-enhanced CT combined with three-dimensional reconstruction, which requires radiologists to pay close attention to it to avoid missing diagnoses. Of the 13 reported cases, a feeding artery was identified on MRI in only one case[17]. Shah *et al*[13], Zucker *et al*[18] and Gawlitza *et al*[19] all indicated that torsion of the PS could be considered, even if the classic findings of a vascular pedicle were not identified on imaging examinations.

Most cases of ELS are diagnosed antenatally, and are treated aggressively with surgery, even if asymptomatic. However, some pediatric ELS are not identified during prenatal examination; such patients are usually in good health, and may only be admitted to the hospital because of pulmonary infarction and hemorrhage caused by torsion of the blood vessel pedicle. These patients also require immediate surgery. Currently, thoracoscopic surgery is an important treatment for ELS associated with torsion, less intraoperative bleeding, and better recovery and prognosis[20].

CONCLUSION

ELS with torsion usually presents in children and adolescents, and is associated with a high risk of missed or misdiagnosis because of its atypical symptoms. Clinicians should consider the possibility of ELS with torsion in previously

healthy school-aged children with chief complaints of abdominal pain, sometimes accompanied by chest pain, vomiting, and fever. Chest imaging should also be performed as early as possible, particularly in cases with remarkable findings on physical examination of the lungs suggestive of ELS with torsion. A high index of suspicion for ELS with torsion should be maintained when contrast-enhanced chest CT reveals a soft tissue mass shadow with no or mild enhancement, accompanied by bloody pleural effusion, unclear blood supply arteries, and other characteristic changes. As such, thorascopic ELS resection should be performed immediately.

ACKNOWLEDGEMENTS

We would like to thank the patient's family members for providing detailed treatment information.

FOOTNOTES

Author contributions: Jiang MY contributed to manuscript writing and data collection; Lu ZW contributed to data analysis and manuscript review and editing; Wang YX and Zheng YJ contributed to manuscript review and editing; all authors have read and approved the final manuscript.

Supported by Shenzhen Fund for Guangdong Provincial High-level Clinical Key Specialties, No. SZGSP012; and Shenzhen Key Medical Discipline Construction Fund, No. SZXK032.

Informed consent statement: Patients were not required to give informed consent to the study because the analysis used anonymous clinical data that were obtained after each patients' parents/guardians agreed to treatment by written consent.

Conflict-of-interest statement: All authors declare that they have no conflicts of interest to disclose.

CARE Checklist (2016) statement: The authors have read the CARE Checklist (2016), and the manuscript was prepared and revised according to the CARE Checklist (2016).

Open-Access: This article is an open-access article that was selected by an in-house editor and fully peer-reviewed by external reviewers. It is distributed in accordance with the Creative Commons Attribution NonCommercial (CC BY-NC 4.0) license, which permits others to distribute, remix, adapt, build upon this work non-commercially, and license their derivative works on different terms, provided the original work is properly cited and the use is non-commercial. See: <https://creativecommons.org/licenses/by-nc/4.0/>

Country of origin: China

ORCID number: Zhi-Wei Lu 0000-0001-5153-1571.

S-Editor: Qu XL

L-Editor: A

P-Editor: Yu HG

REFERENCES

- 1 **Chakraborty RK**, Modi P, Sharma S. Pulmonary Sequestration. 2023 Jul 24. In: StatPearls [Internet]. Treasure Island (FL): StatPearls Publishing; 2024 Jan- [PMID: 30335347]
- 2 **Yildirim G**, Güngördük K, Aslan H, Ceylan Y. Prenatal diagnosis of an extralobar pulmonary sequestration. *Arch Gynecol Obstet* 2008; **278**: 181-186 [PMID: 18236057 DOI: 10.1007/s00404-008-0569-8]
- 3 **Gao Y**, Xu W, Li W, Chen Z, Li Q, Liu Z, Liu H, Dai L. Epidemiology and prevalence of pulmonary sequestration in Chinese population, 2010-2019. *BMC Pulm Med* 2023; **23**: 8 [PMID: 36624419 DOI: 10.1186/s12890-023-02308-8]
- 4 **Shih SL**, Lin JC, Chen BF, Chen CC, Chang KL, Liang DC. Extralobar pulmonary sequestration of the left retroperitoneum. *Australas Radiol* 1990; **34**: 356-357 [PMID: 2092669 DOI: 10.1111/j.1440-1673.1990.tb02675.x]
- 5 **Mammen A**, Myers NA, Beasley SW. Torsion and infarction of an extralobar pulmonary sequestration. *Pediatr Surg Int* 1994; **9**: 399-400 [DOI: 10.1007/bf01686013]
- 6 **Yokota R**, Sakamoto K, Urakawa H, Takeshita M, Yoshimitsu K. Torsion of right lung sequestration mimicking a posterior mediastinal mass presenting as acute abdomen: Usefulness of MR imaging. *Radiol Case Rep* 2019; **14**: 551-554 [PMID: 30847012 DOI: 10.1016/j.radcr.2019.02.008]
- 7 **Lima M**, Randi B, Gargano T, Tani G, Pession A, Gregori G. Extralobar pulmonary sequestration presenting with torsion and associated hydrothorax. *Eur J Pediatr Surg* 2010; **20**: 208-210 [PMID: 20072966 DOI: 10.1055/s-0029-1241837]
- 8 **Walcutt J**, Abdessalam S, Timmons Z, Winningham P, Beavers A. A rare case of torsion and infarction of an extralobar pulmonary sequestration with MR, CT, and surgical correlation. *Radiol Case Rep* 2021; **16**: 3931-3936 [PMID: 34712371 DOI: 10.1016/j.radcr.2021.09.045]
- 9 **Yang L**, Yang G. Extralobar pulmonary sequestration with a complication of torsion: A case report and literature review. *Medicine (Baltimore)* 2020; **99**: e21104 [PMID: 32702859 DOI: 10.1097/MD.00000000000021104]

- 10 **Kirkendall ES**, Guiot AB. Torsed pulmonary sequestration presenting with gastrointestinal manifestations. *Clin Pediatr (Phila)* 2013; **52**: 981-984 [PMID: 22890328 DOI: 10.1177/0009922812453197]
- 11 **Chen W**, Wagner L, Boyd T, Nagarajan R, Dasgupta R. Extralobar pulmonary sequestration presenting with torsion: a case report and review of literature. *J Pediatr Surg* 2011; **46**: 2025-2028 [PMID: 22008345 DOI: 10.1016/j.jpedsurg.2011.07.017]
- 12 **Ehrhardt JD**, Weber C, Carey FJ, Lopez-Ojeda W. Anatomy, Thorax, Greater Splanchnic Nerves. 2024 Jan 31. In: StatPearls [Internet]. Treasure Island (FL): StatPearls Publishing; 2024 Jan- [PMID: 29763202]
- 13 **Shah R**, Carver TW, Rivard DC. Torsed pulmonary sequestration presenting as a painful chest mass. *Pediatr Radiol* 2010; **40**: 1434-1435 [PMID: 20155261 DOI: 10.1007/s00247-010-1558-1]
- 14 **Uchida DA**, Moore KR, Wood KE, Pysker TJ, Downey EC. Infarction of an extralobar pulmonary sequestration in a young child: diagnosis and excision by video-assisted thoracoscopy. *J Laparoendosc Adv Surg Tech A* 2010; **20**: 399-401 [PMID: 20235879 DOI: 10.1089/lap.2009.0217]
- 15 **Son SA**, Do YW, Kim YE, Lee SM, Lee DH. Infarction of torsed extralobar pulmonary sequestration in adolescence. *Gen Thorac Cardiovasc Surg* 2020; **68**: 77-80 [PMID: 30875002 DOI: 10.1007/s11748-019-01105-7]
- 16 **Ou J**, Lei X, Fu Z, Huang Y, Liu E, Luo Z, Peng D. Pulmonary sequestration in children: a clinical analysis of 48 cases. *Int J Clin Exp Med* 2014; **7**: 1355-1365 [PMID: 24995095]
- 17 **Choe J**, Goo HW. Extralobar pulmonary sequestration with hemorrhagic infarction in a child: preoperative imaging diagnosis and pathological correlation. *Korean J Radiol* 2015; **16**: 662-667 [PMID: 25995698 DOI: 10.3348/kjr.2015.16.3.662]
- 18 **Zucker EJ**, Tracy DA, Chwals WJ, Solky AC, Lee EY. Paediatric torsed extralobar sequestration containing calcification: Imaging findings with pathological correlation. *Clin Radiol* 2013; **68**: 94-97 [PMID: 22749813 DOI: 10.1016/j.crad.2012.05.008]
- 19 **Gawlitza M**, Hirsch W, Weißer M, Ritter L, Metzger RP. Torsion of extralobar lung sequestration - lack of contrast medium enhancement could facilitate MRI-based diagnosis. *Klin Padiatr* 2014; **226**: 38-39 [PMID: 24158892 DOI: 10.1055/s-0033-1351319]
- 20 **Iga N**, Nishi H, Miyoshi S. Video-assisted thoracoscopic surgery for bilateral intralobar pulmonary sequestration. *Int J Surg Case Rep* 2018; **53**: 333-336 [PMID: 30471625 DOI: 10.1016/j.ijscr.2018.10.060]

Behcet's disease-related panuveitis following COVID-19 vaccination: A case report

Rou-Ting Lin, Pei-Kang Liu, Chia-Wei Chang, Kai-Chun Cheng, Kuo-Jen Chen, Yo-Chen Chang

Specialty type: Ophthalmology

Provenance and peer review:

Unsolicited article; Externally peer reviewed.

Peer-review model: Single blind

Peer-review report's classification

Scientific Quality: Grade B

Novelty: Grade B

Creativity or Innovation: Grade A

Scientific Significance: Grade A

P-Reviewer: Said ZNA

Received: May 25, 2024

Revised: August 15, 2024

Accepted: August 23, 2024

Published online: September 28, 2024

Processing time: 124 Days and 16.6 Hours



Rou-Ting Lin, School of Medicine, College of Medicine, Chung Shan Medical University, Taichung 40201, Taiwan

Rou-Ting Lin, Chia-Wei Chang, Department of Clinical Education and Training, Kaohsiung Medical University Hospital, Kaohsiung 80756, Taiwan

Pei-Kang Liu, Kai-Chun Cheng, Yo-Chen Chang, Department of Ophthalmology, School of Medicine, College of Medicine, Kaohsiung Medical University, Kaohsiung 80737, Taiwan

Pei-Kang Liu, Kai-Chun Cheng, Yo-Chen Chang, Department of Ophthalmology, Kaohsiung Medical University Hospital, Kaohsiung 80756, Taiwan

Kuo-Jen Chen, Yo-Chen Chang, Department of Ophthalmology, Kaohsiung Municipal Siaogang Hospital, Kaohsiung Medical University, Kaohsiung 81201, Taiwan

Corresponding author: Yo-Chen Chang, MD, PhD, Associate Professor, Chief Physician, Department of Ophthalmology, School of Medicine, College of Medicine, Kaohsiung Medical University, No. 100 Zihyou 1st Road, San-Ming District, Kaohsiung 80737, Taiwan.

ycchang@kmu.edu.tw

Abstract

BACKGROUND

Behcet's disease (BD) is an inflammatory disorder known for various symptoms, including oral and genital ulcers and ocular inflammation. Panuveitis, a severe eye condition, is rare as the first sign of BD.

CASE SUMMARY

We present an unusual case of a 30-year-old man who developed panuveitis after receiving the mRNA-based coronavirus disease 2019 (COVID-19) vaccine (Moderna). Laboratory tests ruled out infections, but he had a positive HLA-B51 result and a history of genital ulcer and oral ulcers, leading to a BD diagnosis. Treatment with corticosteroids improved his condition. Interestingly, he had another episode of panuveitis after the second mRNA vaccine dose, which also responded to corticosteroids.

CONCLUSION

This case highlights the rare onset of BD following mRNA COVID-19 vaccination, suggesting a potential link between these vaccines and BD's eye symptoms, emphasizing the importance of quick treatment in similar cases.

Key Words: Behcet's disease; mRNA COVID-19 vaccine; Ocular inflammation; Panuveitis; Case report

©The Author(s) 2024. Published by Baishideng Publishing Group Inc. All rights reserved.

Core Tip: This case report highlights a rare instance of panuveitis as the first manifestation of Behcet's disease in a 30-year-old man following mRNA-based coronavirus disease 2019 vaccination (Moderna). The patient developed recurrent uveitis after both doses of the vaccine. This case suggests a potential link between mRNA vaccines and ocular inflammation in genetically predisposed individuals, particularly those with HLA-B51. It underscores the importance of considering Behcet's disease in patients presenting with panuveitis post-vaccination and calls for further research to confirm this association and understand the underlying mechanisms.

Citation: Lin RT, Liu PK, Chang CW, Cheng KC, Chen KJ, Chang YC. Behcet's disease-related panuveitis following COVID-19 vaccination: A case report. *World J Radiol* 2024; 16(9): 460-465

URL: <https://www.wjgnet.com/1949-8470/full/v16/i9/460.htm>

DOI: <https://dx.doi.org/10.4329/wjr.v16.i9.460>

INTRODUCTION

Uveitis, a term used to describe inflammation of the uvea, can lead to significant vision loss if not diagnosed promptly and managed appropriately[1]. It can be triggered by various causes, including infections, autoimmune diseases, malignancies, and possibly, vaccines[2]. This array of etiologies highlights the complexity and the importance of recognizing the presenting symptoms of uveitis to guide effective management.

Behcet's disease, an inflammatory disorder of unknown cause, is one of the systemic diseases that can lead to uveitis [3]. The disease is characterized by recurrent oral and genital ulcers, skin lesions, and uveitis. Genetic predisposition, particularly the presence of HLA-B51, has been associated with Behcet's disease[4]. With the ongoing global coronavirus disease 2019 (COVID-19) pandemic, the focus of medical attention has recently been on vaccines, particularly mRNA vaccines, as a potential trigger for uveitis[5]. These vaccines, including the mRNA-1273 severe acute respiratory syndrome coronavirus 2 (SARS-CoV-2) vaccine (Moderna), have proven to be highly effective in combating the spread of the SARS-CoV-2. However, a handful of cases have reported the onset or recurrence of uveitis following the administration of these vaccines. In this article, we present a unique case of a 30-year-old Taiwanese male patient who experienced recurrent uveitis following administration of the mRNA-1273 vaccine. The case provides an opportunity to explore and elucidate potential links between COVID-19 vaccination and the onset or exacerbation of uveitis.

CASE PRESENTATION

Chief complaints

A 30-year-old healthy Taiwanese man visited the clinic with a complaint of foggy vision for about 5 d in both eyes.

History of present illness

The patient complained of foggy vision in both eyes approximately 1 wk after receiving his first dose of the mRNA-1273 SARS-CoV-2 vaccine (Moderna).

History of past illness

The patient's medical history was devoid of any conditions, including the absence of other diseases such as hypertension, diabetes mellitus, heart disease, or tuberculosis. However, since his adulthood, he had recurrent episodes of oral ulceration occurring approximately every 2 months.

Personal and family history

The patient reported no family history of any disease or cancerous growth.

Physical examination

At the time of presentation, the patient's best-corrected visual acuity (BCVA) was 20/25 in the right eye and 20/20 in the left eye. Intraocular pressures were within the normal range in both eyes. On examination, bilateral fine keratic precipitates were observed, along with 3+ cells in the anterior chamber (AC) and 2+ cells in the anterior vitreous body of the right eye. Additionally, trace cells were noted in the AC, along with 1+ cells in the anterior vitreous of the left eye. In addition to intraocular inflammation, oral ulcer and genital ulcer were found in this patient.

Laboratory examinations

Laboratory investigations for infectious and inflammatory causes were all unremarkable, except for a slightly elevated erythrocyte sedimentation rate (18 mm/h) and a positive result for HLA-B51.

Imaging examinations

Fundus examination revealed prominent vitreous haze of the right eye and disc congestion and venous engorgement in both eyes (Figure 1A and B).

Optical coherence tomography (OCT) demonstrated prominent bilateral disc edema (Figure 1C and D) and increased thickness of the inner retina in the macula of the right eye (Figure 1E and F). Fluorescein angiography (FA) revealed predominant phlebitis with perivascular staining at the periphery in both eyes (Figure 1G-J).

FINAL DIAGNOSIS

According to the international criteria for Behcet's disease, all these features were consistent with a diagnosis of Behcet's disease.

TREATMENT

The patient was initiated on topical 1% prednisolone acetate suspension, administered four times daily, and oral prednisolone at a dose of 40 mg per day.

OUTCOME AND FOLLOW-UP

Two weeks after the treatment, the BCVA improved to 20/20 in both eyes. The cells in the AC were reduced to trace in the right eye and were clear in the left eye. Fundus examination showed resolution of vitreous haze of the right eye and disc congestion in both eyes (Figure 1K and L). Four weeks after the initial treatment, the BCVA remained at 20/20 in both eyes. In the right eye, there were trace cells in the AC and anterior vitreous body, while both the AC and anterior vitreous body in the left eye were clear. Oral prednisolone was gradually tapered to a lower dose. However, as the patient and his wife were planning to undergo *in vitro* fertilization, he did not receive immunomodulatory therapy due to potential teratogenic side effects. Additionally, we delayed administering the patient's second dose of vaccine because the inflammation within his eye had not completely resolved. The patient was maintained on 7.5 mg of oral prednisolone, and his eye condition remained stable thereafter.

Unfortunately, 6 mo after the initial episode of uveitis, the patient experienced a recurrence of foggy vision in both eyes, approximately 1 wk after receiving his second dose of mRNA-1273 SARS-CoV-2 vaccine (Moderna). At the time of recurrence, his BCVA was 20/30 in the right eye and 20/25 in the left eye. Examination revealed 3+ cells in the AC, 2+ cells in the anterior vitreous body of the right eye, and 1+ cells in the AC and 1+ cells in the anterior vitreous body of the left eye. The patient was once again treated with topical 1% prednisolone acetate suspension administered four times daily, along with oral prednisolone at a dose of 40 mg per day. One week after treatment, the BCVA improved to 20/25 in the right eye and 20/20 in the left eye. The cells in the AC and anterior vitreous body decreased to 1+ in the right eye and trace in the left eye. Two weeks after treatment, the BCVA in both eyes was 20/20. The cells in the AC and anterior vitreous body were trace in the right eye, while the AC and anterior vitreous body were clear in the left eye. Oral prednisolone was tapered gradually to a lower dose.

The patient is currently maintained on a daily dose of 7.5 mg of oral prednisolone, and the condition of both eyes has remained stable without any recurrence over the following 18 mo. Timeline of the disease course of this patient is illustrated in Figure 2.

DISCUSSION

This case raises the possibility of an association between mRNA-based COVID-19 vaccines and the development of panuveitis as the first manifestation of Behcet's disease in susceptible individuals. Behcet's disease is a rare systemic vasculitis with ocular involvement, typically uveitis, occurring in approximately 50%-70% of patients[6]. Panuveitis is a more severe form of uveitis, involving inflammation of the entire uveal tract, and is associated with poorer visual prognosis[7]. The exact etiology of Behcet's disease is unknown, but it is believed to involve genetic and environmental factors, as well as dysregulation of immune responses. The HLA-B51 allele is strongly associated with Behcet's disease[8], and it is hypothesized that exposure to certain environmental factors or infections may trigger an immune response in genetically susceptible individuals, leading to the development of the disease.

The role of vaccines in triggering autoimmune and inflammatory reactions has been previously reported[9]. In our case, the patient developed panuveitis following two mRNA-based COVID-19 vaccine administrations, suggesting a potential association. The mRNA vaccines have a novel mechanism of action, as they introduce synthetic mRNA

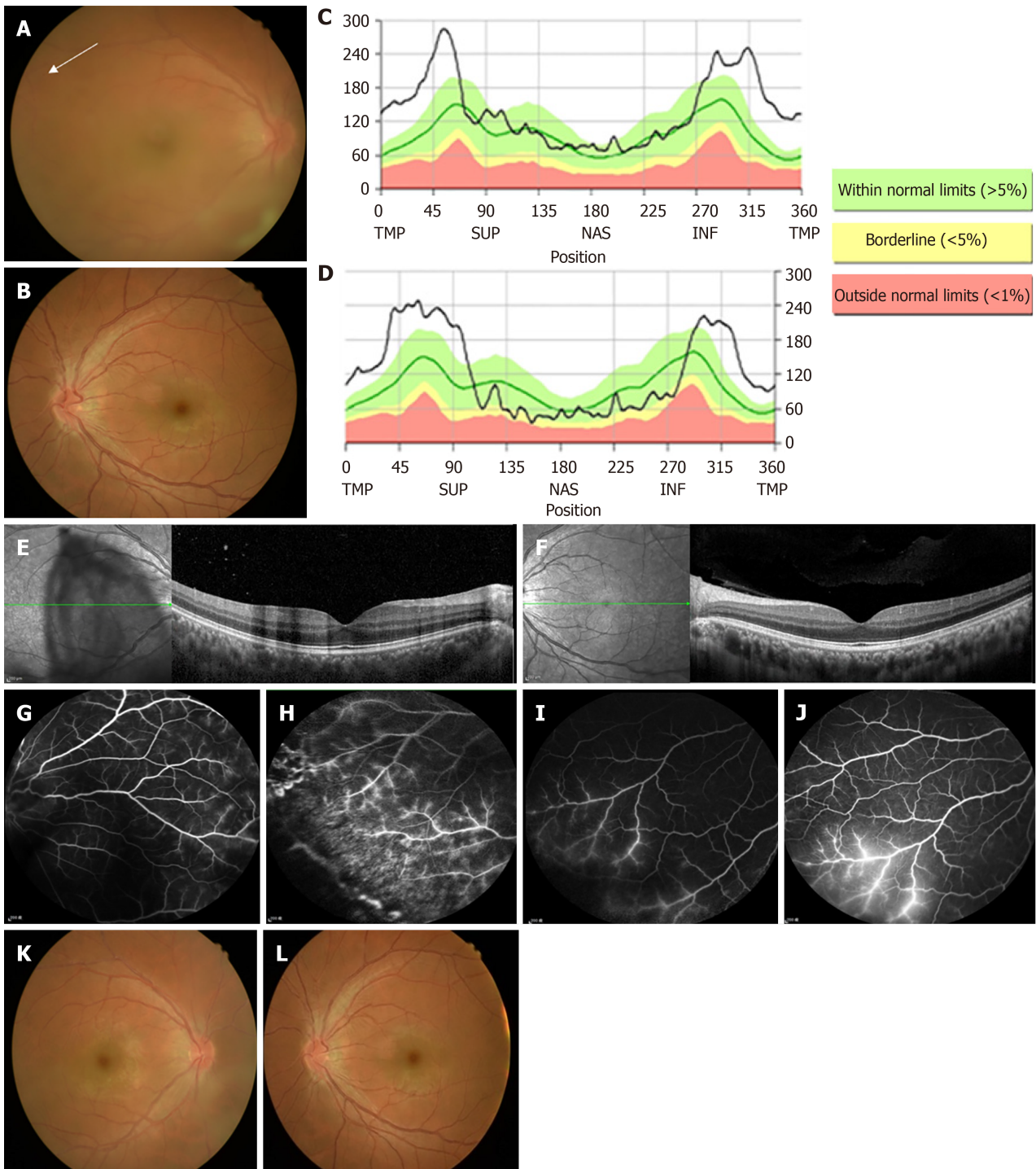


Figure 1 Fundus examination. A and B: Fundus photographs revealing disc congestion, venous engorgement, and retinal hemorrhage at periphery (white arrow) in right eye (A) and left eye (B); C-F: Optical coherence tomography showed prominent bilateral disc edema (C and D) and increased inner retina thickness of macula in his right eye (E). The thickness of the left macula was unremarkable (F); G-J: Fluorescein angiography disclosed predominant phlebitis with perivascular staining at periphery in right eye (G and H) and left eye (I and J); K and L: Two weeks after treatment, the fundus of both eyes had cleared up.

encoding the SARS-CoV-2 spike protein, which then leads to the production of the protein and an immune response[10]. It is possible that in genetically predisposed individuals, the immune response to the vaccine could trigger an aberrant reaction, leading to the development of Behcet's disease and panuveitis. However, the exact mechanism underlying this association remains unknown. This case report raises several important questions. First, it highlights the need for further research to determine whether mRNA-based COVID-19 vaccines can trigger panuveitis as the first manifestation of Behcet's disease in susceptible individuals. Second, it emphasizes the importance of a comprehensive evaluation for underlying systemic diseases in patients presenting with panuveitis following vaccination. Finally, this case underscores the need for a tailored approach to the management of Behcet's disease-associated panuveitis, taking into consideration the potential risks and benefits of immunosuppressive therapy.

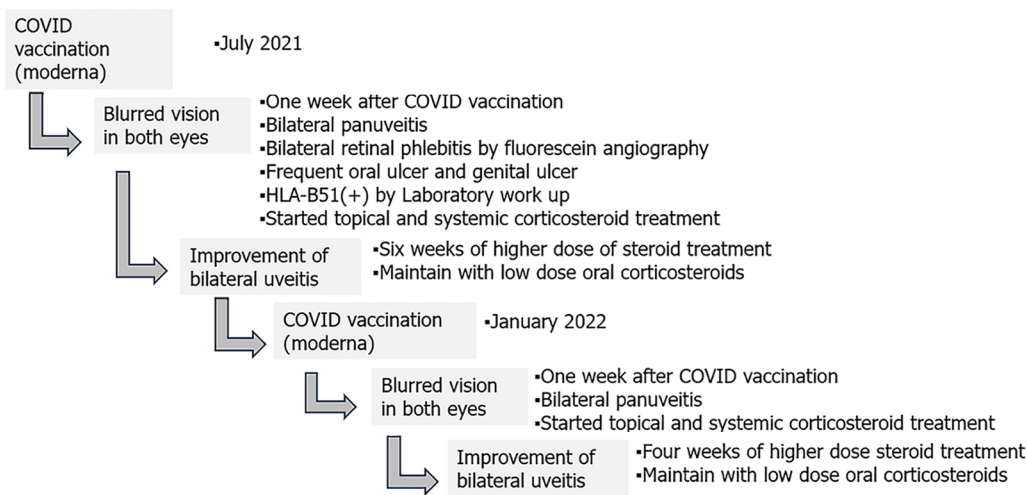


Figure 2 The patient’s timeline. COVID: Coronavirus disease.

In addition to ocular adverse effects, the majority of adverse effects reported following Moderna vaccine administration are mild to moderate. Common adverse effects are injection site reactions (pain, swelling, and redness), fatigue, headache, muscle pain, fever, *etc.* These effects are generally considered signs of the body's immune response to the vaccine and are not a cause for significant concern[11]. Some less frequent but notable adverse effects have been reported, including lymphadenopathy and delayed local reactions[12]. While rare, some serious adverse effects have been associated with the Moderna vaccine such as anaphylaxis[13], myocarditis and pericarditis[14], and thrombosis with thrombocytopenia syndrome[15]. Most vaccine-associated adverse effects resolve within days to weeks after treatment. However, there are also rare side effects that can cause long-term effects. Long post-COVID vaccination syndrome (LPCVS) is a rare but severe adverse effect, causing patients to develop various neurocognitive symptoms, including headache, dizziness, and impaired thinking and concentration, and there is no effective treatment so far[16].

CONCLUSION

In summary, we present a unique case of panuveitis as the first manifestation of Behcet's disease following mRNA-based COVID-19 vaccination. Although the association between mRNA-based COVID-19 vaccines and panuveitis in Behcet's disease remains to be confirmed, this case highlights the importance of considering such a possibility in the evaluation and management of patients with similar presentations. Further studies are needed to elucidate the underlying mechanisms and establish a definitive causal relationship between mRNA-based COVID-19 vaccines and the development of panuveitis in Behcet's disease.

ACKNOWLEDGEMENTS

We would like to express our gratitude to our patient and his family for allowing us to publish this case report.

FOOTNOTES

Author contributions: Lin RT and Chang YC were the major contributor in writing the manuscript and reviewing the literature; Liu PK, Chang CW, Cheng KC, and Chen KJ created the figures and patient images; Chang YC was the chief physician of the patient. All authors revised the manuscript and approved the final version.

Informed consent statement: Informed written consent was obtained from the patient for the publication of this case report.

Conflict-of-interest statement: All authors declare that there are no conflicts of interest for this paper.

CARE Checklist (2016) statement: The authors have read the CARE Checklist (2016), and the manuscript was prepared and revised according to the CARE Checklist (2016).

Open-Access: This article is an open-access article that was selected by an in-house editor and fully peer-reviewed by external reviewers. It is distributed in accordance with the Creative Commons Attribution NonCommercial (CC BY-NC 4.0) license, which permits others to distribute, remix, adapt, build upon this work non-commercially, and license their derivative works on different terms, provided the original work is properly cited and the use is non-commercial. See: <https://creativecommons.org/licenses/by-nc/4.0/>

Country of origin: Taiwan

ORCID number: Yo-Chen Chang 0000-0001-8751-3148.

Corresponding Author's Membership in Professional Societies: The Ophthalmological Society of Taiwan, A1261; Taiwan Academy of Ophthalmology, M0121.

S-Editor: Liu JH

L-Editor: Wang TQ

P-Editor: Yu HG

REFERENCES

- 1 **Bodaghi B**, Cassoux N, Wechsler B, Hannouche D, Fardeau C, Papo T, Huong DL, Piette JC, LeHoang P. Chronic severe uveitis: etiology and visual outcome in 927 patients from a single center. *Medicine (Baltimore)* 2001; **80**: 263-270 [PMID: 11470987 DOI: 10.1097/00005792-200107000-00005]
- 2 **Gritz DC**, Wong IG. Incidence and prevalence of uveitis in Northern California; the Northern California Epidemiology of Uveitis Study. *Ophthalmology* 2004; **111**: 491-500; discussion 500 [PMID: 15019324 DOI: 10.1016/j.ophtha.2003.06.014]
- 3 **Davatchi F**, Chams-Davatchi C, Shams H, Shahram F, Nadji A, Akhlaghi M, Faezi T, Ghodsi Z, Sadeghi Abdollahi B, Ashofteh F, Mohtasham N, Kavosi H, Masoumi M. Behçet's disease: epidemiology, clinical manifestations, and diagnosis. *Expert Rev Clin Immunol* 2017; **13**: 57-65 [PMID: 27351485 DOI: 10.1080/1744666X.2016.1205486]
- 4 **de Menthon M**, Lavalley MP, Maldini C, Guillevin L, Mahr A. HLA-B51/B5 and the risk of Behçet's disease: a systematic review and meta-analysis of case-control genetic association studies. *Arthritis Rheum* 2009; **61**: 1287-1296 [PMID: 19790126 DOI: 10.1002/art.24642]
- 5 **Bacherini D**, Biagini I, Lenzetti C, Virgili G, Rizzo S, Giansanti F. The COVID-19 Pandemic from an Ophthalmologist's Perspective. *Trends Mol Med* 2020; **26**: 529-531 [PMID: 32470381 DOI: 10.1016/j.molmed.2020.03.008]
- 6 **Evereklioglu C**. Current concepts in the etiology and treatment of Behçet disease. *Surv Ophthalmol* 2005; **50**: 297-350 [PMID: 15967189 DOI: 10.1016/j.survophthal.2005.04.009]
- 7 **Belkhadir K**, Boutimzine N, Laghmar M, Amazouzi A, Tachfouti S, Cherkaoui O. [Prognostic factors of ocular involvement in Behçet's disease]. *J Fr Ophtalmol* 2019; **42**: 612-617 [PMID: 31088739 DOI: 10.1016/j.jfo.2019.03.009]
- 8 **Direskeneli H**. Behçet's disease: infectious aetiology, new autoantigens, and HLA-B51. *Ann Rheum Dis* 2001; **60**: 996-1002 [PMID: 11602462 DOI: 10.1136/ard.60.11.996]
- 9 **Yasaka Y**, Hasegawa E, Keino H, Usui Y, Maruyama K, Yamamoto Y, Kaburaki T, Iwata D, Takeuchi M, Kusahara S, Takase H, Nagata K, Yanai R, Kaneko Y, Iwahashi C, Fukushima A, Ohguro N, Sonoda KH; JOIS Uveitis Survey Working Group. A multicenter study of ocular inflammation after COVID-19 vaccination. *Jpn J Ophthalmol* 2023; **67**: 14-21 [PMID: 36417027 DOI: 10.1007/s10384-022-00962-9]
- 10 **Corbett KS**, Edwards DK, Leist SR, Abiona OM, Boyoglu-Barnum S, Gillespie RA, Himansu S, Schäfer A, Ziwawo CT, DiPiazza AT, Dinnon KH, Elbashir SM, Shaw CA, Woods A, Fritch EJ, Martinez DR, Bock KW, Minai M, Nagata BM, Hutchinson GB, Wu K, Henry C, Bahl K, Garcia-Dominguez D, Ma L, Renzi I, Kong WP, Schmidt SD, Wang L, Zhang Y, Phung E, Chang LA, Loomis RJ, Altaras NE, Narayanan E, Metkar M, Presnyak V, Liu C, Louder MK, Shi W, Leung K, Yang ES, West A, Gully KL, Stevens LJ, Wang N, Wrapp D, Doria-Rose NA, Stewart-Jones G, Bennett H, Alvarado GS, Nason MC, Ruckwardt TJ, McLellan JS, Denison MR, Chappell JD, Moore IN, Morabito KM, Mascola JR, Baric RS, Carfi A, Graham BS. SARS-CoV-2 mRNA vaccine design enabled by prototype pathogen preparedness. *Nature* 2020; **586**: 567-571 [PMID: 32756549 DOI: 10.1038/s41586-020-2622-0]
- 11 **Baden LR**, El Sahly HM, Essink B, Kotloff K, Frey S, Novak R, Diemert D, Spector SA, Rouphael N, Creech CB, McGettigan J, Khetan S, Segall N, Solis J, Brosz A, Fierro C, Schwartz H, Neuzil K, Corey L, Gilbert P, Janes H, Follmann D, Marovich M, Mascola J, Polakowski L, Ledgerwood J, Graham BS, Bennett H, Pajon R, Knightly C, Leav B, Deng W, Zhou H, Han S, Ivarsson M, Miller J, Zaks T; COVE Study Group. Efficacy and Safety of the mRNA-1273 SARS-CoV-2 Vaccine. *N Engl J Med* 2021; **384**: 403-416 [PMID: 33378609 DOI: 10.1056/NEJMoa2035389]
- 12 **Blumenthal KG**, Freeman EE, Saff RR, Robinson LB, Wolfson AR, Foreman RK, Hashimoto D, Banerji A, Li L, Anvari S, Shenoy ES. Delayed Large Local Reactions to mRNA-1273 Vaccine against SARS-CoV-2. *N Engl J Med* 2021; **384**: 1273-1277 [PMID: 33657292 DOI: 10.1056/NEJMc2102131]
- 13 **Shimabukuro TT**, Cole M, Su JR. Reports of Anaphylaxis After Receipt of mRNA COVID-19 Vaccines in the US-December 14, 2020-January 18, 2021. *JAMA* 2021; **325**: 1101-1102 [PMID: 33576785 DOI: 10.1001/jama.2021.1967]
- 14 **Gargano JW**, Wallace M, Hadler SC, Langley G, Su JR, Oster ME, Broder KR, Gee J, Weintraub E, Shimabukuro T, Scobie HM, Moulia D, Markowitz LE, Wharton M, McNally VV, Romero JR, Talbot HK, Lee GM, Daley MF, Oliver SE. Use of mRNA COVID-19 Vaccine After Reports of Myocarditis Among Vaccine Recipients: Update from the Advisory Committee on Immunization Practices - United States, June 2021. *MMWR Morb Mortal Wkly Rep* 2021; **70**: 977-982 [PMID: 34237049 DOI: 10.15585/mmwr.mm7027e2]
- 15 **MacNeil JR**, Su JR, Broder KR, Guh AY, Gargano JW, Wallace M, Hadler SC, Scobie HM, Blain AE, Moulia D, Daley MF, McNally VV, Romero JR, Talbot HK, Lee GM, Bell BP, Oliver SE. Updated Recommendations from the Advisory Committee on Immunization Practices for Use of the Janssen (Johnson & Johnson) COVID-19 Vaccine After Reports of Thrombosis with Thrombocytopenia Syndrome Among Vaccine Recipients - United States, April 2021. *MMWR Morb Mortal Wkly Rep* 2021; **70**: 651-656 [PMID: 33914723 DOI: 10.15585/mmwr.mm7017e4]
- 16 **Finsterer J**. A Case Report: Long Post-COVID Vaccination Syndrome During the Eleven Months After the Third Moderna Dose. *Cureus* 2022; **14**: e32433 [PMID: 36644105 DOI: 10.7759/cureus.32433]

Hyperparathyroidism presented as multiple pulmonary nodules in hemodialysis patient status post parathyroidectomy: A case report

Ping-Han Chiang, Kai-Hsiung Ko, Yi-Jen Peng, Tsai-Wang Huang, Shih-En Tang

Specialty type: Radiology, nuclear medicine and medical imaging

Provenance and peer review:

Unsolicited article; Externally peer reviewed.

Peer-review model: Single blind

Peer-review report's classification

Scientific Quality: Grade D

Novelty: Grade B

Creativity or Innovation: Grade B

Scientific Significance: Grade C

P-Reviewer: He XH

Received: June 15, 2024

Revised: August 7, 2024

Accepted: August 28, 2024

Published online: September 28, 2024

Processing time: 103 Days and 14.8 Hours



Ping-Han Chiang, Department of Surgery, Tri-Service General Hospital, Taipei 114202, Taiwan

Kai-Hsiung Ko, Department of Radiology, National Defense Medical Center, Tri-Service General Hospital, Taipei 114, Taiwan

Yi-Jen Peng, Department of Pathology, Tri-Service General Hospital, National Defense Medical Center, Taipei 114, Taiwan

Tsai-Wang Huang, Division of Thoracic Surgery, Department of Surgery, Tri-Service General Hospital, National Defense Medical Center, Taipei 114202, Taiwan

Shih-En Tang, Division of Thoracic Medicine, Department of Internal Medicine, Tri-Service General Hospital, Taipei 114202, Taiwan

Corresponding author: Tsai-Wang Huang, MD, PhD, Attending Doctor, Chief Doctor, Surgeon, Division of Thoracic Surgery, Department of Surgery, Tri-Service General Hospital, National Defense Medical Center, No. 325 Section 2, Chenggong Road, Neihu District, Taipei 114202, Taiwan. chi-wang@yahoo.com.tw

Abstract

BACKGROUND

Primary hyperparathyroidism is typically caused by a single parathyroid adenoma. Ectopic parathyroid adenomas occur as well, with cases involving various sites, including the mediastinum, presenting in varying frequencies. Secondary hyperparathyroidism develops in the context of chronic kidney disease, primarily due to vitamin D deficiency, hypocalcemia, and hyperphosphatemia. It is frequently diagnosed in patients undergoing dialysis. This article presents a rare case of hyperparathyroidism involving multiple hyperplastic parathyroid glands with pulmonary seeding in a 50-year-old female patient undergoing hemodialysis (HD).

CASE SUMMARY

The patient had a history of parathyroidectomy 10 years prior but developed recurrent hyperparathyroidism with symptoms of pruritus and cough with sputum during a period of routine dialysis. Radiographic imaging revealed multiple nodules in both lungs, with the largest measuring approximately 1.35 cm. Surgical histopathology confirmed the presence of hyperplastic parathyroid glands within the pulmonary tissue. After tumor resection surgery *via* video-assisted thoracic surgery with wedge resection, the patient was discharged in

stable condition and in follow-up her symptoms showed improvement.

CONCLUSION

This article describes hyperparathyroidism presenting as pulmonary nodules in a patient undergoing post-parathyroidectomy HD, highlighting diagnostic challenges and a positive outcome from tumor resection surgery.

Key Words: Hypertension; End-stage renal disease; Hyperparathyroidism; Pulmonary nodules; Hemodialysis; Video-assisted thoracic surgery; Hyperplastic parathyroid glands; Case report

©The Author(s) 2024. Published by Baishideng Publishing Group Inc. All rights reserved.

Core Tip: This case highlights a rare occurrence of hyperplastic parathyroid gland seeding in pulmonary tissue in a patient with end-stage renal disease and recurrent hyperparathyroidism. The study underscores the diagnostic challenge posed by atypical presentations of hyperparathyroidism in patients undergoing dialysis, emphasizing the crucial role of comprehensive imaging and histopathological examination. Surgical resection proved effective in alleviating symptoms, suggesting its therapeutic utility in managing such complex cases. Further research is needed to refine management strategies and improve outcomes for similar clinical scenarios.

Citation: Chiang PH, Ko KH, Peng YJ, Huang TW, Tang SE. Hyperparathyroidism presented as multiple pulmonary nodules in hemodialysis patient status post parathyroidectomy: A case report. *World J Radiol* 2024; 16(9): 466-472

URL: <https://www.wjgnet.com/1949-8470/full/v16/i9/466.htm>

DOI: <https://dx.doi.org/10.4329/wjr.v16.i9.466>

INTRODUCTION

There are many conditions that can cause hyperparathyroidism. In primary hyperparathyroidism, 85% of cases are caused by a single parathyroid adenoma[1] and are almost always due to benign overgrowth of parathyroid tissue as a single gland (80% of cases) or as a multiple gland disorder (15%-20% of cases)[2]. Ectopic parathyroid adenomas are occasionally found in the mediastinum (28% paraesophageal, 26% in the mediastinum, 24% intrathymic, 11% intrathoroidal, 9% in the carotid sheath, and 2% in a high cervical position)[3]. In contrast to primary hyperparathyroidism, secondary hyperparathyroidism develops in chronic kidney disease due to a combination of vitamin D deficiency, hypocalcemia, and hyperphosphatemia, with most patients diagnosed undergoing dialysis[4]. Tertiary hyperparathyroidism develops as a result of prolonged secondary hyperparathyroidism and is characterized by excessive secretion of parathyroid hormone after longstanding secondary hyperparathyroidism, in which hypercalcemia has ensued.

Herein, we describe a rare case of a patient undergoing hemodialysis (HD) who was diagnosed with hyperparathyroidism presenting as multiple pulmonary nodules.

CASE PRESENTATION

Chief complaints

A 50-year-old female patient presented with complaints of itchy skin and cough with sputum experienced during routine HD.

History of present illness

The symptoms of itching skin and cough with sputum had persisted for several months during the routine HD treatment for pre-existing severe renal failure due to chronic kidney disease, which had been diagnosed decades previously with dialysis initiated in 1987. The persistence of these symptoms had caused her to seek help at our thoracic medicine outpatient department. A chest x-ray taken at admission revealed bilateral opacities over her lungs, prompting admission for further evaluation and treatment.

History of past illness

The patient had a decades-long history of hypertension (the precise start-date was lost to time) and end-stage renal disease which initiated in 1987. She developed tertiary hyperparathyroidism post-parathyroidectomy under regular HD.

Personal and family history

The patient reported no abnormal past medical or family history.

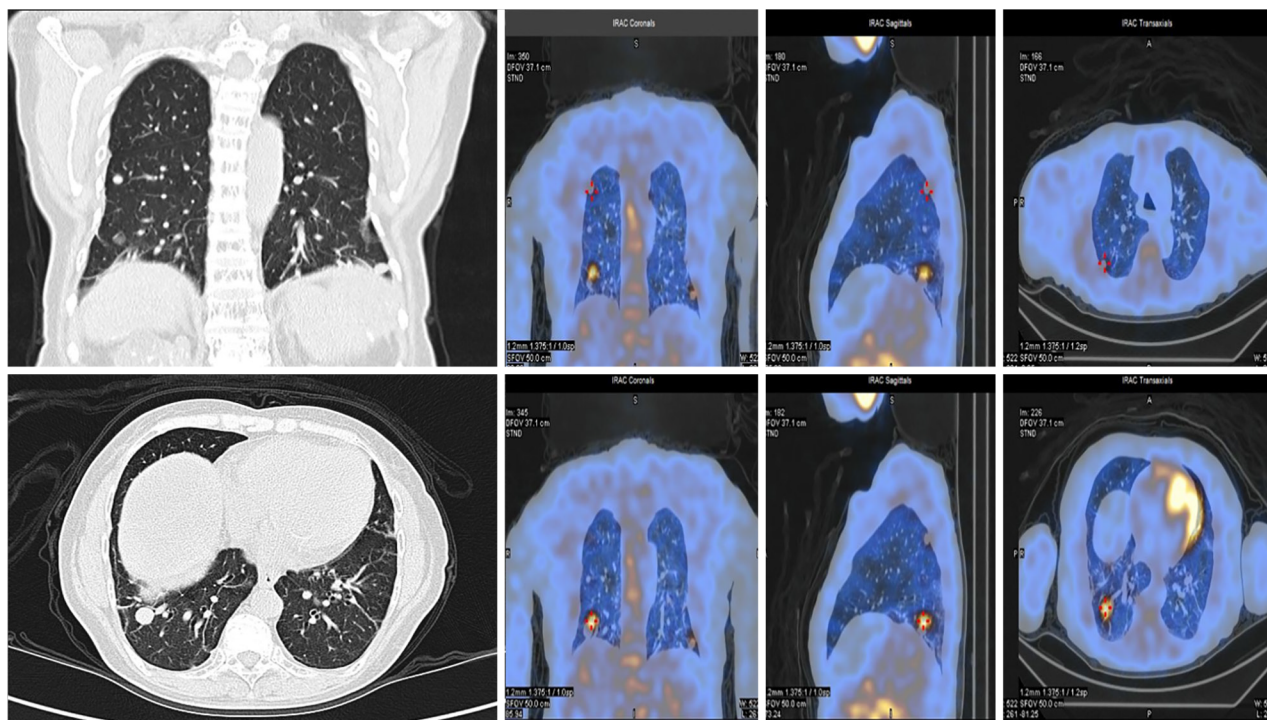


Figure 1 Chest computed tomography. Multiple nodules are apparent in the lung area, and 99mTc-methoxyisobutyl-isonitrile scintillation scan showed accumulation of radioactive isotopes over the lesions.

Physical examination

Skin turgor was normal with no skin rash or ecchymosis. There was no jugular vein engorgement, lymph node enlargement, or palpable goiter in the neck region. Lung inspection showed symmetrical and full expansion with bilateral rales detected on auscultation but no wheezing. Overall, no abnormal findings were noted upon physical examination at admission.

Laboratory examinations

The complete blood count and differential blood count results were normal. Other relevant blood tests revealed the following abnormal results: (1) Creatinine at 8.4 mg/dL (normal range: 0.5-0.9 mg/dL); (2) Serum parathyroid hormone at 1891 pg/mL (normal range: 10-69 pg/dL); and (3) Calcium at 10.3 mg/dL (normal range: 8.6-10.2 mg/dL). The following tests were performed and results were found to be in the normal range: (1) Thyroid stimulating hormone at 0.49 IU/mL (normal range: 0.25-5.00 IU/mL); (2) Free-T4 at 1.12 ng/mL (normal range: 0.89-1.78 ng/mL); and (3) Thyroglobulin at 20.06 ng/mL (normal range: 0-25.00 ng/mL). These results indicated that the patient had hyperparathyroidism, though the underlying cause had yet to be determined.

Imaging examinations

The chest x-ray revealed several bilateral opacities in the lungs. A contrast-enhanced computed tomography (CT) scan of the chest identified multiple nodules in both lungs, with the largest nodule measuring approximately 1.35 cm (Figure 1). A methoxyisobutyl-isonitrile (MIBI) scan was performed and did not reveal any significant abnormalities except for the presence of multiple pulmonary nodules with dominant MIBI uptake in the lung regions (Figure 1). These findings suggested the possibility of pulmonary malignancy or metastases. A neck ultrasound revealed a normally sized thyroid gland with a multinodular goiter (Figure 2). A CT scan of the neck did not clearly identify the parathyroid glands.

FINAL DIAGNOSIS

The tentative diagnosis was multiple pulmonary nodules in bilateral lungs with the nature of the nodules unknown (Figure 3). Surgical intervention was required to obtain pathological evidence to inform the final diagnosis. After surgery, the final diagnosis was hyperparathyroidism presenting with multiple pulmonary nodules.

TREATMENT

Video-assisted thoracic surgery [commonly referred to as video-assisted thoracic surgery (VATS)] with wedge resection

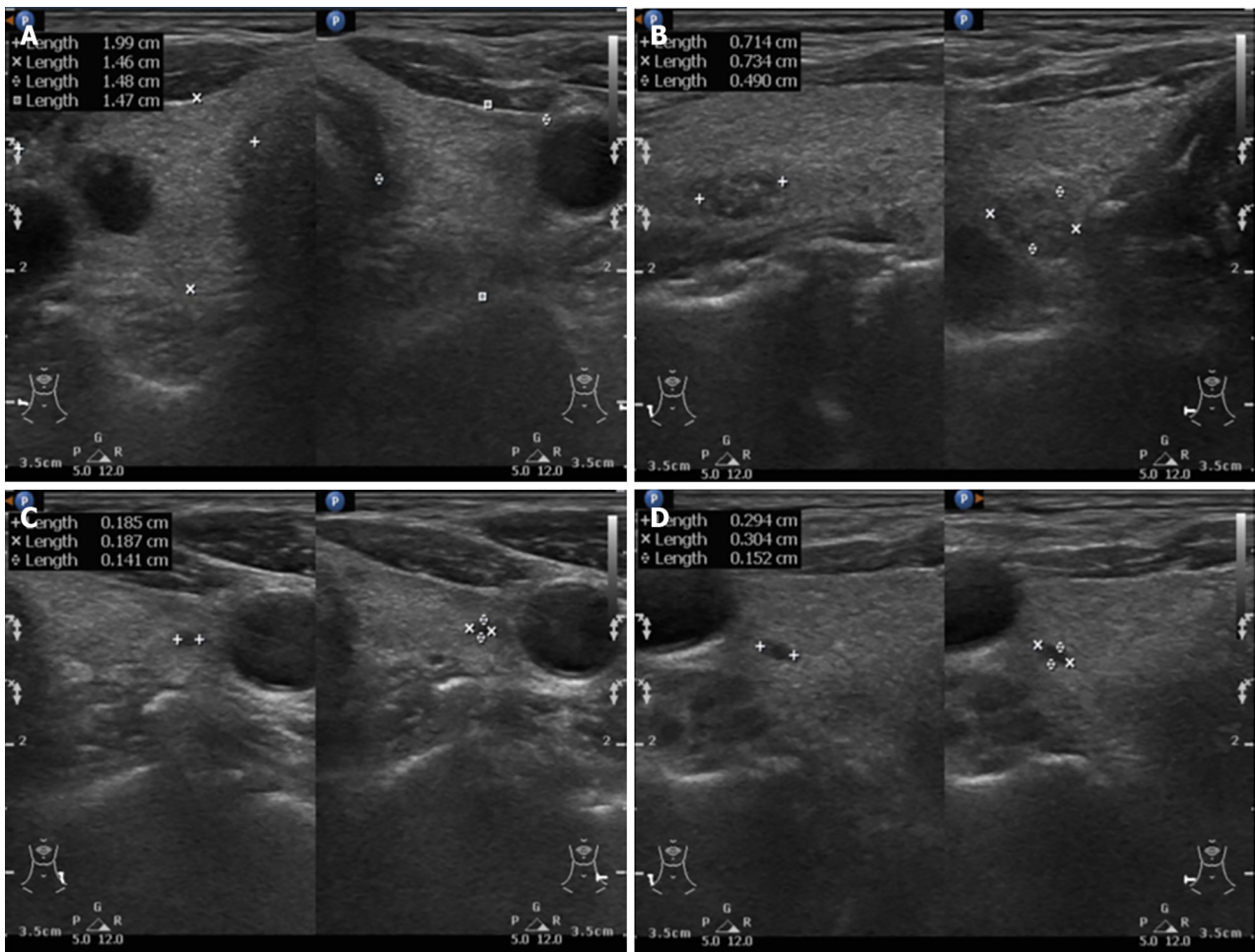


Figure 2 Neck sonography shows right and left lobe thyroid and multinodular goiter. A: Right and left lobe thyroid; B: Right side nodular goiter 0.73 cm × 0.49 cm × 0.71 cm; C: Left side nodular goiter 0.18 cm × 0.14 cm × 0.18 cm; D: Right side nodular goiter 0.30 cm × 0.15 cm × 0.29 cm.

was performed on the right side to remove the ectopic hyperplastic parathyroid gland tissue and to obtain samples for diagnosis. After the two nodules were resected from the right side, the one nodule on the other side was left intact.

OUTCOME AND FOLLOW-UP

At 14 days after surgery, the patient was discharged from the hospital in stable condition. The 14-day postoperative recovery was favorable with a noticeable improvement in symptoms, which continued throughout the 3 years of follow-up. Surgical intervention allowed for the acquisition of valuable tissue samples that contributed to the final diagnosis and management of her condition. The patient was advised on follow-up care (wound care) and monitoring (outpatient department blood exams) to ensure continued recovery and to address any further needs as part of her treatment plan.

DISCUSSION

Before surgery, imaging studies were conducted to locate the lesion. A chest x-ray revealed multiple nodules in the lung area, with the largest measuring approximately 1.35 cm. These nodules appeared round and well-defined. Additionally, ^{99m}Tc -MIBI scintillation scans indicated the accumulation of radioactive isotopes in the suspected right lower lobe lung tumor (Figure 1). Previous studies demonstrated that some lesions such as primary lung cancers show an accumulation of MIBI[5,6], and others have suggested that ^{99m}Tc -MIBI could be useful to differentiate between benign and malignant lesions for solitary pulmonary nodules[7,8]. Under the impression that the patient had multiple pulmonary bilateral nodules in the lungs, we arranged VATS with wedge resection of the right lung for pathological confirmation and to remove the nodule tissue. Surprisingly, the postoperative pathological results were hyperplastic parathyroid gland with pulmonary seeding. Within 14 days after the operation, the patient's symptoms subsided.

Differential diagnosis included ectopic parathyroid glands and malignant carcinoma. However, ectopic adenomas are usually located in the paraesophageal area or mediastinum as a single lesion[9]. To the best of our knowledge, there are only a few reports of ectopic parathyroid glands in lung tissue[9]. However, it is difficult to make a precise pathological

Table 1 Cases of hyperparathyroidism due to parathyroid hyperplasia or adenomas extending to the lungs

Case report title	Year	Lesion	Treatment	Outcome
Persistent hyperparathyroidism secondary to ectopic parathyroid adenoma in lung: Case report[15]	2022	Right side	Video-assisted thoracic surgery	Symptom improved
Recurrent hyperparathyroidism due to parathyroid and pulmonary tumors showing features of parathyroid adenoma[9]	2020	Right side	Surgically removed	Symptom improved
A patient with lung ectopic parathyroid coexistent with primary hyperparathyroidism and end-stage renal diseases[16]	2014	Mono-side	Surgically removed	Symptom improved

hyperparathyroidism presenting as multiple pulmonary nodules in a HD patient is likely.

CONCLUSION

In conclusion, we present a rare case of hyperparathyroidism stemming from multiple hyperplastic parathyroid glands with pulmonary seeding. This underscores the importance of comprehensive evaluation in HD patients presenting with hyperparathyroidism. Diagnostic measures such as neck ultrasound and chest CT should be employed to assess the possibility of parathyroid hyperplasia or adenomas extending to the lungs. If there is a chance of hyperplastic parathyroid glands with pulmonary seeding, surgical removal could be a good option for symptom improvement and to confirm pathological findings. Moreover, integrating clinical data with imaging findings is crucial for gauging the malignant potential of tumors, apart from pathological findings. It is important to always keep in mind that patients' conditions should be followed after treatment.

FOOTNOTES

Author contributions: Chiang PH organized the patient information, generated the data and wrote the manuscript; Ko KH, Peng YJ, Huang TW, and Tang SE were the patient's attending physicians and participated in clinical and intellectual discussions related to the article; all authors have read and approved the final manuscript.

Informed consent statement: Informed consent was obtained before the article was written.

Conflict-of-interest statement: All authors declare that they have no conflicts of interest.

CARE Checklist (2016) statement: Guidelines of the CARE Checklist (2016) have been adopted.

Open-Access: This article is an open-access article that was selected by an in-house editor and fully peer-reviewed by external reviewers. It is distributed in accordance with the Creative Commons Attribution NonCommercial (CC BY-NC 4.0) license, which permits others to distribute, remix, adapt, build upon this work non-commercially, and license their derivative works on different terms, provided the original work is properly cited and the use is non-commercial. See: <https://creativecommons.org/licenses/by-nc/4.0/>

Country of origin: Taiwan

ORCID number: Ping-Han Chiang 0009-0007-6819-8745; Kai-Hsiung Ko 0000-0002-6562-4901; Yi-Jen Peng 0000-0003-4630-2103; Tsai-Wang Huang 0000-0001-8741-9223.

S-Editor: Luo ML

L-Editor: A

P-Editor: Yu HG

REFERENCES

- 1 **Colognesi A**, de Tullio D, Messina F, Ferrocci G, Stano R, Azzena G. Primary hyperparathyroidism related to a parathyroid adenoma: the dramatic clinical evolution of a misdiagnosed patient and its surgical solution. *Minerva Chir* 2006; **61**: 51-56 [PMID: 16568023]
- 2 **Bilezikian JP**, Bandeira L, Khan A, Cusano NE. Hyperparathyroidism. *Lancet* 2018; **391**: 168-178 [PMID: 28923463 DOI: 10.1016/S0140-6736(17)31430-7]
- 3 **Shen W**, Düren M, Morita E, Higgins C, Duh QY, Siperstein AE, Clark OH. Reoperation for persistent or recurrent primary hyperparathyroidism. *Arch Surg* 1996; **131**: 861-867 [PMID: 8712911 DOI: 10.1001/archsurg.1996.01430200071013]
- 4 **Lau WL**, Obi Y, Kalantar-Zadeh K. Parathyroidectomy in the Management of Secondary Hyperparathyroidism. *Clin J Am Soc Nephrol* 2018; **13**: 952-961 [PMID: 29523679 DOI: 10.2215/CJN.10390917]
- 5 **Santini M**, Fiorello A, Mansi L, Rambaldi PF, Vicidomini G, Busiello L, Messina G, Nargi P. The role of technetium-99m hexakis-2-

- methoxyisobutyl isonitrile in the detection of neoplastic lung lesions. *Eur J Cardiothorac Surg* 2009; **35**: 325-331 [PMID: 18996706 DOI: 10.1016/j.ejcts.2008.09.033]
- 6 **Abdel-Dayem HM**, Scott A, Macapinlac H, Larson S. Tracer imaging in lung cancer. *Eur J Nucl Med* 1994; **21**: 57-81 [PMID: 8088287 DOI: 10.1007/BF00182307]
- 7 **Nikoletic K**, Lucic S, Peter A, Kolarov V, Zeravica R, Srbovan D. Lung 99mTc-MIBI scintigraphy: impact on diagnosis of solitary pulmonary nodule. *Bosn J Basic Med Sci* 2011; **11**: 174-179 [PMID: 21875420 DOI: 10.17305/bjbm.2011.2570]
- 8 **Zhang S**, Liu Y. Diagnostic Performances of 99mTc-Methoxy Isobutyl Isonitrile Scan in Predicting the Malignancy of Lung Lesions: A Meta-Analysis. *Medicine (Baltimore)* 2016; **95**: e3571 [PMID: 27149482 DOI: 10.1097/MD.0000000000003571]
- 9 **Miyauchi R**, Yamada T, Kumano R, Aida Y, Takagi M. Recurrent hyperparathyroidism due to parathyroid and pulmonary tumors showing features of parathyroid adenoma. *Radiol Case Rep* 2020; **15**: 1289-1294 [PMID: 32595814 DOI: 10.1016/j.radcr.2020.05.024]
- 10 **Erickson LA**, Jin L, Wollan P, Thompson GB, van Heerden JA, Lloyd RV. Parathyroid hyperplasia, adenomas, and carcinomas: differential expression of p27Kip1 protein. *Am J Surg Pathol* 1999; **23**: 288-295 [PMID: 10078919 DOI: 10.1097/00000478-199903000-00007]
- 11 **Osawa N**, Onoda N, Kawajiri H, Tezuka K, Takashima T, Ishikawa T, Miyauchi A, Hirokawa M, Wakasa K, Hirakawa K. Diagnosis of parathyroid carcinoma using immunohistochemical staining against hTERT. *Int J Mol Med* 2009; **24**: 733-741 [PMID: 19885612 DOI: 10.3892/ijmm_00000286]
- 12 **Lebastchi AH**, Donovan PI, Udelsman R. Paradigm shift in the surgical management of multigland parathyroid hyperplasia: an individualized approach. *JAMA Surg* 2014; **149**: 1133-1137 [PMID: 25188005 DOI: 10.1001/jamasurg.2014.1296]
- 13 **Neff MS**, Eiser AR, Slifkin RF, Baum M, Baez A, Gupta S, Amarga E. Patients surviving 10 years of hemodialysis. *Am J Med* 1983; **74**: 996-1004 [PMID: 6859068 DOI: 10.1016/0002-9343(83)90799-4]
- 14 **Yu N**, Leese GP, Smith D, Donnan PT. The natural history of treated and untreated primary hyperparathyroidism: the parathyroid epidemiology and audit research study. *QJM* 2011; **104**: 513-521 [PMID: 21266486 DOI: 10.1093/qjmed/hcq261]
- 15 **Valizadeh M**, Ebadijeh A, Amouzegar A, Zakeri A. Persistent hyperparathyroidism secondary to ectopic parathyroid adenoma in lung: Case report. *Front Endocrinol (Lausanne)* 2022; **13**: 988035 [PMID: 36583007 DOI: 10.3389/fendo.2022.988035]
- 16 **Kowalska B**, Lomna-bogdanov E, Pukajlo K, Kaluzny M, Jedrzejuk D, Doskocz K. A patient with lung ectopic parathyroid coexistent with primary hyperparathyroidism and end-stage renal diseases. *EJEA* 2014; **35**: 303 [DOI: 10.1530/endoabs.35.P303]

Secondary rectal linitis plastica caused by prostatic adenocarcinoma - magnetic resonance imaging findings and dissemination pathways: A case report

Andres Antonio Labra, Giancarlo Schiappacasse, Rolando Alfonso Cocio, Jorge Tomás Torres, Fernando Omar González, Joaquin Alberto Cristi, Marcela Schultz

Specialty type: Radiology, nuclear medicine and medical imaging

Provenance and peer review:

Unsolicited article; Externally peer reviewed.

Peer-review model: Single blind

Peer-review report's classification

Scientific Quality: Grade C

Novelty: Grade B

Creativity or Innovation: Grade B

Scientific Significance: Grade B

P-Reviewer: Wu Y

Received: June 19, 2024

Revised: August 28, 2024

Accepted: September 3, 2024

Published online: September 28, 2024

Processing time: 100 Days and 6.5 Hours



Andres Antonio Labra, Giancarlo Schiappacasse, Rolando Alfonso Cocio, Jorge Tomás Torres, Fernando Omar González, Joaquin Alberto Cristi, Department of Radiology, Facultad de Medicina Clínica Alemana-Universidad del Desarrollo, Santiago 7650568, Región Metropolitana, Chile

Marcela Schultz, Department of Pathology, Clínica Alemana de Santiago, Santiago 7650568, Región Metropolitana, Chile

Corresponding author: Jorge Tomás Torres, MD, Department of Radiology, Facultad de Medicina Clínica Alemana-Universidad del Desarrollo, Av. Vitacura 5951, Vitacura, Santiago 7650568, Región Metropolitana, Chile. jttorres@alemana.cl

Abstract

BACKGROUND

Secondary rectal linitis plastica (RLP) from prostatic adenocarcinoma is a rare and poorly understood form of metastatic spread, characterized by a desmoplastic response and concentric rectal wall infiltration with mucosal preservation. This complicates endoscopic diagnosis and can mimic gastrointestinal malignancies. This case series underscores the critical role of magnetic resonance imaging (MRI) in identifying the distinct imaging features of RLP and highlights the importance of considering this condition in the differential diagnosis of patients with a history of prostate cancer.

CASE SUMMARY

Three patients with secondary RLP due to prostatic adenocarcinoma presented with varied clinical features. The first patient, a 76-year-old man with advanced prostate cancer, had rectal pain and incontinence. MRI showed diffuse prostatic invasion and significant rectal wall thickening with a characteristic "target sign" pattern. The second, a 57-year-old asymptomatic man with elevated prostate-specific antigen levels and a history of prostate cancer exhibited rectoprostatic angle involvement and rectal wall thickening on MRI, with positron emission tomography/computed tomography PSMA confirming the prostatic origin of the metastatic spread. The third patient, an 80-year-old post-radical prostatectomy, presented with refractory constipation. MRI revealed a neoplastic mass infiltrating the rectal wall. In all cases, MRI consistently showed stratified thickening,

concentric signal changes, restricted diffusion, and contrast enhancement, which were essential for diagnosing secondary RLP. Biopsies confirmed the prostatic origin of the neoplastic involvement in the rectum.

CONCLUSION

Recognizing MRI findings of secondary RLP is essential for accurate diagnosis and management in prostate cancer patients.

Key Words: Rectal linitis plastica; Prostatic adenocarcinoma; Signet ring cell carcinoma; Metastatic spread; Magnetic resonance imaging; Concentric wall infiltration; Case report

©The Author(s) 2024. Published by Baishideng Publishing Group Inc. All rights reserved.

Core Tip: This study presents three cases of secondary rectal linitis plastica (RLP) due to prostate cancer, emphasizing the rarity and diagnostic challenges of this condition. The preservation of mucosa in RLP complicates endoscopic detection, making magnetic resonance imaging (MRI) crucial for early, accurate diagnosis. MRI findings, including stratified parietal thickening, restricted diffusion, and contrast enhancement, are pivotal in identifying RLP. Recognizing these patterns is essential for timely and appropriate management of metastatic rectal involvement, highlighting the need to consider RLP in patients with a history of prostate cancer.

Citation: Labra AA, Schiappacasse G, Cocio RA, Torres JT, González FO, Cristi JA, Schultz M. Secondary rectal linitis plastica caused by prostatic adenocarcinoma - magnetic resonance imaging findings and dissemination pathways: A case report. *World J Radiol* 2024; 16(9): 473-481

URL: <https://www.wjgnet.com/1949-8470/full/v16/i9/473.htm>

DOI: <https://dx.doi.org/10.4329/wjr.v16.i9.473>

INTRODUCTION

Linitis plastica involves circumferential tumor infiltration of a hollow organ, which generates a desmoplastic reaction, causing stiffness and retraction of its walls[1,2]. The stomach is the most frequently affected organ; however, the small intestine, colon, and rectum can also be invaded[3,4]. The radiological expression of rectal linitis plastica (RLP) is less well known and can be confused with other etiologies, mainly of infectious or actinic inflammatory origin[5].

Secondary RLP caused by prostate neoplasia is a rare form of dissemination and has been poorly reported in the literature[4]. Histologically, it is characterized by an exuberant desmoplastic response, with concentric tumor infiltration of the submucosal, muscular, and subserosal layers, with the integrity of the mucosa[5], resulting in the normal anatomy becoming more pronounced, which has been described *via* magnetic resonance (MR) imaging (MRI) as concentric wall thickening, determining the "target sign" (Figure 1). The preservation of the rectal mucosa complicates its endoscopic diagnosis since epithelial lesions suggesting parietal involvement are not usually identified or are of minimal magnitude [6,7] (Figure 2).

The diagnosis is particularly challenging because these patients are often referred for MRI with a presumptive diagnosis of either inflammatory rectal disease or prostate cancer, leading to an MRI protocol tailored to these conditions. Moreover, diffuse involvement of the rectal layers may be easily overlooked if the referral lacks a precise differential diagnosis. Therefore, recognizing the characteristic MRI findings and understanding the pathways of metastasis from the prostate to the rectum are fundamental to guiding early and accurate diagnosis of RLP, directing therapeutic management to the appropriate stage of secondary pelvic involvement.

Here, we report 3 cases of rectal neoplastic dissemination of the "linitis plastica" type secondary to prostate cancer, which were diagnosed *via* MRI with histological and/or functional confirmation. The objective is to demonstrate the metastatic involvement of the rectum by prostate cancer, with emphasis on the imaging findings on MRI and its routes of dissemination.

CASE PRESENTATION

Chief complaints

Patient 1: A 76-year-old man presented with rectal pain and fecal incontinence.

Patient 2: A 57-year-old asymptomatic man was found to have elevated prostate-specific antigen (PSA) levels during routine follow-up.

Patient 3: An 80-year-old man presented with refractory constipation.

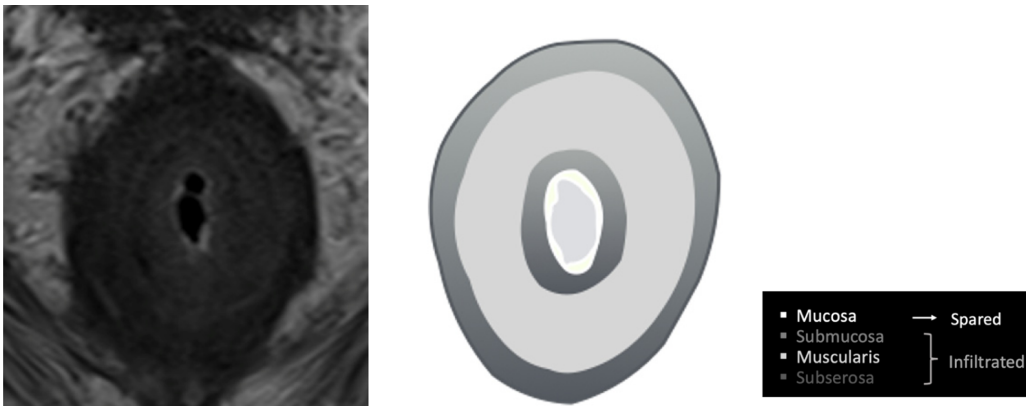


Figure 1 Illustration depicting the concentric "target-like" involvement of the rectal parietal wall due to secondary linitis plastica, with preservation of the mucosa.



Figure 2 The sigmoidoscopy reveals a narrowing of the rectal lumen accompanied by non-ulcerated underlying mucosa. The preserved mucosa complicates endoscopic detection, emphasizing the importance of radiological evaluation for accurate diagnosis.

History of present illness

Patient 1: He reported persistent rectal pain and new-onset fecal incontinence.

Patient 2: He presented with no symptoms.

Patient 3: He developed refractory constipation after initial management.

History of past illness

Patient 1: The patient had been diagnosed with locally advanced prostate cancer with a Gleason score of 5 + 3 and was receiving hormone therapy.

Patient 2: The patient had a history of prostate cancer and was diagnosed *via* systematic transrectal biopsy (Gleason score of 4 + 3).

Patient 3: The patient had undergone radical prostatectomy and lymphadenectomy for prostate cancer 12 years prior (Gleason score of 4 + 3).

Physical examination

Patient 1: The physical examination revealed a hard prostate that was adherent to adjacent tissues.

Patient 2: Physical examination did not reveal any abnormal findings.

Patient 3: Physical examination revealed a 3 cm nodule in the right lobe.

Laboratory examinations

Patient 1: A laboratory study revealed a PSA level of 8.4 ng/mL, with no other relevant findings.

Patient 2: The PSA level was significantly elevated at 100 ng/mL.

Patient 3: Laboratory examination details were not available.

Imaging examinations

Patient 1: An MRI of the prostate revealed diffuse neoplastic involvement of the prostatic parenchyma in both the peripheral and transitional zones. The images revealed poorly defined hypointense areas in the T2 sequence, restricted diffusion in diffusion-weighted imaging (DWI), and early enhancement in the inferior vena cava (IVC) study. Additionally, significantly stratified parietal thickening of the rectal wall was observed, with concentric areas of intermediate signal intensity in the T2 sequence, restricted diffusion in DWI, and contrast enhancement in the IVC study, involving both the submucosal and muscular planes. (Figure 3 and Figure 4).

Patient 2: MRI revealed diffuse neoplastic involvement of the prostatic parenchyma in both the transitional and peripheral zones, with poorly defined hypointense areas in the T2 sequence, restricted diffusion in DWI, and early enhancement in the IVC study. Notably, there was involvement of the rectoprostatic angles, infiltration of the right neurovascular complex, and extension to the rectal wall, characterized by stratified parietal thickening, concentric areas of intermediate signal intensity in the T2 sequence, restricted diffusion in DWI, and contrast enhancement in the IVC study, involving both the submucosal, muscular, and subserosal planes, suggestive of a "linitis plastica" pattern (Figure 5 and Figure 6). Positron emission tomography/computed tomography (PET/CT) PSMA confirmed the prostatic origin of neoplastic infiltration with significant uptake of the radiotracer at the rectal level (Figure 7).

Patient 3: MRI revealed changes following radical prostatectomy, highlighting a neoplastic mass located at the vesicourethral anastomosis, infiltrating the floor of the bladder wall, and locally extending to the rectal wall with concentric neoplastic involvement suggestive of a "linitis plastica" pattern, with areas of intermediate signal intensity in the T2 sequence, restricted diffusion in DWI, and stratified enhancement in the IVC study (Figure 8).

FINAL DIAGNOSIS

Patient 1

To confirm the diagnosis, a colonoscopy was performed, revealing a reduced lumen, increased consistency, and loss of parietal elasticity, as well as incipient involvement of the mucosa. Biopsies were performed, confirming neoplastic involvement of the large intestine wall due to prostatic adenocarcinoma (Figure 9).

Patient 2

Biopsy confirmed secondary RLP due to prostatic adenocarcinoma.

Patient 3

Endoscopic biopsy confirmed the presence of poorly differentiated neoplastic infiltrates compatible with prostatic origin.

TREATMENT

The specific treatment details were not available at the time of reporting.

OUTCOME AND FOLLOW-UP

Outcome and follow-up details were not available at the time of reporting.

DISCUSSION

Secondary infiltration of the rectum with a "linitis plastica" pattern is uncommon, and most publications are case reports [8-10]. A pattern of concentric rings or a "bull's-eye sign" is observed in T2-, T1-, and DWI-weighted MR images, as confirmed in the presented cases. This pattern is likely caused by an exaggerated growth of normal anatomy due to the interposition of infiltrating tumor and desmoplastic tissue in the submucosa and around the muscular layer. Some authors have proposed that subserosal involvement may also exist. A consensus exists in most of the cases described in the literature that the mucosa is preserved or that its involvement is not related to the extent of parietal involvement [9-11].

Initially, this radiological pattern was considered exclusive to signet ring cell carcinoma, an advanced stage of a subtype of primary rectal adenocarcinoma [12], which is a very uncommon disease, with an incidence of < 1% among all colorectal malignancies [11,13]. However, it is now known that rectal infiltration can be secondary to metastasis from other pelvic organs, such as the prostate or bladder, and even from the metastasis of gastric, vesicle, and lobular breast carcinomas and, less frequently, to the prostate, as demonstrated in our cases [5-10]. The literature review underscores the

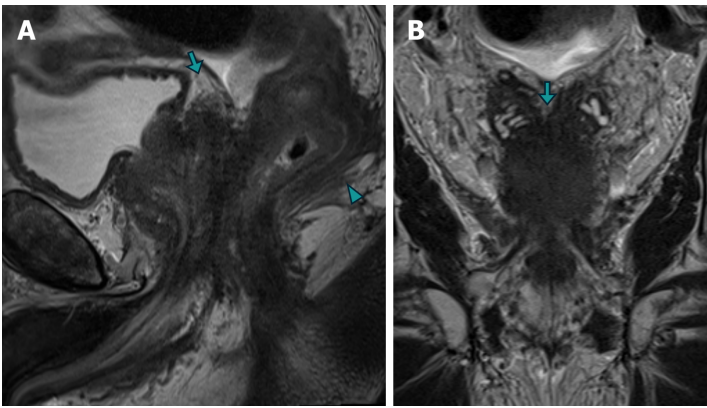


Figure 3 Magnetic resonance imaging images of case 1 demonstrating advanced prostate adenocarcinoma with rectal involvement. A and B: The sagittal (A) and Coronal (B) T2 turbo spin echo images reveal diffuse neoplastic involvement of the prostatic parenchyma, with extension into the rectal wall (arrowhead) and base of the seminal vesicles (arrow).

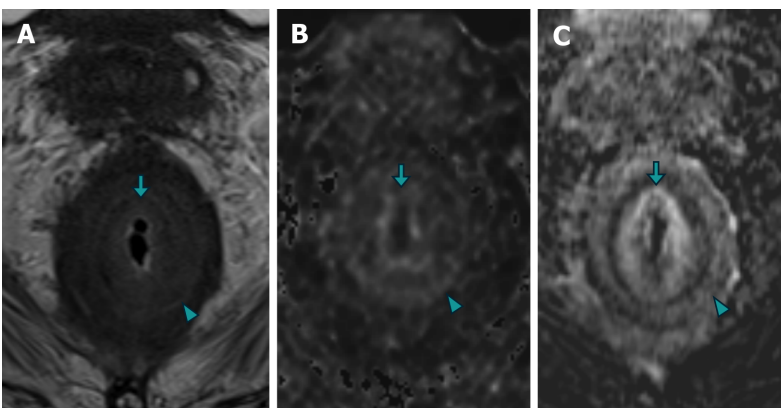


Figure 4 Magnetic resonance imaging images of case 1 demonstrating concentric "target-like" involvement of the rectal parietal wall due to secondary linitis plastica. A: The axial images obtained from T2 turbo spin echo sequence; B: Diffusion-weighted imaging (DWI); C: T1 gradient recalled echo volumetric interpolated breath-hold examination with contrast-enhanced subtraction technique revealed a stratified parietal thickening of the rectal wall. This thickening displayed concentric areas of intermediate signal intensity on T2-weighted images, restricted diffusion on DWI, and enhancement on contrast-enhanced images, affecting both the submucosal (arrow) and muscular (arrowhead) layers.

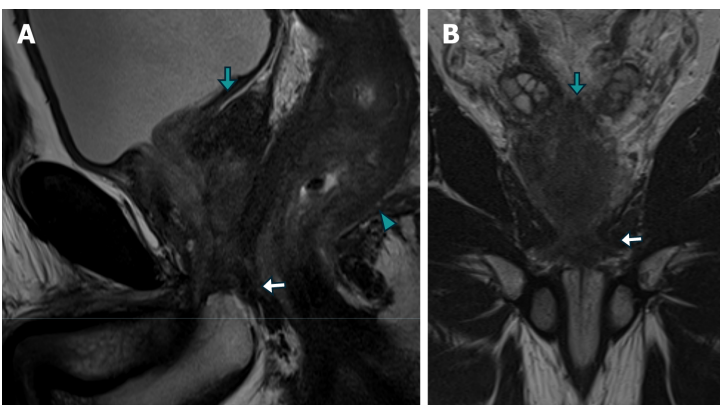


Figure 5 Magnetic resonance imaging images of case 2 demonstrating metastatic prostate adenocarcinoma. A and B: The sagittal (A) and Coronal (B) T2-weighted turbo spin echo images demonstrate diffuse neoplastic involvement of the prostatic parenchyma, with extension to the rectal wall (arrowhead), base of the seminal vesicles (green arrow), and external urethral sphincter (white arrow).

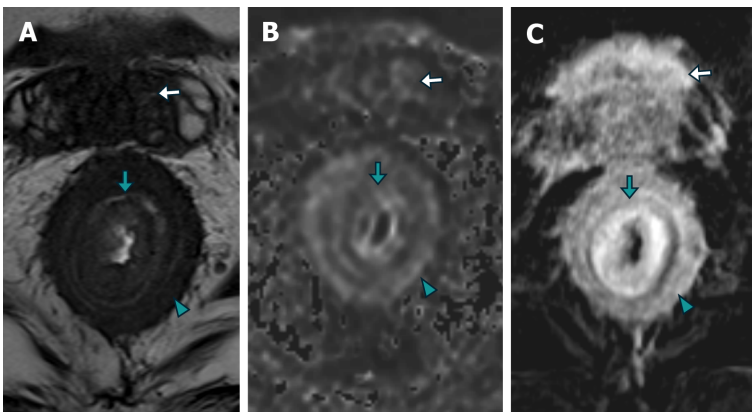


Figure 6 Axial magnetic resonance imaging of case 2. A-C: The imaging findings reveal a stratified parietal thickening of the rectal wall, characterized by concentric areas of intermediate signal intensity on T2-weighted imaging (A), restricted diffusion on diffusion-weighted imaging (B), and contrast enhancement on post-contrast T1-weighted volumetric interpolated breath-hold examination imaging with subtraction (C), affecting both the submucosal (green arrow) and muscular/subserosal planes (arrowhead) resembling a "linitis plastica" appearance. In addition, there is neoplastic involvement of the base of the seminal vesicles (white arrow).

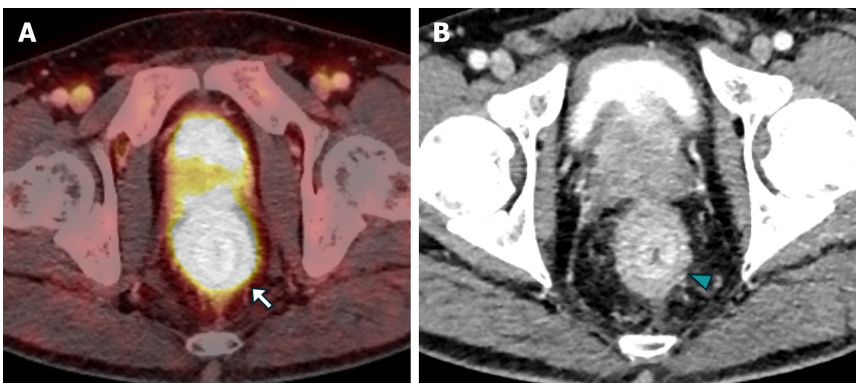


Figure 7 The positron emission tomography/computed tomography PSMA images in case 2. A and B: Axial FUSION (A) and computed tomography (B) of abdomen and pelvis with intravenous contrast revealed a stratified parietal thickening of the rectal wall, displaying significant uptake of the radiotracer, thus confirming the prostatic origin of the neoplastic infiltration (white arrow). Furthermore, concentric impregnation with intravenous contrast (green arrowhead) was also observed.

rarity of this condition, with most reports documenting only a single case. In contrast, our study consolidates the experience of three patients who presented at our center, providing a broader perspective on the clinical and radiological characteristics of secondary RLP caused by prostatic adenocarcinoma. In our series, all patients presented concentric parietal involvement and thickening of the rectal layers, which is compatible with the findings described in the literature.

There are also nonneoplastic causes that can mimic this pattern on MRI, such as inflammatory bowel diseases, infections such as cytomegalovirus, and post-radiation pelvic proctitis. Therefore, although the concentric ring pattern is characteristic of RLP, it is not specific or sensitive and should be interpreted with caution, in accordance with the clinical and histopathological background of the patients[4].

Patients with RLP secondary to prostate cancer can present asymptotically or may experience abdominal and/or rectal pain, alteration of the intestinal rhythm, or rectal bleeding, so the clinical presentation may be confused with digestive neoplasia and usually includes a lower digestive endoscopy. Endoscopic biopsy, which generally penetrates the mucosa and part of the submucosa, sometimes does not demonstrate the presence of malignancy because the disease usually affects the layers of the submucosa and the muscular propria with preservation of the mucosa, so a diagnostic effort must be made to search for histological confirmation[6]. An example of this is Case No. 1, where the presence of scarce malignant cells in the submucosal plane and some in the mucosal plane confirmed the diagnosis. Analyzing similar case reports, in the study by You *et al*[10], upon suspicion of "linitis plastica" imaging findings and an initial negative endoscopic biopsy, a full-thickness transanal excision biopsy was performed, which confirmed deep rectal involvement secondary to metastatic prostate adenocarcinoma. This highlights the importance of recognizing imaging findings and an adequate interpretation of the clinical background.

The patients varied in age, presented with initial symptoms, and had general conditions. The imaging techniques and pathological findings were consistent across cases in terms of tumor characteristics; however, the extent and pattern of involvement differed. All patients were receiving treatment for prostate cancer, but specific options and management strategies differed on the basis of the stage, extent, and response to prior treatments. This variability in presentation and treatment highlights the need for a tailored approach to patient care. Additionally, the lack of detailed treatment infor-

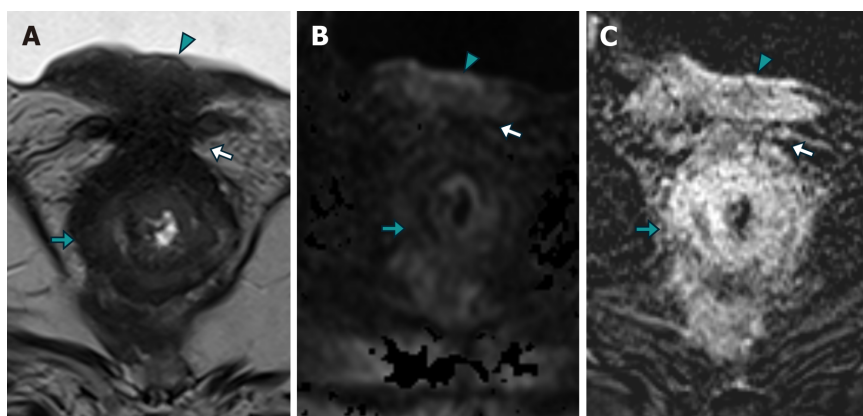


Figure 8 Magnetic resonance imaging findings in case 3. A-C: T2-weighted turbo spin-echo axial imaging (A), diffusion-weighted axial imaging (B), and T1-weighted volumetric interpolated breath-hold examination imaging with contrast-enhanced subtraction (C). The imaging findings revealed a concentric neoplastic involvement of the rectal wall, characterized by areas of intermediate signal intensity on T2-weighted imaging (A), as well as restricted diffusion on diffusion-weighted imaging (correlating with a hypointense region on the apparent diffusion coefficient map, which was not shown; B), and a stratified enhancement pattern on contrast-enhanced imaging (green arrow; C). Notably, the imaging also showed neoplastic involvement of the vesico-rectal plane (white arrow) and the bladder floor wall (green arrowhead).

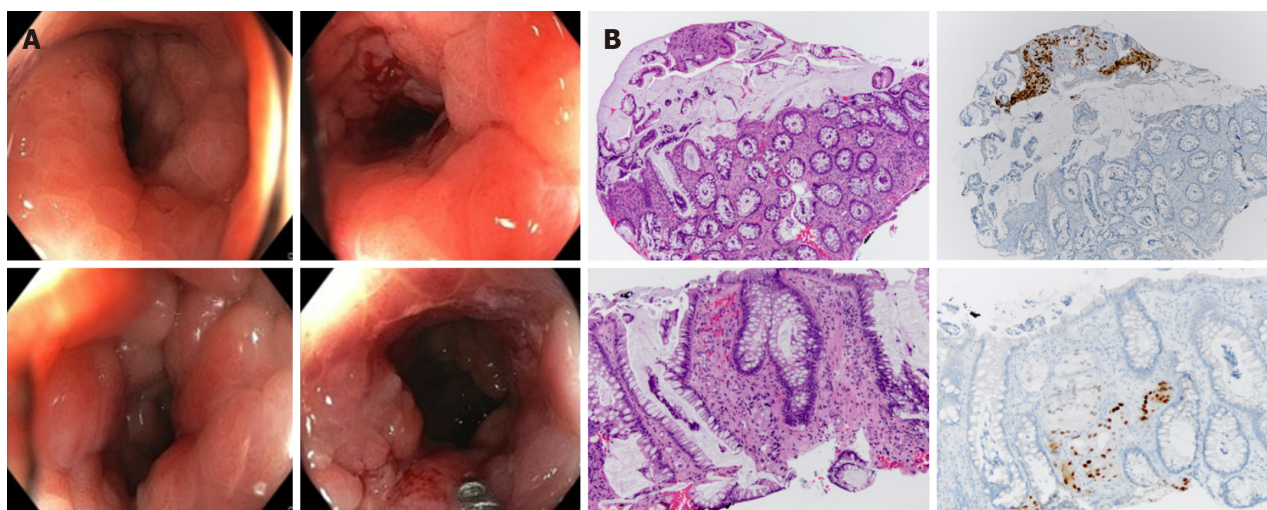


Figure 9 Colonoscopy and histological images of case 1 demonstrating advanced metastatic prostate adenocarcinoma. A: Colonoscopy image showing a reduced rectal lumen with congestive mucosa exhibiting increased consistency and loss of elasticity; B: Histological images of metastatic prostate adenocarcinoma utilizing Hematoxylin and Eosin staining in conjunction with immunohistochemical evaluation for the NKX marker. Groups of neoplastic cells arranged in nests and tubular structures. These cells exhibited atypical nuclei with prominent nucleoli and were positive for NKX, a highly specific marker for, albeit not exclusively indicative of, prostate origin.

mation in some cases underscores the importance of understanding the full therapeutic approach for each patient to optimize outcomes.

In relation to the dissemination pathways, three proposed routes exist for cases of adenocarcinoma of the prostate involving the rectum[14] (Figure 10).

Direct extension through the rectoprostatic fascia. Although Denonvilliers' fascia usually prevents the posterior extension of prostate cancer, direct dissemination may occur and is related to unresected advanced tumors. Cases 2 and 3 probably correspond to this type of dissemination.

Retrograde lymphatic/venous dissemination. Since the prostate and rectum share some drainage routes to pelvic lymph node groups and venous drainage, this may constitute the dissemination pathway for patient 1[15].

Neoplastic cells were seeded along the route of needle biopsy in the rectal wall or perirectal tissue. These cases are extremely rare and controversial[16]. However, studies that demonstrate causality are lacking.

Given the rarity of RLP as a metastatic manifestation of prostate adenocarcinoma, early and accurate identification *via* MRI is critical not only for distinguishing this condition from primary gastrointestinal malignancies but also for guiding treatment strategies. Recognizing characteristic imaging patterns, such as concentric wall thickening and the "target sign", enables clinicians to tailor therapeutic interventions, potentially avoiding unnecessary surgical procedures and focusing on targeted therapies. Additionally, these findings provide valuable insights into the likely disease course, allowing for a more informed prognosis. Integrating these radiological insights into a multidisciplinary approach enhances personalized

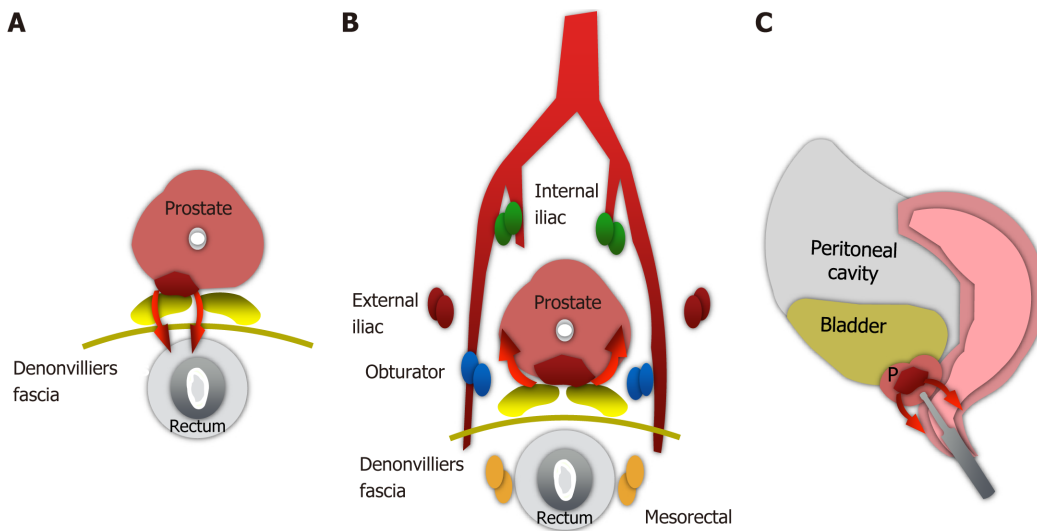


Figure 10 Postulated pathways of prostatic adenocarcinoma metastatic dissemination to the rectum. These include direct extension through the rectoprostatic fascia or Denonvilliers' fascia (A), lymphatic and/or retrograde venous spread (B), and tumoral implantation (C) following transrectal prostate biopsy.

care and ultimately improves outcomes for patients with this complex metastatic disease.

The study acknowledges that the limited number of cases constrains the generalizability of the findings, as the observed clinical presentations, imaging characteristics, and outcomes may not fully capture the broader spectrum of secondary RLP caused by prostatic adenocarcinoma. Additionally, the retrospective nature of the study introduces potential selection bias, as cases were identified and analyzed on the basis of available records, possibly excluding those with atypical presentations or incomplete data. Recognizing these limitations enhances the transparency of the research and underscores the need for future studies with larger cohorts and prospective designs to validate the findings and broaden our understanding of this rare metastatic condition.

As a projection for future research, it is crucial to emphasize the need for larger cohort studies with long-term follow-up of patients with prostatic neoplasia. Such studies could more accurately determine the incidence of RLP and facilitate the development of diagnostic algorithms that recognize this condition as a potential manifestation of prostate cancer dissemination MR. Research aimed at refining imaging techniques or integrating MRI with other modalities, such as PET/CT, could significantly increase diagnostic accuracy and reduce the risk of misdiagnosis. Addressing these areas in future research would build upon the valuable insights presented in this study, ultimately improving patient outcomes and advancing the management of secondary RLP in clinical practice.

CONCLUSION

Metastatic rectal neoplastic dissemination of the "linitis plastica" type is poorly understood and must be included in the dissemination forms of prostate cancer. Owing to the increasing use of MRI in monitoring rectal and prostate neoplasms, it is crucial for radiologists to be aware of and master their manifestations on MRI to perform accurate neoplastic staging. Distinguishing between primary rectal carcinoma and prostate carcinoma metastasis in the rectum is highly important because of the different treatments and prognoses involved. Proper imaging interpretation and immunohistochemical study of biopsies can prevent high-morbidity surgical interventions and direct treatments to therapies adapted to the corresponding dissemination stage.

FOOTNOTES

Author contributions: Labra AA, Schiappacasse G and Cocio RA formulated the objective and designed the structure of this case report; Cocio RA, Torres JT and González FO conducted literature search; Cristi JA and Schultz M analyzed the data and made the figures; Cocio RA and Torres JT wrote the different sections of this manuscripts.

Informed consent statement: Informed written consent was obtained from the patients for publication of this report and any accompanying images.

Conflict-of-interest statement: The authors declare that they have no conflict of interest to disclose.

CARE Checklist (2016) statement: The authors have read the CARE Checklist (2016), and the manuscript was prepared and revised according to the CARE Checklist (2016).

Open-Access: This article is an open-access article that was selected by an in-house editor and fully peer-reviewed by external reviewers. It is distributed in accordance with the Creative Commons Attribution NonCommercial (CC BY-NC 4.0) license, which permits others to distribute, remix, adapt, build upon this work non-commercially, and license their derivative works on different terms, provided the original work is properly cited and the use is non-commercial. See: <https://creativecommons.org/licenses/by-nc/4.0/>

Country of origin: Chile

ORCID number: Jorge Tomás Torres [0000-0001-8555-0535](https://orcid.org/0000-0001-8555-0535).

S-Editor: Lin C

L-Editor: A

P-Editor: Zhang YL

REFERENCES

- 1 Fernet P, Azar HA, Stout AP. Intramural (tubal) spread of linitis plastica along the alimentary tract. *Gastroenterology* 1965; **48**: 419-424 [PMID: [14275076](https://pubmed.ncbi.nlm.nih.gov/14275076/)]
- 2 Laufman H, Saphir O. Primary linitis plastica type of carcinoma of the colon. *AMA Arch Surg* 1951; **62**: 79-91 [PMID: [14789350](https://pubmed.ncbi.nlm.nih.gov/14789350/) DOI: [10.1001/archsurg.1951.01250030082009](https://doi.org/10.1001/archsurg.1951.01250030082009)]
- 3 Ba-Ssalamah A, Prokop M, Uffmann M, Pokieser P, Teleky B, Lechner G. Dedicated multidetector CT of the stomach: spectrum of diseases. *Radiographics* 2003; **23**: 625-644 [PMID: [12740465](https://pubmed.ncbi.nlm.nih.gov/12740465/) DOI: [10.1148/rg.233025127](https://doi.org/10.1148/rg.233025127)]
- 4 Mouaqit O, Mohsine R, Chenna, Ktaibi R, Sergi B, Boubouh A, El Malki O, Ifrine L, Belkouchi A. La linitis plastique rectale primitive: une tumeur exceptionnelle. *J Afr Cancer* 2010; **2**: 54-56 [DOI: [10.1007/s12558-009-0051-y](https://doi.org/10.1007/s12558-009-0051-y)]
- 5 Liu ZH, Li C, Kang L, Zhou ZY, Situ S, Wang JP. Prostate cancer incorrectly diagnosed as a rectal tumor: A case report. *Oncol Lett* 2015; **9**: 2647-2650 [PMID: [26137121](https://pubmed.ncbi.nlm.nih.gov/26137121/) DOI: [10.3892/ol.2015.3100](https://doi.org/10.3892/ol.2015.3100)]
- 6 Dumontier I, Roseau G, Palazzo L, Barbier JP, Couturier D. Endoscopic ultrasonography in rectal linitis plastica. *Gastrointest Endosc* 1997; **46**: 532-536 [PMID: [9434221](https://pubmed.ncbi.nlm.nih.gov/9434221/) DOI: [10.1016/s0016-5107\(97\)70009-9](https://doi.org/10.1016/s0016-5107(97)70009-9)]
- 7 Khor V, Khairul-Asri MG, Fahmy O, Hamid SA, Lee CKS. Linitis plastica of the rectum secondary to metastatic prostate cancer: A case report of a rare presentation and literature review. *Urol Ann* 2021; **13**: 442-445 [PMID: [34759661](https://pubmed.ncbi.nlm.nih.gov/34759661/) DOI: [10.4103/UA.UA_188_20](https://doi.org/10.4103/UA.UA_188_20)]
- 8 Mommersteeg MC, Kies DA, van der Laan J, Wonders J. Linitis plastica of the rectum secondary to prostate carcinoma. *BMJ Case Rep* 2022; **15** [PMID: [36460309](https://pubmed.ncbi.nlm.nih.gov/36460309/) DOI: [10.1136/bcr-2021-248462](https://doi.org/10.1136/bcr-2021-248462)]
- 9 Schmeusser B, Wiedemer J, Fichtenbaum E. Linitis prostatica: A unique case of circumferential narrowing of the rectum. *J Clin Images Med Case Rep* 2022; **3**: 2122 [DOI: [10.52768/2766-7820/2122](https://doi.org/10.52768/2766-7820/2122)]
- 10 You JH, Song JS, Jang KY, Lee MR. Computed tomography and magnetic resonance imaging findings of metastatic rectal linitis plastica from prostate cancer: A case report and review of literature. *World J Clin Cases* 2018; **6**: 554-558 [PMID: [30397613](https://pubmed.ncbi.nlm.nih.gov/30397613/) DOI: [10.12998/wjcc.v6.i12.554](https://doi.org/10.12998/wjcc.v6.i12.554)]
- 11 Rudralingam V, Dobson MJ, Pitt M, Stewart DJ, Hearn A, Susnerwala S. MR imaging of linitis plastica of the rectum. *AJR Am J Roentgenol* 2003; **181**: 428-430 [PMID: [12876021](https://pubmed.ncbi.nlm.nih.gov/12876021/) DOI: [10.2214/ajr.181.2.1810428](https://doi.org/10.2214/ajr.181.2.1810428)]
- 12 Nguyen MD, Plasil B, Wen P, Frankel WL. Mucin profiles in signet-ring cell carcinoma. *Arch Pathol Lab Med* 2006; **130**: 799-804 [PMID: [16740030](https://pubmed.ncbi.nlm.nih.gov/16740030/) DOI: [10.5858/2006-130-799-MPISCC](https://doi.org/10.5858/2006-130-799-MPISCC)]
- 13 Burgain C, Germain A, Bastien C, Orry X, Choné L, Claudon M, Laurent V. Computed tomography features of gastrointestinal linitis plastica: spectrum of findings in early and delayed phase imaging. *Abdom Radiol (NY)* 2016; **41**: 1370-1377 [PMID: [26814502](https://pubmed.ncbi.nlm.nih.gov/26814502/) DOI: [10.1007/s00261-016-0652-8](https://doi.org/10.1007/s00261-016-0652-8)]
- 14 Barbosa FG, Queiroz MA, Nunes RF, Viana PCC, Marin JFG, Cerri GG, Buchpiguel CA. Revisiting Prostate Cancer Recurrence with PSMA PET: Atlas of Typical and Atypical Patterns of Spread. *Radiographics* 2019; **39**: 186-212 [PMID: [30620699](https://pubmed.ncbi.nlm.nih.gov/30620699/) DOI: [10.1148/rg.2019180079](https://doi.org/10.1148/rg.2019180079)]
- 15 Murray SK, Breau RH, Guha AK, Gupta R. Spread of prostate carcinoma to the perirectal lymph node basin: analysis of 112 rectal resections over a 10-year span for primary rectal adenocarcinoma. *Am J Surg Pathol* 2004; **28**: 1154-1162 [PMID: [15316314](https://pubmed.ncbi.nlm.nih.gov/15316314/) DOI: [10.1097/01.pas.0000131543.80147.3d](https://doi.org/10.1097/01.pas.0000131543.80147.3d)]
- 16 Vaghefi H, Magi-Galluzzi C, Klein EA. Local recurrence of prostate cancer in rectal submucosa after transrectal needle biopsy and radical prostatectomy. *Urology* 2005; **66**: 881 [PMID: [16230172](https://pubmed.ncbi.nlm.nih.gov/16230172/) DOI: [10.1016/j.urology.2005.04.005](https://doi.org/10.1016/j.urology.2005.04.005)]

***Pneumocystis* pneumonia in stage IIIA lung adenocarcinoma with immune-related acute kidney injury and thoracic radiotherapy: A case report**

Ya-Wen Zheng, Jia-Chao Pan, Jin-Feng Wang, Jian Zhang

Specialty type: Oncology

Provenance and peer review:

Unsolicited article; Externally peer reviewed.

Peer-review model: Single blind

Peer-review report's classification

Scientific Quality: Grade C

Novelty: Grade B

Creativity or Innovation: Grade B

Scientific Significance: Grade B

P-Reviewer: Miyake K

Received: July 11, 2024

Revised: August 16, 2024

Accepted: September 3, 2024

Published online: September 28, 2024

Processing time: 77 Days and 16.3 Hours



Ya-Wen Zheng, Jian Zhang, Department of Oncology, Central Hospital Affiliated to Shandong First Medical University, Jinan 250000, Shandong Province, China

Jia-Chao Pan, Department of Gastroenterology, Central Hospital Affiliated to Shandong First Medical University, Jinan 250000, Shandong Province, China

Jin-Feng Wang, Department of Pulmonary and Critical Care Medicine, Central Hospital Affiliated to Shandong First Medical University, Jinan 250000, Shandong Province, China

Co-corresponding authors: Ya-Wen Zheng and Jian Zhang.

Corresponding author: Ya-Wen Zheng, MD, PhD, Associate Chief Physician, Department of Oncology, Central Hospital Affiliated to Shandong First Medical University, No. 105 Jiefang Road, Jinan 250000, Shandong Province, China. zyawen06@126.com

Abstract

BACKGROUND

Immune checkpoint inhibitors (ICIs) are therapeutic agents for advanced and metastatic non-small cell lung cancer (NSCLC) with high clinical antitumor efficacy. However, immune-related adverse events occur in 20% of these patients and often requiring treatment with immunosuppressive agents, such as corticosteroids. Consequently, this may increase the risk of patients to opportunistic infections. *Pneumocystis jirovecii* pneumonia (PJP), a rare but serious opportunistic infection typically observed in patients with human immunodeficiency virus, can also occur in cancer patients undergoing long-term glucocorticoid treatment.

CASE SUMMARY

We report a case of a 56-year-old male with squamous NSCLC treated with triplimab combined with paclitaxel, carboplatin, and radical thoracic radiation therapy. Following this regimen, he developed acute kidney injury (AKI) with elevated creatinine levels. After concurrent radical chemoradiotherapy ended, he developed a grade 3 immune-related AKI. High-dose corticosteroids were administered to treat AKI, and renal function gradually recovered. Corticosteroids were reduced to a dose of 10 mg prednisone equivalent daily eight weeks later; however, he developed severe pneumonia with spontaneous pneumothorax. Next-generation sequencing of the bronchoscopic lavage revealed PJP co-infection with herpes simplex virus 1 and cytomegalovirus. The inflammation was more

severe in areas exposed to radiation. Piperacillin-tazobactam, acyclovir, sulfamethoxazole, and trimethoprim were used to control the infection. The patient recovered, and immunotherapy was terminated.

CONCLUSION

PJP is rare but can occur in patients with ICI adverse events and should be differentiated from tumor progression or immune-related adverse events. Thoracic radiation may increase risk, necessitating careful monitoring and prevention.

Key Words: *Pneumocystis pneumonia*; Immunerelated adverse events; Immunotherapy; Thoracic radiotherapy; Acute kidney injury; Case report

©The Author(s) 2024. Published by Baishideng Publishing Group Inc. All rights reserved.

Core Tip: A patient with squamous lung cancer was treated with triplimab combined with paclitaxel, carboplatin, and radical thoracic radiation therapy. Despite the good therapeutic effect, he developed a grade 3 immune-related acute kidney injury, prompting high-dose corticosteroids treatment. Eight weeks later, the patient developed severe pneumonia with spontaneous pneumothorax, and was diagnosed with *Pneumocystis jirovecii pneumonia* (PJP) co-infection with the herpes simplex virus 1 and cytomegalovirus. PJP is rare but might occur in patients with immune checkpoint inhibitor adverse events, highlighting the need to be differentiated from tumor progression or immune-related adverse events.

Citation: Zheng YW, Pan JC, Wang JF, Zhang J. *Pneumocystis pneumonia* in stage IIIA lung adenocarcinoma with immune-related acute kidney injury and thoracic radiotherapy: A case report. *World J Radiol* 2024; 16(9): 482-488

URL: <https://www.wjgnet.com/1949-8470/full/v16/i9/482.htm>

DOI: <https://dx.doi.org/10.4329/wjr.v16.i9.482>

INTRODUCTION

Immunotherapy-related adverse reactions have increased owing to the widespread use of immunotherapies. Glucocorticoid therapy is an effective method for inhibiting overactivated immune responses[1]. Long-term glucocorticoid therapy renders the patient immunocompromised, and more patients with cancer are at risk of opportunistic infections[2]. *Pneumocystis jirovecii* (*P. jirovecii*) pneumonia (PJP) is an opportunistic infection caused by *P. jirovecii*. PJP is prevalent among patients with human immunodeficiency virus (HIV) infection but rarely in patients with cancer. Patients presenting with PJP may exhibit fever, cough, dyspnea, and respiratory failure in severe cases.

Here, we report a rare case of PJP with spontaneous pneumothorax in a 56-year-old male patient with advanced non-small cell lung cancer (NSCLC) who received eight weeks of glucocorticoid therapy to treat an immune-related acute kidney injury (AKI). Owing to prompt diagnosis and use of sulfamethoxazole, trimethoprim, and other antipathogenic drugs, the patient recovered fully.

CASE PRESENTATION

Chief complaints

The patient diagnosed with squamous lung cancer 4 months ago presented with sudden dyspnea for the past 3 days.

History of present illness

A 56-year-old man who was a former smoker with an Eastern Cooperative Oncology Group performance status of 0 was diagnosed with stage IIIA NSCLC (cTabN2M0, squamous lung cancer, PD-L1 10%; **Figure 1A**). After multidisciplinary discussion, including consideration of the patient's will, triplimab (a PD-1 inhibitor) combined with radical chemoradiotherapy was chosen as the treatment regimen. After one cycle of induction treatment, the patient received triplimab and concurrent chemoradiotherapy from May 15, 2023, to June 23, 2023. After completing thoracic radiation therapy, AKI was observed on June 24, 2023. The level of creatinine suddenly increased to 226 $\mu\text{mol/L}$, increasing further to 358 $\mu\text{mol/L}$ two days later. Computed tomography (CT) revealed that the volume of the bilateral kidney increased by approximately 20% without hydronephrosis (**Figure 1B**), and the patient refused a renal biopsy. The patient subsequently received methylprednisolone (60 mg) twice per day and antibiotics for bacterial infection prevention. The creatinine level decreased gradually, and methylprednisolone was slowly tapered in tandem (**Figure 1C**). On July 20, 2023, chest imaging revealed a partial response without radiation pneumonia. The timeline of treatment is showed in **Figure 1D**.

In August 2023, the patient was administered prednisone (10 mg) once daily (equivalent to 8 mg of methylprednisolone). On August 24, 2023, he suddenly developed fever and dyspnea, which worsened over three days, and the patient was urgently admitted to the hospital.

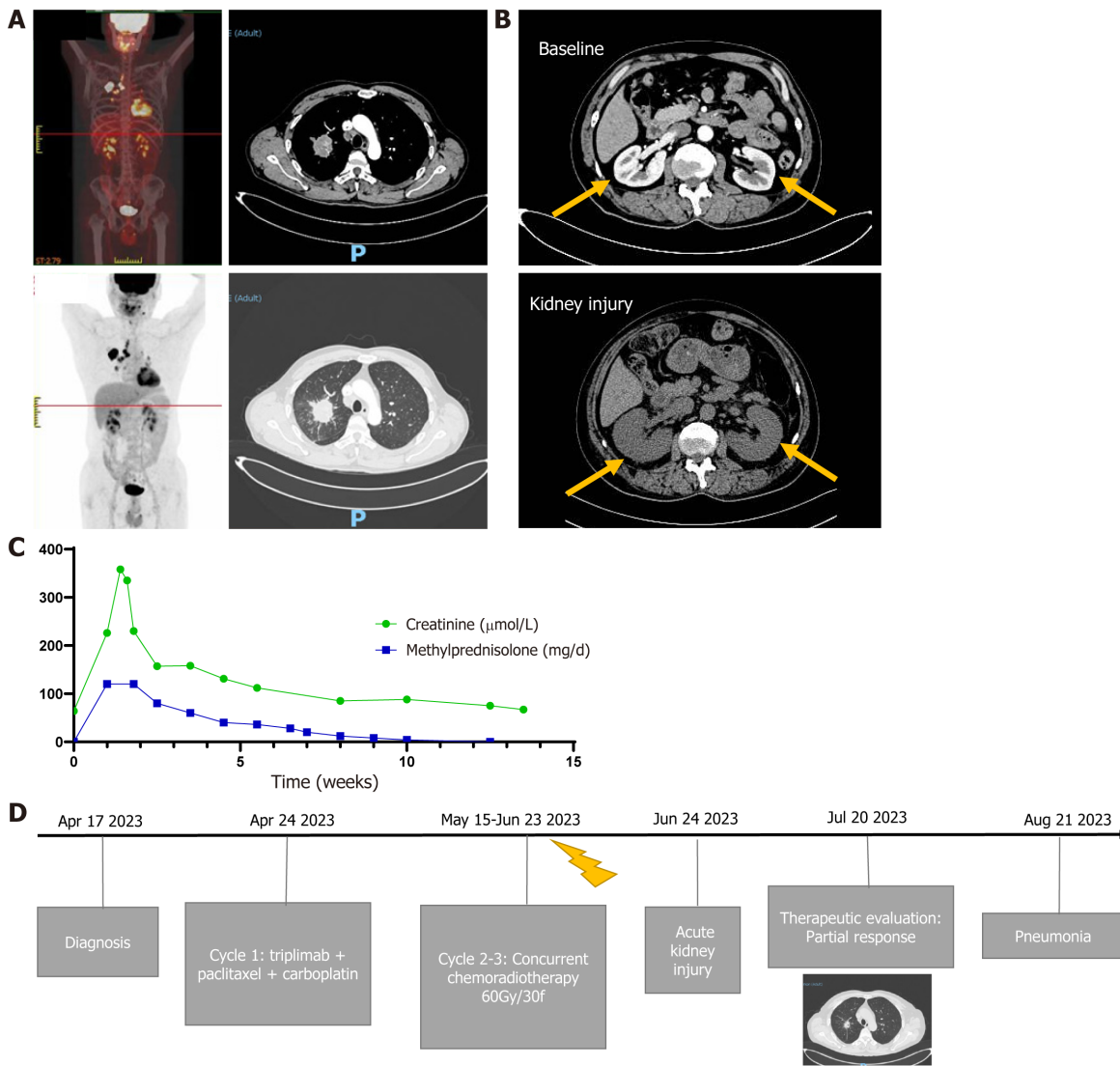


Figure 1 Time line of treatment. A: Positron emission tomography image at diagnosis; B: Images of acute kidney injury; C: Changes in creatinine and methylprednisolone levels; D: Treatment timeline.

History of past illness

The patient had no significant medical history.

Personal and family history

No family history of any malignant disease was reported.

Physical examination

Upon admission, his vital signs were unstable: Blood pressure, 138/89 mmHg; body temperature, 38.2 °C; heart rate, 115 beats/minute; and breathing rate, 24 breaths/minute. The oxygen saturation during oxygen inhalation was 95%. Breath sounds over the right lung were diminished, and moist rales were heard on the left lung.

Laboratory examinations

Blood test results were as follows: White blood cell count: $5.06 \times 10^9/\text{L}$; lymphocyte count: $0.65 \times 10^9/\text{L}$; C-reactive protein: 52.58 mg/L; and procalcitonin level: 0.077 ng/mL. The tests for pathogens (traditional laboratory test results) were negative. Serological test results for *Aspergillus* were normal.

Imaging examinations

CT showed diffuse lesions in both lungs and right pneumothorax (Figure 2A). After closed drainage of the right thoracic cavity, diffuse lesions in the right lung became more severe. Bronchoscopy with bronchoalveolar lavage was performed since no neoplasm was observed, and transbronchial biopsy deemed unnecessary. Bronchoscopy revealed numerous yellowish-white secretions in the bronchus, bronchial mucosal hyperemia, erosion, and bleeding (Figure 2B).

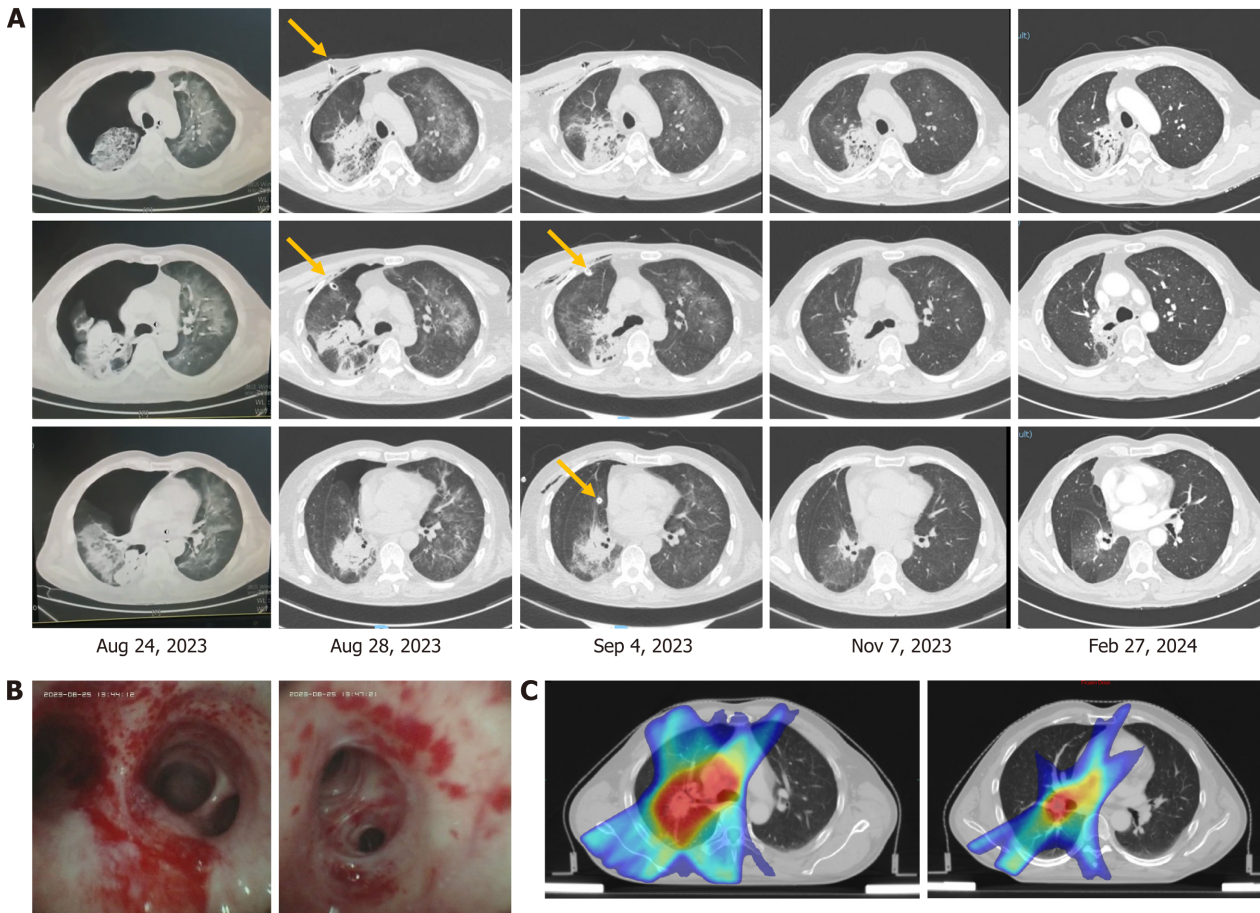


Figure 2 Radiographic and tracheoscopy findings. A: The computed tomography image changes before and after PJP treatment. The orange arrow shows the drainage tube. B: Tracheoscopy findings. C: Tumor irradiation field.

FINAL DIAGNOSIS

PJP infection was suspected, and thus the patient received piperacillin-tazobactam (4.5 g) three times per day combined with sulfamethoxazole and trimethoprim (TMP-SMX) (1.2 g/0.24 g) three times per day as empiric antibiotic therapy. The lavage fluid was sent to KingMed Diagnostics for targeted sequencing of multiple respiratory pathogens. Three days later, the next-generation sequencing of the lavage fluid confirmed PJP, herpes simplex virus 1, and cytomegalovirus.

TREATMENT

Acyclovir (0.25 g) was administered twice a day. One week later, the inflammation and symptoms were alleviated. Piperacillin-tazobactam and acyclovir were used for two weeks, and TMP-SMX was used continuously. Two months later, the inflamed bilateral lung was absorbed; however, the area with radiation developed chronic inflammation, with slight displacement of the mediastinum (Figure 2A and C).

OUTCOME AND FOLLOW-UP

On February 27, 2024, chronic inflammation was absorbed further and TMP-SMX was discontinued. The patient's daily activities eventually returned to the previous level. No further immunotherapies were administered. The patient remains alive without recurrence as of April 01, 2024.

DISCUSSION

PJP is a fungal infection that commonly affects immunocompromised patients and can be life-threatening in severe cases. The World Health Organization has listed it as one of 19 priority invasive fungal diseases, calling for increased research and public health action[3]. Typically, at-risk patients are those with underlying disease states that alter host immunity,

Table 1 *Pneumocystis jirovecii* pneumonia after steroid use due to immune-related adverse reactions

References	Country	Age and Sex	Cancer type	Patient condition	Treatment	AE and immunosuppression	Pathogens	Prognosis
Schwarz <i>et al</i> [23], 2019	Austria	79, Male	NSCLC	ECOG performance status 2, history of smoking, COPD	Chemotherapy-thoracic radiation-nivolumab	Immune-related pneumonitis, steroids for 6 weeks	<i>Pneumocystis jirovecii</i>	Died
		53, Male	NSCLC	ECOG performance status 0, history of smoking	Chemotherapy-thoracic radiation + nivolumab	Immune-related pneumonitis, steroids, and mycophenolate mofetil for 5 weeks	<i>Pneumocystis jirovecii</i> , cytomegalovirus	Died
Duarte <i>et al</i> [15], 2020	Belgium	68, Male	Melanoma	NA	Nivolumab-ipilimumab	Immune-related hepatitis and colitis, steroids for 10 weeks and infliximab	<i>Pneumocystis jirovecii</i>	Recovered
		24, Female	Hodgkin's lymphoma	NA	Multi cycle chemotherapy-pembrolizumab	Macrophage-activating syndrome, steroids for 6 months	<i>Pneumocystis jirovecii</i>	Recovered
Arriola <i>et al</i> [24], 2015	England	69, Female	Melanoma	Chronic lymphocytic leukemia	Chemotherapy-ipilimumab	Immune-related colitis, steroids for 12 weeks, and infliximab	<i>Pneumocystis jirovecii</i>	Recovered
		63, Female	Melanoma	NA	Ipilimumab	A capillary leak syndrome, steroids for 4 weeks	<i>Pneumocystis jirovecii</i>	Recovered

NSCLC: Non-small cell lung cancer; ECOG: Eastern cooperative oncology group; COPD: Chronic obstructive pulmonary disease; AE: Adverse event; NA: Not available.

such as HIV infection, transplant recipients, or those taking immunosuppressive therapies and medications[4]. The incidence of PJP in patients with solid tumors was documented at 0.013% (20/151718)[5].

Over the past 20 years, immune checkpoint inhibitors (ICIs) have been widely used[6]. However, these therapies can result in a variety of immune-related adverse events that can occur in any organ, including the kidneys[7]. AKI is the most common form of nephrotoxicity and is classically related to acute interstitial nephritis[8]. A noninvasive modality for the definite diagnosis of ICI-AKI remains unavailable[9,10]; however, CT imaging showed that the volume of the bilateral kidney increased in our patient. The estimated incidence of AKI directly related to ICI is approximately 3–5% [11]. Most patients had stage 1 or 2 while 10% had stage 3 AKI[12]. In our case, the patient had stage 3 AKI; fortunately, efficient and timely glucocorticoid therapy resulted in the recovery of kidney function. However, glucocorticoids can significantly impact both the innate and adaptive immune responses, and long-term steroid use increases the risk of opportunistic infections.

Our patient developed PJP and viral infection after receiving glucocorticoids for more than two months. PJP prophylaxis is recommended for patients expected to receive ≥ 20 mg daily prednisone equivalent for ≥ 4 weeks in the National Comprehensive Cancer Network guidelines of Management of Immunotherapy-Related Toxicities (Version 1.2024). Additionally, a study by Shah *et al*[13] highlighted the degree of immunosuppression and the relative risk of opportunistic infections. In 112 patients who received 20 mg daily of a prednisone equivalent for four weeks to manage immune-related adverse events, only eight had opportunistic infections; among them, one patient developed PJP[13]. Similarly, Sadek *et al*[14] revealed that only two PJP cases were found in patients treated with an ICI (480 patients received ICIs during that period). The incidence of PJP after steroid use due to immune-related adverse reactions is considerably low, and only six cases have been reported in the literature (Table 1). Considering the relatively common adverse effects of TMP-SMX at prophylactic doses[4], we wonder whether PJP prophylaxis is efficacious or necessary in all patients with cancer receiving steroids for immune-related adverse events. Conversely, steroids were frequently used in patients with cancer for a variety of other reasons. PJP has also been observed in patients with cancer receiving corticosteroids for malignant spinal cord compression[15] and weight loss[16]. Miyake *et al*[17] reported that the incidence of PJP in immunosuppressed non-HIV patients was 0.18% (32/17733), a monthly average dose of ≥ 13.7 mg daily prednisolone was a significant independent risk factors for PJP, and prophylaxis with ≥ 34.3 mg/day of TMP-SMX is to be recommended[17]. Therefore, further studies are required to determine whether patients with cancer require precise PJP prophylaxis.

In addition to steroids, multiple other factors, such as lymphocytopenia and radiation to the chest, may contribute to PJP in patients with solid tumors in a composite manner[3]. In patients with lymphocytopenia, especially those with low CD4+ T cell counts, *P. jirovecii* can proliferate, causing a mononuclear cell response with inflammation. McAleese *et al*[18] advocated prophylaxis in patients with a lymphocyte count $< 0.6 \times 10^9/L$. Fu *et al*[19] reported seven patients with thoracic neoplasms experiencing radiation pneumonitis complicated by PJP. Similar to radiation pneumonia, PJP presents with various atypical radiographic characteristics, including the relationship between photographic findings and the planning target volume. Similarly, the right side of the lung that received radiation had a more severe infection in our

case, which resulted in pneumothorax. Pneumothorax is a rare complication of PJP, occurring in only 3% of the HIV-positive patients with PJP[20]. This finding indicates that thoracic radiation may worsen the risk of PJP.

With the emergence of targeted therapies and immunotherapies, as well as the continuous development of novel radiotherapies, we have entered an era of novel treatment paradigms for locally advanced NSCLC[21]. The feasibility of induction with ICIs and chemotherapy before definitive chemoradiotherapy for locally advanced-NSCLC has been explored[22]. Notably, multiple factors interacted with each other in our case; although radiation pneumonia did not occur, handling immune-related adverse events leading to opportunistic infections still worsened the lung injury. In addition, we also differentiated PJP from immune and radiation pneumonia during treatment. Because no sign of inflammation was evident one month before the symptoms, immune and radiation pneumonia were not initially considered. A short-term reexamination after anti-inflammatory treatments confirmed the validity of our judgment.

CONCLUSION

A special feature of our case was that the patient developed double-lung PJP complicated by viral pneumonia accompanied by spontaneous pneumothorax during immune-related adverse event treatment. The patient's prognosis was good after timely anti-inflammatory treatments. Appropriate chemoprophylaxis to reduce the risk of PJP is necessary with comprehensive consideration of steroid use, lymphocytopenia, other chemotherapies, immunotherapies, and radiation therapy.

FOOTNOTES

Author contributions: Zheng YW and Zhang J conceived the manuscript; Zheng YW, Wang JF and Zhang J treated the patient; Zheng YW and Pan JC collected the patient information and acquired the data; Zheng YW and Pan JC analyzed the data and wrote the manuscript; Zheng YW and Zhang J jointly formulated the patient's treatment plan, with equal contributions to the manuscript as co-corresponding authors; Zheng YW takes primary responsibility for communication with the journal during the manuscript submission, peer review and publication processes; all authors reviewed the manuscript critically and approved the content.

Supported by Shandong Natural Science Foundation, No. ZR2021QH034; and China Postdoctoral Science Foundation, No. 2023M731305.

Informed consent statement: The authors certify that they have obtained all appropriate patient consent forms prior to study enrollment.

Conflict-of-interest statement: The authors declare that the research was conducted in the absence of any commercial or financial relationships that could be construed as a potential conflict of interest.

CARE Checklist (2016) statement: The authors have read the CARE Checklist (2016), and the manuscript was prepared and revised according to the CARE Checklist (2016).

Open-Access: This article is an open-access article that was selected by an in-house editor and fully peer-reviewed by external reviewers. It is distributed in accordance with the Creative Commons Attribution NonCommercial (CC BY-NC 4.0) license, which permits others to distribute, remix, adapt, build upon this work non-commercially, and license their derivative works on different terms, provided the original work is properly cited and the use is non-commercial. See: <https://creativecommons.org/licenses/by-nc/4.0/>

Country of origin: China

ORCID number: Ya-Wen Zheng 0000-0003-4230-1883; Jia-Chao Pan 0000-0002-7915-4656; Jin-Feng Wang 0009-0006-5946-0791; Jian Zhang 0009-0002-3077-9855.

S-Editor: Lin C

L-Editor: A

P-Editor: Zhang YL

REFERENCES

- 1 **Esfahani K**, Elkrief A, Calabrese C, Lapointe R, Hudson M, Routy B, Miller WH Jr, Calabrese L. Moving towards personalized treatments of immune-related adverse events. *Nat Rev Clin Oncol* 2020; **17**: 504-515 [PMID: 32246128 DOI: 10.1038/s41571-020-0352-8]
- 2 **Chastain DB**, Spradlin M, Ahmad H, Henao-Martinez AF. Unintended Consequences: Risk of Opportunistic Infections Associated With Long-term Glucocorticoid Therapies in Adults. *Clin Infect Dis* 2024; **78**: e37-e56 [PMID: 37669916 DOI: 10.1093/cid/ciad474]
- 3 **Xue T**, Kong X, Ma L. Trends in the Epidemiology of Pneumocystis Pneumonia in Immunocompromised Patients without HIV Infection. *J Fungi (Basel)* 2023; **9** [PMID: 37623583 DOI: 10.3390/jof9080812]
- 4 **Weyant RB**, Kabbani D, Doucette K, Lau C, Cervera C. Pneumocystis jirovecii: a review with a focus on prevention and treatment. *Expert Opin Pharmacother* 2021; **22**: 1579-1592 [PMID: 33870843 DOI: 10.1080/14656566.2021.1915989]
- 5 **Takeda K**, Harada S, Hayama B, Hoashi K, Enokida T, Sasaki T, Okamoto K, Nakano K, Ohkushi D. Clinical characteristics and risk factors associated with Pneumocystis jirovecii infection in patients with solid tumors: study of thirteen-year medical records of a large cancer center.

- BMC Cancer* 2021; **21**: 987 [PMID: 34479519 DOI: 10.1186/s12885-021-08727-2]
- 6 Liu SM, Zheng MM, Pan Y, Liu SY, Li Y, Wu YL. Emerging evidence and treatment paradigm of non-small cell lung cancer. *J Hematol Oncol* 2023; **16**: 40 [PMID: 37069698 DOI: 10.1186/s13045-023-01436-2]
 - 7 O'Leary CL, Pierce N, Patel SP, Naidoo J. Immune-Related Toxicity in NSCLC: Current State-of-the-Art and Emerging Clinical Challenges. *J Thorac Oncol* 2024; **19**: 395-408 [PMID: 38012985 DOI: 10.1016/j.jtho.2023.11.018]
 - 8 Miao J, Sise ME, Herrmann SM. Immune checkpoint inhibitor related nephrotoxicity: Advances in clinicopathologic features, noninvasive approaches, and therapeutic strategy and rechallenge. *Front Nephrol* 2022; **2**: 1017921 [PMID: 37674988 DOI: 10.3389/fneph.2022.1017921]
 - 9 Capaccione KM, Valiplackal JP, Huang A, Roa T, Fruauff A, Liou C, Kim E, Khurana S, Maher M, Ma H, Ngyuen P, Mak S, Dumeer S, Lala S, D'souza B, Laifer-Narin S, Desperito E, Ruzal-Shapiro C, Salvatore MM. Checkpoint Inhibitor Immune-Related Adverse Events: A Multimodality Pictorial Review. *Acad Radiol* 2022; **29**: 1869-1884 [PMID: 35382975 DOI: 10.1016/j.acra.2022.03.007]
 - 10 Longhitano E, Muscolino P, Lo Re C, Ferrara SA, Cernaro V, Gembillo G, Tessitore D, Speranza D, Figura F, Santarpia M, Silvestris N, Santoro D, Franchina T. Immune Checkpoint Inhibitors and the Kidney: A Focus on Diagnosis and Management for Personalised Medicine. *Cancers (Basel)* 2023; **15** [PMID: 36980777 DOI: 10.3390/cancers15061891]
 - 11 Rao Ullur A, Côté G, Pelletier K, Kitchlu A. Immunotherapy in oncology and the kidneys: a clinical review of the evaluation and management of kidney immune-related adverse events. *Clin Kidney J* 2023; **16**: 939-951 [PMID: 37261008 DOI: 10.1093/ckj/sfad014]
 - 12 Knox A, Cloney T, Janssen H, Solomon BJ, Alexander M, Ruderman I, John T. Immune-related acute kidney injury in Australian non-small cell lung cancer patients: Real-world results. *Lung Cancer* 2023; **184**: 107325 [PMID: 37573702 DOI: 10.1016/j.lungcan.2023.107325]
 - 13 Shah NJ, Cook MR, Wu T, Lev-Ari S, Blackburn MJ, Serzan MT, Alaoui A, Ahn J, Atkins MB. The Risk of Opportunistic Infections and the Role of Antibiotic Prophylaxis in Patients on Checkpoint Inhibitors Requiring Steroids. *J Natl Compr Canc Netw* 2022; **20**: 800-807.e1 [PMID: 35830888 DOI: 10.6004/jnccn.2022.7020]
 - 14 Sadek M, Loizidou A, Drowart A, Van den Wijngaert S, Gomez-Galdon M, Aspeslagh S. Pneumocystis Infection in Two Patients Treated with Both Immune Checkpoint Inhibitor and Corticoids. *J Immunother Precis Oncol* 2020; **3**: 27-30 [PMID: 35756180 DOI: 10.4103/JIPO.JIPO_23_19]
 - 15 Duarte C, Gilbert D, Sheridan AD, PharmaD SDW, Lam ET. Pneumocystis jirovecii Pneumonia in Patients With Metastatic Prostate Cancer on Corticosteroids for Malignant Spinal Cord Compression: Two Case Reports and a Guideline Review. *Oncology (Williston Park)* 2020; **34** [PMID: 32212136]
 - 16 Sanka P, Hsu A. A Case of Pneumocystis jirovecii in a Patient with Non-Small Cell Lung Cancer Treated with Immunotherapy. *RI Med J (2013)* 2023; **106**: 11-13 [PMID: 36706199]
 - 17 Miyake K, Kawamura T, Nakahara Y, Sasaki S. A single-center, person-month-based analysis of the risk of developing Pneumocystis pneumonia (PCP) in immunosuppressed non-HIV patients: Preventive effects of trimethoprim-sulfamethoxazole. *J Infect Chemother* 2023; **29**: 1097-1102 [PMID: 37499901 DOI: 10.1016/j.jiac.2023.07.012]
 - 18 McAleese J, Mooney L, Walls GM. Reducing the Risk of Death From Pneumocystis jirovecii Pneumonia After Radical Radiation Therapy to the Lung. *Clin Oncol (R Coll Radiol)* 2021; **33**: 780-787 [PMID: 34253423 DOI: 10.1016/j.clon.2021.06.010]
 - 19 Fu Z, Yang X, Bi N, Zhai Y, Chen D, Wang W, Deng L, Zhang T, Zhou Z, Liang J. Radiation pneumonitis complicated by Pneumocystis carinii in patients with thoracic neoplasia: a clinical analysis of 7 cases. *Cancer Commun (Lond)* 2019; **39**: 47 [PMID: 31443740 DOI: 10.1186/s40880-019-0392-6]
 - 20 Christe A, Walti L, Charimo J, Rauch A, Furrer H, Meyer A, Huynh-Do U, Heverhagen JT, Mueller NJ, Cavassini M, Mombelli M, van Delden C, Frauenfelder T, Montet X, Beigelman-Aubry C, Arampatzis S, Ebner L. Imaging patterns of Pneumocystis jirovecii pneumonia in HIV-positive and renal transplant patients - a multicentre study. *Swiss Med Wkly* 2019; **149**: w20130 [PMID: 31580472 DOI: 10.4414/smw.2019.20130]
 - 21 Miao D, Zhao J, Han Y, Zhou J, Li X, Zhang T, Li W, Xia Y. Management of locally advanced non-small cell lung cancer: State of the art and future directions. *Cancer Commun (Lond)* 2024; **44**: 23-46 [PMID: 37985191 DOI: 10.1002/cac2.12505]
 - 22 Wang Y, Zhang T, Wang J, Zhou Z, Liu W, Xiao Z, Deng L, Feng Q, Wang X, Lv J, Ma X, Xue Q, Wang J, Wang Z, Bi N. Induction Immune Checkpoint Inhibitors and Chemotherapy Before Definitive Chemoradiation Therapy for Patients With Bulky Unresectable Stage III Non-Small Cell Lung Cancer. *Int J Radiat Oncol Biol Phys* 2023; **116**: 590-600 [PMID: 36623605 DOI: 10.1016/j.ijrobp.2022.12.042]
 - 23 Schwarz M, Kocher F, Niedersuess-Beke D, Rudzki J, Hochmair M, Widmann G, Hilbe W, Pircher A. Immunosuppression for Immune Checkpoint-related Toxicity Can Cause Pneumocystis Jirovecii Pneumonia (PJP) in Non-small-cell Lung Cancer (NSCLC): A Report of 2 Cases. *Clin Lung Cancer* 2019; **20**: e247-e250 [PMID: 30635258 DOI: 10.1016/j.clcc.2018.12.006]
 - 24 Arriola E, Wheeler M, Krishnan R, Smart J, Foria V, Ottensmeier C. Immunosuppression for ipilimumab-related toxicity can cause pneumocystis pneumonia but spare antitumor immune control. *Oncimmunology* 2015; **4**: e1040218 [PMID: 26451305 DOI: 10.1080/2162402X.2015.1040218]

Prolonged course of Paxlovid administration in a centenarian with COVID-19: A case report

Yi-Xue Zhang, Juan Tang, Dan Zhu, Chun-Yan Wu, Mei-Lan Liang, Yuan-Tao Huang

Specialty type: Radiology, nuclear medicine and medical imaging

Provenance and peer review:

Unsolicited article; Externally peer reviewed.

Peer-review model: Single blind

Peer-review report's classification

Scientific Quality: Grade C

Novelty: Grade B

Creativity or Innovation: Grade B

Scientific Significance: Grade B

P-Reviewer: Latsios G

Received: July 30, 2024

Revised: August 27, 2024

Accepted: September 10, 2024

Published online: September 28, 2024

Processing time: 58 Days and 16.1 Hours



Yi-Xue Zhang, Juan Tang, Chun-Yan Wu, Mei-Lan Liang, Yuan-Tao Huang, Department of Healthcare, Haikou Affiliated Hospital of Central South University Xiangya School of Medicine, Haikou 570208, Hainan Province, China

Dan Zhu, Department of Healthcare, Hainan Chengmei Hospital, Haikou 570000, Hainan Province, China

Corresponding author: Yuan-Tao Huang, Doctor, Chief Doctor, Department of Healthcare, Haikou Affiliated Hospital of Central South University Xiangya School of Medicine, No. 43 Renmin Avenue, Meilan District, Haikou 570208, Hainan Province, China.
hyt951232@163.com

Abstract

BACKGROUND

According to the population statistics in 2023, there were 110000 people aged over 100 years in China, and the experience of using Paxlovid (nirmatrelvir/ritonavir) for centenarians is particularly valuable. This article reports our experience of using Paxlovid in a centenarian with the novel coronavirus disease 2019 (COVID-19) infection.

CASE SUMMARY

A 103-year-old female with mild COVID-19 and renal insufficiency was given sufficient Paxlovid for 2 days and a half dose for 3 days. During treatment, the patient was complicated with lung infection and heart failure, and nucleic acid remained positive. After expert consultation, a full dose of Paxlovid was given again on the 9th day of admission for 2 days and a half dose for 3 days. Meanwhile, anti-heart failure and antibiotics were administered; the heart failure and pulmonary infection were improved. Finally, on the 33th day of admission, nucleic acid turned negative, body temperature returned to normal, cough and sputum, fatigue, poor appetite and other symptoms basically improved. The patient was given Paxlovid *via* nasal feeding for 2 courses without deterioration of liver and kidney function, diarrhea, nausea and vomiting, myalgia, chest tightness and other side effects, and was discharged from hospital with good recovery.

CONCLUSION

This case suggests that Paxlovid can be used cautiously in centenarians with renal insufficiency and two courses of treatment can be considered in patients with persistent positive nucleic acid.

Key Words: COVID-19; Paxlovid; Centenarians; Renal insufficiency; Heart failure; Lung infection; Case report

©The Author(s) 2024. Published by Baishideng Publishing Group Inc. All rights reserved.

Core Tip: We report a 103-year-old female with renal insufficiency and a history of hypertension. The patient was treated with two courses of Paxlovid at a full dose for 2 days and a half dose for 3 days. Although she had lung infection and heart failure during the treatment, they all improved after treatment and she was discharged from hospital 40 days after admission. This case suggested that Paxlovid can be applied cautiously in centenarians with coronavirus disease 2019 patients with renal insufficiency, and but the liver and kidney function of the patient should be closely monitored.

Citation: Zhang YX, Tang J, Zhu D, Wu CY, Liang ML, Huang YT. Prolonged course of Paxlovid administration in a centenarian with COVID-19: A case report. *World J Radiol* 2024; 16(9): 489-496

URL: <https://www.wjgnet.com/1949-8470/full/v16/i9/489.htm>

DOI: <https://dx.doi.org/10.4329/wjr.v16.i9.489>

INTRODUCTION

Coronavirus disease 2019 (COVID-19) is a pandemic virus that has swept the globe in recent years. According to the World Health Organization (WHO), as of February 21, 2023, the total number of confirmed cases of COVID-19 in the world had exceeded 750 million, and the death rate exceeded 6.85 million. Although the WHO declared in May 2023 that COVID-19 no longer constitutes a "public health emergency of international concern", COVID-19 still occur. Paxlovid is approved by the United States Food and Drug Administration on December 22, 2021 for mild to moderate COVID-19 patients over the age of 12 years and weighing at least 40 kg. Paxlovid is the first oral COVID-19 drug approved in the United States[1]. We here report a case of a 103-year-old COVID-19 patient who received two courses of Paxlovid, with good outcome.

CASE PRESENTATION

Chief complaints

A 103-year-old elderly female was admitted to hospital 4 days after being found to have poor mental performance and poor appetite.

History of present illness

On December 24, 2022, the patient developed poor mental state, fatigue, poor appetite, oliguria, occasional cough and sputum. Her temperature was not monitored and no special attention was given. On December 27, her family members developed symptoms of influenza, and a throat swab tested positive for nucleic acid, while the patient was also tested positive for a throat swab.

History of past illness

She had a history of right femoral neck injury, on a wheelchair for 8 years, hypertension for more than 1 year, and highest blood pressure of 180/100 mmHg, without any medication, and Alzheimer's disease, and has not been vaccinated against COVID-19. The patient had no history of smoking, alcohol, drug or food allergies.

Personal and family history

There was no family history of genetic disorders.

Physical examination

Body temperature: 36.6 °C, blood pressure 152/76 mmHg, breathing 24 times /min, blood oxygen saturation at rest state 94%, oxygen inhalation 3 L/min 97%, body weight 50 kg, mental fatigue, shallow coma, uncooperative physical examination, tingling response, a little dry and wet rale could be heard in the upper lung, low respiratory sound in the lower right lung. Heart rate 95 beats/min, in the aortic auscultation area 3/6 grade diastolic wind like murmurs could be heard. Abdominal tenderness, no tenderness, no rebound pain, no edema in lower extremities were observed.

Laboratory examinations

Blood routine examination showed white blood cells $9.93 \times 10^9/L$, neutrophil percentage 80.6%, lymphocyte count $1.21 \times 10^9/L$, sodium 170 mmol/L, chlorine 130.2 mmol/L, creatinine 250 $\mu\text{mol/L}$, nucleic acid positive, Ct value 29, D-2 polymer 5.0 mg/L, Procalcitonin 0.107 ng/mL, C-reactive protein 20.07 mg/L, N-terminal pro-brain natriuretic peptide

(NT-proBNP) 1604 pg/mL, interleukin-6 29.19 pg/mL, ferritin 100.58 ng/mL, D2 polymer 5.0 mg/L, blood gas analysis (after oxygen absorption): PH 7.306, carbon dioxide partial pressure 44.5 mmHg, oxygen partial pressure 164 mmHg, oxygen saturation 99%, and lactate 2.3 mmol/L. Lactate dehydrogenase, myocardial enzyme, liver function and blood coagulation routine were all normal. On January 6, 2023, NT-proBNP reached the highest value of 6258 pg/mL, white blood cells and neutrophils were the highest on the first day of admission, $9.93 \times 10^9/L$ and 80.6%, respectively, and lymphocyte count was the lowest on the 14th day of admission, $0.56 \times 10^9/L$, as shown in [Figure 1](#). The highest value of procalcitonin was 0.107 pg/mL at the first check after admission, and the lowest value of epidermal growth factor receptor (eGFR) was 7.2% at admission and then gradually increased, as shown in [Table 1](#).

Imaging examinations

Upon admission, the patient's chest computed tomography (CT) revealed a mass in the upper lobe of the right lung, infectious lesions in both lungs, and a small amount of fluid on both sides, mainly on the right side. Upon discharge, chest CT indicated that inflammation of both lungs was slightly improved, as shown in [Figure 2](#). Heart color ultrasonography showed ejection fraction 58%, and the left ventricular wall was slightly thickened (12 mm).

FINAL DIAGNOSIS

According to the therapeutics and COVID-19: Living guideline of WHO[2], the patient was diagnosed with mild-to-moderate COVID-19 at admission: Pulmonary infection, heart failure, and electrolyte disturbance during hospitalization.

TREATMENT

The hospital organized consultations among experts inside and outside the hospital. On December 28, 2022, 150 mg of Nirmatrelvir and 100 mg of ritonavir were given for the first time, and on December 31, 300 mg of nirmatrelvir and 100 mg of ritonavir were given every 12 hours, with a full dose for 3 days and a half dose for 2 days. As the patient had dementia, she had poor cooperation with eating, and a gastric tube was inserted. All food and medication were administered *via* the gastric tube. The lowest Ct value of the patient was 19 on December 29, 2022. After Paxlovid and symptomatic treatment, the patient's mental state, cough, poor appetite and fatigue symptoms were improved significantly. Upon admission, the patient was complicated with pulmonary infection and heart failure, and was given moxifloxacin orally and piperacillin and tazobactam intravenously. The patient's body temperature fluctuated repeatedly, reaching a maximum of 38.9 °C on the fifth day of admission. After January 12, 2023, the body temperature basically returned to normal, as shown in [Figure 3](#). NT-proBNP rose to the highest value 6258 pg/mL on January 6, and the patient's shortness of breath became worse. The patient was successively given sacubitril valsartan sodium, nitroglycerin and recombinant human brain natriuretic peptide for anti-heart failure. NT-proBNP dropped to 2890 pg/mL on January 19, and the heart failure was improved. After a course of Paxlovid, the nucleic acid Ct value of the patient gradually increased but remained positive, and the Ct value dropped to 24 on January 9, 2023, which could not rule out the recovery of COVID-19 and the worsening of heart failure. On January 10, after remote consultation with out-of-hospital experts and communication with family members, we decided to give the patient another cycle of Paxlovid treatment, with a full dose for 3 days and a half dose for 2 days again, nucleic acid turned negative on January 31, nucleic acid throat swabs tested on February 1 and 3 were negative, and the Ct values of COVID-19 throat swabs fluctuated as shown in [Figure 4](#). Liver and kidney functions were closely monitored during medication, and the indicators were acceptable. The values of creatinine during hospitalization are shown in [Figure 5](#).

OUTCOME AND FOLLOW-UP

The patient was discharged from hospital on February 8, 2023 with no fever, no obvious cough and sputum, no shortness of breath, and with mental recovery. [Figure 6](#) shows the comparison in the status of the patient at hospitalization and discharge. The patient's mental state was fine during a telephone follow-up 3 months after discharge, and she continued to be fed through a nasal feeding tube.

DISCUSSION

With the development of economy and the improvement of living standards, the number of long-lived people in China is increasing. According to the population statistics in 2023, there were 110000 people aged over 100 years in China. The experience of medication for centenarians is particularly valuable. We report a case of a 103-year-old female suffering from COVID-19. The experience of using Paxlovid for 2 courses in this patient is worth learning. From December 8, 2022 to January 12, 2023, a total of 59938 COVID-19 related deaths were reported[3] in medical institutions across China, according to the National Health Commission. According to the Xinhua net the majority of COVID-19 deaths were among the elderly, with an average age of 80.3 years, and 90.1% aged 65 or above, and 56.5% aged 80 or above. The

Table 1 Changes of various indexes after admission

Date	White blood cells ($\times 10^9/L$)	Ratio of white blood cells (%)	Lymphocyte count ($\times 10^9/L$)	NT-proBNP (pg/mL)	Creatinine ($\mu\text{mol/L}$)	Creatinine clearance rate (%)	Procalcitonin (pg/mL)
December 28	9.93	80.60%	1.21		250	7.7	
December 29					208	9.2	
December 30	8.26	78.40%	0.8	1604	178	10.8	0.107
January 1	9.03	76.10%	1.44		142	13.5	0.147
January 3	6.81	73.80%	1.09		134	14.3	
January 6	6.94	78.8	0.62	6258	99	19.4	0.095
January 7					102	18.8	
January 9	7.31	75.50%	0.76	5992			
January 11	5.15	78.40%	0.56	5266	104	18.5	0.113
January 13	5.78	54.40%	1.71				0.091
January 14	4.98	65.10%	1.07	4890	90	21.4	0.1
January 16	5.39	57.80%	1.26	4201	98	19.6	0.087
January 18	5.49	63.70%	0.94				
January 19	5.87	61%	1.1	2890			
January 25	6.59	60.70%	1.39				

NT-proBNP: N-terminal pro-brain natriuretic peptide.

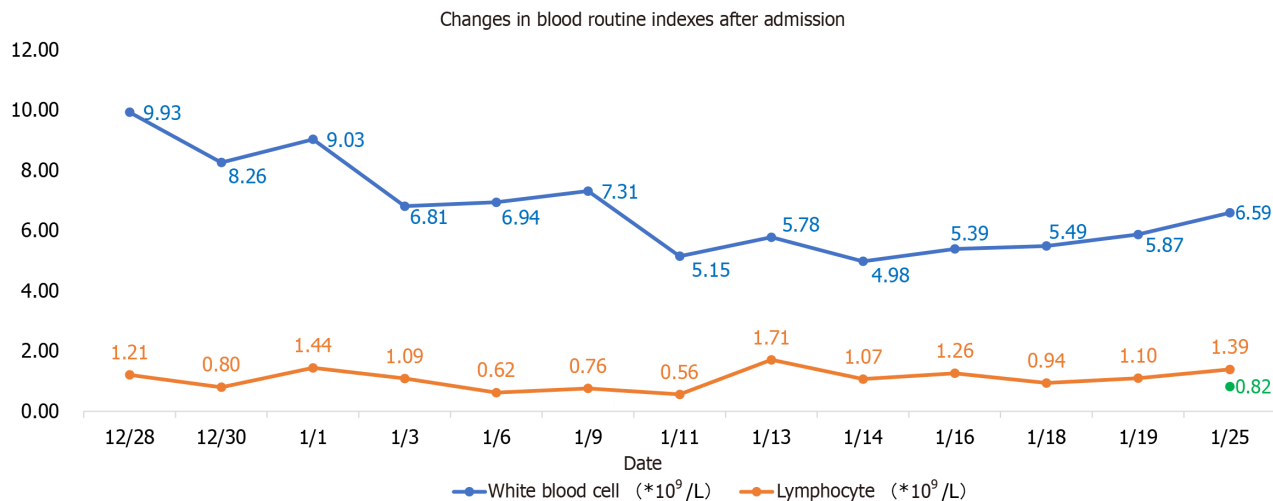


Figure 1 Changes in blood routine indexes after admission: High white blood cells in the early stage of admission, and basically normal in the later stage.

elderly with cardiovascular diseases, obesity, diabetes and weakened immunity, are vulnerable groups[4-6]. The severe disease rate and death rate in elderly COVID-19 patients are significantly higher than those of the general population. The mechanism may be related[7] to inflammatory and immune factors in this aging group. The patient reported in this paper is 103 years old, and has a history of hypertension and belongs to a high-risk COVID-19 patient, which meets the indications for Paxlovid administration[8-9]. Wiersinga *et al*[10] reports among patients hospitalized in the intensive care unit, the case fatality is up to 40%. The "COVID-19 Diagnosis and Treatment Protocol (Trial Version 9)" issued in March 2022 Lists Paxlovid as the first choice for antiviral treatment. The United States Phase III clinical trial showed that Paxlovid can reduce the hospitalization rate and mortality rate of COVID-19 patients by 89%[1]. Paxlovid is indicated for the treatment of adults with mild-to-moderate COVID-19 who have a high risk of progression to severe disease, such as advanced age, chronic kidney disease, diabetes, cardiovascular disease, chronic lung disease and other high risk factors or

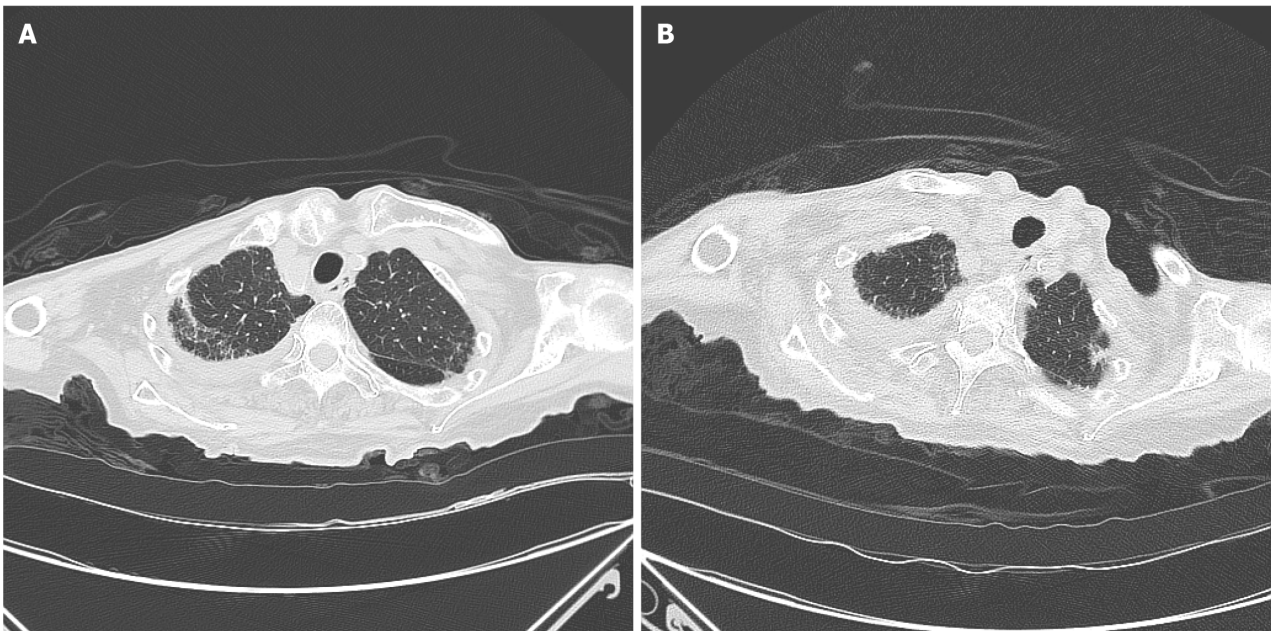


Figure 2 Comparison of lung computed tomography findings. A: Chest computed tomography (CT) findings upon admission on December 29, 2022: Infectious lesions were present in both lungs with a small amount of fluid on both sides, mainly on the right side; B: Chest CT findings before the patient was discharged on January 6, 2023.

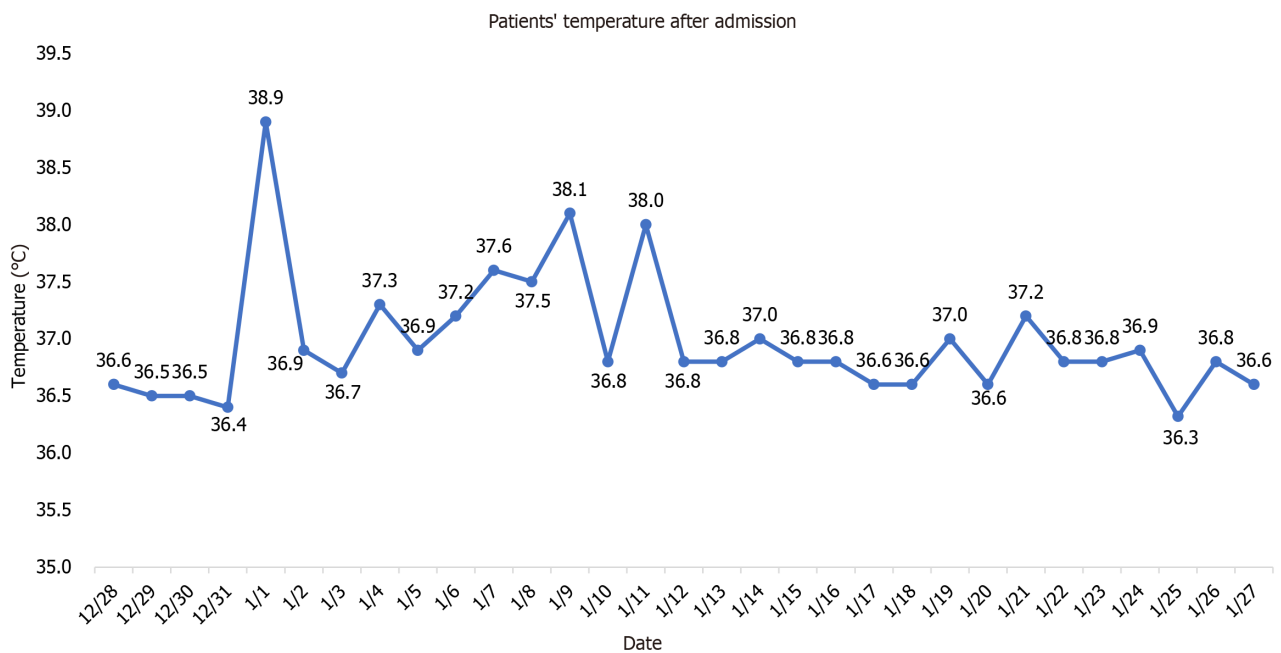


Figure 3 Changes in the patient's body temperature after admission: The patient's body temperature reached the highest 38.9 °C on January 1, 2023, and returned to normal after January 12.

severe disease[11-14]. Lu *et al*[15] studied 180 patients with an average age of 77 years and an average duration of treatment of 10 days, suggesting that the key factors leading to the prolonged treatment of elderly patients with COVID-19 in China are the lack of Paxlovid treatment and the absence of vaccination. All of the above proved that Paxlovid is effective and safe in the treatment of COVID-19.

There are four lessons worth learning from the use of Paxlovid for the long-lived elderly in this case. The first is the treatment plan, full dose for 3 days and half dose for 2 days. This dose is based on the antiviral effect of sufficient dose, and the patient is a long-lived elderly person with low eGFR (less than 30 mL/min), so as to minimize the side effects of the drug. The second is to use two courses of treatment, the second course of treatment is based on the fact that the patient's nucleic acid was positive and the Ct value had a downward trend. Considering the rise of viral load or the signs of the novel coronavirus recurrence, and the drug resistance of centenarians being weaker than that of ordinary people, the antiviral course may be longer. The obvious increase in Ct value after the second course of treatment also verifies our

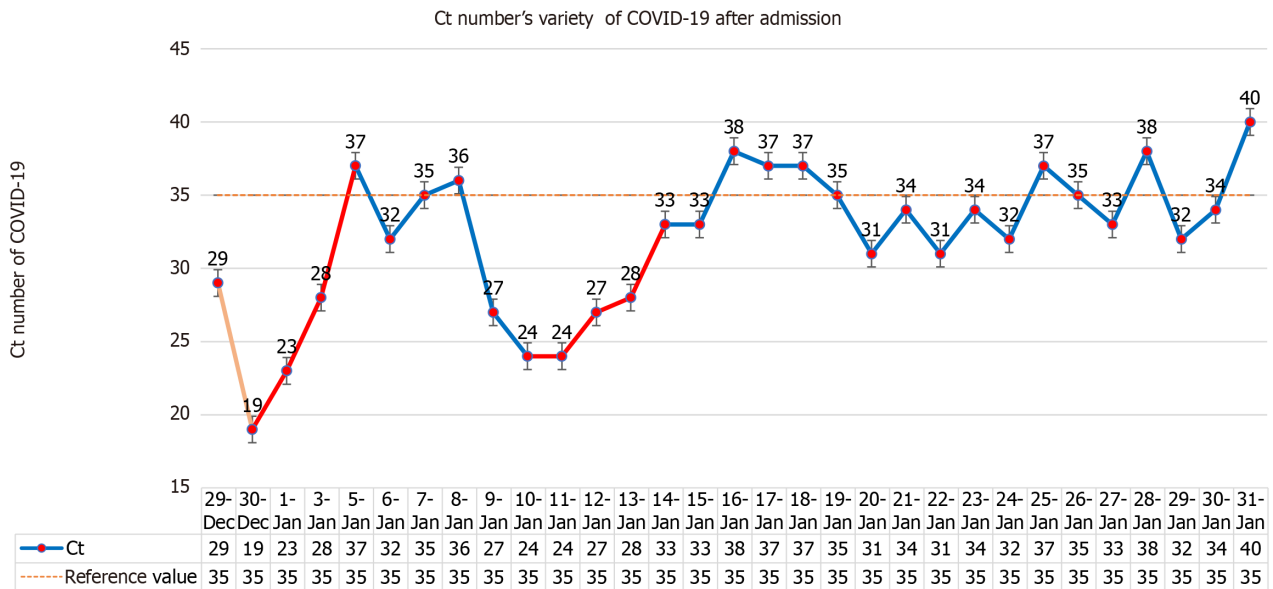


Figure 4 Ct values in this coronavirus disease 2019 patient during hospitalization. COVID-19: Coronavirus disease 2019.

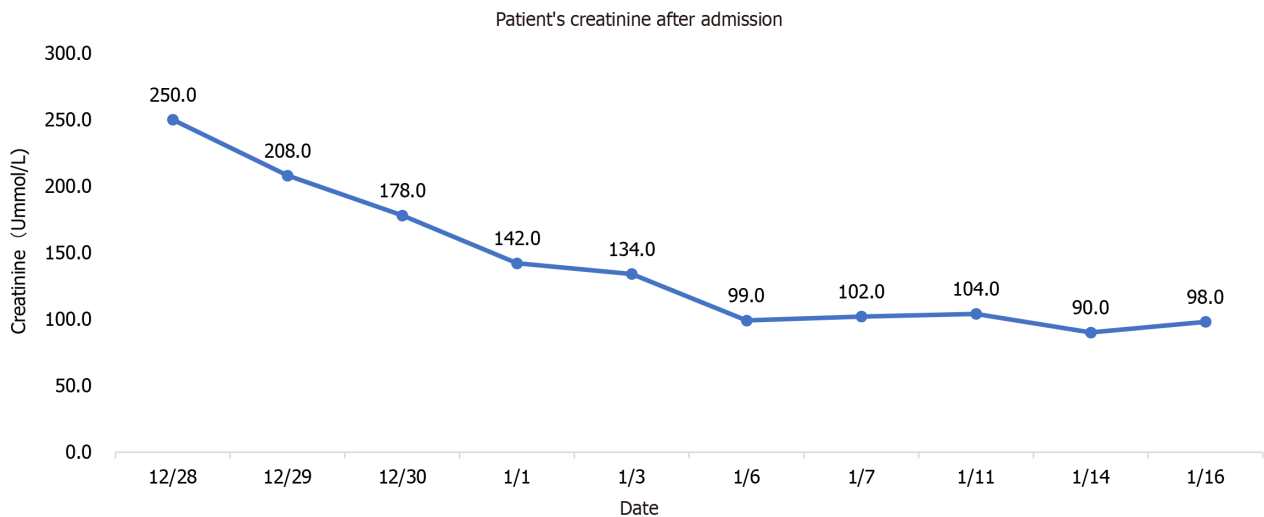


Figure 5 Creatinine changes after admission. The patient's creatinine reached the highest value of 250 $\mu\text{mol/L}$ on December 28, 2022, then gradually decreased, and basically recovered to normal value on January 14, 2023.

idea. The third is $\text{eGFR} < 30 \text{ mL/min}$, which is prohibited according to the instructions. Since patient had no previous history of kidney disease, had low intake of food and fever after infection with COVID-19, and the creatinine increase was considered to be prerenal, nasal feeding is applied to supply fluid and food and the creatinine was significantly reduced. This suggests that the use of some drugs is limited by eGFR . However, we should distinguish whether the patient has underlying kidney disease or renal insufficiency secondary to this disease. If the latter is the case, we can use drugs more aggressively, but in either case, kidney function needs to be closely monitored. The fourth is the use of nasal feeding, the use in the drug instructions is oral, patients with Alzheimer's disease have basically lost their ability to eat autonomously, nasal feeding is the only route to ensure the normal intake of drugs. Although these four drugs are off-label, they are all appropriate treatments for the patient's condition. They are carried out under the condition of repeatedly informing the patient's family of the related risks and closely monitoring liver and kidney function, electrolytes and the patient's condition. The new effects and new use methods of many commonly used drugs in clinical practice are proved by continuous practice. Although the present patient is an individual case, it still provides us with some experience in the use of antiviral drugs for centenarians. The centenarians should use antiviral drugs as soon as possible after diagnosis of COVID-19, which can be given nasally if oral administration is not possible. The course of antiviral drugs may be longer than that of the general population, and the eGFR limit is not so strict, but the liver and kidney function should be closely monitored.

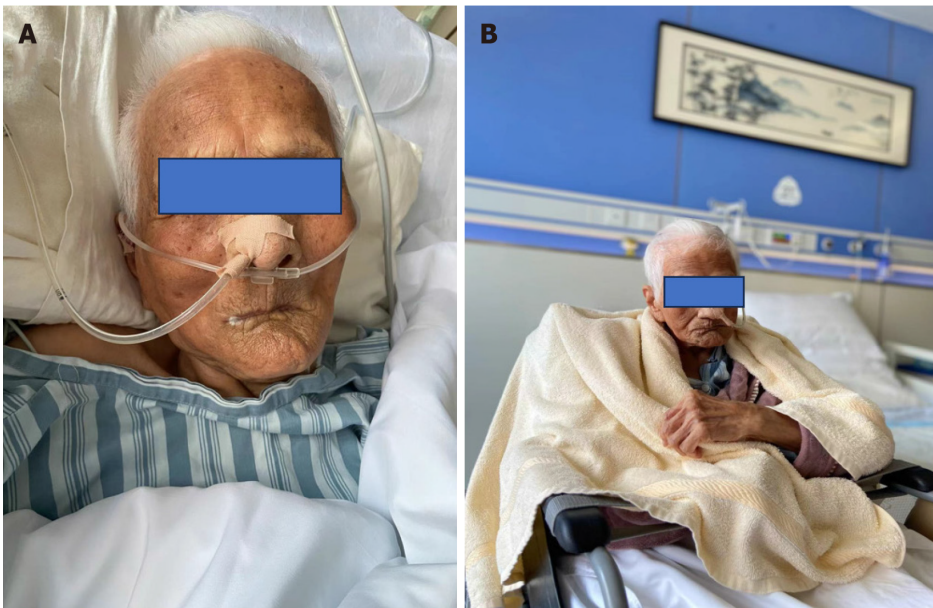


Figure 6 Comparison of the status of the patient during hospitalization and after discharge. A: Indicates the state of the patient at admission: Mental fatigue; B: Is the state of the patient before discharge: Mental fitness, able to sit and stand for half a day.

CONCLUSION

For centenarians infected with COVID-19, Paxlovid should be used as soon as possible to avoid the development of severe disease. If oral administration is not possible, nasal feeding can be used. Generally, one course of treatment is recommended. Due to immune senescence in the elderly, if the nucleic acid has not turned negative, two courses can be used, and the reference standard for eGFR for centenarians can be appropriately adopted. However, close monitoring of liver and kidney function is required.

FOOTNOTES

Author contributions: Zhang YX collected and recorded patient data and wrote the manuscript; Tang J, Zhu D, Wu CY, Liang ML reviewed the literature; Huang YT modified the manuscript. All authors have read and approved the final manuscript.

Informed consent statement: Informed written consent was obtained from the patient for publication of this report and any accompanying images.

Conflict-of-interest statement: The authors declare no conflict of interest.

CARE Checklist (2016) statement: The authors have read the CARE Checklist (2016), and the manuscript was prepared and revised according to the CARE Checklist (2016).

Open-Access: This article is an open-access article that was selected by an in-house editor and fully peer-reviewed by external reviewers. It is distributed in accordance with the Creative Commons Attribution NonCommercial (CC BY-NC 4.0) license, which permits others to distribute, remix, adapt, build upon this work non-commercially, and license their derivative works on different terms, provided the original work is properly cited and the use is non-commercial. See: <https://creativecommons.org/licenses/by-nc/4.0/>

Country of origin: China

ORCID number: Yi-Xue Zhang 0009-0003-5565-5012; Yuan-Tao Huang 0000-0002-6465-7795.

S-Editor: Liu H

L-Editor: A

P-Editor: Wang WB

REFERENCES

- 1 Najjar-Debbiny R, Gronich N, Weber G, Khoury J, Amar M, Stein N, Goldstein LH, Saliba W. Effectiveness of Paxlovid in Reducing Severe

- Coronavirus Disease 2019 and Mortality in High-Risk Patients. *Clin Infect Dis* 2023; **76**: e342-e349 [PMID: 35653428 DOI: 10.1093/cid/ciac443]
- 2 Therapeutics and COVID-19: living guideline [Internet]. Geneva: World Health Organization, 2022 [PMID: 35917393]
- 3 **Mardomi A**, Khosroshahi HT. Dialysis-Induced Immune Dysregulations and Their Possible Impacts on COVID-19. *Iran J Kidney Dis* 2021; **15**: 161-167 [PMID: 33994374]
- 4 **Bailey A**, Harris MA, Bogle D, Jama A, Muir SA, Miller S, Walters CA, Govia I. Coping With COVID-19: Health Risk Communication and Vulnerable Groups. *Disaster Med Public Health Prep* 2021; **17**: e22 [PMID: 34247692 DOI: 10.1017/dmp.2021.225]
- 5 **Zhu Q**, Zhang Y, Kang J, Chen Z, Peng M, Chen M, Zhang G, Xiang D, Xiao S, Li H, Mei Y, Yang J, Qi X, Cai D, Ren H. Weakened humoral and cellular immune response to the inactivated COVID-19 vaccines in Chinese individuals with obesity/overweight. *Genes Dis* 2023; **10**: 608-617 [PMID: 36466314 DOI: 10.1016/j.gendis.2022.10.023]
- 6 **Plumb ID**, Feldstein LR, Barkley E, Posner AB, Bregman HS, Hagen MB, Gerhart JL. Effectiveness of COVID-19 mRNA Vaccination in Preventing COVID-19-Associated Hospitalization Among Adults with Previous SARS-CoV-2 Infection - United States, June 2021-February 2022. *MMWR Morb Mortal Wkly Rep* 2022; **71**: 549-555 [PMID: 35421077 DOI: 10.15585/mmwr.mm7115e2]
- 7 **Panda A**, Arjona A, Sapey E, Bai F, Fikrig E, Montgomery RR, Lord JM, Shaw AC. Human innate immunosenescence: causes and consequences for immunity in old age. *Trends Immunol* 2009; **30**: 325-333 [PMID: 19541535 DOI: 10.1016/j.it.2009.05.004]
- 8 **Piroth L**, Cottenet J, Mariet AS, Bonniaud P, Blot M, Tubert-Bitter P, Quantin C. Comparison of the characteristics, morbidity, and mortality of COVID-19 and seasonal influenza: a nationwide, population-based retrospective cohort study. *Lancet Respir Med* 2021; **9**: 251-259 [PMID: 33341155 DOI: 10.1016/S2213-2600(20)30527-0]
- 9 **Stokes EK**, Zambrano LD, Anderson KN, Marder EP, Raz KM, El Burai Felix S, Tie Y, Fullerton KE. Coronavirus Disease 2019 Case Surveillance - United States, January 22-May 30, 2020. *MMWR Morb Mortal Wkly Rep* 2020; **69**: 759-765 [PMID: 32555134 DOI: 10.15585/mmwr.mm6924e2]
- 10 **Wiersinga WJ**, Rhodes A, Cheng AC, Peacock SJ, Prescott HC. Pathophysiology, Transmission, Diagnosis, and Treatment of Coronavirus Disease 2019 (COVID-19): A Review. *JAMA* 2020; **324**: 782-793 [PMID: 32648899 DOI: 10.1001/jama.2020.12839]
- 11 **Hammond J**, Leister-Tebbe H, Gardner A, Abreu P, Bao W, Wisemandle W, Baniecki M, Hendrick VM, Damle B, Simón-Campos A, Pypstra R, Rusnak JM; EPIC-HR Investigators. Oral Nirmatrelvir for High-Risk, Nonhospitalized Adults with Covid-19. *N Engl J Med* 2022; **386**: 1397-1408 [PMID: 35172054 DOI: 10.1056/NEJMoa2118542]
- 12 **Singh AK**, Singh A, Singh R, Misra A. Molnupiravir in COVID-19: A systematic review of literature. *Diabetes Metab Syndr* 2021; **15**: 102329 [PMID: 34742052 DOI: 10.1016/j.dsx.2021.102329]
- 13 **Senderovich H**, Vinoraj D, Stever M, Waicus S. Efficacy of COVID-19 treatments among geriatric patients: a systematic review. *Ther Adv Infect Dis* 2022; **9**: 20499361221095666 [PMID: 35677110 DOI: 10.1177/20499361221095666]
- 14 **Catlin NR**, Bowman CJ, Campion SN, Cheung JR, Nowland WS, Sathish JG, Stethem CM, Updyke L, Cappon GD. Reproductive and developmental safety of nirmatrelvir (PF-07321332), an oral SARS-CoV-2 M(pro) inhibitor in animal models. *Reprod Toxicol* 2022; **108**: 56-61 [PMID: 35101563 DOI: 10.1016/j.reprotox.2022.01.006]
- 15 **Lu G**, Zhang Y, Zhang H, Ai J, He L, Yuan X, Bao S, Chen X, Wang H, Cai J, Wang S, Zhang W, Xu J. Geriatric risk and protective factors for serious COVID-19 outcomes among older adults in Shanghai Omicron wave. *Emerg Microbes Infect* 2022; **11**: 2045-2054 [PMID: 35924388 DOI: 10.1080/22221751.2022.2109517]



Published by **Baishideng Publishing Group Inc**
7041 Koll Center Parkway, Suite 160, Pleasanton, CA 94566, USA
Telephone: +1-925-3991568
E-mail: office@baishideng.com
Help Desk: <https://www.f6publishing.com/helpdesk>
<https://www.wjgnet.com>

